

Acoustic detection of ultra-high energy cascades in ice

DISSERTATION

zur Erlangung des akademischen Grades
doctor rerum naturalium
(Dr. rer. nat.)
im Fach Physik

eingereicht an der
Mathematisch-Naturwissenschaftlichen Fakultät I
Humboldt-Universität zu Berlin

von
Herrn Dipl.-Phys. Sebastian Böser
geboren am 08.12.1977 in Starnberg

Präsident der Humboldt-Universität zu Berlin:
Prof. Dr. Christoph Marksches

Dekan der Mathematisch-Naturwissenschaftlichen Fakultät I:
Prof. Dr. Christian Limberg

Gutachter:

1. Prof. Dr. Hermann Kolanoski
2. Prof. Dr. Allan Hallgren
3. Prof. Dr. David Z. Besson

eingereicht am:	13. Oktober 2006
Tag der mündlichen Prüfung:	8. Dezember 2006

Abstract

Current underwater optical neutrino telescopes are designed to detect neutrinos from astrophysical sources with energies in the TeV range. Due to the low fluxes and small cross sections, no high energy neutrinos of extraterrestrial origin have been observed so far. Only the Cherenkov neutrino detectors on the km^3 scale that are currently under construction will have the necessary volume to observe these rare interactions. For the guaranteed source of neutrinos from interactions of the ultra-high energy cosmic at EeV energies rays with the ambient cosmic microwave background, event rates of only one per year are expected in these experiments.

To measure the flux and verify the predicted cross sections of these cosmogenic neutrinos, an observed volume of the order of 100 km^3 will be necessary, that will not be feasible with existing detection techniques. Alternative methods are required to build a detector on these scales.

One promising idea is to record the acoustic waves generated in hadronic or electromagnetic cascades following the neutrino interaction. The higher amplitudes of the sonic signal and the large expected absorption length of sound favour South Polar ice instead of sea water as a medium. The prerequisites for an estimate of the potential of such a detector are suitable acoustic sensors, a verification of the model of thermo-acoustic sound generation and a determination of the acoustic properties of the ice. In a theoretical derivation the mechanism of thermo-elastic excitation of acoustic waves was shown to be equivalent for isotropic solids and liquids. Following a detailed analysis of the existing knowledge a simulation study of a hybrid optical-radio-acoustic detector has been performed. Ultrasonic sensors dedicated to in-ice application were developed and have been used to record acoustic signals from intense proton and laser beams in water and ice. With the obtained experience, the hitherto largest array of acoustic sensors and transmitters was devised and implemented, with the aim to study the ultrasonic properties of the South Polar ice in-situ. Results from all of these first efforts will be presented in this work.

Keywords:

neutrino, acoustic, cascade, South Pole

Zusammenfassung

Existierende optische Unterwasser-Neutrino-teleskope sind für den Nachweis von Neutrinos aus astrophysikalischen Quellen mit Energien im TeV Bereich optimiert. Aufgrund der geringen Flüsse und Wirkungsquerschnitte wurden jedoch bislang keine hochenergetischen Neutrinos extraterrestrischen Ursprungs beobachtet. Erst die derzeitlich im Bau befindlichen kubikkilometer-großen Cherenkov-Neutrino-detektoren werden das notwendige Volumen haben, um diese seltenen Wechselwirkungen nachzuweisen. Für die garantierte Quelle von Neutrinos aus Wechselwirkungen der ultrahochenergetischen kosmischen Strahlung im EeV-Bereich mit dem kosmischen Mikrowellenhintergrund wird dennoch nicht mehr als ein Ereignis im Jahr in diesen Experimenten erwartet.

Nachweisvolumen in der Größenordnung von 100 km^3 werden notwendig sein, um den Fluß dieser Neutrinos zu bestimmen und die vorhergesagten Wirkungsquerschnitte zu überprüfen. Existierende Detektionsmethoden sind dafür nicht geeignet, so daß alternative Meßtechniken erforderlich sind, um einen Detektor dieses Ausmaßes zu realisieren.

Eine vielversprechende Idee ist die Erfassung akustischer Wellen aus den in der Neutrino-wechselwirkung erzeugten hadronischen und elektromagnetischen Kaskaden. Aufgrund der höheren Signalstärke und der erwarteten großen Schalldämpfungslängen ist dafür die Eiskecke des Südpols dem Wasser der Ozeane als Medium vorzuziehen. Als Voraussetzungen zur Abschätzung des Potentials eines solchen Detektors sind jedoch zunächst geeignete Sensoren, eine Überprüfung des Modells der thermo-akustischen Schallerzeugung und genaue Kenntnisse der akustischen Eigenschaften des Eises von Nöten. In einer theoretischen Ableitung konnte die Äquivalenz der Mechanismen der Erzeugung akustischer Wellen durch thermo-elastische Anregung in Flüssigkeiten und isotropen Festkörpern gezeigt werden. Einer detaillierten Analyse des existierenden Wissensstandes folgte die Simulation eines kombinierten Cherenkov-Radiowellen-Ultraschall-Detektors. Für den Einsatz im Eis wurden spezielle akustische Sensoren entwickelt und zur Erfassung der Schallemission von intensiven Protonen- und Laserstrahlen im Wasser und Eis eingesetzt. Mit den gewonnenen Erfahrungen wurde der bislang größte akustische Sender- und Empfänger-Aufbau entwickelt, mit der Zielsetzung, die Ultraschalleigenschaften des südpolaren Eises in-situ zu untersuchen. Die Ergebnisse aller dieser ersten Bemühungen werden in dieser Arbeit vorgestellt.

Schlagwörter:

Neutrino, Akustik, Kaskade, Südpol

Contents

1	Preface	1
2	Motivation	5
2.1	Ultra-high energy cosmic rays	5
2.1.1	Charged cosmic ray spectrum	5
2.1.2	The GZK cutoff	7
2.2	Neutrinos in cosmic rays	12
2.2.1	Cosmogenic neutrinos	12
2.2.2	Other UHE neutrino sources	14
2.2.3	Neutrino flavours	19
2.2.4	Detection methods	20
3	Prerequisites	29
3.1	Cosmogenic neutrino flux	29
3.2	Neutrino interactions	33
3.2.1	Cross sections	33
3.3	Secondaries and cascades	35
3.3.1	Neutrino flavours	35
3.3.2	Cascades	36
3.3.3	Longitudinal shower profile	37
3.3.4	Radial shower profile	39
3.4	Thermo-acoustic model	41
3.4.1	In liquids	41
3.4.2	In solids	43
3.5	Ultrasonic ice properties	48
3.5.1	Velocity of sound	49
3.5.2	Absorption	50
3.5.3	Scattering	52
3.5.4	Ambient noise	54
3.6	Ultrasonic sensors	55
4	Simulation of a hybrid optical – radio – acoustic detector	57
4.1	Motivation	57
4.2	Simulation	58
4.3	Results	60

5	Sensor and transmitter developement	63
5.1	Sensor principles	63
5.1.1	Piezoelectric ceramics	63
5.1.2	Impedance and materials	65
5.1.3	Resonances	66
5.1.4	Amplifier	69
5.2	Sensor prototypes	71
5.3	Sensor evaluation	74
5.3.1	Calibration methods	74
5.3.2	Calibration in water	75
5.3.3	Evaluation in ice	80
5.4	Transmitter	87
6	Thermo-acoustic sound generation	91
6.1	Signal predictions	91
6.2	Experimental results	93
6.2.1	Water as a target	95
6.2.2	Ice as a target	98
7	South Pole acoustic test setup (SPATS)	105
7.1	Overview	105
7.2	Sensors and transmitters	107
7.2.1	Sensor design	108
7.2.2	Sensor calibration	108
7.2.3	Transmitter design	113
7.2.4	Transmitter calibration	115
7.3	System control, data aquisition, communication and time synchronisation . .	116
7.4	System verification	119
7.4.1	Performance at low temperatures	119
7.4.2	Interference with ICECUBE	121
7.4.3	Performance over long distances	122
7.5	Principle of measurements and performance estimates	126
7.5.1	Ambient background noise	126
7.5.2	Refraction and velocity of sound	128
7.5.3	Absorption length	130
8	Summary and outlook	133

List of Figures

2.1	Flux of ultra-high energetic cosmic rays measured by different experiments (from [GSS05]).	5
2.2	Total energy loss length (solid line) for high energy protons (left) and iron nuclei (right). The different contributions are pair-production (e^+e^-), photo-production of pions (πN) on the cosmic microwave background and photo-disintegration on the optical (OP), infrared (IR) and microwave background (CMB). Energy loss due to redshift is also shown in the left figure (from [DM05]).	7
2.3	Energy spectrum of cosmic rays as observed by AGASA (left) and HiRES (right). The spectra are scaled with E^3 . The lines show a fit for a spectral shape as expected for a uniform source distribution with absolute flux and spectral shape as free parameters (from [H ⁺ 00] and [Ber05b]).	10
2.4	Angular correlation function for AGASA events with $E > 4 \cdot 10^{19}$ eV. The dotted line shows the expectation for a uniform distribution of the sources (from [H ⁺ 00]).	11
2.5	Composition of ultra-high energetic cosmic rays as measured by AKEANO (A1), AGASA, HiRES, VULCANO RANCH (VR) and HAVERAH PARK (HP). (from [H ⁺ 00]).	11
2.6	Flux of electron (blue, solid) and muon (red, dashed) GZK neutrinos relative to a generic input spectrum (green band) for different propagation distances (from [ESS01]).	13
2.7	Flux of GZK neutrinos for different primary masses (from [HTS05]).	13
2.8	Per-flavour flux of GZK neutrinos for a <i>low</i> prediction from [ESS01] and a <i>high</i> prediction with $E_{max} = 10^{23}$ eV from [KKSS02b]. Experimental limits (see section 2.2.4, grey areas) and indirect bounds from cosmic ray observations [FKRT03a] (pink areas with dashed lines) are shown as well.	14
2.9	Unified model of an active galactic nucleus: the characteristic properties depend on the viewing angle of the observer (from [Urr03]).	15
2.10	Per-flavour neutrino flux predictions for <i>active galactic nuclei</i> (AGN) [Man95] and photo-production of pions in the cosmic ray sources [A ⁺ 05c]. Also shown are theoretical bounds from cosmic and gamma ray observations assuming the cosmic ray sources to be neutrino sources [MPR01, WB99, BW01] (dotted lines) and current experimental limits (grey areas).	15
2.11	Cross-sections for various $\nu\nu$ interactions (from [Sec98]).	17

2.12	Per-flavour neutrino flux predictions from the <i>Z-burst</i> model: a generic model with $m_\nu = 0.5 \text{ eV}$ [KKSS02a] and the peak fluxes assuming a <i>single source</i> of cosmic rays or a <i>uniform</i> distribution [FKR02]. The current experimental limits are shown as grey areas.	17
2.13	Schematic illustration of the generation of topological defects (from [Gan03]).	18
2.14	Per-flavour neutrino flux predictions for <i>normal</i> and <i>hidden</i> topological defects with $m_{TD} = 2 \cdot 10^{14} \text{ eV}$ and $m_\nu = 1 \text{ eV}$ [KKSS02b]. The current experimental limits are shown as grey areas.	18
2.15	Limits on the extraterrestrial neutrino flux from AMANDA-II [A ⁺ 04a] and FLY'S EYE [B ⁺ 85]. A selection of flux predictions is shown for comparison (see section 2.2.2).	21
2.16	Schematic view of the EUSO experiment (from [Bot05]).	21
2.17	Model independent limits on the neutrino flux from RICE [K ⁺ 06], ANITA-LITE [B ⁺ 06b], GLUE [G ⁺ 04] and FORTE [LGJRD04]. A selection of flux predictions is shown for comparison (see section 2.2.2).	23
2.18	Time-aligned radio pulses from an air shower recorded with the LOPES antennas (from [H ⁺ 06]).	23
2.19	Model independent neutrino flux limit from SAUND [VGL05]. A selection of flux predictions is shown for comparison (see section 2.2.2).	25
3.1	Cosmogenic neutrino flux for a source evolution parameter $m = 4$ and two different values of Ω_Λ [ESS01].	30
3.2	Cosmogenic neutrino flux for a source evolution parameter $m = 3$, a maximum source energy of $E_{max} = 3 \cdot 10^{22}$ and different values of α [KKSS02b].	30
3.3	Cosmogenic neutrino flux for a source evolution parameter $m = 3$, an input spectral index $\alpha = 1.5$ and different values of E_{max} [KKSS02b].	31
3.4	Cosmogenic neutrino flux for different source evolution parameters m and z_{max} and an input spectrum with index $\alpha = 2$ up to $E_{max} = 1 \cdot 10^{22}$ [YT93].	31
3.5	Cosmogenic neutrino flux predictions from various authors – for details see text (adapted from [G ⁺ 05]).	32
3.6	Total cross section (charged plus neutral current) for neutrino-nucleon interactions for various parton distribution functions (from [Rin06]).	33
3.7	Neutrino-nucleon cross section for the Standard Model $\sigma_{\nu N}^{cc}$ compared to the range of predictions from the electro-weak instanton models ($\sigma_{\nu N}^{(I)}$) [FKRT04] and p-brane models ($\sigma_{\nu N}^{(p)}$) [AFG02].	33
3.8	$\bar{\nu}$ interaction length vs. energy for total, charged and neutral current cross sections (from [GQRS96]).	34
3.9	Mean inelasticity for ν and $\bar{\nu}$ vs. neutrino energy (from [GQRS96]).	34
3.10	Average position of the shower maximum in e^- and γ initiated showers from a simulation in water. Error bars give standard deviations for a single cascade event. The line indicates extrapolations with and without inclusion of the LPM effect (from [NB05]).	38
3.11	Examples of longitudinal development of LPM extended cascades in water at various energies (from [NB05]).	38
3.12	Longitudinal development of the electron density in hadronic cascades for various energies (from [AMZ99]).	39

3.13	Probability to have a photon with energy E_γ or larger in a hadronic cascade of energy E_0 (from [AMZ99]).	39
3.14	Normalized radial energy density distribution at the shower maximum x_{max} for $E_0 = 500$ TeV. The solid lines show two different parameterisations (from [Nie05]).	40
3.15	Time profile of the acoustic pressure amplitude in sea water at a perpendicular distance of 400 m from a 10 PeV cascade as calculated by [Lea79] (1), [ADKM79] (2) and [D ⁺ 94] (3) (from [D ⁺ 97b]).	43
3.16	Dependence of the peak pressure amplitude ΔP on the angle relative to the cascade axis for a 10 PeV shower in a 10 km distance from the cascade. $\theta = 0$ denotes the plane perpendicular to the cascade (from [D ⁺ 97a]).	43
3.17	Phase diagram of water/ice.	48
3.18	Temperature profile of the antarctic ice at South Pole (from [PNB ⁺ 02]). . . .	49
3.19	Density profile of the upper layers in antarctic ice at South Pole (from [Alb98]).	49
3.20	Velocity of sound for longitudinal and transversal waves at South Pole derived from density data in [Alb98].	50
3.21	All-depth sound velocity profile (red, dashed) and ray-traces (blue, solid) of a hypothetical point sources at a depth of 100 m for different emission angles (from [Van04]).	50
3.22	Absorption length of sea water with contributions from MgSO_4 and $\text{B}(\text{OH})_3$ (from [Pri06]).	51
3.23	Predicted absorption length of Ih ice for different temperatures (from [Pri06]).	52
3.24	Predicted absorption profile for acoustic waves in the bulk ice at South Pole (from [Van04]).	52
3.25	Velocity of sound in monocrystalline ice for longitudinal (L) and transversal ($T_{1 2}$) modes in dependence of the angle γ to the crystal axis. Values for different pressures in kbar are given. (from [GKCW88]).	53
3.26	Scattering coefficient from grain boundaries for polycrystalline Ih ice for different grain sizes (from [Pri06]).	53
3.27	Spectral power density of ambient noise in open seas in dependence of wind speed. Numbers in parenthesis give integral probabilities for these or better conditions. The spectrum of a neutrino induced acoustic signal in arbitrary units is overlaid (from [LAG ⁺ 02]).	54
4.1	Top-view of the simulated array of radio, acoustic and additional optical receivers around the planned ICECUBE array.	59
4.2	Effective neutrino volume versus energy for the different detection methods and their combinations: ICECUBE (I), optical (O), radio (R) and acoustic (A).	61
5.1	Perovskite crystal structure of lead zirconate titanate (<i>PZT</i>) above and below the Curie temperature T_C	64
5.2	Picture of commercially available <i>PZT</i> ceramics in various shapes.	64
5.3	Induced surface charge Q for a <i>PZT</i> ceramic loaded with a mass m and measured with different shunt resistor values R_{shunt}	65
5.4	Measured and simulated impedance of a free piezo-ceramic. (from [Ste04]) .	67

5.5	Schematic drawing of an embedded sensor (left) and a sensor in a pressure housing (right).	68
5.6	Measured overall amplification factor of the 3-stage amplifier.	69
5.7	Noise development with temperature for different sensor types. The solid line is the theoretical prediction.	69
5.8	Pictures of the <i>glass bowl</i> sensor (left) an acoustic channel (middle) and a schematic drawing (right).	71
5.9	Pictures (left) and schematic drawing (right) of an <i>epoxy sensor</i>	73
5.10	Picture (left) and schematic drawing (right) of the <i>glass ball</i> sensor.	73
5.11	Pictures of the <i>iron ball</i> sensor (left) and a schematic drawing (right).	73
5.12	Scheme of the different input pulses (top), the corresponding sensor response (middle) and its Fourier spectrum (bottom) for the <i>gated burst</i> (left) and <i>single pulse</i> (right) method.	76
5.13	Example of the sensor response of the reference hydrophone to a <i>gated burst</i> signal (top) and a <i>single pulse</i> (bottom). The fit to determine the amplitude for the <i>gates burst</i> signal (top) and the electrical input signal to the transmitter (bottom) are also shown.	76
5.14	Sensitivity of the <i>glass ball</i> sensor relative to the reference hydrophone determined with the <i>gated burst</i> and <i>single pulse</i> method.	78
5.15	Sensitivity of the <i>iron ball</i> sensor relative to the reference hydrophone determined with the <i>gated burst</i> and <i>single pulse</i> method.	78
5.16	Setup for growing large blocks of clear ice (from [Kri06]).	81
5.17	Clear ice from a small test volume (from [Kri06]).	82
5.18	Epoxy sensor in a ≈ 40 cm thick block of clear ice (from [Kri06]).	82
5.19	Electric signal applied at a <i>PZT</i> element.	83
5.20	Emmitted acoustic signal.	83
5.21	Spectrum of acoustic signal.	83
5.22	Signal amplitude of 1 st peak vs. peak frequency for the <i>iron ball</i> , <i>glass bowl</i> and <i>epoxy sensor</i> for $U_{in} = 0.2$ V in water (from [Ste04]).	84
5.23	Signal amplitude of 1 st peak vs. input peak amplitude for the <i>iron ball</i> and <i>epoxy sensor</i> for $f_{peak} = 25$ kHz in ice (from [Ste04]).	84
5.24	Directional acoustic emitter with parabolic reflector (from [Kri06]).	85
5.25	Amplitude of acoustic signal vs. polar angle in a water setup for $f_{peak} = 20$ kHz and $f_{peak} = 40$ kHz (from [Kri06]).	86
5.26	Amplitude of acoustic signal vs. polar angle in an ice setup for $f_{peak} = 20$ kHz and $f_{peak} = 35$ kHz (from [Kri06]).	86
5.27	Transmitter with a cylindrical <i>PZT</i> element cast in epoxy.	87
5.28	Transmitter with a ring-shaped <i>PZT</i> element sealed with o-rings.	87
5.29	Transmitter with a ring-shaped <i>PZT</i> element cast in epoxy.	87
5.30	Acoustic signal amplitude vs. peak electric input amplitude for a ring-shaped piezo-ceramic in water.	88
5.31	Acoustic signal spectrum of ring-shaped and cylindrical <i>PZT</i> emitters activated by a white noise electrical signal at different geometric configurations.	88
5.32	Pulse amplitude vs. polar angle of cylindrical ceramics for different ceramic diameters (from [Kri06]).	89

5.33	Pulse amplitude vs. polar angle of cylindrical ceramics for different values of f_{peak} (from [Kri06]).	89
5.34	Signal amplitude vs. inverse distance for a ring-shaped ceramic in a large water tank (from [Fis06]).	90
5.35	Signal amplitude vs. distance for a surface mounted transmitter on a small ice block (from [Ste04]).	90
6.1	Calculated energy deposit as a function of radius r and distance z along the beam axis for a <i>Nd:YAG</i> laser of 62.4 PeV per pulse in ice.	92
6.2	Simulated energy deposit as a function of radius r and distance z along the beam axis for a 38.7 PeV bunch of protons at 177 MeV in ice.	92
6.3	Acoustic amplitude as generated by a 177 MeV proton beam in water for a bunch energy of 18 PeV at the time $t = 0.2$ ms (from [Gra04])	93
6.4	Acoustic signal amplitude from a proton beam for various materials, corrected for penetration depth (from [S ⁺ 79]).	94
6.5	Characteristic frequency f as a function of beam width σ_{beam} (from [S ⁺ 79]).	94
6.6	Picture of the water setup at the proton beam (from [Gra04], left) and laser beam (from [GAH ⁺ 06], right).	96
6.7	Temperature dependence of thermo-acoustic signal amplitude in water from a laser [GAH ⁺ 06].	96
6.8	Temperature dependence of thermo-acoustic signal amplitude in water from a proton-beam [GAH ⁺ 06].	96
6.9	Schematic drawing of the setup in the water tank (from [Gra04]).	97
6.10	Signal amplitude vs. distance for the proton beam setup in water [GAH ⁺ 06].	97
6.11	Picture of the ice setup at the proton beam without (left) and with (right) insulation.	98
6.12	Schematic drawing of the setup in the two ice blocks.	98
6.13	Acoustic signal amplitude vs. proton bunch energy for the setup with the <i>glass ball</i> sensor at $T = -25^\circ\text{C}$ and $d = 65$ cm (from [Ste04]).	99
6.14	Acoustic signal amplitude vs. proton bunch energy for the setup with the <i>iron ball</i> sensor at $T = -15^\circ\text{C}$ and $d = 20$ cm (from [Ste04]).	99
6.15	Signal shape of the <i>epoxy sensor</i> at different beam energies at $T = -25^\circ\text{C}$ and $d = 65$ cm (from [Ste04]).	100
6.16	Signal shape of the <i>glass ball</i> sensor for different beam profiles at similar energies at $T = -15^\circ\text{C}$ and $d = 20$ cm (from [Ste04]).	100
6.17	Signal amplitude vs. distance for the <i>iron ball</i> and <i>epoxy sensor</i> . The lines show a (combined) near-field and far-field fit.	101
6.18	Temperature dependent signal amplitude of the <i>glass ball</i> and <i>epoxy sensor</i> excited with a proton beam (from [Ste04]).	102
6.19	Temperature dependent signal amplitude of the <i>epoxy sensor</i> excited with a laser beam (from [Kri06]).	102
7.1	Schematic drawing of the SOUTH POLE ACOUSTIC TEST SETUP.	106
7.2	Picture of an acoustic stage.	107
7.3	Picture and schematic drawing of an open SPATS sensor module seen from above.	108

7.4	Schematic of the setup to measure the d_{33} coefficient of a piezo-ceramic. . . .	109
7.5	Measured d_{33} coefficient versus piezo-ceramic numbers. The red lines indicate the range of ceramics used for the SPATS sensors.	109
7.6	Schematic illustration of the noise contribution to a steady sensor response for a single frequency in the complex plane.	110
7.7	Difference of <i>white noise</i> amplitude spread σ_N to amplitude spread in presence of a signal σ_{S+N} for different frequencies.	110
7.8	Sensitivity spectrum of SPATS sensor module #3 for all three channels: A (black), B(red), C(green) and amplifier gain (blue).	111
7.9	Sensitivity range per frequency and mean sensitivity of all SPATS sensors. .	112
7.10	Equivalent self noise spectrum for the three channels: A (black), B(red) and C(green) in the SPATS sensor module #3 and for the reference hydrophone (purple).	113
7.11	Range of the equivalent self noise spectrum for all SPATS sensors: channels are A(black), B(red) and C(green) respectively.	113
7.12	Ring-shaped ceramics cast in epoxy as used for the SPATS transmitters. . .	113
7.13	Superimposed electrical high-voltage pulses generated with SPATS transmitter #1.	114
7.14	Amplitude of acoustic pulse versus peak amplitude of the high-voltage pulse applied to the ceramics.	114
7.15	Peak pulse amplitude of ring transmitter in the azimuthal plane.	115
7.16	Peak pulse amplitude of ring transmitter in the polar plane.	115
7.17	Acoustic pulse generated by a SPATS transmitter and recorded with the reference hydrophone.	116
7.18	Distribution of the gradient of a linear fit of acoustic pulse amplitude versus high-voltage pulse for all SPATS transmitters.	116
7.19	Top-view into an <i>acoustic box</i>	117
7.20	Top-view into the <i>Master-PC</i>	118
7.21	Peak-to-peak amplitude versus temperature of two channels of a SPATS module for acoustic transmission through air.	120
7.22	Temperature development over 24 hours at different positions in the freezer: at the bottom (pink), in the air next to (yellow) and inside (green) the <i>acoustic box</i> and on the outside of the DSL modem (red). The <i>String-PC</i> was powered up at 5 : 30 hrs.	120
7.23	Setup of an acoustic stage connected by 430 m test cables to an <i>acoustic box</i> in the freezer.	121
7.24	Picture of the equipment used in the long range SPATS module test at the frozen lake <i>Torneträsk</i> in northern Sweden.	123
7.25	Signal from a SPATS transmitter recorded with a SPATS sensor at a distance of ≈ 800 m in water.	123
7.26	Picture of the large scale setup at Abisko: the position of the data acquisition shelter, the 400 m <i>north</i> hole and the 400 m <i>south</i> hole (outside the picture on the left) are indicated.	123
7.27	Calculated sensor transmitter distance d_{S-T} vs. signal arrival time for different assumptions of the transmitter depth (colours) and best fit values.	124

7.28	Delay Δt_{ref} of reflected signal relative to the direct signal vs. depth of the sensor. The solid lines is a theoretical prediction (from [Des06]).	124
7.29	Variation of signal amplitude for different transmitter modules and different piezo-ceramics at the same transmitter module at a distance of 100 m averaged over the depth (from [Des06]).	125
7.30	Signal amplitude averaged over 10 events for various distances and depth (colours) using different transmitters (from [Des06]).	125
7.31	Scheme of a refracted acoustic wave emitted from transmitter T and received by sensor S. In the presence of a velocity gradient $\frac{\partial v}{\partial d}$ the wave will travel along the curved path x	127
7.32	Arrival time delay Δt at different sender-receiver distances Δr as expected at different depth levels d . The points and error bars show the expected configuration in the SPATS setup.	127
7.33	Offset corrected time difference of rising edges from external square wave and <i>IRIG-B</i> time code.	129
7.34	Distribution of resulting velocity gradients $\frac{\partial v}{\partial d}$ and difference to nominal speed of sound Δv for fits to the simulated time and distance measurements for various depth levels d . The contour lines show 50 %,10 % and 1 % of the peak values, the dots give the nominal values.	129
7.35	Sensitivity and transmittivity independent amplitude ratio vs. distance for one possible detector configuration. The red line indicates the fit result. . . .	130
7.36	Distribution of absorptivity derived from the fit. The blue line shows a Gaussian fit to the distribution.	130
7.37	Derived mean absorptivity (red points) and Gaussian error (blue points and lines) vs. input absorptivity.	132

List of Tables

2.1	Most relevant parameters for acoustic neutrino detection in the ocean, in ice or in rock salt (from [Pri06]).	26
4.1	Number of cosmogenic neutrino events per year from the simulation detected by the different methods and their combinations.	62
5.1	Acoustic properties of various materials (from [Mil87]). The values are temperature dependent.	66
5.2	Relative sensitivities at different frequencies obtained with the <i>gated burst</i> and the <i>single pulse</i> method.	79
5.3	Equivalent self noise level in the frequency range from 5 – 65 kHz.	79
5.4	Geometry and polarisation direction with respect to the symmetry axis for the different <i>PZT</i> elements.	89
6.1	Properties of the proton beams used in the different experiments to verify the thermo-acoustic effect.	95
6.2	Properties of the laser beams used to verify the thermo-acoustic effect. . . .	95
6.3	Beam width in horizontal (σ_x) and vertical (σ_y) direction for the three different beam configurations	100

Chapter 1

Preface

One of the fundamentals of cognition is the concept of perception. Information about the surrounding reality is continuously registered by all the senses, which themselves are sensitive to different aspects of the reality. With the eyes for example various states of brightness can be distinguished, while the skin, amongst other things, is sensitive to changes in temperature. The combined *information* is transferred to the brain, where from the multitude of neural stimuli the perception is created. In some cases, based on previous experience, from the perception also a conclusion is drawn, such as "the sun is shining".

In a similar way, physicists draw conclusion from an experiment. The *eyes* and *ears*, i.e. the means by which information is obtained, is the experimental apparatus. The gathered data is combined, processed and finally may – or may not – allow some conclusion on the reality, i.e. the underlying physics process that the experimentalist sought to probe. The conclusion that is drawn by the physicist may not be unambiguous. As in the case of human perception, the same state of the senses or results from the experiment might be generated from different processes in reality. In a difficult situation, the human will therefore tend to use all of the information provided by the various senses at the same time. When crossing a busy street, we will not only look to the left and right, but we will also automatically listen for approaching cars. The same, the experimental physicist will try to use different *senses*, i.e. different experimental techniques to constrain the various possibilities and substantiate his conclusion.

For this reason, the concept of multi-component detectors is widely spread in all areas of physics. Well known are the complex detectors used at collider experiments in high energy physics, that are typically build in several *shells*. Each of the shells is usually dedicated to a specific purpose, such as accurately measuring the point of origin of the particles in the vertex detector or determination of the energy in the calorimeters.

But also in astro-particle physics, this concept is applied. As an example the PIERRE AUGER OBSERVATORY can be given which aims at measuring the high-energy end of the spectrum of cosmic particles by which the earth is permanently bombarded. Despite having first been detected by Victor Hess already in 1912, the location and the mechanism of the sources of these cosmic rays still remain unknown. Even more puzzling, cosmic rays are observed with energies exceeding 10^{20} eV, where they are theoretically assumed to be effectively absorbed by the interaction with the ambient cosmic microwave background – the so-called GZK cutoff. The experimental situation is complicated, since the flux at these energies is

extremely low. Even in detectors spanning several hundred square kilometres, event rates of no more than a few events per year are achieved. Due to the statistical nature of the interaction process of the cosmic ray and of the shower of secondaries evolving in the atmosphere, the signature of single events will allow only rough estimates of important parameters such as its energy or mass. These are further systematically biased by the presumptions taken for example on the respective interaction cross sections, that have to be extrapolated from measurements at lower energies. At the PIERRE AUGER OBSERVATORY, two approaches are taken to detect these events, either by the fluorescence light created in the shower or the flux of particles reaching the ground. From observation of an event by both methods complementary constraints can be achieved that significantly decrease the uncertainty on the critical parameters.

For another part of the cosmic ray spectrum, the flux of high-energy neutrinos, only one method could so far be established. Currently, the interactions of high energy neutrinos – that are even less frequent than cosmic rays at the same energies – are only detected via the Cherenkov light emitted by the relativistic charged secondaries. Evidence for neutrinos from cosmic ray interactions in the atmosphere with energies beyond 1 TeV has been found by the BAIKAL and AMANDA detectors this way.

Yet the even lower flux of neutrinos of extra-terrestrial origin has not been experimentally established so far, albeit its detection could shed new light on the puzzles of cosmic ray physics. In many theoretical models, neutrino production is closely linked to the production of charged cosmic rays. Also in the GZK cutoff introduced above, *cosmogenic* neutrinos are supposed to be generated along with the absorption of the cosmic rays. Therefore cubic-kilometre sized detectors such as ICECUBE or KM3NET are build or planned in large transparent natural media, such as deep sea water or the antarctic ice.

While neutrinos from the sources of the cosmic rays in the TeV to PeV might be detected by these experiments, for cosmogenic neutrinos their detection volume is still too small. To contribute to the resolution of the GZK puzzle by a measurement of the corresponding neutrino flux, an observed target volume in the order of 100 km^3 will be necessary, that cannot easily be achieved by the optical detection method.

Other technological approaches are needed to extend the range for neutrino observation to these extreme energies. Complementary detection techniques such as the detection of radio waves or acoustic waves arising from the compact electromagnetic or hadronic particle showers following a neutrino interaction are being investigated. Radio waves emerge from the relativistic excess charge in the cascade. Acoustic waves are generated in the thermal energy deposit, that leads to a small, but quasi-instantaneous heating of the cascade volume that is followed by a thermal expansion.

However, in contrast to the detection of Cherenkov light, the energy threshold is significantly higher in the radio and acoustic method. Acoustic detection is best suited for EeV energies while depending on the detector geometry for a radio wave detector the threshold may be somewhat lower. Moreover, as in the case of air showers, parameters like interaction cross-sections have to be extrapolated from lower energies, causing high systematic uncertainties. For the existing neutrino telescopes systematic studies are done with deeply penetrating muons from cosmic ray air showers. No such flux exists at EeV energies.

So again, it is the coincident detection by more than one method that yields the most powerful tool for systematic investigations, here. In a combined detector sensitive to Cherenkov light as well as radio and acoustic waves, significant overlap can be achieved among the event samples recorded with the three techniques. Favourable conditions, for the optical as well as for the radio and the acoustic method are found in the antarctic ice, such as long absorption lengths for all three types of radiation. Extending the ICECUBE array not only with optical modules, but also with radio and acoustic sensors, will open the unique opportunity of a hybrid detector sensitive to neutrinos with energies from several 10 GeV to the 100 EeV scale.

For radio waves, the feasibility of such an approach has already been established experimentally, and a small prototype in-ice radio detector is operated at South Pole. Acoustic detection has not been investigated as extensively, and thus was chosen as the topic of this thesis.

In chapter 2, first of all the current experimental status of cosmic ray observations at the GZK cutoff and the mechanisms of neutrino generation in these processes is investigated. A summary of the cosmogenic neutrino flux predictions, the relevant neutrino interaction processes, thermo-acoustic generation of sound waves in liquids and solids and their propagation in antarctic ice is presented in chapter 3. Experimental verification of the mechanism of thermo-elastic sound generation in ice, details of its ultrasonic properties at South Pole and the lack of suitable ultrasound sensors are identified as key problems. Based on the prerequisites discussed in chapter 3, a simulation study of an extension of the ICECUBE detector with radio and acoustic sensors is presented in chapter 4. Showing the high potential of the approach, the key problems are addressed in the following chapters. The development and calibration of acoustic sensors for in-ice application is discussed in chapter 5. Using these sensors, a first verification of the thermo-acoustic mechanism of sound generation using intense proton and laser beams is presented in 6. Finally, exploiting the experience gained in these two efforts, a dedicated setup to in-situ measure the acoustic ice properties at South Pole has been developed and is presented in chapter 7. Concludingly, a short summary and outlook are given in chapter 8.

Chapter 2

Motivation

2.1 Ultra-high energy cosmic rays

2.1.1 Charged cosmic ray spectrum

Since the first discovery of cosmic rays, many experiments have been performed to measure their flux over the very large range of energies from 10^6 eV up to 10^{21} eV. However, especially at the high energy end of the spectrum shown in figure 2.1, where the flux falls well below one particle per year and km^2 , the measurements get more and more difficult. The predominant technique in this energy regime is the detection of air showers induced by the cosmic rays either by the particle shower reaching the ground or by the fluorescence and Cherenkov light emitted in the atmosphere.

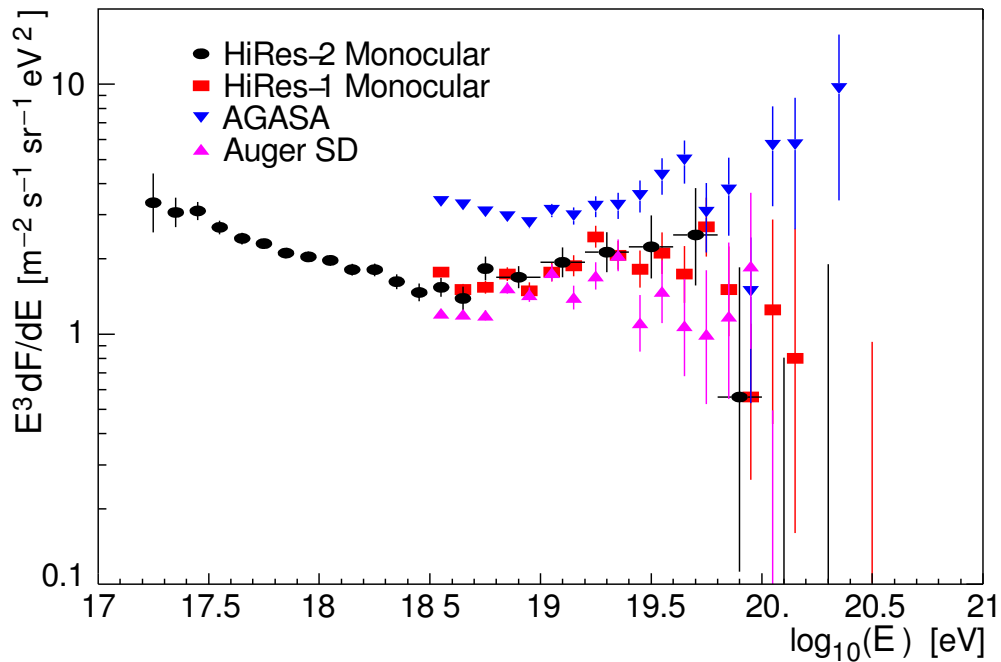


Figure 2.1: Flux of ultra-high energetic cosmic rays measured by different experiments (from [GSS05]).

With a particle flux as low as $10^{-4} \text{ km}^{-2} \text{ year}^{-1} \text{ EeV}^{-1}$ for energies above 100 EeV, extremely large apertures are needed. Currently, the most accurate measurements of the cosmic ray flux measurements at these energies are provided by three experiments:

HiRES The HIGH RESOLUTION FLY’S EYE experiment [A⁺05a] - the successor of the previous FLY’S EYE experiment [B⁺93] - is a fluorescence detector located in the Utah desert. It consists of two observation sites – HiRES-1 and HiRES-2 – separated by about 12.6 km. Both sites have several 5.1 m^2 mirrors to collect the fluorescence light on cameras of 265 photomultipliers. Both stations can only be operated in clear moonless nights, but are then able to detect showers up to 30 km away. While HiRES-1 with 21 circularly arranged mirrors and a field of view of nearly $14^\circ \times 360^\circ$ started data taking in 1997, data from HiRES-2, which consists of two rings of 42 mirrors in total with a field of view of $28^\circ \times 360^\circ$, is only available since 1999. Figure 2.1 shows the energy spectrum as measured by the two sites independently and for a lifetime of 1850 hrs for HiRES-1, respectively 540 hrs for HiRES-2. In addition, about 1000 hrs lifetime of stereo event data are available by now, that will yield a strongly improved directional resolution [RS01].

AGASA The AKEANO GREAT AIR SHOWER ARRAY (AGASA) [Shi06] located in Japan is a surface detector array. Each of its 111 detector stations, that are spread over an area of $\approx 100 \text{ km}^2$, is built of a 5 cm thick 2.2 m^2 scintillator plate which is read out by a 5 inch photomultiplier tube. In contrast to HiRES where the full shower is observed, only the part of the shower reaching the array at 900 m above sea level is registered.

Both methods are highly complementary and subject to very different systematic effects. In contrast to the fluorescence telescopes, the surface detectors do not depend on daytime and cloud conditions, but for example on the temperature profile in the atmosphere. Their smaller target volume is compensated by a nearly 100% duty cycle. Thus, comparable statistics is reached in both experiments.

AUGER While both AGASA and HiRES are already finished or running since a couple of years, the PIERRE AUGER OBSERVATORY (AUGER) [Man05] is still in the construction phase. It combines the fluorescence and the surface detector techniques to reduce the systematic errors. In its final configuration it will consist of 1600 water Cherenkov detectors that are distributed over an area of 3000 km^2 . These are encompassed by four fluorescence detector stations, each with six telescopes of $30^\circ \times 30^\circ$ field of view at the edges of the array. AUGER will yield the largest aperture of all air shower experiments ever built. It may be complemented with the AUGER North array of similar dimensions that is planned for the northern hemisphere.

Already with the data collected in the first half of the construction phase, the integrated event rate is competitive to those of the AGASA and HiRES experiments. Figure 2.1 shows the spectrum obtained with the surface detectors from the first 1.5 years of operation. The energy estimate has been calibrated using hybrid events that triggered both surface and fluorescence detectors [Som05].

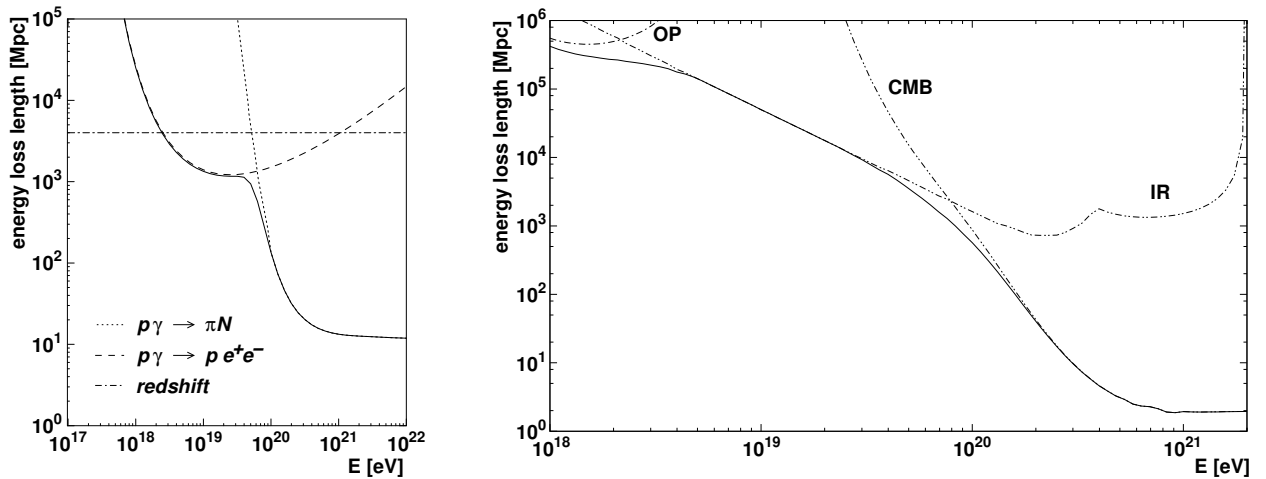


Figure 2.2: Total energy loss length (solid line) for high energy protons (left) and iron nuclei (right). The different contributions are pair-production (e^+e^-), photo-production of pions (πN) on the cosmic microwave background and photo-disintegration on the optical (OP), infrared (IR) and microwave background (CMB). Energy loss due to redshift is also shown in the left figure (from [DM05]).

It is evident that the shapes of the spectra measured by the individual experiments do not agree within the statistical uncertainties shown in figure 2.1. Apart from an absolute flux that is about 25% higher for the AGASA measurement than for HiRES and AUGER, there is also a significant steepening of the spectrum in the HiRES measurements around 10^{20} eV, that does not show up in the AGASA spectrum. From the sparse sampling of the shower in the surface detectors high **statistical** errors arise on the energy estimate – 30% at $10^{18.5}$ eV up to 50% at 10^{20} eV for AUGER [Man05] and 30% at $10^{19.5}$ to 25% at 10^{20} for AGASA. Yet these cannot explain the systematically higher rates observed by AGASA, even if renormalised for the integral flux.

This discrepancy in the absolute normalisation has to be seen with respect to the **systematic** uncertainties on the energy estimate that is stated for the different detection techniques. Both AGASA and HiRES claim an 18% systematic uncertainty in the energy determination [Shi06, A⁺05a]. This can equally be transformed in an uncertainty in the flux which is 27% for HiRES due to the steepness of the spectrum. Combined with uncertainty of 15% on the flux from the limited knowledge of atmospheric properties, the total systematic error for HiRES is stated to be 31%. So below 10^{20} eV, where the spectral shapes start to deviate, within the systematic errors all measurements are still consistent.

2.1.2 The GZK cutoff

Most noticeable, however, is the existence of events with energies above 100 EeV in the spectra measured by some of the experiments introduced in section 2.1.1. Due to the interaction of the ultra-high energy protons with the ambient cosmic microwave background, these events are highly unexpected. At a cosmic ray energy of around $4 \cdot 10^{19}$ eV, the centre of mass energy gets high enough for resonant production of the Δ^+ baryon, that immediately

decays into a pion and a remaining nucleus:

$$p_{\text{UHE}} + \gamma_{\text{CMB}} \rightarrow \Delta^+ \rightarrow \begin{aligned} &\pi^0 + p \\ &\rightarrow \pi^+ + n \end{aligned} \quad (2.1)$$

At higher energies, also multi-pion production becomes relevant, e.g. via

$$p_{\text{UHE}} + \gamma_{\text{CMB}} \rightarrow \pi^+ + \pi^- + p. \quad (2.2)$$

These mechanisms have first been independently discussed by Greisen [Gre66] and Zatsepin, Kuzmin [ZK66]. Due to the strong steepening of the spectrum, it is most often referred to as the GREISEN-ZATSEPIN-KUZMIN (GZK) cutoff. In addition, the propagation of cosmic rays at these energies is affected by pair production on the same microwave background radiation

$$p_{\text{UHE}} + \gamma_{\text{CMB}} \rightarrow p + e^+ + e^-, \quad (2.3)$$

and for heavier nuclei also by photo-disintegration.

Figure 2.2 shows the *energy loss length* – i.e. the propagation length before the energy is decreased by a factor $1/e$ – resulting from the processes above. For protons it strongly decreases above $4 \cdot 10^{19}$ eV due to the abrupt increase in cross section close to the resonance, so they will not propagate unaffected for more than 50 Mpc at energies above 10^{20} eV. Thus for remote sources one would expect a rather sharp cutoff in the spectrum if the cosmic rays were protons.

For an iron nucleus of a certain energy the individual nucleons will only carry a fraction of that energy. Since nuclear binding energies are small in comparison, they can be treated as independent for the photo-production of pions and electron-positron pairs. The threshold energy for these effects $E_{\text{thr}}(A) = A \cdot E_{\text{thr}}(p)$ scales with the mass number A and they become important only at correspondingly higher energies. As shown on the right side of figure 2.2, photo-dissociation, i.e. the breaking up of the nucleus by the emission of one or more nucleons after interaction with a cosmic background photon, is the dominant process at all energies. The fraction of energy lost in photo-dissociation is roughly proportional to the relative decrease in mass number of the nucleus. For heavy nuclei it is small compared to interactions involving photo-production of new particles. So the actual interaction length is much shorter than the energy loss length, and any heavy nucleus will have dissolved into a lighter one with shorter loss length long before having reached the one photo-disintegration loss length distance.

No hadronic cosmic rays, neither *light* nor *heavy*, are thus expected to travel over distance further than 100 Mpc with energies higher than 10^{20} eV [DM05, YT93]. On the other side, the gyro-radius of EeV protons in the galactic magnetic fields is much larger than the dimensions of our galaxy itself. Since no powerful enough sources of cosmic rays are known within our galaxy, it is generally assumed that, at these energies, cosmic rays are produced well outside of it. This is also supported by the observation of a mass-dependent break in spectral index in the charged cosmic ray spectrum around 10^{15} eV [A⁺05d], that is attributed to breaking of the confinement of cosmic rays in the galactic magnetic field.

Assuming a generic power law emission spectrum at the source(s), two different extreme scenarios can now be considered [YT93]:

- In the **single source** model it is assumed that all high energy cosmic rays are generated at a single nearby source outside of our galaxy. Due to the absorption mechanism discussed above, this source must then be located at a redshift $z \leq 0.02$, as otherwise a very sharp cutoff is expected even below an energy of 10^{20} eV. A possible source candidate in this scenario is the Virgo cluster at $z \approx 0.004$, hosting e.g. the super-heavy galaxy M87, that is believed to be an Active Galactic Nucleus and thus a possible candidate for cosmic ray production [DPR03].
- On the other hand, the universe is rather homogeneous on large scales [Col03]. Thus it is natural to assume that the unknown sources of the ultra high energy cosmic rays would also be homogeneously distributed.

In this **uniform source distribution** scenario, the cosmic rays reaching the earth will come from sources at very different redshifts. We must therefore also take into account the evolution of the source density $n(z_e)$ at the redshift of emission z_e , which is often parametrised as

$$n(z_e) = n_0(1 + z_e)^m \quad \text{for } z_e < z_{max}, \quad (2.4)$$

where m is called the *cosmological evolution* parameter and z_{max} is the redshift at which the first sources of cosmic rays appear.

The propagation of cosmic rays over significant redshift distances is also affected by the cosmological evolution, which in case of the approximation of an Einstein-de-Sitter universe leads to an adiabatic *redshift* energy loss of

$$-\frac{dE}{dL} = H_0(1 + z)^{\frac{3}{2}}E, \quad (2.5)$$

where $H_0 \approx 72 \text{ km sec}^{-1} \text{ Mpc}^{-1}$ is the Hubble constant and z the redshift. As shown on the left hand side of figure 2.2, it is the dominant mechanism of energy loss only for energies below 10^{18} eV.

Considering the energy loss mechanisms mentioned above, one can fit the expected spectral shape in case of a homogeneous source distribution and in presence of the GZK mechanism [YT93] to the observed flux of cosmic rays as shown in figure 2.3. The chance probability to observe the spectrum measured by AGASA under this assumption is calculated to be $3 \cdot 10^{-8}$, corresponding to 4σ . The significance decreases to 2.7σ , or a chance probability of $2.7 \cdot 10^{-4}$ if the spectrum is shifted by 18% towards lower energies according to the systematic uncertainty [Shi06]. In addition, an anisotropy in the cosmic rays is observed in the AGASA data. Figure 2.4 shows the correlation function, – i.e. the number of observed event pairs that are within a certain opening angle – for the arrival direction of all AGASA events above $4 \cdot 10^{19}$ eV. The deviation from an isotropic distribution, for which the correlation function is indicated by the dotted line, is 3.5σ . There are several clusters in the arrival direction distribution of the events detected by AGASA, none of them however, pointing to a known candidate acceleration site.

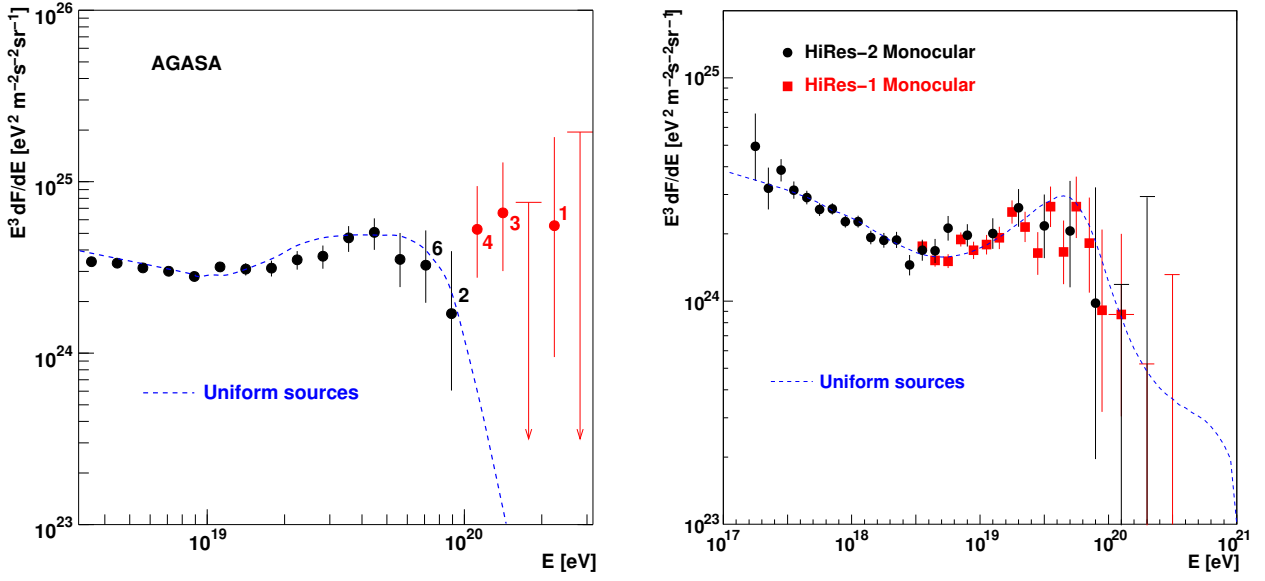


Figure 2.3: Energy spectrum of cosmic rays as observed by AGASA (left) and HiRES (right). The spectra are scaled with E^3 . The lines show a fit for a spectral shape as expected for a uniform source distribution with absolute flux and spectral shape as free parameters (from [H⁺00] and [Ber05b]).

These results are in some contradiction to the data obtained by HiRES. A fit with a simple power-law over all energies disfavours the continuation of the spectrum with a chance probability of only $2.4 \cdot 10^{-4}$ [A⁺05a]. In contrast, assuming a uniform source model as shown in figure 2.3 the data can be much better fitted with $\frac{\chi^2}{\text{NDF}} = 1.20$ [Ber05b]. At the same time, no anisotropy is observed in the HiRES data.

So while the AGASA results favour the cosmic rays to come from a few sources, the HiRES results hint towards a uniform source distribution. Since the sensitivity of both experiments to these feeble fluxes is rather limited, this ambiguity will not be solved without the data of more sensitive experiments, such as AUGER with an order of magnitude higher event rates at these energies.

Other questions such as the one of the *chemical composition*, i.e. the mass number of the cosmic rays, might be even more difficult to assess. In air shower experiments, the composition can only be determined by the very indirect measurement of the penetration depth of the shower in the atmosphere. At the energies discussed here, the binding energy of the nucleus can be mostly neglected. A shower generated by e.g. an iron nucleus with mass number A can in good approximation be treated as a superposition of A single proton-induced showers. Since each of them will only carry $1/A$ of the total energy, it will not penetrate as deep in the atmosphere as a proton induced shower. For a given inclination, the shower maximum X_{max} , which gives the atmospheric depth where the shower has the largest number of particles, is roughly logarithmically dependent on the energy of the primary. This yields approximately a 45% difference in X_{max} for an iron nucleus with $A = 56$ in contrast to a proton. However, this effect is not only smeared out by the statistical nature of the shower development, but also strongly dependent on quantities of the shower development

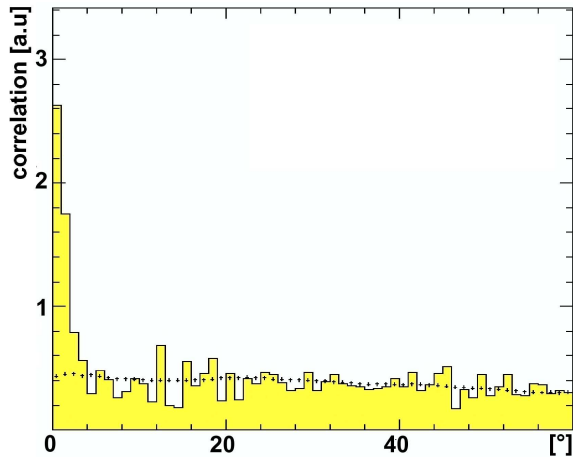


Figure 2.4: Angular correlation function for AGASA events with $E > 4 \cdot 10^{19}$ eV. The dotted line shows the expectation for a uniform distribution of the sources (from [H⁺00]).

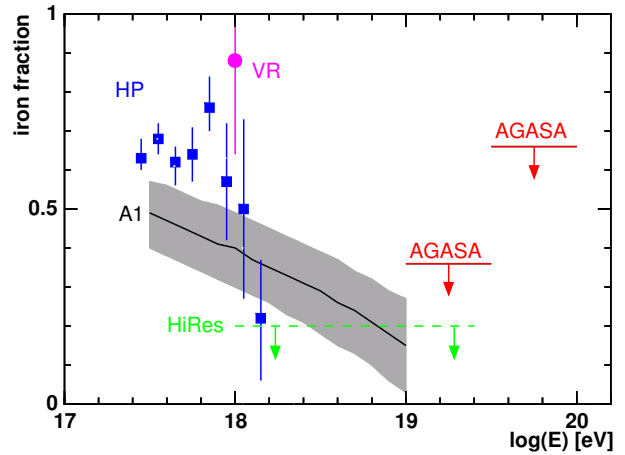


Figure 2.5: Composition of ultra-high energetic cosmic rays as measured by AKEANO (A1), AGASA, HiRES, VULCANO RANCH (VR) and HAVERAH PARK (HP). (from [H⁺00]).

with high systematic uncertainties, such as the cross sections of the individual processes. Already at lower energies, this makes it very hard to draw definite conclusions on the primary composition of the cosmic ray flux [A⁺05d].

Moreover, only in fluorescence detectors the shower maximum can be directly derived from the maximum of the fluorescence light emission along the shower track, but needs to rely on a proper geometrical reconstruction. In the surface detectors, it can only be indirectly derived, either from the curvature of the shower front, or from the relative excess of electrons over muons. The latter are more abundant for showers generated higher in the atmosphere since most of the muons generated in a shower will reach ground level, whereas the electromagnetic component has its maximum at X_{max} and will then continually decrease.

The general composition of high energy cosmic rays is rather unclear. In the 10^{15} eV to 10^{17} eV the average composition is observed to become heavier. Extrapolating from measurements in the range of 10^{18} eV to 10^{19} eV, it is expected that at the very highest energies the cosmic ray flux is predominantly composed of protons or light nuclei. Due to the limited statistics, only limits have so far been derived for energies $E > 10^{19}$ eV. Figure 2.5 shows a summary of results from different experiments. Even the contribution of photons as primaries can only be limited to 36% at the moment [R⁺06].

So while the quest for the origin of highest energy cosmic rays may be solved in the nearer future, the question of the composition of cosmic rays might not be resolved soon.

2.2 Neutrinos in cosmic rays

To obtain more constraints, both on models for sources and composition of ultra-high energy cosmic rays, other sources of information are necessary. One of them is provided by the process of absorption of the cosmic rays themselves. It gives rise to a flux of neutrinos that, either due to the effect they are created in, are referred to as GZK *neutrinos* or, due to their cosmological origin, are called *cosmogenic neutrinos*.

2.2.1 Cosmogenic neutrinos

Two distinct ways of neutrino generation exist from the photo-production of pions and the photo-disintegration processes introduced in section 2.1.2 [HTS05].

- As shown in equation 2.1, charged and neutral pions are generated. The charged pions decay into muons, that themselves will then decay. In both cases neutrinos are emitted:

$$\begin{aligned} \pi^+ &\rightarrow \mu^+ + \nu_\mu \\ &\hookrightarrow e^+ + \nu_e + \bar{\nu}_\mu . \end{aligned} \quad (2.6)$$

In both decays, the neutrino will carry a significant part of the energy of the decaying primary.

- Neutrons are generated either along with the charged pions in photo-production of pions or by photo-disintegration of heavier nuclei. These will as well decay, producing more neutrinos:

$$n \rightarrow p + e^- + \bar{\nu}_e . \quad (2.7)$$

Above $4 \cdot 10^{20}$ eV, neutrons are more likely to interact than to decay, so that this process is only relevant for lower energies [ESS01].

Figure 2.6 shows the flux of neutrinos expected after a certain propagation length for a generic proton input spectrum of

$$\frac{dN_p}{dE_p} \propto E_p^{-2} \cdot \exp\left(\frac{-E_p}{E_{max}}\right) . \quad (2.8)$$

To avoid divergence in the calculated flux, the input spectrum has to be mitigated at the maximal energy expected at the production site. A value of $E_{max} = 10^{21.5}$ eV is assumed in [ESS01]. For ν_μ solely produced in equation 2.6 the flux peaks at around 10^{19} eV. For ν_e , two *bumps*, one from pion decays in equation 2.6 peaking at around 10^{19} eV, and one from neutron decays as in equation 2.7 with a maximum at 10^{16} eV can be clearly distinguished. It is also evident, that the neutrino yield is strongest in the first ≈ 100 Mpc from the source.

In the absence of neutrino oscillations, that will be discussed in section 2.2.3, these spectra directly apply for a single source. But also for a homogeneous source distribution a calculation of the flux of these cosmogenic neutrinos is possible under a certain assumption on the cosmological evolution, and has been performed by various authors. An overview is shown in figure 3.5 and will be discussed in section 3.1.

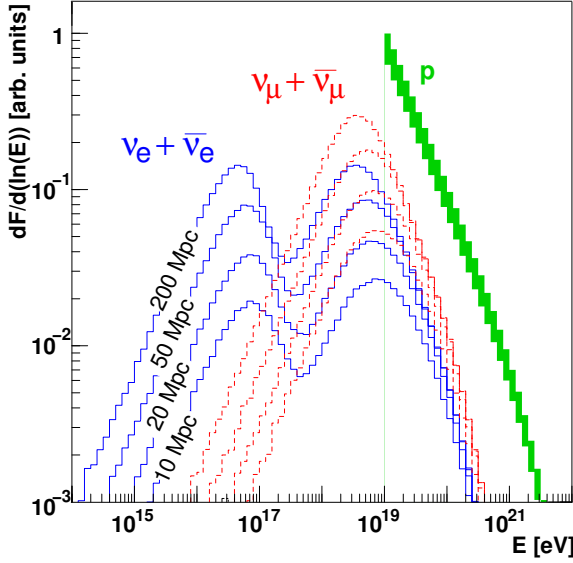


Figure 2.6: Flux of electron (blue, solid) and muon (red, dashed) GZK neutrinos relative to a generic input spectrum (green band) for different propagation distances (from [ESS01]).

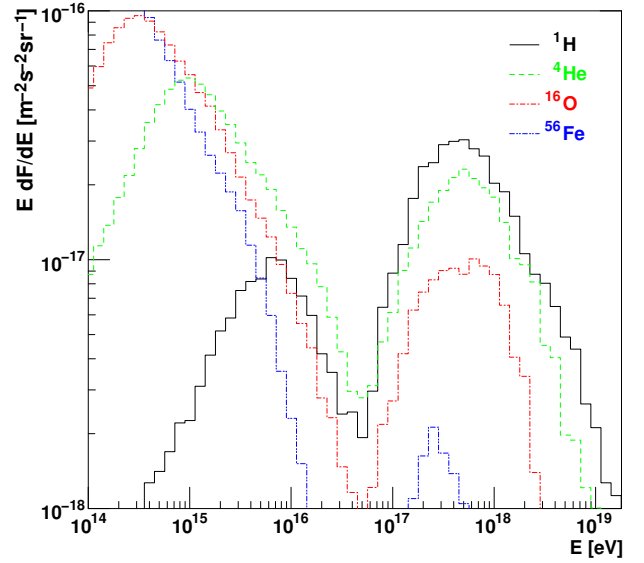


Figure 2.7: Flux of GZK neutrinos for different primary masses (from [HTS05]).

One example from a Monte Carlo simulation and an evolution model as described in [ESS01] is shown in figure 2.7. Different primary masses have been assumed for the input cosmic ray flux, with a large impact on the resulting neutrino spectrum. As discussed in section 2.1.2, which of the two energy loss processes for cosmic rays is dominant strongly depends on the composition. For light nuclei photo-production of pions and neutrino generation via the processes in equation 2.6 will prevail. Only the neutrons from photo-production contribute to the lower energy peak. For heavy nuclei, the threshold for photo-production is larger, resulting in less neutrinos from the pion decay (eqn. 2.6). At the same time, many more neutrons will be created in photo-disintegration, giving a much stronger contribution from neutron decays (eqn. 2.7). So apart from the cosmological evolution, the flux is very sensitive to the mass composition of the primary cosmic rays.

Despite being in the energy range for which current neutrino telescopes are optimised [A⁺04b, Bec06], even for a pure iron composition, neutrinos from neutron decay will not be observable due to the overwhelming background of atmospheric neutrinos. For the high energetic part from pion decay, in contrast, no known sources of background exist, but here the sensitivity of the existing neutrino telescopes is not high enough. Figure 2.8 shows the flux per flavour $F = \frac{1}{3} \sum_{e,\mu,\tau} F_{\nu_l} + F_{\bar{\nu}_l}$ for two different models yielding a comparatively low [ESS01] or high [KKSS02b] flux. Current experimental limits shown as grey exclusion areas in figure 2.8 are well above these expectations.

At the same time a measurement of these neutrinos would give constraints that are highly complementary to the air shower experiments, since it will not suffer from two major effects:

1. The measurement of the neutrino flux will **not** depend on interaction models for high energetic air showers. The only interactions that have to be taken into account are those of the neutrino creating processes in equation 2.6 (that occur at low centre of mass energies accessible by current experiments and are rather well known [EHO⁺05]) and those of the neutrino interaction, for which the measurement of the neutrinos themselves might yield good constraints as will be explained in section 3.2.
2. A measurement of the flux will also probe the composition of the cosmic rays **not** at the earth, but along the path of propagation. Even for a pure iron composition at the source, due to photo-disintegration, practically no iron nucleus will reach the earth as explained in section 2.1.2 and only protons will be detected [ER98]. However, since the nucleus is disintegrating and not producing pions, the neutrino flux will be severely reduced in this case.

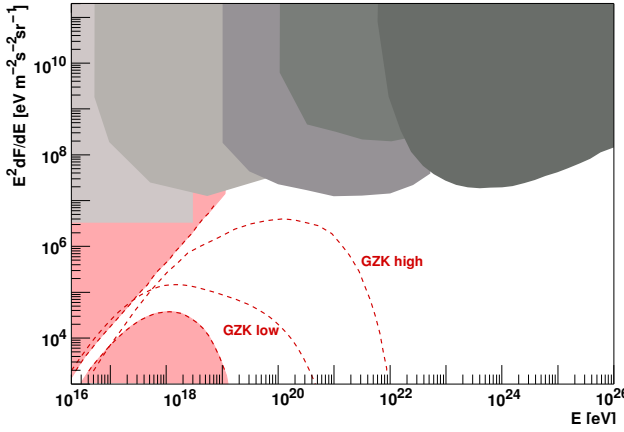


Figure 2.8: Per-flavour flux of GZK neutrinos for a *low* prediction from [ESS01] and a *high* prediction with $E_{max} = 10^{23}$ eV from [KKSS02b]. Experimental limits (see section 2.2.4, grey areas) and indirect bounds from cosmic ray observations [FKRT03a] (pink areas with dashed lines) are shown as well.

In addition, it has been argued that measuring the charged cosmic ray flux will not constrain the cosmological evolution of the sources and the source spectrum at the same time [SS05]. In contrast to the constraints from the cosmic ray flux itself, that is heavily affected by propagation effects, the flux of cosmogenic neutrinos yields an unprecedented handle not only on the cosmic ray composition, but also on the flux and spectrum close to their source(s). The detection of this cosmogenic flux is therefore the main motivations to search for neutrinos at ultra-high energies.

2.2.2 Other UHE neutrino sources

Apart from the *guaranteed* flux discussed in the last chapter, a large variety of other predictions for ultra-high energy neutrino fluxes exist. Probing these astrophysical or elementary physics models increases the incentive to look for neutrinos at EeV energies. Some common models will be briefly introduced here.

Active galactic nuclei

One promising candidate for the sources of the charged cosmic rays at highest energies are so called *active galactic nuclei* (AGN). These are among the most powerful known cosmological

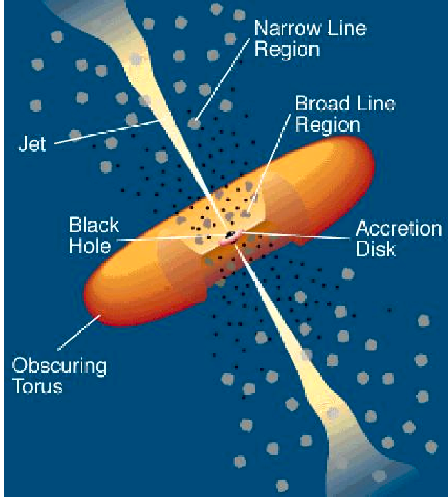


Figure 2.9: Unified model of an active galactic nucleus: the characteristic properties depend on the viewing angle of the observer (from [Urr03]).

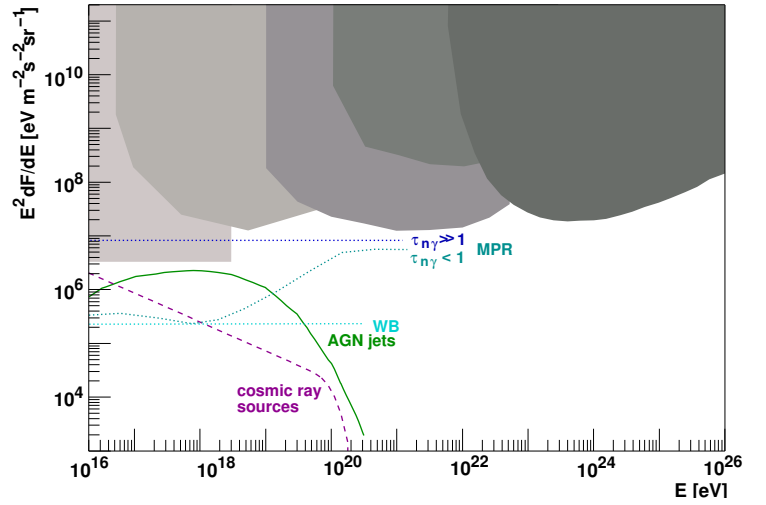


Figure 2.10: Per-flavour neutrino flux predictions for *active galactic nuclei* (AGN) [Man95] and photo-production of pions in the cosmic ray sources [A⁺05c]. Also shown are theoretical bounds from cosmic and gamma ray observations assuming the cosmic ray sources to be neutrino sources [MPR01, WB99, BW01] (dotted lines) and current experimental limits (grey areas).

objects, with a luminosity of an entire galaxy but a variability limiting the size of the emission region to the size of our solar system. The electromagnetic spectrum ranges from radio to TeV gamma rays, with a prominent thermal ultraviolet peak at 40 eV, corresponding to a black body temperature of $\approx 10^5$ K.

In the unified AGN model [Urr03], this ultraviolet emission is powered by the gravitational energy of matter from the host galaxy accreted on a very massive black hole $\mathcal{O}(10^8 M_\odot)$, which heats the core. In addition, matter is ejected at relativistic velocities in so called *jets* along the rotation axis of the accretion disc to account for the conservation of the angular momentum. This model describes a variety of observations with very different characteristics, summarised in figure 2.9: if the accretion disc is observed edge-on, narrow lines from the absorption of the visible light in dust clouds are found, that are significantly broadened if the line of sight is such that the accretion disc is not obscured. If the jets are pointed towards the observer, the highly variable luminosity with a high degree of polarisation typical for a *blazar* is observed. It is for example in these jets where shock waves are assumed to form and accelerate particles by the first order Fermi acceleration mechanism. Depending on whether the particles are electrons or protons, the observed gamma rays are subscribed to either of two mechanisms: in case of electrons, synchrotron radiation is emitted in the strong magnetic field where the synchrotron photons gain energy in Compton scattering. In case of accelerated protons the same pion photo-production processes discussed in equation 2.1 from decays of the neutral $\pi^0 \rightarrow \gamma\gamma$ and secondary electromagnetic cascades in the dense photon field of the shock are in place. Only in the latter case neutrinos are generated along with the gamma rays from the decay of the charged pions.

Figure 2.10 shows a flux prediction from a model for *radio-loud* AGNs [Man95], that are mostly found in elliptical galaxies. It is assumed that the high energy gammas are

generated in neutral pion decays in the AGN jets. The neutrino luminosity is scaled relative to the integrated observed diffuse gamma ray luminosity above $E_\gamma > 100 \text{ MeV}$ based on a homogeneous source distribution ($m = 3, z_{max} = 4$ in equation 2.4).

It is worth to be noted that the protons accelerated in the jets are typically not considered to contribute significantly to the very high energy flux, since they are trapped in the strong magnetic fields of the jet and thus subject to adiabatic energy losses. Instead it is usually assumed that the cosmic ray flux itself is originating from the neutrons generated in pion photo-production (e.g. $p\gamma \rightarrow n\pi^+$) which can escape from the jets.

Based on the assumption that the sources of high-energy protons and neutrinos are originating in the same photo-production processes, one can also calculate a flux relative to the observed cosmic ray flux. In [A⁺05c] it is assumed that $E_{\pi^+}/E_n = 0.28$ in the photo-production of pions and that $3/4$ of that energy is converted to neutrinos. From a fit the onset of the extragalactic component at $E_{CR} = 10^{17.6} \text{ eV}$ with a spectral index of $\gamma = -2.54$ for a cosmological evolution $m = 3.45$ is obtained. The resulting neutrino flux is also shown in figure 2.10. In the same fashion, a limit can be derived as done in [MPR01], where $E_\nu/E_n = 0.04$ is assumed together with an onset of the extragalactic component at $E_{CR} \approx 10^{19} \text{ eV}$. A source distribution following a cosmological evolution of the radio luminosity ($m \approx 3, z_{max} \approx 4$) with varying input spectra is considered. For a range of E_{max} values, the flux is limited not to violate the observed charged cosmic ray flux. For each energy the minimum of the constraints from the cosmic ray flux and observations of the extragalactic background light is taken. The latter only holds in case that the neutrons are emerging the source, i.e. the normalised optical depth $\tau_{n\gamma} < 1$. If the neutrons are trapped in the jets, $\tau_{n\gamma} \gg 1$ and only the weaker upper limit shown in figure 2.10 can be derived. At the same, assuming that only one class of sources is generating the cosmic rays with always the same injection spectrum and value of E_{max} automatically leads to the lower bound shown in figure 2.10 at the level where the above method is most stringent [WB99, BW01].

The Z-burst model

A more speculative prediction for neutrino fluxes is provided by the so called *Z-burst* model, where the extragalactic charged cosmic rays are assumed to be produced in the resonant interaction of neutrinos at even higher energies with the ambient cosmic neutrino background predicted by the standard cosmological evolution.

While the actual source of these ultra-high energy neutrinos is left open in most cases, the predicted cosmic neutrino background always stems from the decoupling of the neutrinos at $\approx 1 \text{ sec}$ after the big bang. Due to the expansion of the universe it has now cooled down to a temperature of $T_\nu = 1.95 \text{ K}$ with a per-flavour density of $n_{\nu_i} = 56 \text{ cm}^{-3}$. Neutrinos might interact with other neutrinos by production of real Z^0 -bosons

$$\nu + \bar{\nu} \rightarrow Z^0 \quad , \quad E_{res} = \frac{m_{Z^0}^2}{2m_\nu} \quad \text{for} \quad m_\nu \gg k_B T_\nu \quad , \quad (2.9)$$

with a resonance energy E_{res} depending on the neutrino and Z^0 masses. Some cross sections as a function of center-of-mass energy are shown in figure 2.11. At higher energies, also production of W -bosons in $\nu\gamma \rightarrow l^- W^+$ will become relevant [Sec98].

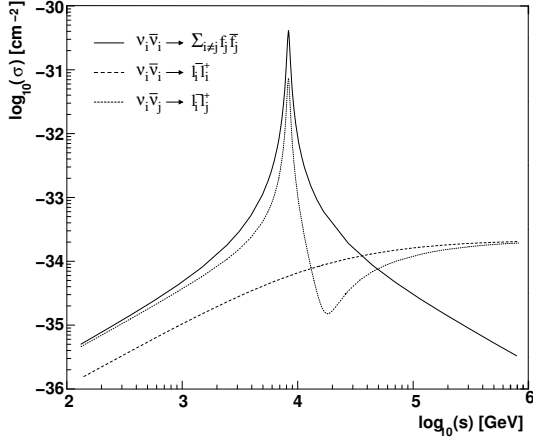


Figure 2.11: Cross-sections for various $\nu\nu$ interactions (from [Sec98]).

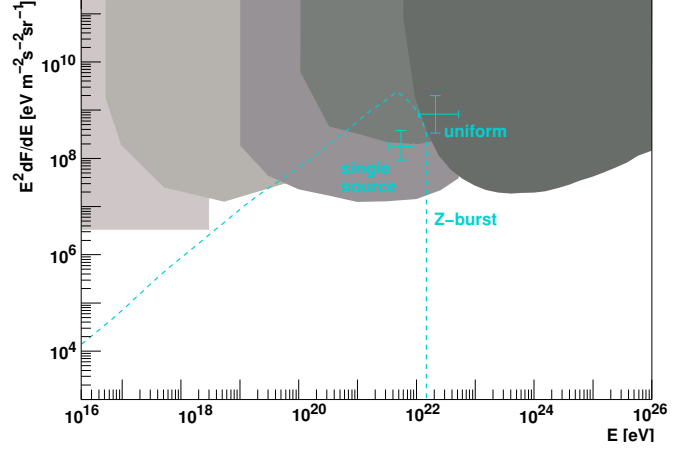


Figure 2.12: Per-flavour neutrino flux predictions from the *Z-burst* model: a generic model with $m_\nu = 0.5 \text{ eV}$ [KKSS02a] and the peak fluxes assuming a *single source* of cosmic rays or a *uniform* distribution [FKR02]. The current experimental limits are shown as grey areas.

Assuming that the protons generated in the hadronic decay of the Z^0 contribute significantly to the cosmic ray flux above $E_{CR} = 2.5 \cdot 10^{19} \text{ eV}$, one can now fit the input neutrino spectrum for a neutrino mass of $m_\nu = 0.5 \text{ eV}$ to the observed cosmic ray flux, as shown in figure 2.12 [KKSS02a]. However, this model exceeds the current limits on the neutrino flux at the peak energy. In another approach, only part of the charged cosmic ray flux is subscribed to the *Z-burst* mechanism [FKR02], contributing to the spectrum in addition to either a single source or an uniform source distribution (see section 2.1.2). The peak fluxes for both models are also shown in figure 2.12.

However, it has to be stated that all these models are heavily constrained, not only by the experimental limits shown in figure 2.12. Gamma rays can be produced in the same Z^0 decays. These gamma rays undergo pair production on the cosmic microwave, infrared and radio background, cascading down to the pair production limit in the GeV range. In order not to exceed the fluxes observed by the EGRET experiment, only evolution parameters $m \ll 3$ are allowed in *Z-burst* models. This is well below the values usually assumed, e.g. from observations of the star formation rate.

Being excluded as a dominant source of cosmic rays, the continuing interest in this model can be justified by the fact that this is currently the only way by which a proof of the existence of the cosmic neutrino background can be imagined. Due to the mass dependence of the resonance energy, it would also provide a handle on the absolute neutrino masses [ERSW04].

Topological defects

In contrast to the so-called *bottom-up* scenarios introduced above, also a set of models exists referred to as *top-down*, where neutrinos are generated in the decay of hypothetical, very massive particles.

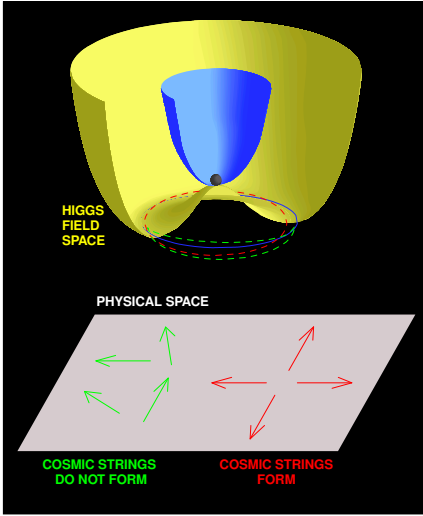


Figure 2.13: Schematic illustration of the generation of topological defects (from [Gan03]).

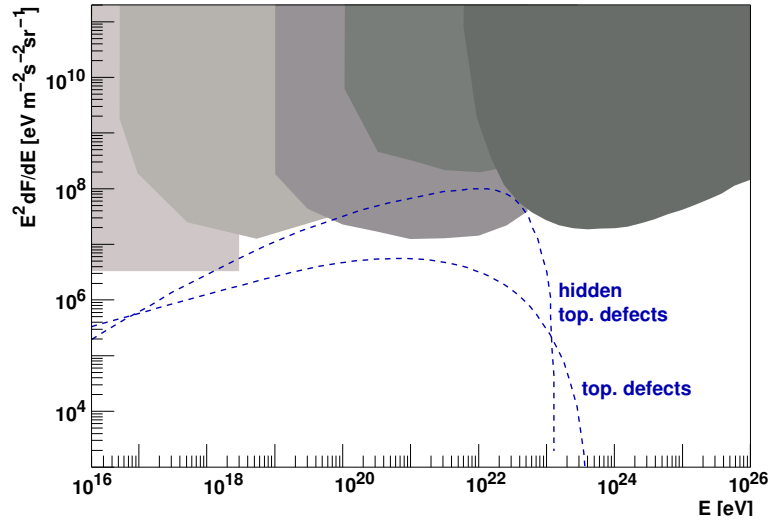


Figure 2.14: Per-flavour neutrino flux predictions for *normal* and *hidden* topological defects with $m_{TD} = 2 \cdot 10^{14}$ eV and $m_\nu = 1$ eV [KKSS02b]. The current experimental limits are shown as grey areas.

One popular example are so called *topological defects*, which are predicted in many GUT models. In the symmetry breaking of the Higgs potential (inner and outer surfaces in figure 2.13) different *orientations*, i.e. different states of the new vacuum are realised (arrows in figure 2.13) at the causally not connected points where the phase transition starts. Depending on the manifold of the vacuum states (solid line in figure 2.13), it can have a non-trivial homotopy class. While in most adjoining regions the vacuum states will adapt (green, left arrows and dashed line), there exists the possibility that the vacuum states created in different regions cannot be transformed into each other by continuous transformations. These non-contractible solutions are stable (red, right arrows and dashed line). Depending on the homotopy class of the vacuum manifold, one speaks of *domain walls*, *cosmic strings*, *monopoles* or *textures*. In any case there is a *boundary* where the vacuum state has to change from one orientation to another, which happens in a transition region where the energy is that of the unbroken Higgs field. The topological defect therefore has the natural mass scale on the order of the GUT symmetry breaking, typically assumed to be $M_{GUT} \approx 10^{15}$ GeV [Gan03, BS00].

For dimensional reasons, the injection rate \dot{n} of the topological defects with mass m_{TD} is related to the cosmic time t by $\dot{n} \propto m_{TD}^{-1} t^{-3}$ [BHS92]. The topological defects themselves are often assumed to be stable, but *defects* and *anti-defects* may interact usually producing lepton and quark pairs, which then hadronize, finally giving rise to proton, gamma and neutrino fluxes. Similar to the Z-burst model, they are therefore constrained by the observed gamma and cosmic ray fluxes. Figure 2.14 shows an optimistic flux estimate for $m_{TD} = 2 \cdot 10^{14}$ GeV that is still consistent with observed gamma ray and cosmic ray data [KKSS02b]. These limitations can also be circumvented by the introduction of so-called *mirror matter*, which is generated from ordinary matter by a mirror operator I_s that transforms the left states of ordinary matter to right states of the mirror matter and vice versa. This mirror matter

will then only interact gravitationally with ordinary matter, leaving only neutrinos to be exchanged by gravitational mixing of the ordinary and mirror neutrino states. Since only mirror particles are created in the decay of topological defects in this system, they are also called *hidden*. An upper bound can only be given by the observational neutrino limits, as assumed for the model shown in figure 2.14 [Ber05a].

While it is not un-likely that topological defects were created in the GUT symmetry breaking of the early universe, there is no natural explanation why the life-time of the topological defect should be about the age of the universe, i.e. why topological defects should not have annihilated right away. In models where the high energetic cosmic rays stem from topological defects, the annihilation cross-section therefore needs to be adjusted on ad-hoc assumptions, which is known as the *fine-tuning* problem [dVS03]. In addition, the existence of topological defects is not supported (but also not ruled out) by the current detail of observation of anisotropy in the cosmic microwave background.

2.2.3 Neutrino flavours

Recent measurements, e.g. of the very well predictable neutrino flux from the sun [MSTV03, Fuk03], have revealed a different flavour composition than expected from the generation mechanisms. This is attributed to the effect that neutrinos are not massless, but have finite rest masses, with flavour eigenstates that do not correspond directly to the mass eigenstates. Instead, similar to the CKM-matrix in the quark sector, the flavour eigenstates $\alpha = (e, \mu, \tau)$ are related to the mass eigenstates $i = (1, 2, 3)$ by the unitary MAKI-NAKAGAWA-SAKATA (MNS) matrix U^* [Kay06]:

$$|\nu_\alpha\rangle = \sum_{i=1}^3 U_{\alpha i}^* |\nu_i\rangle . \quad (2.10)$$

The evolution in time τ in the rest frame of a neutrino mass eigenstate in vacuum is described by the Schrödinger equation

$$|\nu_i(\tau)\rangle = e^{-im_i\tau} |\nu_i(\tau=0)\rangle . \quad (2.11)$$

The rest masses m_i are different for each eigenstate, so that as a consequence, the flavour eigenstates given by equation 2.10 oscillate during the propagation. The probability for an oscillation from flavour α to flavour β after a distance x is:

$$P(\nu_\alpha \rightarrow \nu_\beta; x) = |\langle \nu_\beta | \nu_\alpha(x) \rangle|^2 = \delta_{\alpha\beta} - \sum_{i \neq j} U_{\alpha i}^* U_{i\beta} U_{\beta j}^* U_{j\alpha} \left(1 - \exp\left(\frac{-i\Delta m_{ij}^2 x}{2E}\right) \right) , \quad (2.12)$$

depending on the matrix elements of U^* , the squared-mass difference $\Delta m_{ij}^2 = m_i^2 - m_j^2$ between two mass eigenstates and the energy E of the neutrino. Assuming only two neutrino flavours and eigenstates, one can then define an oscillation length L_{ij} as the distance between two maxima of $P(\nu_\alpha \rightarrow \nu_\alpha; x)$:

$$L_{ij} = \frac{4\pi\hbar E}{\Delta m_{ij}^2 c^3} = 2.48 \text{ km} \left(\frac{E}{\text{GeV}} \right) \left(\frac{\text{eV}^2}{\Delta m_{ij}^2} \right) . \quad (2.13)$$

Not only from observation of the oscillation, but also from direct limits on the absolute neutrino masses one finds $\Delta m_{ij}^2 \lesssim \mathcal{O}(10^{-5} - 10^0 \text{ eV}^2)$ [Giu06], depending on the considered flavours. So even at energies $E = 10^{21} \text{ eV}$ the oscillation length $L_{ij} \ll 1 \text{ Mpc}$ is short compared to cosmological distances. Assuming sources distributed over cosmic length scales, one can thus average over the oscillations to find the probability $P_{\alpha\beta} = \langle P(\nu_\alpha \rightarrow \nu_\beta; x) \rangle_x$ to measure the flavour β if neutrinos of flavour α are emitted at the sources. From 2.12 one can infer the probability matrix [AJY00]

$$P_{\alpha\beta} = \delta_{\alpha\beta} - \sum_{i \neq j} U_{\alpha i}^* U_{i\beta} U_{\beta j}^* U_{j\alpha} = \sum_i |U_{\alpha i}^*|^2 |U_{\beta i}^*|^2, \quad (2.14)$$

which relates the flavour-separated fluxes

$$\Phi_{\oplus}(\beta) = \sum_{\alpha} P_{\alpha\beta} \cdot \Phi_{\odot}(\alpha) \quad (2.15)$$

measured at earth to the generated fluxes at the sources $\Phi_{\odot}(\alpha)$. In the GZK mechanism shown in section 2.2.1, neutrinos appear in pion- and subsequent muon decay, leading to a flavour ratio of $\Phi_{\odot}(\nu_e) : \Phi_{\odot}(\nu_\mu) : \Phi_{\odot}(\nu_\tau) = 1 : 2 : 0$. Using equation 2.15 a flavour ratio of $\Phi_{\oplus}(\nu_e) : \Phi_{\oplus}(\nu_\mu) : \Phi_{\oplus}(\nu_\tau) = 1 : 1 : 1$ at the earth is obtained [AJY00]. The oscillation process itself is independent of energy for the cosmological distances and energies considered here. Alternative production flavour ratios are discussed in dense sources [KW05] such as the AGN jets discussed in section 2.2.2. An energy dependent suppression of the muon decay may lead to $\Phi_{\odot}(\nu_e) : \Phi_{\odot}(\nu_\mu) : \Phi_{\odot}(\nu_\tau) = 1 : 0 : 0$ at the source and to a flavour ratio of $\Phi_{\oplus}(\nu_e) : \Phi_{\oplus}(\nu_\mu) : \Phi_{\oplus}(\nu_\tau) = 1 : 1.8 : 1.8$ at the earth.

Some detection methods described in the next section are equally sensitive to all neutrino flavours and will only measure the total flux. Yet, flavour ratios are important for those methods that are especially sensitive to one of the neutrino flavour fluxes, and may thus either gain or loose from an equal flavour spreading.

2.2.4 Detection methods

Neutrinos can only be detected by their interaction products. As will be discussed in section 3.2, in the Standard Model this is only possible via exchange of the weak vector bosons Z^0 and W^\pm . Even in the exotic interaction models discussed there, the cross sections are still small as compared to other Standard Model processes. Thus, the detection of neutrinos at these energies always involves very large targets with a mass $M_T = V_T \varrho_T \geq 1 \text{ km}^3 \text{ gcm}^{-3}$. Only large homogeneous volumes of natural media can be employed for this purpose, such as air, water, ice or rock salt. Financial and technical reasons also prohibit a dense spacing of detectors on these scales, so that in most cases only the long reaching radiation such as fluorescence and Cherenkov light or radio and acoustic waves from the neutrino interaction can be detected. This can be used as a useful classification scheme for the planned and existing experiments.

Optical detection

The most common neutrino detection technique at larger than MeV energies is by the Cherenkov light that is emitted by the generated lepton or the electromagnetic or hadronic

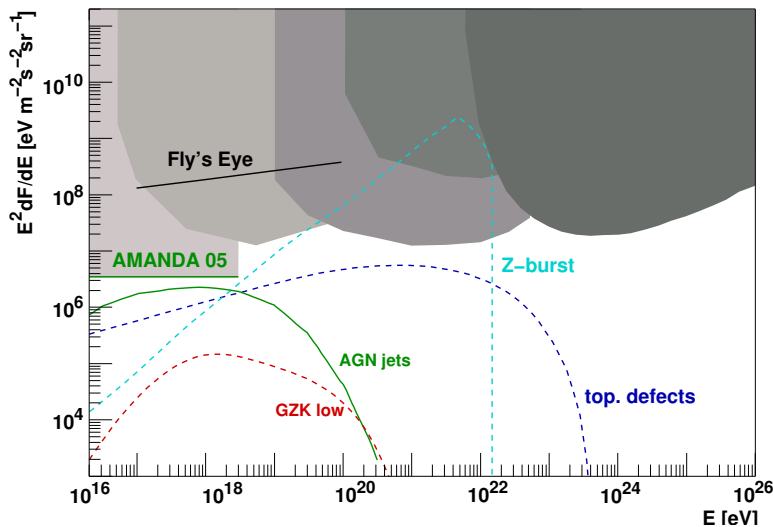


Figure 2.15: Limits on the extraterrestrial neutrino flux from AMANDA-II [A⁺04a] and FLY'S EYE [B⁺85]. A selection of flux predictions is shown for comparison (see section 2.2.2).

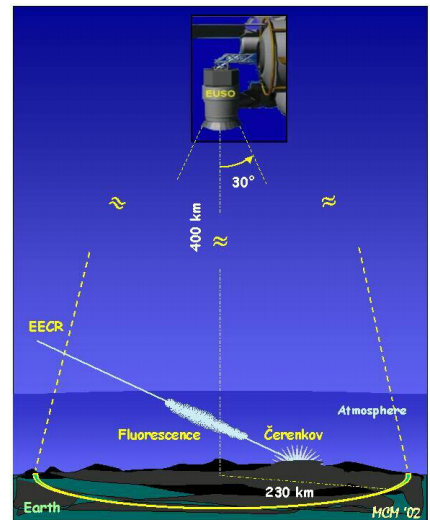


Figure 2.16: Schematic view of the EUSO experiment (from [Bot05]).

showers created in its interaction discussed in section 3.2. This method is used to detect e.g. the neutrino flux from the sun or the flux of *atmospheric neutrinos* generated as secondaries in air showers [Fuk03, MSTV03]. Since about one decade, the technique is also successfully expanded into the GeV to TeV range [A⁺06b, A⁺04a, Bec06] with the aim to discover neutrinos from the hadronic accelerators of the charged cosmic rays at these energies. Such neutrinos can be separated from the dominant atmospheric neutrino background by resolving point sources or their presumably harder spectrum. As no neutrinos of extraterrestrial origin have been detected, only upper limits are published so far [A⁺04a] (see figure 2.15). Currently constructed [DeY05] and future experiments [Kat06] aim at detector volumes on the order of 1 km³, using either the deep ocean or the South Polar ice sheet as a Cherenkov medium. In natural ice the effective attenuation length of light by absorption and scattering of dust particles is limiting the spacing of optical sensors. In water the high background rate from bioluminescence and ⁴⁰K decays makes coincident photon detection in several close sensors necessary. Combined with high technical requirements due to the high ambient pressures which make the final optical sensor module expensive, as well as time consuming and expensive installation procedures, this restricts the volumes that can be instrumented to the order of magnitude that is currently attempted. Therefore Cherenkov neutrino telescopes are not believed to yield event rates significantly larger than $\approx 1 \text{ yr}^{-1}$ from the GZK effect. For probing cosmogenic neutrino fluxes (section 2.2.1) or exotic neutrino interaction models (section 3.2) on a reasonable time scale, about a factor of ten is necessary in event rate and thus in effective target volume.

The largest target volumes for optical detectors are currently achieved in air shower experiments. Neutrinos can be detected in the same way as charged cosmic rays by the electromagnetic and hadronic showers they induce. Separation from charged cosmic ray induced showers can be achieved in two ways:

- by the penetration depth of the shower: while charged cosmic rays will always interact at the top of the atmosphere, it is nearly transparent to neutrinos. For close to vertical showers where the shower maximum is easily determined by the Cherenkov telescopes, the atmosphere is even too thin to yield a promising event rate. Therefore mostly horizontal showers are considered here. The large penetration depth of the neutrino before inducing a shower can be derived either from the electromagnetic component, that is more strongly absorbed for deeply penetrating hadron-induced showers, or by direct observation of the shower maximum in fluorescence light. So, together with a very low event rate, air shower arrays such as AUGER are facing similar problems for neutrino detection as for the determination of the composition of hadron-induced showers.
- by the orientation of the shower: while neutrinos are no longer able to penetrate the earth through the center, there is a small angular range close to but below the horizon where *skimming* neutrinos can come close to the detector. Secondary cascades can then extend in the air above the detector and can be observed as an *upward* oriented shower. For ν_μ and ν_e the geometrical probability for this is very small. This is different for ν_τ , that can be re-generated in the decay of the τ -lepton which has a suitable decay length. Still even for the AUGER detector event rates of $< 1 \text{ yr}^{-1}$ for cosmogenic neutrinos are expected [MPP06].

In any case the above methods suffer either from too much neutrino absorption in the earth or not enough neutrino interactions in the atmosphere. Only upper limits could be placed so far by the FLY'S EYE fluorescence detectors [B⁺85].

Since only the projected area counts for surface detectors if looking for very inclined showers, future experiments such as EUSO and OWL aim at increasing the observable fluorescence target volume by placing high resolution cameras in space. For EUSO one 200.000 pixel camera with 4.2 m^2 and a 60° field of view is planned to be placed on the ISS at $\approx 430 \text{ km}$ altitude (see figure 2.16). For OWL stereo observation with two independent satellites equipped with 500.000 pixel cameras of 4 m^2 and a 45° field of view orbiting at $\approx 1000 \text{ km}$ is proposed. Apart from a high-threshold, this method is of course affected by background light from the moon or stars reflected on earth, limiting the duty cycle to $\approx 15 - 25 \%$. The angular resolution is very low for vertical showers, but will be $\approx 1^\circ$ for the more numerous horizontal neutrino induced showers [Gor06]. Even though 200 times more sensitive than AUGER if only considering the events detected in hybrid mode from deeply penetrating inclined showers, EUSO will still not be able to detect the cosmogenic neutrino flux [Bot05]. For OWL, which has a similar sensitivity for ν_e , an initial phase with close orbits dedicated to detect skimming ν_τ as discussed above is planned [S⁺04b].

In summary, optical detection techniques for the ultra-high energy neutrinos discussed here in general do not yield satisfactory event rates.

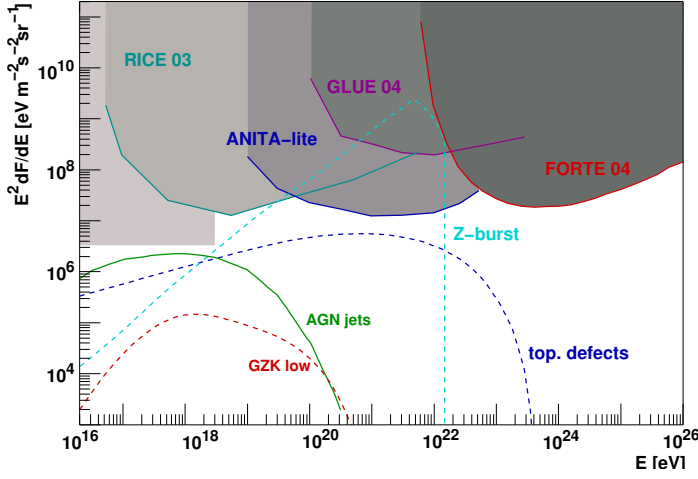


Figure 2.17: Model independent limits on the neutrino flux from RICE [K⁺06], ANITA-LITE [B⁺06b], GLUE [G⁺04] and FORTE [LGJRD04]. A selection of flux predictions is shown for comparison (see section 2.2.2).

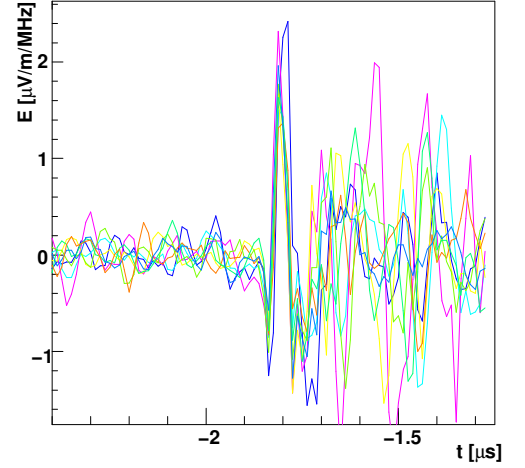


Figure 2.18: Time-aligned radio pulses from an air shower recorded with the LOPES antennas (from [H⁺06]).

Radio detection

The aim of alternative methods must therefore be to gain access to very large and dense volumes using radiation that is not strongly attenuated. In this respect, the detection of neutrino induced showers by their electromagnetic emission at radio wavelength seems very promising. The Cherenkov radiation spectrum is steeply falling towards lower frequencies. Yet the photons will become coherent when the wavelength exceeds the dimensions of the emission region, i.e. the electromagnetic or hadronic shower. Although this does not increase the radiated power, it drastically enhances the electromagnetic field strength – an effect that was first discussed and is therefore named after Gurgen Askar’yan [Ask62].

Since water is not transparent in the wavelength range of $\mathcal{O}(1\text{ m})$, it cannot be used as a target. Both a dense medium and a long attenuation length of $\mathcal{O}(1\text{ km})$ are given in the South Polar ice cap. Taking advantage of this, the RICE experiment, which consists of only 19 radio receivers in a comparatively small volume ($\approx 200\text{ m} \times 200\text{ m} \times 200\text{ m}$) is currently providing the strongest bound on the neutrino flux around 10^{19} eV (see figure 2.17) [K⁺06] – despite many transient background events of anthropogenic origin at the ice surface and from other instrumentation in the ice.

The same method can also be used in natural salt domes, that exist with high purities in volumes up to 50 km^3 . In addition, the density of rock salt $\rho_{\text{Salt}} = 2.4\rho_{\text{ice}}$ is larger than that of ice, leading to a comparable increase in neutrino interactions per unit volume for the proposed *Salt dome Shower Array* (SALSA) experiment [Rei05].

Being very transparent to radio waves, the atmosphere would also be a good target material, but the refractive index of air and therefore the Cherenkov yield is very low. However, radio emission of air showers is also provided by the geosynchrotron radiation: the clouds of negative and positive charges in air showers are separated by the earth’s geomagnetic field. The resulting radio emission has first been established about 30 years ago (e.g.

by [ASJ75]), but has recently been confirmed by the LOFAR *Prototype Station* (LOPES) experiment [H⁺05] and the *COsmic ray Detection Array with Logarithmic ElectroMagnetic Antennas* (CODALEMA) [A⁺06a]. The LOPES interferometer consists of 10 digital read-out dipole antennas located inside the KASCADE air shower array. Figure 2.18 shows the electric field strength of the individual antennas with a time shift applied to correct for the shower incidence angle measured with KASCADE. The main advantage of this method against conventional radio antennas is in the possibility of offline beam-forming by storing the individual antenna signals. The method is especially efficient for inclined showers [HF06] and thus for the detection of neutrinos. It is also planned to be implemented on much larger scales by the *LOW Frequency radio ARray* (LOFAR) array [Rot03], where 100 antenna clusters are planned to be spread out over an area of $1.25 \cdot 10^5 \text{ km}^2$, or in conjunction with the AUGER air shower array [G⁺06].

A combination of both advantages – high interaction rates in dense materials and very low absorption in the atmosphere – is used by the *ANtarctic Impulse Transient Antenna* (ANITA) and *Fast On-orbit Recording of Transient Events* (FORTE) experiments. Both are looking for radio pulse from neutrinos interacting just below the surface. The satellite-based FORTE experiment with two log-periodic dipole antennas was originally intended for other purposes, but has been used to observe the Greenland ice from a height of 800 km. Apart from a bad pointing resolution and a hard to control background from lightning, it has a high threshold energy and can only place limits above 10^{22} eV as shown in figure 2.17 [LGJRD04]. In contrast, the 32 horn antenna setup ANITA is dedicated to neutrino detection. It is planned to be carried by a balloon right over Antarctica yielding a much lower energy threshold. This has been demonstrated by a two-antenna predecessor of ANITA called ANITA-LITE, which is setting the most stringent neutrino flux limit from 10^{20} eV to 10^{22} eV [B⁺06b]. In contrast to the experiments above, ANITA will be limited not so much by transient noise events (most of which come from the ANITA payload itself), but by the limited balloon flight time of ≈ 15 days and an instrument recovery period probably limiting the number of flights to one per year. Yet another target was used in *Goldstone Ultra-high energy neutrino Experiment* (GLUE), that observed the rim of the moon with two 70 m and 34 m radio telescopes, searching for neutrinos that interact in the upper few metres of the moon regolith. Not so much the density of $\rho_{\text{regolith}} = 1.7 \text{ g/cm}^3$, but mainly the much larger observed volume of $\mathcal{O}(10^5 \text{ km}^3)$ is what allows this experiment to put a competitive limit with only 120 hrs of lifetime [G⁺04]. For a successor to this idea – the *Lunar Orbital Radio Detector* (LORD) [C⁺06] – it was proposed to build a dedicated 20 – 30 m radio antenna from a light-weight so called *film astrophysical structure* orbiting the moon in $10^3 - 10^4 \text{ km}$ height.

Although radio emission is a very promising method for neutrino detection in this energy range, only upper limits could so far be set. Apart from the low effective volumes in many of the prototype experiments, the main reason for this are mostly the strong anthropogenic backgrounds. In contrast to the thermal and ambient noise, that usually has a non-transient behaviour, these may be very hard to reject in the final data sample. Due to the non-stochastic nature they may also be difficult to treat as a background in investigations at very low event numbers. For this reason it may be very hard to establish evidence for ultra-high energy neutrinos with only the radio method at the very low event rates predicted.

Acoustic detection

Another possible detection method is not based on electromagnetic radiation, but on acoustic waves. From the almost instantaneous deposition of the ionisation energy of an electromagnetic or hadronic shower, stress will occur in the medium by the thermal expansion of the volume in which the particle cascade develops. In a dense medium, this will give rise to a bipolar ultrasonic pulse, that is emitted mostly in directions orthogonal to the shower axis. Although the conversion of the initial neutrino energy in acoustic energy is by orders of magnitude less efficient than the conversion in electromagnetic waves, the large attenuation length is what makes acoustic neutrino detection interesting for some media.

Even before the radio emission, the generation of coherent elastic waves by the thermal energy deposit of a shower in a dense medium was discussed by Askar'yan nearly 50 years ago [Ask57]. Twenty years later, the effect could be established experimentally [S⁺79, HJM⁺81b], in good agreement with more elaborate calculations [AD77, ADKM79, Bow78, Lea79]. Both efforts were mainly motivated by a possible implementation of the technique in the DUMAND experiment [LW93], the first attempt to build an underwater neutrino telescope [Bos96]. While DUMAND did not prove successful as an optical detector, calculations for water [B⁺98, D⁺97b] and ice [Pri96] quickly showed that, despite the much larger absorption length for sonic waves than for optical radiation, the extremely high energy threshold and the feeble fluxes will require detector volumes of $\mathcal{O}(10 - 1000 \text{ km}^3)$.

It is therefore only after the optical detection method has been well established on the km^3 scale (see page 20), that the interest in the acoustic detection method is growing again [NB06, T⁺06].

Both theoretical and experimental efforts are taken up again. Figure 2.19 shows the first flux limit obtained in the *Study of Underwater Acoustic Neutrino Detection* (SAUND) experiment from a lifetime of 195 days [VGL05]. A military array of seven large-bandwidth hydrophones with a spacing of 1.5 km could be used. The very high energy threshold gives sensitivity mostly in the energy range well above what is predicted for the neutrino flux models introduced in sections 2.2.1 and 2.2.2. It partly stems from an unfavourable geometry for acoustic neutrino detection, which may be circumvented by an optimised sensor spacing, but also has an irreducible contribution from the ambient ultra-sonic noise conditions. The low number of hydrophones and small instrumented volume at the same time make the limit non-competitive with the constraints

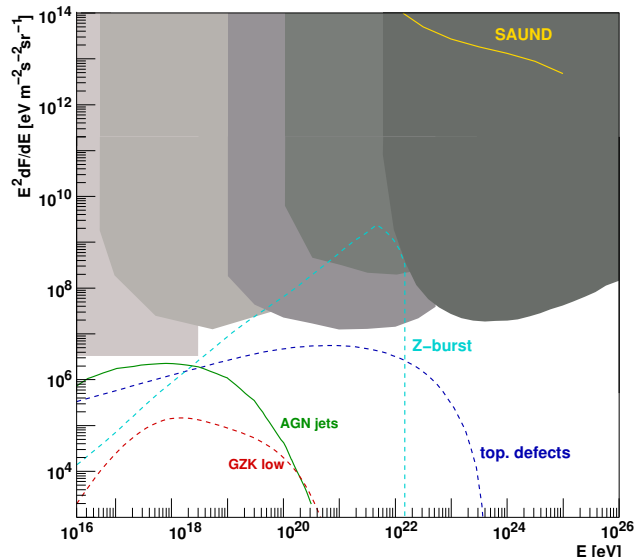


Figure 2.19: Model independent neutrino flux limit from SAUND [VGL05]. A selection of flux predictions is shown for comparison (see section 2.2.2).

the constraints

Parameter	Ocean	Ice	Rock salt
T [°C]	15	−51	30
ρ [$\frac{\text{g}}{\text{cm}^3}$]	1	0.92	2.16
$\langle v_l \rangle$ [$\frac{\text{m}}{\text{s}}$]	1530	3920	4560
α [K^{-1}]	$25.5 \cdot 10^{-5}$	$12.5 \cdot 10^{-5}$	$11.6 \cdot 10^{-5}$
C_p [$\frac{\text{J}}{\text{kgK}}$]	3900	1720	839
γ_G	0.153	1.12	2.87

Table 2.1: Most relevant parameters for acoustic neutrino detection in the ocean, in ice or in rock salt (from [Pri06]).

from radio observations. In accordance with this, elaborate recent simulations [Kar06, Nie05] indicate that in the Mediterranean detector volumes of $1000 - 1500 \text{ km}^3$ may be necessary to detect the flux of GZK neutrinos. Despite this, acoustic detection efforts are currently undertaken in conjecture with all optical underwater neutrino telescope activities [L⁺06, Ric06, A⁺06c], but also as independent activities [KS06, Kur06, Per06, C⁺01].

One way to avoid the extremely large scale infrastructure that is needed for such a detector is to choose another target material. Large natural occurrences of ice (e.g. in Antarctica) or rock salt (e.g. in salt domes) are discussed as possibilities. Three main factors can be identified, that make these favourable for acoustic neutrino detection [Pri06]:

- The dimensionless GRÜNEISEN coefficient

$$\gamma_G = \langle v_l \rangle^2 \frac{\alpha}{C_p}, \quad (2.16)$$

which summarises the efficiency of heat conversion into expansion from the thermal expansion coefficient α and the specific heat capacitance C_p , as well as the level of coherence from the propagation velocity of pressure waves v_l . The amplitude of the acoustic signal at a certain distance will directly scale with this coefficient. A summary of the parameters is given in table 2.1, showing that both ice and salt will yield significantly larger signal amplitudes.

- The neutrino interaction rate will directly scale with the density ρ of the target medium. This has to be taken into account when estimating the event rates of an acoustic detector. As the density values given in table 2.1 show, rock salt will yield significantly higher event rates than water or ice.
- With steeply falling spectra, the energy threshold of an acoustic array will also be a critical parameter for an ultra-high energy neutrino detector. For a single sensor, the threshold will depend on the ratio of signal to noise, where the latter may have two components: one from the intrinsic (e.g. electronic) noise of the receiver and one from the ambient noise conditions. Especially wind and waves are well known sources of ultrasonic noise in the sea, generating sound levels well above the corresponding self-noise of modern receivers. Waves can be excluded as noise sources for ice and salt, although other, yet unknown mechanism may be present.

Despite being apparently well-suited for acoustic detection, both salt and ice have not been extensively studied yet for their potential as acoustic neutrino detector material. Only considering the physical parameters, rock salt seems to be the best material. However, practical considerations, such as the accessibility also have to be taken into account. For ice, the ICECUBE experiment currently being installed at South Pole provides both good infrastructure and deep drilling technology for in-situ installations. For this reason, and for the possibility of a hybrid detector implementing all three of the above mentioned detection methods, the investigations presented in this work will only be focused on ice as a potential target material. To commence with, an analysis of the existing prerequisites and knowledge about antarctic ice with respect to acoustic neutrino detection has been performed, and will be summarised in chapter 3.

Chapter 3

Prerequisites

While in the last chapter a basic motivation for the development of acoustic detection in glacial ice was given, this chapter tries to summarise the existing knowledge and uncertainties related to the method. After a brief discussion of the uncertainties in the neutrino flux and interaction models, the problems of cascade simulations at the EeV energy scale will be presented in section 3.3. The thermo-acoustic model for water and its applicability to ice are discussed in section 3.4. At the end, the current knowledge of the ice properties will be summarised in section 3.5.

3.1 Cosmogenic neutrino flux

As introduced in section 2.2.1, the cosmogenic neutrino flux derives from the interaction of ultra-high energetic protons with the ambient cosmic microwave background. Consequently, its uncertainties are directly related to the uncertainties in assumptions about the cosmic ray input. In contrast to that, both the interaction through the Δ^+ resonance and the cosmic microwave background are much better known.

The energy range of the Δ^+ resonance at $E_{res}^{\Delta^+} = 1232$ MeV is well accessible in collider experiments, yielding precise information on the respective cross sections, branching ratios and momentum distributions [ABS⁺04]. The cosmic microwave background which originates from the photon decoupling after recombination in the early universe has been most accurately measured by the WMAP experiment [S⁺06]. Being decoupled, it is only subject to redshift and its dependence on cosmological time can easily be applied in flux calculations for uniform source distributions, where the integration over the sources is usually done in *redshift space*. Only moderate redshifts are taken into account, the result is only slightly dependent on the evolution parameters of the universe [ESS01, KKSS02b]. Figure 3.1 shows the predicted flux for a flat mass-dominated universe ($\Omega_M = 1.0$) and a flat universe with a contribution from a cosmological constant ($\Omega_M = 0.3$, $\Omega_\Lambda = 0.7$). In the latter model, that is well supported by recent observations [Car01, S⁺06], only the effect of the cosmological constant on the propagation of cosmic rays is considered. If also the source evolution is affected, the effect might cancel out [ESS01]. In any case the enhancement over the mass-dominated model is smaller than a factor of two.

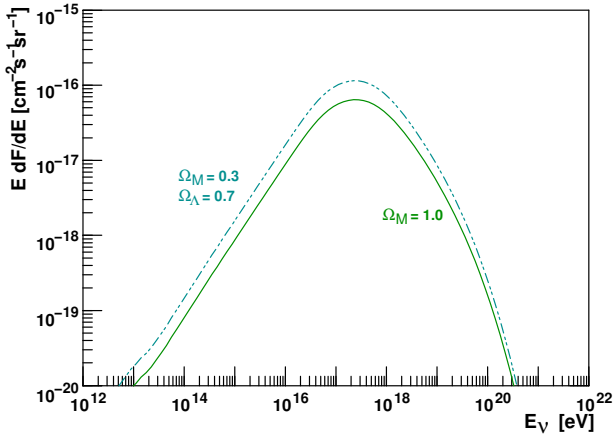


Figure 3.1: Cosmogenic neutrino flux for a source evolution parameter $m = 4$ and two different values of Ω_Λ [ESS01].

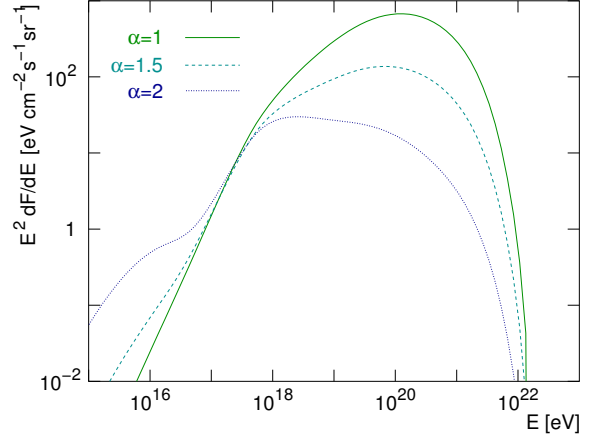


Figure 3.2: Cosmogenic neutrino flux for a source evolution parameter $m = 3$, a maximum source energy of $E_{max} = 3 \cdot 10^{22}$ and different values of α [KKSS02b].

Remain the sources themselves, which – not being identified – provide the predominant contribution to the uncertainty by their unknown distribution and spectra. Since slightly favoured by the data presented in section 2.1, only uniform source distribution models shall be discussed here. Four critical parameters can be identified:

- α : A power law $\frac{dN}{dE} \propto E^{-\alpha}$ extending over several orders of magnitude is observed for the cosmic ray spectrum at the earth. This is also assumed for the cosmic ray spectrum at the source, however with a spectral index that is not supposed to be identical to the one obtained in the measurements. At energies below $E \approx 10^{18}$ eV, the spectrum is affected by energy-dependent gyration radii of the charged cosmic rays in the galactic magnetic fields. At the highest energies above 10^{19} eV, where charged cosmic rays are energetic enough to travel in straight lines, they get absorbed in the GZK effect, which again alters the spectrum. The transition region where the measured spectrum could reveal the emitted spectrum is rather small, leaving sufficient room for speculation. As supported by the widely accepted first order Fermi acceleration a spectral index of $\alpha = 2$ is most commonly used. Figure 3.2 shows an example of how the spectral index influences the neutrino spectrum. For a harder input spectrum also more high-energy neutrinos are produced. All spectra are normalised to the same photon output, so that for a softer input spectrum, more neutrinos can be attributed to the neutron decay introduced in equation 2.7. This leads to the second *bump* appearing at lower energies.
- E_{max} : Assuming a Fermi acceleration mechanism, where the particles are trapped in magnetic fields while undergoing repetitive acceleration steps, it is natural to assume a maximum energy E_{max} as introduced in equation 2.8, up to which the particles can be accelerated. This reflects the limited size of the acceleration region which limits the number of scatter processes on the shock wave, and the limited magnetic field strength. Obviously, as shown in figure 3.3, the result of increasing the maximum energy can only be an enhancement of the neutrino flux at high energies, while the low energy part remains unaffected.

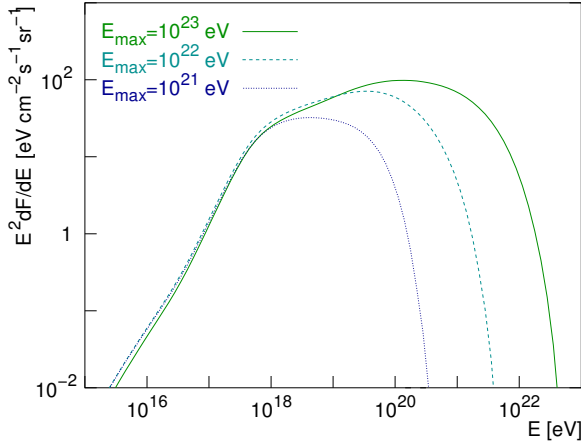


Figure 3.3: Cosmogenic neutrino flux for a source evolution parameter $m = 3$, an input spectral index $\alpha = 1.5$ and different values of E_{max} [KKSS02b].

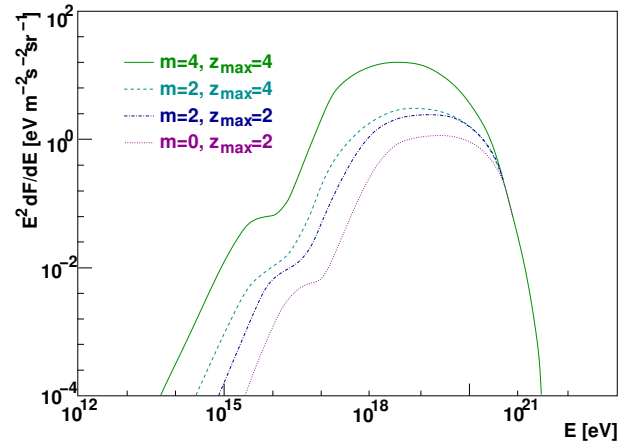


Figure 3.4: Cosmogenic neutrino flux for different source evolution parameters m and z_{max} and an input spectrum with index $\alpha = 2$ up to $E_{max} = 1 \cdot 10^{22}$ [YT93].

- m and z_{max} : The main uncertainty in the calculation of the cosmogenic neutrino flux is the input source distribution. Assumed to follow the star formation rate or radio galaxy luminosity distribution, it is usually modelled as a power law in redshift. But as sources cannot have been infinitely dense in the beginning of the universe, a maximum redshift z_{max} is introduced, resulting in the equation

$$n(z) = \begin{cases} n_0(1+z)^m & \text{for } z < z_{max} \\ n_0(1+z_{max})^m & \text{for } z \geq z_{max} \end{cases} . \quad (3.1)$$

In some cases, an exponential decrease for very high redshifts (e.g [ESS01]) or a smoother model of the source density distribution [DMSS06] is introduced to account for the formation of the sources in the universe. Due to the expansion of the universe, the effect of changes in $n(z > z_{max})$ are diluted and integration with a constant density above $z \geq z_{max}$ does not yield a significant difference. In contrast, the choice of m and z_{max} does. Figure 3.4 shows the effect on the cosmogenic neutrino fluxes in a calculation from [YT93]. Especially larger m , but also larger z_{max} lead to an increase in integral number of sources and thus in total flux. The high energy end of the spectrum is yet still determined by the choice of E_{max} and α for the input spectrum.

The absolute normalisation can be done in two ways: In [YT93] an integral flux of cosmic rays consistent with the observations on earth is assumed. The flux at the sources is then scaled to fit the cosmic ray observations. Since the neutrinos are generated in the absorption of exactly these cosmic rays an assumption has to be made on the unabsorbed spectrum. In most calculations, for the normalisation also the γ -rays from the decays of neutral pions $\pi^0 \rightarrow \gamma\gamma$ stemming from the same interaction 2.1 as the charged pions are taken into account. The high energetic part of the flux is obscured by $\gamma\gamma \rightarrow e^+e^-$ interactions on ambient photon backgrounds. An electromagnetic cascade is initiated, in which photon energies are lowered down to the pair production threshold. Yet below $E_\gamma = 10$ GeV the universe is transparent out to redshifts of $z \gg 100$ [LM00]. The gamma ray fluxes measured by the satellite based

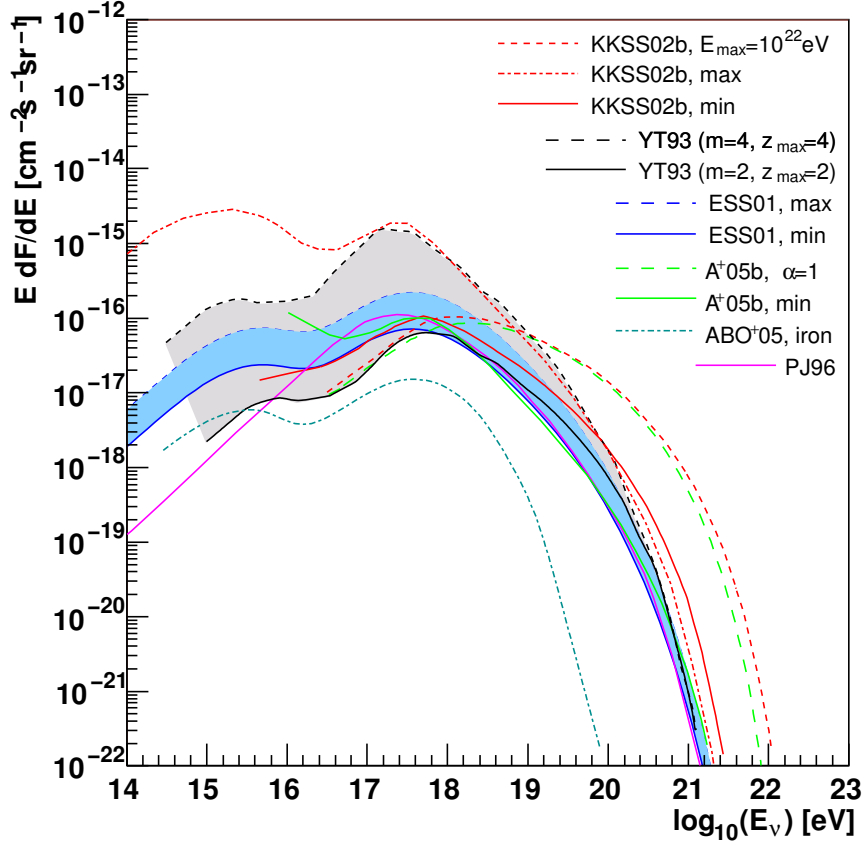


Figure 3.5: Cosmogenic neutrino flux predictions from various authors – for details see text (adapted from [G⁺05]).

EGRET experiment can thus be used to constrain the initial proton and resulting neutrino fluxes.

Figure 3.5 shows a summary of different model calculations:

- an early calculation by [PJ96] using a recursive matrix method instead of a Monte Carlo simulation for the propagation,
- two models by [YT93] with the extreme assumptions $m = 2, z_{max} = 2$ and $m = 4, z_{max} = 4$ yielding very low and high fluxes,
- a model giving a minimal and a maximal flux by [ESS01] where also all parameters have been varied, but in more reasonable bounds,
- two maximised flux models and one minimal flux by [KKSS02b], where m, z_{max} and E_{max} are maximised respectively to fulfil the bound by lower energy gamma ray observations,
- a model with a harder injection spectrum and a minimal flux model from [A⁺05e],
- and a model assuming a pure iron flux at the source [ABO⁺05].

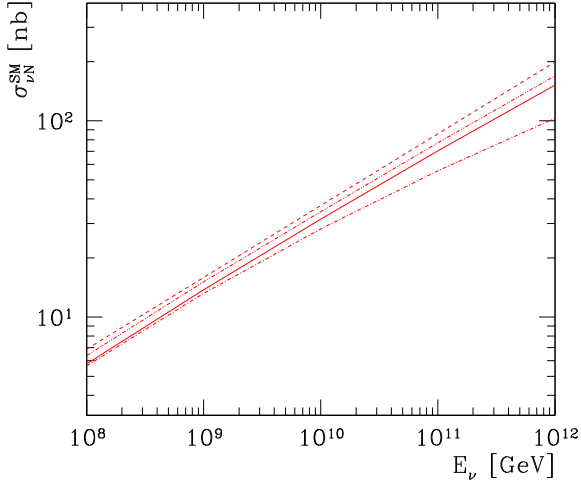


Figure 3.6: Total cross section (charged plus neutral current) for neutrino-nucleon interactions for various parton distribution functions (from [Rin06]).

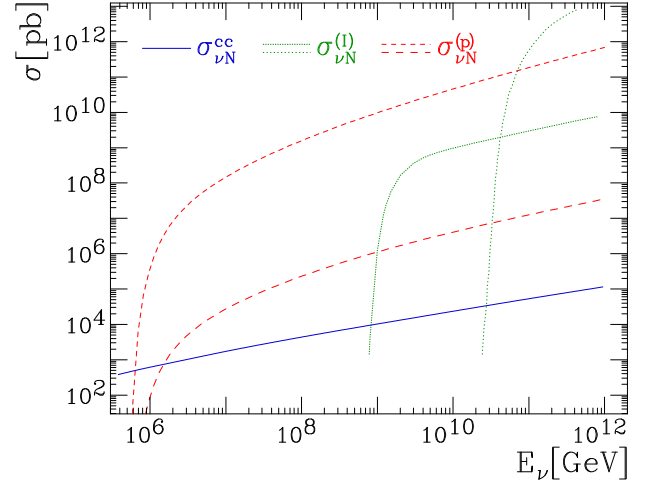


Figure 3.7: Neutrino-nucleon cross section for the Standard Model $\sigma_{\nu N}^{cc}$ compared to the range of predictions from the electro-weak instanton models ($\sigma_{\nu N}^{(I)}$) [FKRT04] and p-brane models ($\sigma_{\nu N}^{(p)}$) [AFG02].

It is evident that especially at lower energies the uncertainties exceed more than one order of magnitude in the predicted flux. An analysis of a higher and lower limit (shown in figure 2.8) solely based on features of the observed cosmic ray spectrum is presented in [FKRT03a]. It constrains the lower energy part much stronger, but results in no significant enhancement at the flux peak. However, despite the uncertainties on the source distribution in the universe, the models yielding a minimal flux for proton induced cosmogenic neutrino rates are in astonishingly good agreement. To obtain a conservative estimate and allow comparison with other publications, the minimal flux model by [ESS01] will be used in chapter 4, where a potential hybrid detector including acoustic sensors is discussed.

3.2 Neutrino interactions

3.2.1 Cross sections

In the Standard Model, neutrino interactions are described by charged current interactions:

$$\nu_l + N \xrightarrow{W^+} l^+ + \text{had.casc} \quad (3.2)$$

$$\bar{\nu}_l + N \xrightarrow{W^-} l^- + \text{had.casc} \quad (3.3)$$

and neutral current interactions:

$$\nu + N \xrightarrow{Z^0} \nu + \text{had.casc} . \quad (3.4)$$

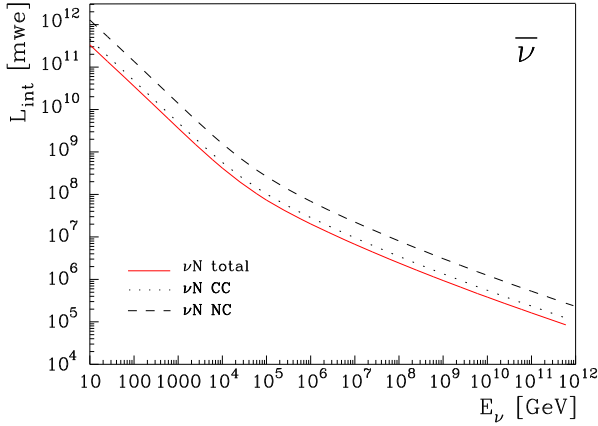


Figure 3.8: $\bar{\nu}$ interaction length vs. energy for total, charged and neutral current cross sections (from [GQRS96]).

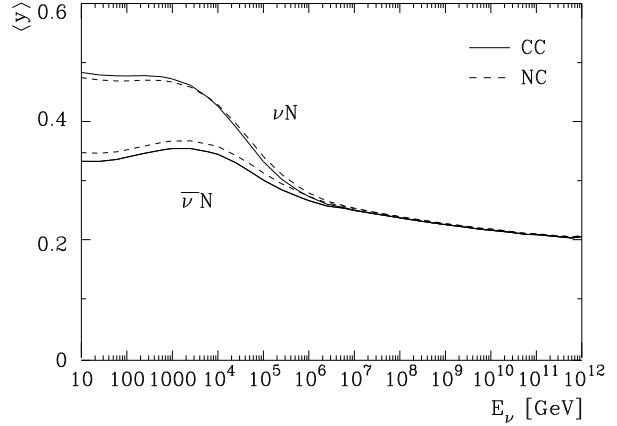


Figure 3.9: Mean inelasticity for ν and $\bar{\nu}$ vs. neutrino energy (from [GQRS96]).

The centre of mass energy

$$\sqrt{s_{\nu N}} = \sqrt{2m_N E_\nu} \approx 45 \text{ TeV} \cdot \sqrt{E_\nu / 10^{18} \text{ eV}} \quad (3.5)$$

in the range of neutrino energies E_ν considered here is well above what can be tested at current collider experiments. Yet due to precise measurements at lower energies the cross sections can be reliably extrapolated. Figure 3.6 shows the predicted total cross section $\sigma_{\nu N}^{tot} = \sigma_{\nu N}^{CC} + \sigma_{\nu N}^{NC}$ for different perturbative QCD summation approaches [Rin06].

It has to be mentioned that besides the Standard Model also other interaction models are discussed [HH04b], such as parton interactions induced by electro-weak instantons [FKRT03b] or p-branes [AFG02]. As these typically result in cross sections that are orders of magnitude larger (see figure 3.7), they may cause a large number of neutrino induced air-showers starting high in the atmosphere, which could explain the observed excess of events above the GZK cutoff discussed in section 2.1.2 [FKRT04]. On the other hand, assuming that the neutrinos that cause these events are *only* produced in the GZK mechanism, the observed cosmic ray spectrum is already imposing limitations to these models [ART06].

For underground detectors, care has to be taken in the choice of the installation depth. In contrast to neutrinos in the GeV to PeV range, the absorption length $L_{abs}(E_\nu) = (n_T \sigma_{\nu N}^{tot}(E_\nu))^{-1}$ for the neutrino energies discussed here is short enough that for targets with number density $n_T > 10^{29} \text{ km}^{-3}$ (such as the earth), absorption is no longer negligible. Figure 3.8 shows the anti-neutrino interaction length in units of m.w.e. (*metre water equivalent*), corresponding to a medium with a density of $\rho = 1 \frac{\text{g}}{\text{cm}^3}$. For neutrino telescopes operating at lower energies neutrinos are equally likely to reach the detector from all directions, but are indiscriminable from the atmospheric lepton fluxes initiated by cosmic ray showers. In contrast, at the energies of GZK neutrinos, they are expected to reach the detector only from above. With increasing mass column density $\int_p \rho dl$ along the neutrino path p to the detector, a rapid decrease in flux should appear close to the horizon. Since the density profile of the earth in the upper layers is comparatively well known [DA81], this zenith angle dependence can be exploited in turn to set limits on $\sigma_{\nu N}^{tot}$ independent of

assumptions on the flux. A recent analysis [Con06] has shown that for an experimental resolution of $\Delta\theta = 1^\circ$ a cross section growing as a power law $\sigma_{\nu N}^{tot} \propto E_\nu^{0.363}$ (which for $10^8 \text{ GeV} < E_\nu < 10^{10} \text{ GeV}$ fits well to the Standard Model prediction) can be constrained to within 38% in the absolute normalisation by the observation of 100 neutrino interactions from an isotropic flux. So rather than suffering from systematic uncertainties at this point, experiments capable of detecting a significant amount of neutrinos from the proposed models in sections 2.2.1 and 2.2.2 will give an important input to elementary particle physics.

As will be discussed in section 3.3, the dominant contribution to the acoustic signal will come from the hadronic part of the cascade following the neutrino interaction. The fraction of the initial energy E_ν that is not carried by the emerging lepton, also called the inelasticity

$$y = \frac{E_\nu - E_{lept}}{E_\nu} = \frac{E_{hadr}}{E_\nu}, \quad (3.6)$$

determines the total energy E_{hadr} that goes into the hadronic cascade. For large E_ν , the distribution is rather energy independent and the mean value shown in figure 3.9 approaches $\langle y \rangle = 0.2$. While this is a good approximation for the average behaviour, it should be noted that the underlying distribution of y is very wide, so that the real probability density should be sampled if considering single events.

3.3 Secondaries and cascades

As shown in the next section 3.4, the generated acoustic pulse will only depend on the density and distribution of the energy deposited in the medium. Mainly the hadronic, but also the electromagnetic cascades contribute to the acoustic signal as shall be demonstrated in this section.

3.3.1 Neutrino flavours

Having the same cross sections for nucleon interactions at high energies, the different neutrino flavours have not been distinguished in the discussion, so far. For neutral current interactions in equation 3.4, the emerging lepton will again be a neutrino (of the same flavour) which escapes the detection. Only the hadronic cascade will be observable, so neutrino flavours cannot be distinguished. Due to the higher cross section, the major part of detectable interactions will be charged current interactions (see equation 3.3), for which the emerging lepton is either a e^\pm , μ^\pm or τ^\pm , leading to very distinct signatures:

- Even including the *LPM* effect (see below), at these high energies electrons will emit bremsstrahlung photons above the pair-production threshold with an interaction length of $\mathcal{O}(10 - 100 \text{ cm})$. Thus, electrons will immediately initiate an electromagnetic cascade that contributes to the detectable signal.

- Muons will be well above their critical energy. Nevertheless, the bremsstrahlung dominated relative energy loss is not more than $1/E_\mu \, dE_\mu/dx \leq 10^{-4} \text{ m}^{-1}$ of the muons energy E_μ , leading to energy densities far too small to be detectable by their acoustic emission. Large fluctuations of this energy loss may occur in so called *catastrophic* bremsstrahlung events, but these are becoming increasingly rarer the higher the fraction of the energy that is lost for the muon.
- For tau leptons, the energy loss per unit length is even smaller. For neutrino telescopes operating at lower energies there is a chance to detect the unique signature of the tau decay within the instrumented volume. With decay lengths $\beta\gamma c\tau_\tau \gg 10 \text{ km}$ this will typically happen outside the detector for $E_\tau \gg 1 \text{ PeV}$. Hence also tau leptons are most often lost for acoustic detection.

In summary, only the hadronic vertex cascades from charged and neutral current interactions and the electromagnetic cascades from charged current $\nu_e, \bar{\nu}_e$ interactions need to be considered.

3.3.2 Cascades

Although extensively studied since many decades, at the extreme energies considered here, the accurate description of cascades provides a challenge. Cross sections and momentum distributions have to be extrapolated into an energy range that is not experimentally accessible. Following the cascade development down to lower energies, where the respective interactions are well studied, the simulation of single vertices becomes prohibitive due to the large amount of particles involved. Parametrisations or down-sampling techniques have to be used to describe the shower development in this regime.

Nevertheless, shower calculations not only can be cross-checked at lower energies, but also by comparison to extensive air shower observations, which gives some confidence in the results. Several attempts have been made to calculate electromagnetic [AMZ97] and hadronic showers in ice [AMZ98] and water [NB05], both of which will be presented here. Having the same chemical composition, the main difference from ice to water arises from the density ratio of $\rho_{water}/\rho_{ice} \approx 1/0.92 = 1.09$ by which in first approximation the extensions of the showers in ice have to be scaled relative to the showers in water. Consequently, the radiation length in ice is $X_0^{ice} = 39.6 \text{ cm}$, but only $X_0^{water} = 36.08 \text{ cm}$ in water [Y⁺06].

In order to describe a radial symmetric shower, its energy density distribution $\varepsilon(x, r)$ is usually split into a longitudinal part $f_l(x)$, depending only on the position x along the shower axis, and a radial part $f_r(r, x)$, the depends also on the distance to the shower axis r :

$$\varepsilon(x) = \frac{1}{2\pi} f_l(x) f_r(r, x) . \quad (3.7)$$

Both parts will be treated independently in the following, with a further distinction between electron and hadron induced cascades for the longitudinal shower profile.

3.3.3 Longitudinal shower profile

Electromagnetic showers

For electromagnetic showers up to energies of $\mathcal{O}(\sim 100 \text{ TeV})$ the longitudinal part in equation 3.7 can be well approximated by [Y⁺06]

$$f_l(x) = \frac{E}{X_0} \frac{b \cdot (bu)^{a-1} \cdot e^{-bu}}{\Gamma(a)} \quad \text{with} \quad u = \frac{x}{X_0}, \quad (3.8)$$

where X_0 is the radiation length and a and b are parameters that depend on the energy and type of the initial particle as well as on the medium. The shower maximum will then occur at $x_{max} = (a - 1)/b \cdot X_0$, which for energies below PeV scales logarithmically with energy in good approximation.

For electron energies above $E \gtrsim E_{LPM} = 2 \text{ PeV}$ in ice [AMZ97], the pair production and bremsstrahlung cross sections are significantly decreased by the LANDAU-POMERANSCHUK-MIGDAL (LPM) effect [LP53b, LP53a]. For an electron of energy E_e that interacts and radiates a photon of energy E_γ , one can define the *formation length* [BK05]

$$l_f = \frac{2\hbar c}{m_e^2} \frac{E_e (E_e - E_\gamma)}{E_\gamma} \approx 2\gamma^2 \frac{\hbar c}{E_\gamma} \quad \text{for} \quad E_\gamma \ll E_e. \quad (3.9)$$

The formation length is derived from the longitudinal momentum transfer to the scatter centre and the uncertainty principle. In a descriptive way it gives the length by which the final state particles have to be separated to be treated as independent. At very high energies, the formation length may exceed the scattering length. Quantum mechanical amplitudes from different scattering centres will interfere, usually in an incoherent way [BGK06]. As a result, the cross sections drop with $1/\sqrt{E}$, leading to a significant elongation of the shower.

Figure 3.10 shows the increase in the distance from the vertex to the shower maximum with energy for a simulation in water. A simulation code including the LPM effect [NB05] was developed and tuned to results from the *GEANT4* simulation package at energies $E < 1 \text{ PeV}$. For low energies, a logarithmic scaling with the initial energy E_0 as $x_{max}/X_0 = c \cdot \log_{10}(E_0/1 \text{ eV})$ with $c \approx 1$ is a good approximation. Above $E_0 \gtrsim 20 \text{ PeV}$ the scaling is better described by $c \approx 6$ and even higher in the EeV regime. Assuming that the relative radial distribution is not affected by changes in the longitudinal profile, the energy density then scales in the same way.

However, this neglects the stochastic nature of the shower, which gets strongly enhanced due to the increased interaction length $l_{E>E_{LPM}}^{int}$ for the leading particles. After a few interactions, secondaries will be below E_{LPM} , causing a compact local cascade of length $l_{E<E_{LPM}}^{casc}$. But stemming from the higher energy primaries, these showers may be separated by distances $\mathcal{O}(l_{E>E_{LPM}}^{int}) \gtrsim \mathcal{O}(l_{E<E_{LPM}}^{casc})$ comparable to or larger than their length. This is illustrated in figure 3.11, which shows examples of longitudinal shower profiles at various energies from 10^{17} eV to 10^{20} eV using the same simulation [NB05]. Below 10^{17} eV the shower might be well described by equation 3.8, whereas at 10^{20} eV the stochastic behaviour of (the still few) super- E_{LPM} initial particles is clearly visible.

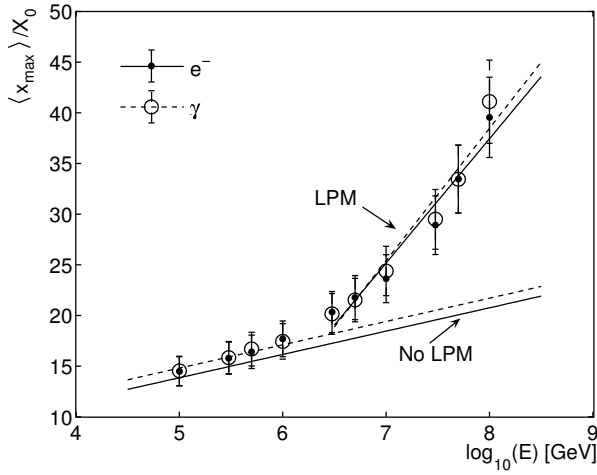


Figure 3.10: Average position of the shower maximum in e^- and γ initiated showers from a simulation in water. Error bars give standard deviations for a single cascade event. The line indicates extrapolations with and without inclusion of the LPM effect (from [NB05]).

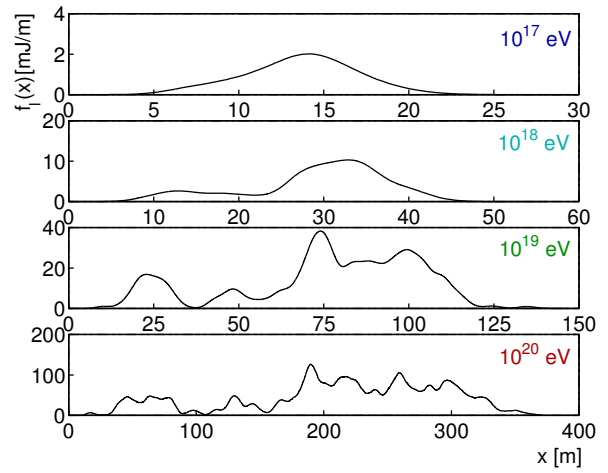


Figure 3.11: Examples of longitudinal development of LPM extended cascades in water at various energies (from [NB05]).

So despite taking on average 80% of the neutrino energy, electromagnetic showers are stretched by a factor of more than six compared to hadronic showers, which brings down the average energy densities to comparable levels. Furthermore, the energy is spread among several subshowers that are stochastically distributed along the shower axis. The maxima of the subshowers will not be at the same position, which further reduces the peak energy deposit. As shown in figure 3.11, the peak energy density increases by less than two orders of magnitude for an increase of 10^3 in cascade energy. Occurring in addition at the vertex of only $1/3$ of the possible neutrino interactions, electromagnetic showers are often neglected for the calculation of acoustic signals.

Hadronic showers

Hadronic showers, i.e. showers initiated by hadrons instead of electrons or photons at very high energies can in general be treated similar to electromagnetic showers. Pions are generated in the fragmentation of the primary and secondary nuclei. Neutral pions will in general decay in two photons. Due to the density of the medium secondary high energy charged pions have a higher probability to interact again instead of to decay. Assuming equipartition in energy among all pions, roughly $1/3$ of the energy is converted to electromagnetic subshowers in each interaction, yielding $E_{EM} = E_0 \cdot (1 - (2/3)^n)$ of the initial energy in electrons and photons after n interactions. Hadronic showers can therefore be thought of as an electromagnetic shower being fed by a high energy hadronic core. So in terms of particle number density, the longitudinal development of hadron-induced showers at low energies is also well described by equation 3.8.

One could now assume, that hadronic showers show the same strong elongation due to the LPM effect as electromagnetic showers. However, there are two counteracting effects:

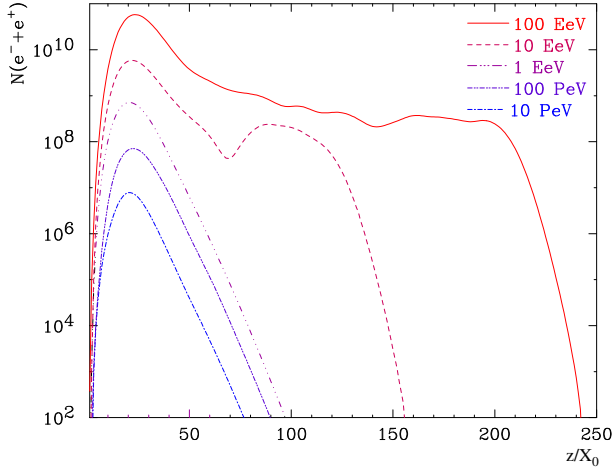


Figure 3.12: Longitudinal development of the electron density in hadronic cascades for various energies (from [AMZ99]).

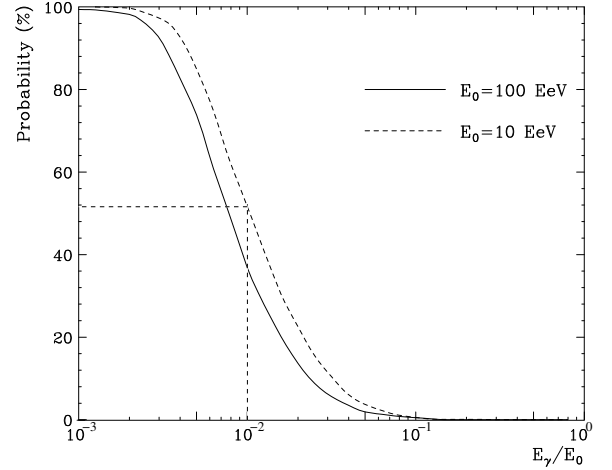


Figure 3.13: Probability to have a photon with energy E_γ or larger in a hadronic cascade of energy E_0 (from [AMZ99]).

- For an energy transfer $E_0 = 1$ EeV to the hadronic system, the average pion multiplicity in the first interaction of the shower is ≈ 14 [AMZ99]. Each of the photons from the $\pi^0 \rightarrow \gamma\gamma$ decays will on average have an energy of ≈ 35 PeV, only marginally inside the LPM regime.
- The effect is further mitigated by the fact that above $E_{\pi^0} = 6.7$ PeV [AMZ98], even the neutral pions are more likely to interact than to decay, by which they further loose energy.

For this reason, below 1 EeV hadronic showers do not show strong elongation due to the LPM effect. Figure 3.12 shows longitudinal distributions for hadron-induced cascades in a hybrid simulation using Monte Carlo methods at high energies and parametrised shower forms at low energies.

Only above 1 EeV deviation of the shower from the generic form can be observed. This is dominantly due to photons from the radiative decay of short-lived resonances such as η and η' . The probability to get a photon with a fraction E_γ/E_0 of the initial energy is shown in figure 3.13. Scaled by the initial energy, the distribution is very similar for $E_0 = 100$ EeV and $E_0 = 10$ EeV. However, in the latter case only $\approx 50\%$ of the cascades will have a photon with an energy above 100 PeV that starts a cascade causing a long tail to the hadronic shower. For $E_0 = 100$ EeV such a photon will be present in practically every shower.

Nevertheless, as seen in figure 3.12, the shower is still clearly peaked at a few radiation lengths, causing high energy densities that provide the dominant contribution to the acoustic signal. Yet, the LPM effect should not be neglected for hadronic showers.

3.3.4 Radial shower profile

In contrast to the longitudinal development of the shower, the radial profile does not vary strongly with energy. Furthermore, being dominantly electromagnetic, the lateral energy

distribution function $f_r(r, x) \propto \rho_e(r, x)$ in good approximation scales with the radial electron density ρ_e . Traditionally, this electron distribution is calculated based on the NISHIMURA–KAMATA–GREISEN (NKG) formula — Greisens approximation to analytic calculations of Nishimura and Kamata to describe purely electromagnetic cascades:

$$\rho_e^{NKG}(r, s(x)) = \frac{N_e}{R_M^2} \frac{\Gamma(4.5 - s)}{2\pi\Gamma(s)\Gamma(4.5 - 2s)} \left(\frac{r}{R_M}\right)^{s-2} \left(1 + \frac{r}{R_M}\right)^{s-4.5}. \quad (3.10)$$

Here the dependence on x is implemented via $s(x) \approx \frac{3x}{x+2x_{max}}$, which is called the *shower age* and is zero at the beginning and $s = 1$ when the shower reaches its maximum. N_e denotes the total number of electrons at a given shower age and R_M is the Molière radius, which determines the lateral extension of the cascade. For ice, a value of $R_M \approx 11 - 13$ cm is found [RSBM01, ZHS92].

The total radial energy deposit for a 500 TeV electron-induced cascade from a *GEANT4* simulation is shown in figure 3.14, along with the NKG parametrisation introduced above. While the NKG formula fits the overall distributions rather well, for small radii $r < 0.1R_m$ there is significant deviation. In [NB05, Nie05] another empirical function is used to describe the radial profile of the energy deposit:

$$\rho(r, x) \propto \begin{cases} r_t^{n_1}/r^{n_1} & \text{for } r \leq r_t \\ r_t^{n_2}/r^{n_2} & \text{for } r > r_t \end{cases}, \quad n_1(x) < n_2(x). \quad (3.11)$$

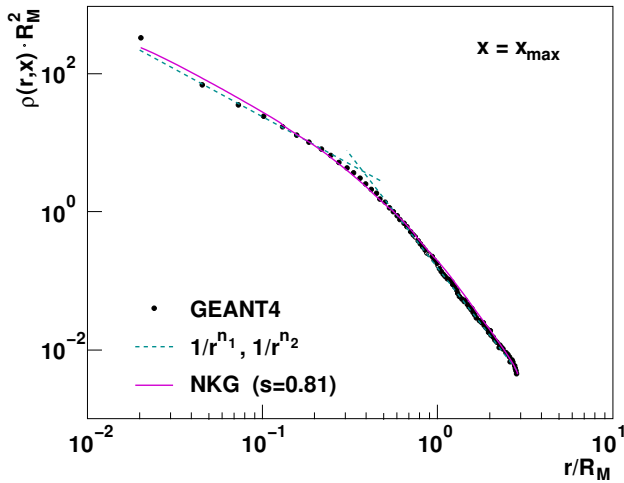


Figure 3.14: Normalized radial energy density distribution at the shower maximum x_{max} for $E_0 = 500$ TeV. The solid lines show two different parameterisations (from [Nie05]).

Again, from the simulation, $n_1(x)$ and $n_2(x)$ are found to scale linearly along the shower in good approximation, while the transition radius r_t does not depend on x . Comparisons with air shower experiments also show reasonable agreement [Nie05].

Yet, the peaking of the distribution at very small radii $r \lesssim 0.02R_m$ is not described in either of the parameterisations, but also found in other simulations [ZHS92, Slo06]. This will especially affect the high frequency component of the acoustic signal. While of minor importance in water, where the high frequency part is strongly damped by viscosity, the importance for ice may be larger. As described in section 3.5,

acoustic attenuation in ice levels off at high frequencies. Only the NKG parametrisation is used up to now in any simulation of acoustic pulses in ice. Alternative approaches, e.g. using the radial distribution functions 3.11 or based on Monte Carlo studies would be desirable. However, since a larger core energy density at higher peak frequencies will enhance the peak signal amplitude, the current NKG-based estimates can be considered conservative.

3.4 Thermo-acoustic model

In the thermo-acoustic model, which was first discussed by [Ask57], ionisation energy from a shower is converted into acoustic energy by the thermal expansion of the liquid or solid in which the energy is deposited. Knowing the parameters of the medium – the velocity of sound v_l , the specific heat capacitance C_p and the thermal expansion coefficient α – it only depends on the spatial and temporal development of the deposited energy density $\varepsilon(\vec{r}, t)$.

3.4.1 In liquids

In liquids, the differential equation for the pressure amplitude $P(\vec{r}, t)$ at a point \vec{r} and time t arising from such an energy deposit is given by

$$\Delta P(\vec{r}, t) - \frac{1}{v_l^2} \frac{\partial^2 P(\vec{r}, t)}{\partial t^2} = -\frac{\alpha}{C_p} \frac{\partial \varepsilon(\vec{r}, t)}{\partial t^2}. \quad (3.12)$$

This formula has been independently derived by several authors [ADKM79, Lea79, Bow78], and also experimentally verified as will be shown in chapter 6. A solution is given by the KIRCHHOFF integral [ADKM79]

$$P(\vec{r}, t) = \frac{\alpha}{4\pi C_p} \int \frac{dV'}{|\vec{r} - \vec{r}'|} \frac{\partial^2}{\partial t^2} \varepsilon\left(\vec{r}', t - \frac{|\vec{r} - \vec{r}'|}{v_l}\right). \quad (3.13)$$

The pressure at a certain time t and space point \vec{r} is causally connected to the energy deposit at another point \vec{r}' by the travel time of the acoustic signal $\frac{|\vec{r} - \vec{r}'|}{v_l}$.

The characteristic timescale $\tau_{HD} \approx l_\perp/v_l$ on which this hydrodynamic mechanism of energy dissipation occurs is determined by the transverse size of the shower $l_\perp = \mathcal{O}(R_M) = \mathcal{O}(10 \text{ cm})$, so that $\tau_{HD} = \mathcal{O}(10^{-5} \text{ s})$. Most of the spatial development of the shower occurs while the particles are still highly relativistic, i.e. even for LPM elongated shower of length $l_\parallel = \mathcal{O}(100 \text{ m})$ on time scales $\tau_{SD} = l_\parallel/c = \mathcal{O}(10^{-7} \text{ s})$. Also the time $\tau_{TM} = \mathcal{O}(10^{-11} \text{ s})$ it takes until the ionisation and excitation energy is thermalised is comparatively short [Bow78]. On the other side, heat dissipation from thermal conductivity $k(\text{H}_2\text{O}) = 0.62 \frac{\text{W}}{\text{mK}}$ has a characteristic time of $\tau_{TC} = l_\perp^2 \cdot \frac{\rho C_p}{k} = \mathcal{O}(10^5 \text{ s})$, which is much larger than the time scale of the thermo-acoustic mechanism. In summary, $\tau_{TM} \ll \tau_{SD} \ll \tau_{HD} \ll \tau_{TC}$, so that for the time scales considered here, the thermalised energy deposit can be considered instantaneous and constant. For a neutrino induced cascade, we can approximate the energy deposit by a space dependent component and a step function in time

$$\frac{\partial}{\partial t} \varepsilon(\vec{r}, t) = \varepsilon(\vec{r}) \delta(t - t_0), \quad (3.14)$$

where t_0 is the time of the neutrino interaction. From inserting 3.14 in 3.13, the resulting pressure pulse can be obtained solely from the knowledge of the spatial energy deposit function $\varepsilon(\vec{r})$. To account for the frequency dependent acoustic absorption, this is usually done in Fourier space. The basic characteristics of the emitted signal may be obtained by integrating 3.13 in Fourier space over a cylindrical volume of length L and diameter d , in

which the energy deposit is homogeneous. The dominant frequency component f_{peak} will be given by the maximal coherence length across the shower, which corresponds to half a wavelength: $f_{peak} = v_l/2d$. In the plane perpendicular to the cascade, the effective pressure amplitude P_{eff} at a distance R in the near field $L \ll R \ll L^2/\frac{2}{\pi}d$ is then [ADKM79]:

$$P_{eff} \propto f_{peak}^2 \frac{\alpha}{C_p} \frac{E}{\sqrt{R}}. \quad (3.15)$$

The material dependent components v_l^2 , α and C_p can be summarised in the GRÜNEISEN parameter introduced in equation 2.16 on page 26. As expected from 3.12, the signal scales linearly with energy. Notable is the $1/\sqrt{R}$ scaling of the amplitude with distance, that results from the strong focusing of the signal in the plane perpendicular to the cascade axis.

For a more elaborate analysis, more precise modelling of the deposited energy density is necessary. Three attempts to calculate the resulting acoustic signal with different assumptions on $\varepsilon(\vec{r})$ shall be mentioned here, all including acoustic absorption in sea water:

1. In [Lea79], equation 3.12 is first solved analytically for a radial symmetric Gaussian heat distribution. The energy deposit of the shower is modelled as a superposition of Gaussian sources along a line.
2. In [ADKM79], an analytic solution to equation 3.13 for a cylindrical source in Fourier space is given. As above, the shower energy deposit is taken as a superposition of cylinders, but assuming an exponential fall-off in the radial shower profile.
3. The authors of [D⁺94] use a lateral and longitudinal energy density deposit obtained from a simulation.

The pressure amplitude as a function of time for a point in the plane perpendicular to the cascade axis at the shower maximum is shown in figure 3.15. A bipolar pulse is created, with a typical peak-to-peak time of $\tau_{pp} = (f_{peak})^{-1} = \mathcal{O}(10 \mu s)$, that is not fully symmetric in time. All three calculations have been done at the same shower energy and using similar longitudinal profiles. The same absorption coefficients have been incorporated to calculate the signal at 400 m from the shower axis. The strong deviations of the peak amplitude are a result of the different radial distributions that have been used. As shown in equation 3.15, the peak amplitude strongly depends on the peak frequency, which in turn depends on the characteristic lateral dimension of the energy deposit. The wider Gaussian profile thus yields lower signal amplitudes than the exponentially falling profile, that is more pointed at small radii. From the simulation, where even higher central energy densities are observed as discussed in section 3.3, even larger peak pressure amplitudes are obtained. More recent calculations based on full shower simulations [NB05, Nie05, Kar06] or more elaborate radial parametrisations [LW93, LAG⁺02] show well compatible results.

Figure 3.16 shows the peak signal amplitude as a function of the angle to the cascade axis. As for a cylindrical source, a strong focusing of the emission in the plane perpendicular to the cascade is observed, even in a distance of 10 km from the cascade. The thermo-acoustic signal from a high energy shower can therefore be imagined as a ring-shaped shock-front,

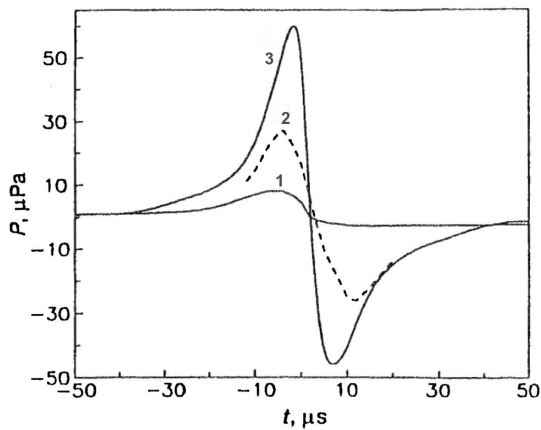


Figure 3.15: Time profile of the acoustic pressure amplitude in sea water at a perpendicular distance of 400 m from a 10 PeV cascade as calculated by [Lea79] (1), [ADKM79] (2) and [D⁺94] (3) (from [D⁺97b]).

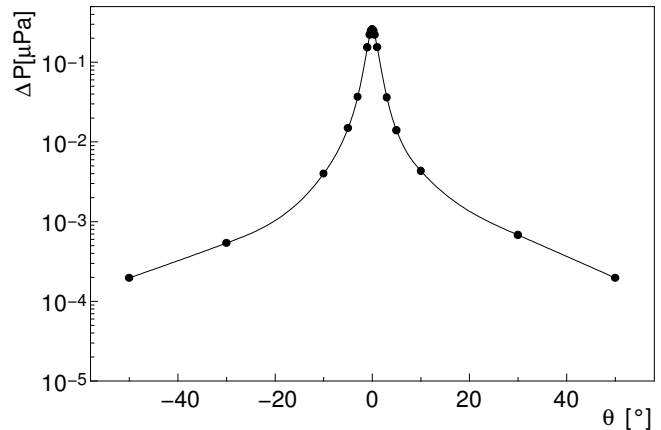


Figure 3.16: Dependence of the peak pressure amplitude ΔP on the angle relative to the cascade axis for a 10 PeV shower in a 10 km distance from the cascade. $\theta = 0$ denotes the plane perpendicular to the cascade (from [D⁺97a]).

closely followed by the anti-shock, that radially expands in the plane perpendicular to the cascade axis. The *width* of the ring is approximately given by l_{\parallel} close to the shower. Due to the large ratio l_{\parallel}/l_{\perp} of longitudinal to lateral extent of the shower, it will not increase strongly with distance. If no deformation occurs, e.g. by refraction as discussed in section 3.5, this will allow excellent directional reconstruction of the shower.

3.4.2 In solids

Thermo-acoustic signal generation has so far only been discussed in liquids, in particular in the case of water as a target medium. A brief discussion of the thermo-acoustic mechanism in an isotropic solid and its applicability to ice as a target material shall be given here. The derivation of the wave equations in the absence of a source and denotation of the variables are based on [RD00].

In contrast to liquids, also transversal waves can be excited in solids. For a hypothetical surface S (and a normal vector $d\vec{S}$) in a medium, the force \vec{F} that is exerted on the medium on the other side of the surface is not necessarily perpendicular to the surface. The scalar property of a *pressure* must therefore be substituted by the vector property of *traction* \vec{T} , that will depend on the orientation of the surface:

$$\vec{T}(d\vec{S}) = \lim_{|d\vec{S}| \rightarrow 0} \left(\frac{d\vec{F}}{|d\vec{S}|} \right). \quad (3.16)$$

From this, the **stress tensor** T_{ij} is defined as

$$T_i = T_{ij} n_j, \quad (3.17)$$

where T_i and n_j are the i -th and j -th component of the traction and unit normal vector $\vec{n} = d\vec{S}/|d\vec{S}|$ respectively. Summation over the doubly appearing indices has been implied in equation 3.17 and will be further on.

To set up the equation of motion in a solid, we start with the equivalent to NEWTON's law of motion

$$\rho \frac{\partial^2 u_i}{\partial t^2} = \frac{\partial T_{ij}}{\partial x_j} , \quad (3.18)$$

where the vector $\vec{u}(\vec{r}, t)$ denotes the *displacement*, i.e. the change of position of a small volume element at $(\vec{r})_i = x_i$ due to application of the stress \vec{T} .

This stress is counter-acted by the internal ability of the solid to restrain the deformation. In the elastic regime, this is given by the linear equation

$$T_{ij} = c_{ijkl} \frac{\partial u_l}{\partial x_k} , \quad (3.19)$$

which is the equivalent to HOOKE's law for a spring. The coefficients c_{ijkl} are the components of the rank four *stiffness* tensor, that relates stress and strain. It is symmetric under exchange of the indices $i \leftrightarrow j$ and $k \leftrightarrow l$, so that in the most general case it has 36 independent components. The most general equation of motion in absence of any external source of stress is then found by inserting 3.19 in 3.18

$$\rho \frac{\partial^2 u_i}{\partial t^2} = c_{ijkl} \frac{\partial^2 u_l}{\partial x_j \partial x_k} . \quad (3.20)$$

We shall now consider an isotropic solid, which by the definition of isotropy must be invariant under any change of the coordinate axes such as rotation or reflection about a point or plane. The stiffness tensor will therefore even show a higher degree of symmetry, leaving only two independent constants, λ and μ ¹, that are called the LAMÉ constants. Equation 3.19 then simplifies to

$$T_{ij} = \lambda \delta_{ij} \sum_k \left(\frac{\partial u_k}{\partial x_k} \right) + \mu \left(\frac{\partial u_i}{\partial x_j} + \frac{\partial u_j}{\partial x_i} \right) , \quad (3.21)$$

where λ is attributed to the *compressional* components, while the *shear* components are governed by μ . This tensor T_{ij} only describes the internal stress from the deformation of the solid. Thermo-acoustic excitation from an additional energy deposit in the medium will add additional (*external*) stress that is not inherent to the propagation of elastic waves. To calculate the amount of stress, let us consider a small volume V , in which an energy E is deposited. The absolute expansion of the volume ΔV will depend on the volume expansion coefficient α as well as the rise in temperature, which is given by the density ρ and heat capacitance C_p :

$$\Delta V = \frac{\alpha}{\rho C_p} \cdot E . \quad (3.22)$$

We can also calculate the volume expansion by integration of the displacement over the surface ∂V of the volume

$$\Delta V = \int_{\partial V} \vec{u} d\vec{S} = \int_V \nabla \cdot \vec{u} dV = \frac{\alpha}{\rho C_p} \cdot E , \quad (3.23)$$

¹Not to be confused with the POISSON ratio, that is also sometimes denoted by μ .

where GAUSS' theorem has been applied to go from a surface integral to a volume integral. Equation 3.23 must hold for any volume, so that for $V \rightarrow 0$ we can assume $\nabla \cdot \vec{u} = \text{const}$ over the volume. For any point \vec{r} and time t , therefore

$$\nabla \vec{u}(\vec{r}, t) = \frac{\partial u_i}{\partial x_i} = \frac{\alpha}{\rho C_p} \varepsilon(\vec{r}, t), \quad (3.24)$$

where we introduce the energy density $\varepsilon(\vec{r}, t) = \lim_{V \rightarrow 0} \frac{E}{V}$ with $\vec{r} \in V$. Inserting 3.24 in equation 3.19, we obtain the *external* stress T_{ij}^{ext} from the expansion of the volume

$$T_{ij}^{\text{ext}} = c_{ijkk} \frac{\partial u_k}{\partial x_k} \delta_{ij} = c_{ijkk} \delta_{ij} \frac{\alpha}{\rho C_p} \varepsilon(\vec{r}, t). \quad (3.25)$$

From the T_{ii} components in 3.21, which are all identical for an isotropic solid, we can see that $c_{ijkk} = \lambda + 2\mu$. To add this source term into the wave equation, we must replace the internal stress by the sum of internal and external stresses $T_{ij} \rightarrow T_{ij} + T_{ij}^{\text{ext}}$. For an isotropic solid, we then obtain the wave equation including a thermo-acoustic source from substituting the sum of 3.25 and 3.21 in equation 3.18

$$\begin{aligned} \rho \frac{\partial^2 u_i}{\partial t^2} &= \frac{\partial T_{ij}}{\partial x_j} + \frac{\partial T_{ij}^{\text{ext}}}{\partial x_j} \\ &= \frac{\partial}{\partial x_j} \left(\delta_{ij} \lambda \sum_k \left(\frac{\partial u_k}{\partial x_k} \right) + \mu \left(\frac{\partial u_i}{\partial x_j} + \frac{\partial u_j}{\partial x_i} \right) \right) + \\ &+ \frac{\partial}{\partial x_j} \left(\delta_{ij} (\lambda + 2\mu) \frac{\alpha}{\rho C_p} \varepsilon(\vec{r}, t) \right). \end{aligned} \quad (3.26)$$

Sorting by derivatives $\frac{\partial}{\partial x_i} \left(\frac{\partial u_j}{\partial x_j} \right)$ and $\frac{\partial^2 u_i}{\partial x_j^2}$ and introducing the LAPLACE operator for scalar fields $\Delta s = \nabla \cdot \nabla s = \sum_k \frac{\partial^2 s}{\partial x_k^2}$ and vector fields $(\Delta \vec{v})_i = (\nabla \cdot \nabla) v_i = \sum_k \frac{\partial^2 v_i}{\partial x_k^2}$, equation 3.26 may be written more compact in vector notation:

$$\rho \frac{\partial^2 \vec{u}}{\partial t^2} = (\lambda + \mu) \nabla (\nabla \cdot \vec{u}) + \mu \Delta \vec{u} + (\lambda + 2\mu) \frac{\alpha}{\rho C_p} \nabla \varepsilon(\vec{r}, t). \quad (3.27)$$

In order to split the compressional and shear components, it is now useful to introduce a scalar potential ϕ and vector potential $\vec{\psi}$ such that

$$\vec{u} = \nabla \phi + \nabla \times \vec{\psi}. \quad (3.28)$$

For any vector potentials, the relation $\nabla \cdot (\nabla \times \vec{\psi}) = 0$ holds. Inserting the potentials in 3.27, and subtracting all terms on the right-hand side, we obtain

$$\begin{aligned} \rho \frac{\partial^2 \nabla \phi}{\partial t^2} + \rho \frac{\partial^2 \nabla \times \vec{\psi}}{\partial t^2} &- (\lambda + \mu) \nabla (\Delta \phi) - \\ &- \mu \Delta (\nabla \phi) - \mu \Delta (\nabla \times \vec{\psi}) - (\lambda + 2\mu) \frac{\alpha}{\rho C_p} \nabla \varepsilon(\vec{r}, t) = 0. \end{aligned} \quad (3.29)$$

Interchanging space and time derivatives, this can be resolved in

$$\begin{aligned} \nabla \cdot \left(\rho \frac{\partial^2 \phi}{\partial t^2} - (\lambda + 2\mu) \left(\Delta \phi + \frac{\alpha}{\rho C_p} \varepsilon(\vec{r}, t) \right) \right) + \\ \nabla \times \left(\rho \frac{\partial^2 \vec{\psi}}{\partial t^2} - \mu \Delta \vec{\psi} \right) = 0. \end{aligned} \quad (3.30)$$

from which we finally obtain two independent wave equations for the scalar and vector potentials:

$$\frac{\partial^2 \phi}{\partial t^2} - v_l^2 \Delta \phi = v_l^2 \frac{\alpha}{\rho C_p} \varepsilon(\vec{r}, t) \quad (3.31)$$

$$\frac{\partial^2 \vec{\psi}}{\partial t^2} - v_t^2 \Delta \vec{\psi} = 0. \quad (3.32)$$

Here we have used the definition of the longitudinal velocity of sound propagation $v_l = \sqrt{\lambda + 2\mu/\rho}$ in 3.31 and for the propagation velocity of transversal waves $v_t = \sqrt{\mu/\rho}$ in 3.32. It is evident, that from a volume expansion term as on the right hand side in equation 3.31 only longitudinal, i.e. compressional waves may arise in an isotropic solid.

For an application to ice, we must note, that crystalline ice is not isotropic, but has the hexagonal crystal structure. So instead of only two components, λ and μ , the *stiffness* tensor will have five independent components as can be deduced from the six-fold symmetry axis of the crystal. The system is only invariant under rotation around one of these axis. This gives rise to so-called *quasi-longitudinal* and *quasi-transversal* waves, which are characterised by a displacement vector \vec{u} that is not parallel or orthogonal to the propagation direction of the wave in the crystal as for longitudinal and transversal waves in the isotropic case. Instead, we obtain three different modes – two quasi-transversal and one quasi-longitudinal, each of which will propagate at its own wave velocity, that will furthermore depend on the angle θ with respect to the crystal axis $v_l \rightarrow v_l(\theta)$. Yet, the modes are still well separated and will not mix [RD00]. This will affect the generated elasto-dynamic signals in three ways:

1. It reduces the efficiency of the thermo-acoustic generation of quasi-longitudinal modes, as the compressional excitation is no longer aligned with the propagation direction of the mode. However, the non-isotropic components of the stiffness tensor are small. For an isotropic material, the stiffness tensor components for the normal stresses are $c_{1122} = c_{1133} = c_{2233} = \lambda$, while for crystalline ice $c_{1133} = c_{2233} = 0.80c_{1122}$ [GKCW88]. This can also be seen from the comparatively small variation of propagation velocity with the direction to the crystal axis shown in figure 3.25. From the ratio of maximal v_l^{\max} and minimal v_l^{\min} value of the quasi-longitudinal propagation velocity we may estimate the maximal angle β between the displacement vector \vec{u} and the propagation direction to

$$\beta = \arccos \left(\sqrt{\frac{v_l^{\min}}{v_l^{\max}}} \right) \approx 14.4^\circ. \quad (3.33)$$

For this direction, the conversion of thermal expansion in a longitudinal acoustic mode will be reduced by a factor $\cos(\beta) \approx 0.97$ with respect to the direction along the crystal

axis where the displacement from the expansion and the wave propagation align. For an effective attenuation of the amplitude, this has to be averaged over all angles. So for the thermo-acoustic generation, the transversal component in the *quasi-longitudinal* mode may be neglected and the quasi-longitudinal mode may be treated as purely longitudinal in first approximation.

2. Furthermore, the ice at South Pole, is not a single crystal but consists of many small crystals at random orientation to each other. For the emission of acoustic signals, this is important, since we must note that in each of the single crystals, the quasi-longitudinal mode is excited in a different direction with respect to the crystal axis, so it will propagate at a different velocity. This effect may weaken the coherence of the emitted acoustic radiation. But since the crystal size $d \ll l_{\perp}$ is small compared to the lateral extension of the cascade l_{\perp} which determines the maximal coherence frequency, again the effect will be small and an angle-averaged value $\langle v_l \rangle_{\theta}$ can be assumed for the propagation.
3. Finally, transversal or quasi-transversal waves may be excited at grain boundaries, where the orientation of the crystal axis changes. But since crystal orientation is random, the generated modes will not be coherent over the extent of the energy deposit, so that no macroscopic transversal waves may be generated this way. The energy that is converted into transversal modes at the boundary is of course lost to the longitudinal mode, but the effect is small as will be shown in section 3.5.

In summary, the quasi-longitudinal waves will be the dominant mode that can be excited thermo-acoustically in ice, while only a very small fraction of the energy will be converted into transversal modes. For the quasi-longitudinal mode, equation 3.31 should be a good approximation.

Finally we can show the analogy to the thermo-acoustic model in liquids. Only the longitudinal components should arise from equation 3.31, i.e. at any point the displacement vector \vec{u} will be parallel to the gradient of the potential $\nabla\phi \parallel \vec{u}$ and thus perpendicular to the propagating wave front. From equation 3.18 by multiplication with the normal vector of the wavefront $\vec{n} \parallel \vec{u}$ we can identify the *normal traction*

$$T_i^n = T_{ii}n_i = \rho \frac{\partial^2 \phi}{\partial t^2}, \quad (3.34)$$

which, similar to the scalar pressure, gives the perpendicular force exerted on the medium adjoining a surface $\perp \vec{n}$. Using the second time derivative of 3.31 and multiplying with $^{-\rho/v_l}$, we obtain

$$\Delta T_i^n - \frac{1}{v_l} \frac{\partial^2 T_i^n}{\partial t^2} = -\frac{\alpha}{C_p} \frac{\partial^2 \varepsilon(\vec{r}, t)}{\partial t^2}, \quad (3.35)$$

which is identical to equation 3.12. The same solutions as shown for liquids will therefore hold also for ice, and as in water a high energy cascade will create a bipolar pulse restricted to the plane perpendicular to the cascade. The amplitude can be obtained from simple scaling with the GRÜNEISEN parameter $\gamma_{\mathbf{G}}$ introduced in equation 2.16. Significantly larger signals than in water will be obtained in ice with the values of $\gamma_{\mathbf{G}}$ listed in table 2.1. It

should also be noted, that – while the wavelength in ice $\lambda \approx l_{\perp}/\pi$ will be the same as for water – the characteristic time $\tau_{pp}(\text{ice}) = v_l(\text{water})/v_l(\text{ice}) \tau_{pp}(\text{water})$ and frequency $f_{peak}(\text{ice}) = v_l(\text{ice})/v_l(\text{water}) f_{peak}(\text{water})$ will scale with the speed of sound. As will be shown in the next section, this will prove advantageous for the detection the acoustic signal, as the absorption flattens off at higher frequencies .

3.5 Ultrasonic ice properties

While water is probably the best studied medium at all, ice has not been investigated nearly as intensive. Not the least due to its remoteness, many basic properties of the antarctic glacial ice were not accessible until in the late sixties. While basic properties such as density and temperatures profiles have been established very early, acoustic measurements have not been of particular interest at that time and only been performed in the seismic frequency range. Yet, the important properties for acoustic neutrino detection – the refraction, scattering and absorption of ultrasonic waves – have at least been theoretically studied and will be shortly summarised here.

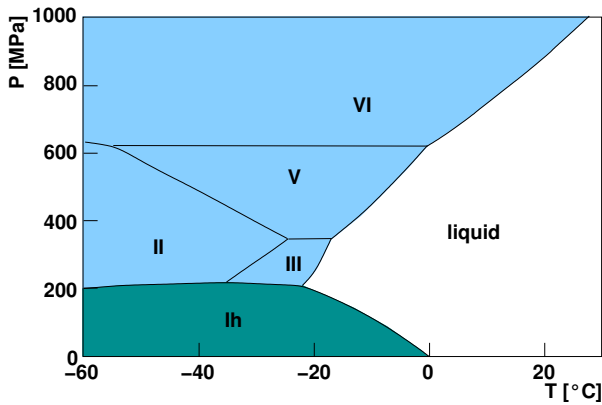


Figure 3.17: Phase diagram of water/ice.

Ice – or frozen H_2O – is a fairly complex structure. It exists in no less than thirteen different crystalline structures. Figure 3.17 shows a phase diagram for moderate temperatures and pressures. Virtually all natural occurrences of ice on earth are in the Ih state, which has the well known hexagonal structure. The density of monocrystalline ice is $0.917 \frac{\text{g}}{\text{cm}^3}$, with a slight dependence on temperature. Most ice on earth, however, is polycrystalline, with a broad range of crystal sizes.

The ice of the antarctic glacier has a thickness of around 2850 m at South Pole, but exceeds 4000 m in height at other places. It grows from the continuous precipitation of very small ice crystals forming from the very low humidity in antarctic air. Still the glacier does not grow in height, since at the same time it slowly flows towards the coast of Antarctica with a speed of around 10 m/yr . The flow is slow enough that the ice retains its horizontal stratification. The uppermost low density layer of small crystals with interconnected air inclusions is called the *firn*. With increasing depth and pressure, pores close off and get smaller, while at the same time the crystal size is growing. At around 1400 m finally all bubbles convert into the clathrate phase, leaving a very homogeneous medium [Pri93].

Figure 3.18 shows a temperature profile of antarctic ice at South Pole. It is lowest at the surface and increases towards the bottom due to heating from the earth core. The heat conductivity of ice (and snow) is very low $\approx 2 - 3 \frac{\text{W}}{\text{mK}}$, so that the annual fluctuations of air temperature at the surface will not penetrate the ice for more than a few metres [Gow62].

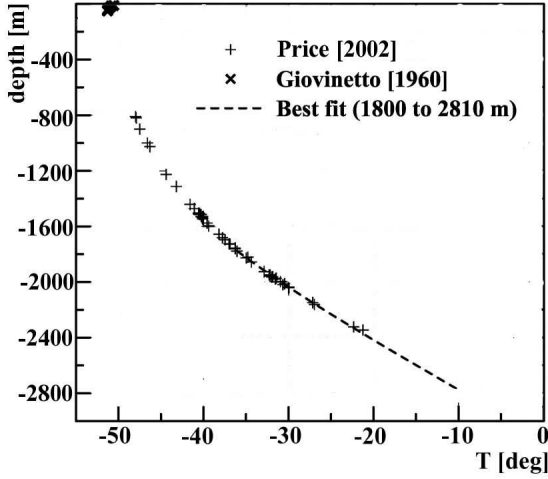


Figure 3.18: Temperature profile of the antarctic ice at South Pole (from [PNB⁺02]).

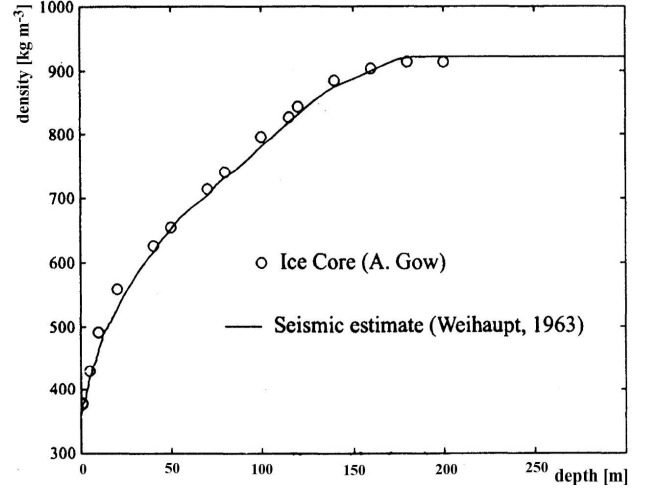


Figure 3.19: Density profile of the upper layers in antarctic ice at South Pole (from [Alb98]).

The density profile of the transition layer from firn to bulk ice has been determined in different ways. Figure 3.19 shows a density profile from bore hole measurements [GR62] and seismic measurements [Wei63]. While strongly increasing in the upper layers, the density reaches a maximum when the pressure gets high enough to compress the air inclusions.

3.5.1 Velocity of sound

Using temperature and density profiles as an input, the longitudinal and transversal sound velocity profiles can be derived. Sound speed in the firn increases rapidly with depth due to the increased density causing sintering and making the ice stiffer. According to [Alb98], an empirical formula for the dependence of compressional wave propagation velocity $v_l(z)$ and density $\rho(z)$ at depth z is given by

$$\rho(z) = \rho_{max} \left(1 + \left(\frac{v_l^{max} - v_l(z)}{2250} \right)^{1.22} \right)^{-1}, \quad (3.36)$$

where ρ_{max} and v_l^{max} are the maximum density and sound velocity at the given location. This is used in [Alb98] to derive the sound velocity from density data as shown in figure 3.20, which is in very good agreement to the seismic measurements by [Wei63]. For larger depth, the density is stable, and the speed of sound shows only a weak decrease of $-2.3 \frac{m}{s}/^\circ C$ [Alb04] due to increased temperature. Much larger values have been obtained for sea ice at lower densities [B⁺58], but the given value is in good agreement with a value of $-2.07 \frac{m}{s}/^\circ C$ from measurements on single ice crystals [Pro66]. Also the increasing pressure will affect the velocity of acoustic waves, but the effect is negligible for the depth considered here as shown by laboratory measurements [GKCW88]. In the same laboratory measurement, it was also confirmed that for monocrystalline ice samples, there is a stronger dependence of speed of sound versus orientation relative to the crystal axis. The effect can reach $\approx 10\%$ for longitudinal waves and $\approx 20\%$ for transversal waves [GKCW88] (see figure 3.25), but at least in

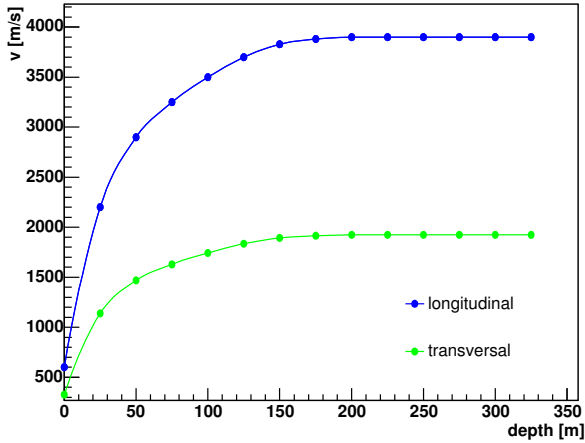


Figure 3.20: Velocity of sound for longitudinal and transversal waves at South Pole derived from density data in [Alb98].

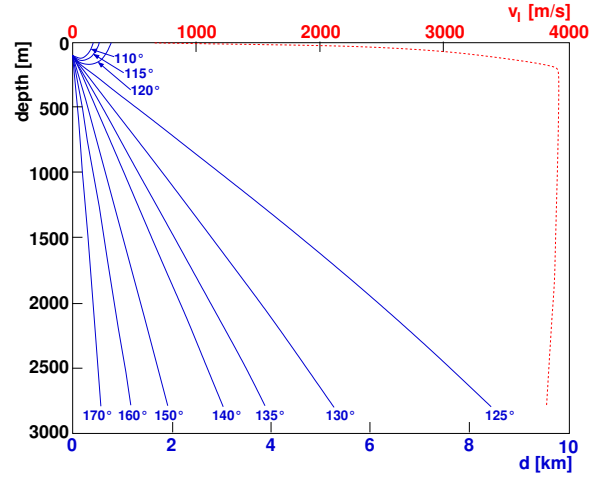


Figure 3.21: All-depth sound velocity profile (red, dashed) and ray-traces (blue, solid) of a hypothetical point sources at a depth of 100 m for different emission angles (from [Van04]).

the upper layers crystals at South Pole are expected to be randomly oriented, leading to a uniform propagation speed [Pri06].

Figure 3.21 shows the predicted sound profile over the full depth range using the direct measurements by [Wei63] up to a depth of 180 m and calculated from the temperature profile from [PNB⁺02] for larger depth. The rapid increase of sound velocity at the top has a strong effect on the propagation of acoustic waves. At lower depth, all waves will propagate on nearly straight lines. In the upper layer, due to refraction, all waves will be strongly bend towards the surface. This is also shown in figure 3.21, where ray traces from a hypothetical point source at a depth of 100 m for different emission angles relative to the vertical axis are plotted. While all emission up to an angle of $\approx 120^\circ$ is redirected back up to the surface, the small part of the downward emission which reaches the deep layers then propagates quasi unaffected. While this region is small and can be circumvented in building a large acoustic detector array, it is of importance for artificial sound generated at or close the ice-air boundary, that will not reach the deep parts of the bulk medium. In contrast to the radio detection method tests at South Pole [K⁺06], acoustic neutrino detection is therefore expected to be much less affected by anthropogenic noise sources at the ice surface.

3.5.2 Absorption

In contrast to the velocity of sound, where measurements are supposed to be frequency independent and can be extrapolated from the seismic regime, absorption is a strongly frequency dependent effect.

Again, it is very well studied in water [FG82a, FG82b]. For pure water, the main contributions stem from viscous effects, leading to an $\alpha_{\text{abs}} \propto f^2$ dependence of the absorptivity α_{abs} on the frequency f . In impure sea water, pressure waves also change the chemical equilibrium between dissolved molecular compounds and their dissociated ions.

Two reactions lead to additional contributions for frequencies below their respective *relaxation frequency* f_r :

- solvation of boric acid ($\text{B(OH)}_3 \leftrightarrow \text{B}^{3+} + 3(\text{OH})^-$) with $f_r \approx 10$ kHz and
- dissociation of magnesium sulphate ($\text{MgSO}_4 \leftrightarrow \text{Mg}^{2+} + \text{SO}_4^{2-}$) with $f_r \approx 100$ kHz.

Figure 3.22 shows the resulting absorptivity, ranging from $\mathcal{O}(10^{-4} \text{ dB/m})$ to $\mathcal{O}(10^{-1} \text{ dB/m})$ in the frequency range of interest from 1 – 100 kHz.

Measurements in ice also exist, but only for sea ice at warmer temperatures. The authors of [PL68] find an average dependence of

$$\alpha_{\text{abs}} [\text{dB/m}] = -11.3 + 10 \log(f [\text{kHz}]) \quad (3.37)$$

from outdoor measurements in the frequency range from 15 kHz to 150 kHz, which are in good agreement with the results from their laboratory measurements. They do not find a strong dependence on salinity. However, this results cannot be applied for glacial fresh-water ice at South Pole.

While in warm ice energy loss in grain boundary sliding is the dominant process, at $\approx -50^\circ\text{C}$ in polar ice the dominant process for acoustic absorption is proton reorientation [Pri06]. The dipole moment of the H_2O molecule may assume one of six directions in the ice crystal. This leads to a temperature dependent energy loss of the acoustic wave in *internal friction*. A passing acoustic wave may cause a movement of one of the two protons, resulting in a reorientation of the dipole moment. An orientational defect with two protons in the same hydrogen bond is created, which can move from one hydrogen bond to another. This causes doubly and non-occupied bonds, which may also occur due to ionisation defects, i.e. missing protons in an $(\text{OH})^-$ or additional protons from an H_3O^+ molecule. Under stress on the crystal lattice, these orientation or ionisation defects can migrate with a typical relaxation time of $\tau_r(T) \approx 10^{-16} \text{ s} \cdot e^{\frac{U}{k_B T}}$. The mechanical activation energy for the relaxation process is $U \approx 0.6 \text{ eV}$. The effect does not depend on crystal size but only on the number density of the defects, which in turn depends on temperature. The resulting absorptivity is given by [Pri06]

$$\alpha_{\text{abs}} [\text{m}^{-1}] = \frac{1}{v_l} \delta_{\text{max}} \frac{4\pi f^2 \tau_r(T)}{1 + 4\pi^2 f^2 \tau_r^2(T)}, \quad (3.38)$$

where δ_{max} is a frequency independent constant. At low frequencies, the absorptivity will increase with frequency as $\alpha_{\text{abs}} \propto f^2$. At high frequencies, the constant part in the denominator can be neglected, and absorptivity becomes frequency independent. The transition

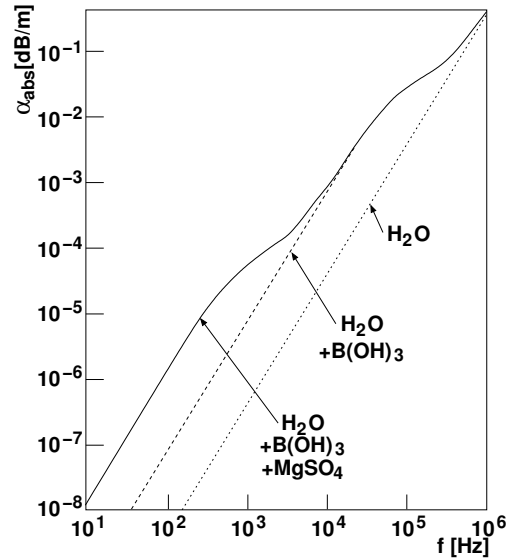


Figure 3.22: Absorption length of sea water with contributions from MgSO_4 and B(OH)_3 (from [Pri06]).

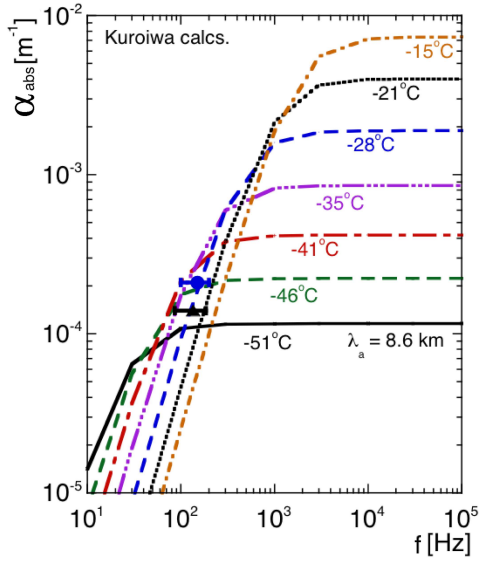


Figure 3.23: Predicted absorption length of Ih ice for different temperatures (from [Pri06]).

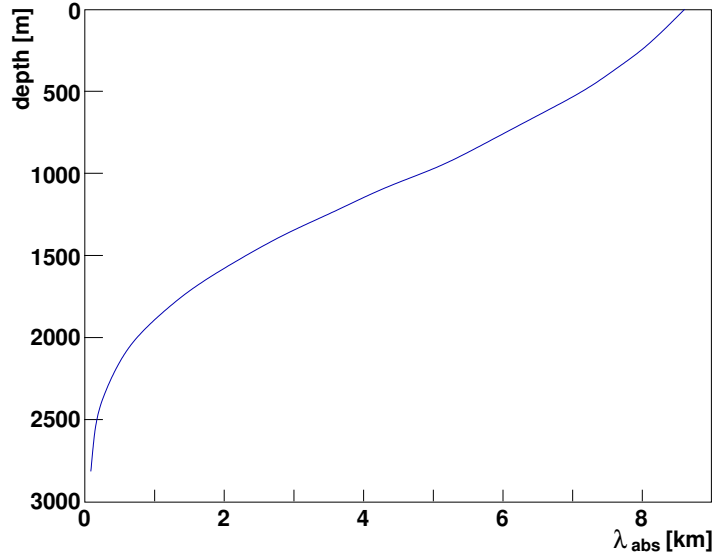


Figure 3.24: Predicted absorption profile for acoustic waves in the bulk ice at South Pole (from [Van04]).

point where $f\tau_r \approx 1/2\pi$ depends on the temperature via $\tau_r(T)$. Figure 3.23 shows the absorptivity calculated in [Pri06], based on laboratory measurements of the relaxation process. Also shown are two data points from measurements in Greenland ice and polar ice at BYRD Station.

In the kHz regime, even for high temperatures no dependence of the absorption on frequency is expected. From equation 3.38 and the temperature profile in figure 3.18 a unique absorption profile can be derived for all frequencies as shown in figure 3.24. According to this model, attenuation lengths should exceed 8 km close to the surface. Note that no effects of the porous firn have been taken into account, and the calculation is only valid in the layers below a depth of a few metres where air bubbles are no longer interconnected.

3.5.3 Scattering

Only absorption was discussed in the last section, but also scattering has to be taken into account for the calculation of an effective attenuation length. Two major contributors to scattering can be identified [Pri06]:

1. **Scattering at bubbles:** Bubbles from the air enclosed during compactification of the firn are abundant in South Pole ice. Their number density was found to be $n_0 = \mathcal{O}(100 \text{ cm}^{-3})$, with a diameter ranging from a $d_b \approx 1 \text{ mm}$ at the top to $d_b \approx 0.1 \text{ mm}$ at a depth of 1400 m. Hence they are small compared to the wavelength, and scattering can be described in the Rayleigh approximation.

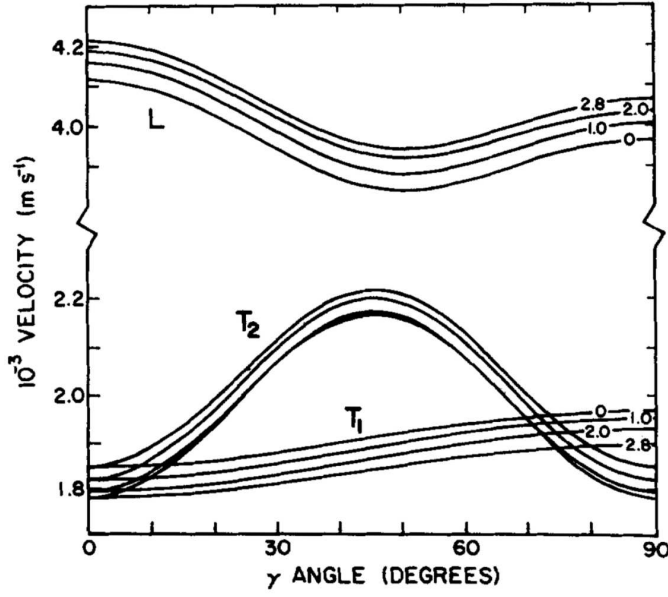


Figure 3.25: Velocity of sound in monocrystalline ice for longitudinal (L) and transversal ($T_{1|2}$) modes in dependence of the angle γ to the crystal axis. Values for different pressures in kbar are given. (from [GKCW88]).

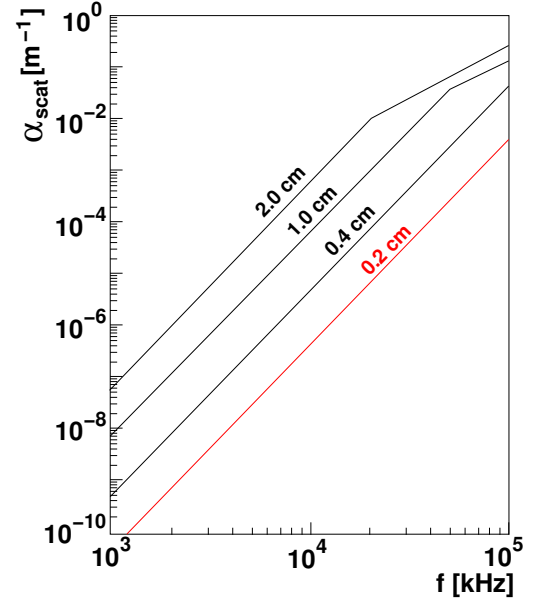


Figure 3.26: Scattering coefficient from grain boundaries for polycrystalline Ih ice for different grain sizes (from [Pri06]).

Calculating the scattering coefficient α_{scat}^b following formula has been obtained [Pri93]:

$$\alpha_{\text{scat}}^b [\text{km}^{-1}] = 2.68 \cdot 10^{-7} \left(\frac{n_0}{200 \text{ cm}^3} \right) \left(\frac{d_b}{0.01 \text{ cm}} \right)^6 \left(\frac{f}{10 \text{ kHz}} \right)^4. \quad (3.39)$$

While bubbles are the main source of scattering in the firn, in all other depths scattering at grain boundaries is supposed to be dominant.

2. **Scattering from grain boundaries:** As shown in figure 3.25, the velocity of sound is non-isotropic in crystalline ice. Abrupt change of the speed of sound may thus occur at the boundary of adjacent crystal grains. While some part of the acoustic wave is reflected, another part is converted from longitudinal to transversal modes and vice-versa. Up to $\mathcal{O}(100 \text{ kHz})$, again the Rayleigh approximation holds. From measurements of the elastic constants of ice, an effective scattering coefficient for longitudinal waves of

$$\alpha_{\text{scat}}^g [\text{km}^{-1}] = 5 \cdot 10^{-4} \left(\frac{d_g}{0.2 \text{ cm}} \right)^3 \left(\frac{f}{10 \text{ kHz}} \right)^4 \quad (3.40)$$

can be derived [Pri06]. While scattering from bubbles depends in sixth power on bubble diameter d_b , grain boundary scattering only depends in third order on the grain diameter d_g . At higher frequencies (310 kHz for $d_g = 0.2 \text{ cm}$) the wavelength $\lambda \approx \pi d_g$ gets in the order of the grain size. The Rayleigh approximation no longer holds and the scattering process enters the stochastic regime, where it will only depend on f^2 .

As a function of frequency, the grain-boundary scattering coefficient is shown in figure 3.26. The total scattering length λ_s can be calculated as $\lambda_s = \frac{1}{\alpha_{\text{scat}}^g + \alpha_{\text{scat}}^b}$. No ice core drilling has been performed at South Pole to depth greater than 300 m, so that the actual grain size development at South Pole remains unknown. A measurement in a depth of 106 m provided a value of less than 0.1 cm [Sta81]. Extrapolations from core drilling at other places let conclude that the grain sizes will not exceed 0.4 cm at a depth of 1500 m. In conclusion, for the bulk ice below the firn attenuation of acoustic waves will strongly be dominated by absorption in the frequency band up to ≈ 30 kHz and maybe higher, but especially for the highest frequencies scattering will be non-negligible.

3.5.4 Ambient noise

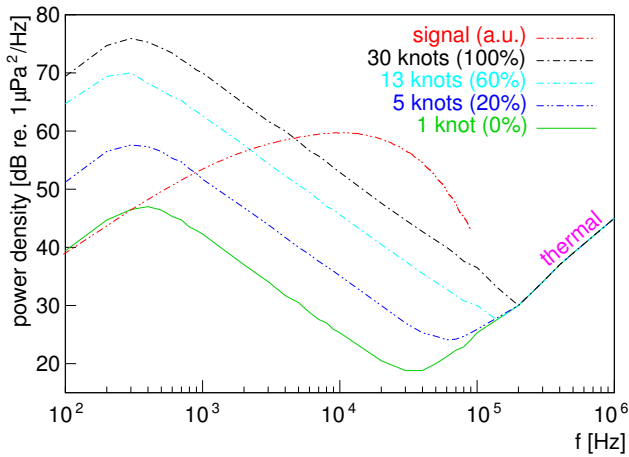


Figure 3.27: Spectral power density of ambient noise in open seas in dependence of wind speed. Numbers in parenthesis give integral probabilities for these or better conditions. The spectrum of a neutrino induced acoustic signal in arbitrary units is overlaid (from [LAG⁺02]).

Ambient noise, in open seas has been extensively studied [Uri96]. At low frequencies it is dominated by anthropogenic sources, such as ship vessels, etc, while at the frequency range of interest for acoustic detection, noise generated by wind and surface waves becomes dominant. Above 300 kHz, thermal noise finally exceeds all other sources. The spectral power density of ambient acoustic noise in open seas and its dependence on the wind speed via the sea state is shown in figure 3.27. To demonstrate that the noise is minimal in the frequency range where the acoustic signal is maximal, the spectral density of an neutrino induced acoustic signal in arbitrary units is overlaid. None the less, the absolute noise level is rather prohibitive for acoustic neutrino detec-

tion: in the frequency band of 3 – 100 kHz the average noise level is 4 mPa for a sea state of zero, but for an often encountered sea state of 4 Bft. (*Beaufort*) – corresponding to wind speeds of 11 – 16 knots and characterised as *moderate breeze* – the noise level in the same interval already exceeds 40 mPa. In an investigation dedicated to neutrino detection, frequent encounters of noise levels of $\mathcal{O}(100 \text{ mPa})$ and higher were reported [VGL05]. These may still be exceeded by transient contributions from marine mammals, such as sperm whales [Ric06].

Little is known again for the polar ice sheet. While it is one of the quietest places in Antarctica in the seismic frequency range [Pri06], no measurements exist in the ultrasonic regime. On the other hand, no strong arguments in favour for any particular source of noise above thermal noise exist. Anthropogenic noise from the surface is effectively suppressed by refraction as explained above. Using the ray traces derived above it can be estimated that – even in absence of absorption in the firn – less than two percent of the emission from a spher-

ical emitting source located at 1 m depth will reach through the firn. It is speculated [Pri06] that the motion of the antarctic glacier over the bedrock may provide a source of background noise. As noted before, the glacier flows towards the sea with a rate of $\approx 10 \text{ m/yr}$ at the surface, but the flow is much decreased at the bedrock. Most of the shear occurs in proximity to the bedrock, providing the possibility of erratic *slip-stick* motion accompanied by acoustic emission at or in the vicinity of the bedrock.

Both surface and bedrock noise should be easily rejected by arrival direction of the wave front in any detector array design. Furthermore, the specific emission pattern of an elongated thermo-acoustic source is a rather unique signature that should provide a second excellent handle on possible backgrounds. It is therefore anticipated that rates of neutrinos detected by their acoustic signature can be measured practically free of backgrounds.

Yet, it must be stated that while from theoretical predictions based on extrapolations south polar ice seems very favourable for acoustic detection of ultra-high energetic cascades, the verification of these properties is still missing. As a consequence, a dedicated setup has been conceived to address these issues and will be presented in chapter 7.

3.6 Ultrasonic sensors

In order to detect the generated acoustic waves, corresponding sensors are needed. In water, especially in the open sea, detection of high-frequency waves is a long-established field. Ultra-sonic sensors – called *hydrophones* – have been developed for many purposes, including echo sounding, marine mammal research and geophysical investigations, but are also widely applied in military and industrial applications such as remote underwater control and underwater vehicle sensing. In more than 50 years of application, the piezo-electric effect was found to be the most flexible, robust and easy to implement way for the detection of elastic waves.

The requirement such sensors need to meet for the application in ice are quite different than for water. Already in the installation of the sensor – which consequently should be called *glaciophones* – very different conditions occur. For a good acoustic coupling the sensor needs to be well attached to the medium, i.e. best frozen in the ice. This can be achieved by *hot-water drilling* as it is used for installation of optical detectors such as ICECUBE *Digital Optical Modules* (DOMs). After drilling through the firn layer, hot water is pumped into the hole, melting the ice at the bottom. The freshly melted water is brought up to the surface, where it is also heated and pumped down into the hole again. This way, a water filled borehole with a diameter of $\approx 50 \text{ cm}$ is achieved. The devices can then be lowered into the borehole, usually bundled on a single line called a *string*. So as in water applications, *glaciophones* will be subject to the same hydrostatic pressures, which – depending on depth – can be $\mathcal{O}(100 \text{ bar})$. This will however not be the only source of ambient pressure. In the refreezing process, due to the lower temperatures the water-filled hole will be closed off at the top, first. This leads to a significant increase in pressure when the now enclosed remainder of the water expands during crystallisation. Additional pressures of more than 120 bar have been observed in the 2.5 km deep holes drilled for the ICECUBE project. While this pressure

will relieve over a period of several days after completion of the freezing, *glaciophones* still need to be able to accommodate for this overpressure. Obviously also an operation range in temperature of down to -55°C is required.

Apart from this, as discussed in section 3.4, the thermo-acoustically emitted wave is focused on the plane perpendicular to the cascade. In the absence of strong refraction and scattering, no defocusing will occur, limiting the spreading of the wave front to the order of the cascade length. Consequently, vertical spacing of the sensors in a string of $\mathcal{O}(10\text{ m})$ is required, which in combination with the much larger volume that has to be instrumented requires a considerably higher number of sensors than in optical or radio detection arrays.

While commercially available hydrophones may well be suited for the given pressure ranges, they typically fail the temperature requirements. Furthermore, in normal use hydrophone sensitivity is usually limited by the ambient noise in the oceans. Efforts of the manufacturers to reduce the self noise of the device stay limited within reaching these ambient values. In summary, no commercial device has been found meeting all of the above criteria. Therefore an own development of *glaciophones* had to be commenced. The resulting designs and the extent to which the properties of these sensors could be determined will be described in chapter 5.

Concludingly, regarding the above analysis of the prerequisites, four main necessities can be identified for evaluating the feasibility of acoustic neutrino detection in antarctic ice, and will be addressed in the following. While lower limits on the prediction of cosmogenic neutrino fluxes from the GZK mechanism seem robust, the size and dimension of an acoustic sensor array yielding a significant number of events needs to be determined. A hybrid array simulation including the optical and radio detection method to allow for cross-calibration is presented in chapter 4. The detection threshold of the single sensors, which in turn depends on the sensitivity and self noise of the ultra-sonic glaciophone, is a key parameter in this simulation. Different sensor designs will be introduced in chapter 5, together with investigations concerning their frequency response and equivalent self-noise levels. A first application of these glaciophones in the verification of the thermo-acoustic effect using intense proton and laser beams is presented in chapter 6. Finally, experience from both investigations was used to design an experimental setup presented in chapter 7 to access the relevant parameters of antarctic ice. This will leave solely the neutrino interactions and resulting cascades as topics not covered any further, here. As shown in the discussion of section 3.2, the former may be clarified by a measurement of the GZK-induced neutrino flux itself, while for the latter no way of improvement of the current situation within the frame of this work seems at hand.

Chapter 4

Simulation of a hybrid optical – radio – acoustic detector

4.1 Motivation

As introduced in section 2.2.4, different methods are used or currently developed to measure ultra-high energetic neutrino fluxes. Depending on the type of radiation detected from the neutrino interaction, these can be roughly grouped in optical, radio and acoustic detection methods as shown in section 2.2.4. While none of them seems to be obviously superior to the others, all of them lack a well controlled test beam for calibration. Combined with the expected small event rates, this makes a strong case for building a hybrid detector that allows cross-calibration of the different methods, as already successfully shown for air shower detection as in the AUGER experiment [Som05, Man05].

One of the unique features of the South Polar ice sheet in this respect is that it seems well suited for all three neutrino detection methods. The study of a hybrid array using all three different techniques is therefore a proximate idea. Doing so, it has to be kept in mind that the status of the development of the single methods is very different. First attempts for optical detection with the AMANDA-A detector have been made in 1993. In 1996, construction of the AMANDA-B10 detector has begun, which has been continuously expanded to finally form the AMANDA-II array that was completed in 2000 and since then is in continuous operation. Although too small to detect extra-terrestrial neutrinos, the experiment yielded good results in measuring the atmospheric muon and neutrino fluxes as well as setting strong limits to the emission from neutrino point sources. The ICECUBE experiment, with an expanded instrumented volume of $\approx 1 \text{ km}^3$, is expected to yield a clearly improved sensitivity – although due to the larger spacing of sensors only at higher energies [A⁺04b]. The full ICECUBE array will consist of 70 strings of optical sensors, whereof the first nine have already been deployed in the polar seasons 2004/2005 and 2005/2006. With the existing detailed and verified Monte Carlo tools incorporating e.g. details of the neutrino interaction, light propagation in the ice and sensor response, the simulation tools for the optical detection method can be considered well-developed.

In contrast to that, simulation tools for in-ice radio detection are not as advanced yet. Although details of the radio transparency of south polar ice have been obtained using dry

hole measurements [BBGS05], only the rather small RICE array of approximately $200\text{ m} \times 200\text{ m} \times 200\text{ m}$ with 19 receivers has been deployed in coincidence with the AMANDA-B10 array. Due to a higher energy threshold, no atmospheric neutrinos can be detected in such a setup, and hence no particle induced events have been observed so far. Sensitivity estimates therefore have to rely on proton beam measurements, but show consistent results for different simulations [K⁺06].

For the acoustic method, finally, no in-ice measurements at South Pole have been performed so far at all. Although a dedicated setup is in preparation (see chapter 7), all parameters in the acoustic part of the simulation rely on laboratory experiments and theoretical predictions. A significant amount of systematic uncertainty has to be taken into account.

Nevertheless, a simulation of a hybrid array incorporating all three different methods has been undertaken building on the existing experience in optical [Bös02], radio [K⁺06] and acoustic [VGL05] detector simulation and will be presented in the following. For the reasons shown above, this should not be considered a detector proposal, but rather a benchmark study to estimate the total and coincident event rates. A more detailed description of this work can be found in [BBN⁺05b, BBN⁺05a].

4.2 Simulation

Neutrino sample

Monoenergetic neutrino fluxes were simulated at different energies from 10 PeV to 100 EeV with statistics of 100.000 events per energy bin. Due to the strong increase of neutrino nucleon cross-section with energy, the neutrino interaction lengths ranges from only $6 \cdot 10^3\text{ km}$ to $2 \cdot 10^2\text{ km}$ [GQRS96], so that the earth is opaque to neutrinos of these energies. They will therefore only reach the detector from the hemisphere above the detector, with a small transition band below the horizon. For simplicity, only a $2\pi\text{ sr}$ isotropic flux was used in this simulation. Neutrino vertices were then generated homogeneously distributed within a cylindrical volume of 10 km radius ranging from the surface to a depth of 3 km.

In the energy range discussed here, the inelasticity $y = E_{had}/E_{lept}$ is nearly independent of energy (see figure 3.9). A mean value of $\langle y \rangle = 0.2$ was assumed for all events. In order to be able to compare the response of the various detectors on an event-by-event basis, a common neutrino interaction sample was used for the simulation. However, the different methods are sensitive to different parts of the interaction:

- The total Cherenkov light emission is proportional to the integrated track length of all particles above the Cherenkov energy. Especially in the case of $\nu_\mu, \bar{\nu}_\mu$ long-ranging muons are generated that travel on the order of several ten kilometers. In principle, also the hadronic cascade and electromagnetic cascades from $\nu_e, \bar{\nu}_e$ and $\nu_\tau, \bar{\nu}_\tau$ including subsequent τ decays can be detected by their Cherenkov light emission. But as these events are much more localised, their light emission might not reach the detector and they are estimated to increase the rate of detected events by at most a factor of two. Only the muonic part was taken care of in this simulation.

- In contrast, both the acoustic and radio method are sensitive to the excess charge density or the deposited energy density respectively, i.e. to the cascade-like part of the interactions. Electromagnetic cascades at these energies are stretched out to hundred of metres by the Landau-Pomeranshuk-Migdal effect (see section 3.3), which weakens the radio and acoustic emission. Their contribution has been neglected for both methods, and only the hadronic cascades have been taken into account.

Hybrid array

Figure 4.1 shows the geometry of the simulated hybrid detector. Around the central ICECUBE array with 80 strings holding 60 equally spaced optical sensor modules in a depth from 1450 m to 2450 m, following an idea described in [HH04a] an additional 13 strings are located in a 1 km circle to enhance the optical detection volume. Since drilling is a main cost factor, for all deep in-ice installations, the larger radio and acoustic arrays use common holes. 5×2 radio antennas with a 100 m spacing from 100 m to 600 m depth are installed in 91 hexagonally arranged strings, each also equipped with 300 equally spaced acoustic receivers in the depth of 5 m to 1500 m. Note that the apparent imbalance in channel number is roughly compensated by the much lower per-channel cost of the acoustic sensors. It should also be mentioned that the string spacing of 1 km is not optimised for the acoustic and radio method. Instead a denser spacing was chosen to achieve a better overlap in the energy range best suited for optical detection.

Detector response

For the simulation of the optical detector response, apart from the event generation, the full Monte Carlo chain as developed for the simulation of the AMANDA and ICECUBE detectors was used. Muons are propagated with the *Muon Monte Carlo (MMC)* code [CR04]. Until reaching the detector, differential energy losses are applied using a *continuous randomization* method. This leads to somewhat coarser modeling, but still well describes the total muon energy loss. Inside a cylinder of 2000 m height and 1660 m diameter around the point of closest approach to the detector the muons are fully stochastically propagated, including generation of all secondaries that contribute to the Cherenkov light emission. Light propagation in a homogeneous *bulk* ice with depth-independent scattering and absorption lengths was chosen from the different ice models available for AMANDA. For very bright high energy events this better describes the long-range behaviour than a *layered* ice model [A⁺05b]. Finally, *hits* are generated in the optical sensor modules by the *AMASIM* code [Hun99] taking into

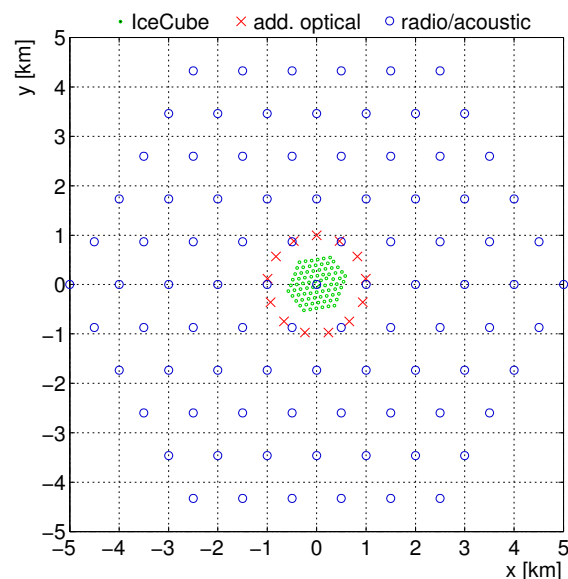


Figure 4.1: Top-view of the simulated array of radio, acoustic and additional optical receivers around the planned ICECUBE array.

account the integrated wavelength and angle dependency of the sensitivities. A two step trigger condition is applied. After a primary trigger of 5 hits in $2.5\,\mu\text{s}$ anywhere in the array local coincidences are formed from two hits in neighbouring or next-to-neighbouring modules within $1\,\mu\text{s}$. Ten local coincidences are required to form the final trigger to accept the event.

Hadronic cascades are parametrised including the LPM effect as described by [AMZ98]. For the radio method, the electric field strength at the receivers is calculated according to the prescription in [HZS91]. Attenuation in the ice is taken into account following the measurements at South Pole Station [BBGS05]. Locally generated anthropogenic noise from this station proved to be a major background source for radio detection [K⁺06]. For a better rejection of these events, two vertical half-wave dipole antennas with a distance of 5 m are simulated at each position in the radio array. The peak frequency of the radio pulse is estimated to be $f_{peak} = 280\,\text{MHz}$. An effective antenna height of 10 cm is assumed for this frequency, falling by no more than 3 dB in a 20 % band around f_{peak} . As currently under development for the successor to RICE, lossless signal transmission to the surface (for example with in-ice digitization) is assumed. At the surface electronics the signal is then transformed into the time domain, resulting in a 10 ns long waveform that is sampled at 0.5 ns intervals for each antenna. After rejection of anthropogenic sources only the thermal noise σ_{kT} remains, that is estimated from the ambient temperature plus a system temperature of 100 K. To form a trigger, two receivers with amplitudes larger than $3.5\sigma_{kT}$ within a $30\,\mu\text{s}$ time window are required.

The same longitudinal parametrisation of the hadronic cascade [AMZ98] is used in the calculation of the acoustic pulse. Unattenuated signals at arbitrary positions are produced by integration over the energy density with a radial distribution following the Nishimura-Kamata-Greisen function. Depth dependent absorption of the acoustic pulses is taken into account following the theoretical calculations described in section 3.5. As the effect is expected to be nearly frequency independent it can be integrated over the path from source to receiver and applied in the time domain. As discussed before, South Pole ice is predicted to be much quieter than ocean water at the relevant frequencies (10 – 60 kHz), due to the absence of waves, currents, or animals. Anthropogenic surface noise will largely be refracted back up to the surface. For the current simulation the ambient noise is assumed to be negligible compared to sensor self-noise. As shown in chapter 5, equivalent self noise levels $\sigma_{ESN} < 10\,\text{mPa}$ have already been achieved in water with non-optimized designs. Due to the better matched impedances, larger sensitivities are expected for ice, so that a value of $\sigma_{ESN} = 3\,\text{mPa}$ seems justified for a future sensor. The acoustic trigger used in this simulation required that three receivers detect pressure pulses above a threshold of $3\sigma_{ESN}$.

4.3 Results

Finally, neutrino effective volumes V_{eff} have been calculated from the number of observed N_{obs} and generated N_{gen} events using the generation volume V_{gen} as a reference:

$$V_{eff} = \frac{N_{obs}}{N_{gen}} \cdot V_{gen} . \quad (4.1)$$

Each method has been considered separately, but also combinations of detector components where the trigger conditions have to be fulfilled simultaneously were investigated. Figure 4.2 shows the effective neutrino volumes obtained with the different methods and combinations.

While the relative increase in effective volume for the additional 13 strings around ICE-CUBE in the optical simulation is consistent with the estimate by [HH04a], both absolute values and energy dependence are not. Neither muon propagation nor light output and detector response are simulated by [HH04a]. Instead a parametrisation of the volume reached by the light of the muon together with a geometric constraint to form a trigger is used to calculate event rates. The absolute normalisation – that is lower by about a factor of ≈ 2 at 10^{20} eV in the work presented here – is probably a combined effect of different ice parameters yielding a lower light flux and the very different trigger conditions. At lower energies, however, the calculated effective volume exceeds those from [HH04a], which is probably a result of rather strict additional constraints in [HH04a] to suppress the atmospheric muon background. Atmospheric muons do not generate cascades and cannot be coincidentally detected by the acoustic or radio method. In this work, events are only counted at *trigger level* with no additional background suppression applied.

Both radio and acoustic effective volumes show a rather strong energy dependence and the array will only be efficient at energies above $\mathcal{O}(\text{EeV})$. At these energies however, the effective volume for a detector requiring a trigger in both the radio and the acoustic method (RA in figure 4.2), is nearly as large as for any of the single methods. The effective volume

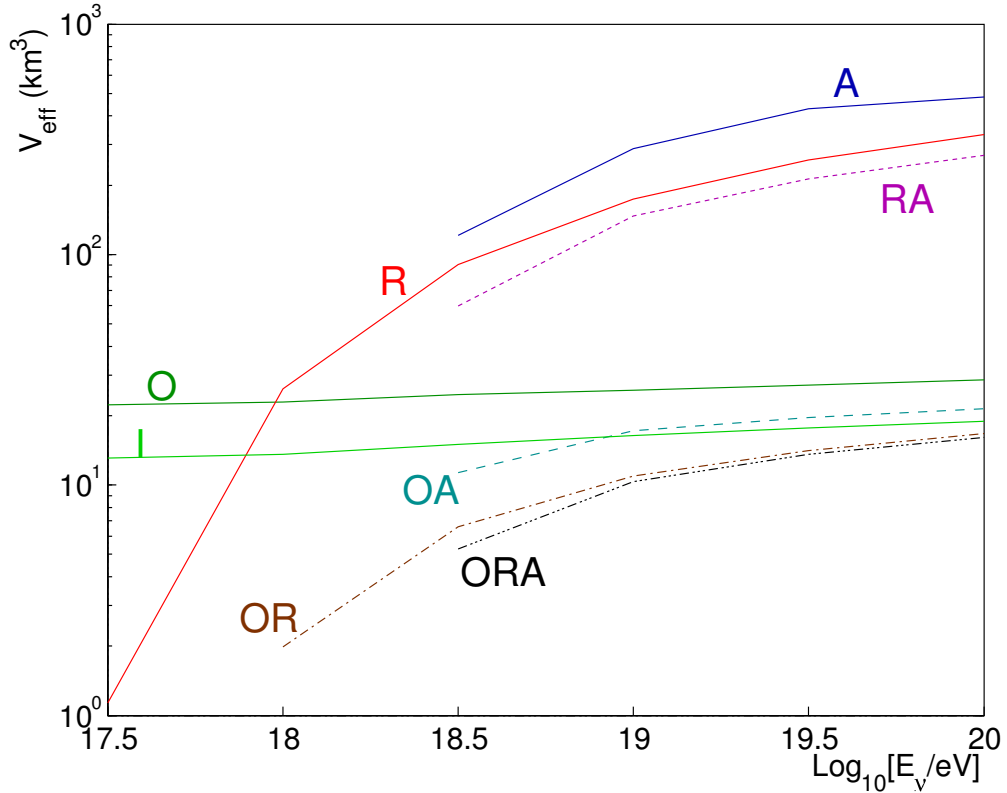


Figure 4.2: Effective neutrino volume versus energy for the different detection methods and their combinations: ICECUBE (I), optical (O), radio (R) and acoustic (A).

	A	R	O	I	RA	OA	OR	ORA
Event rate [yr ⁻¹]	16.0	12.3	1.2	0.7	8.0	0.3	0.2	0.1

Table 4.1: Number of cosmogenic neutrino events per year from the simulation detected by the different methods and their combinations.

of the simulated optical array (**O**) is nearly double as large as that of ICECUBE (**I**), but both are small compared to the other techniques. As a consequence of this low response of the optical array, requiring triggers in coincidence with radio (**OR**) or acoustic (**OA**) decreases the effectiveness for neutrino detection. Nevertheless at the highest energies, around half of the events in the optical array will be detected by all three methods (**ORA**).

To obtain an estimate on the cross-calibration potential this provides, the effective volumes have been folded with a cosmogenic neutrino flux prediction by [ESS01], that is often used as a reference. Following star formation rate measurements, a moderate source evolution parameter of $m = 3$ for homogeneously distributed power-law sources is used in this model. In addition, the effects of a dark energy contribution of $\Omega_\Lambda = 0.7$ in a flat universe is taken into account. The increase in flux by a factor of 1.6 is comparable to other uncertainties in the simulation, as e.g. on the threshold level of the acoustic detector.

Table 4.1 shows the number of events obtained for the different methods. Considering that no elementary physics background sources are expected, the optical and radio methods show sizable event numbers. Not only a clear evidence should be obtained within a short operation time, but also a good overlap fraction of events detected by both methods simultaneously. Despite the small string spacing for the radio and acoustic array which was chosen to reduce the energy threshold, much longer lifetimes will be necessary to study systematic effects in coincidence with the optical method. So for a future hybrid array, new optical sensor technology is needed that allows greatly enhanced instrumented volumes at moderate costs. Alternatively the string spacing can be optimised for a detector only incorporating the radio and acoustic methods, which acts as a high energy extension of the optical array.

A similar study for acoustic detection in sea water is presented in [Kar06]. With a threshold of 5 mPa in sea water and a similar instrumentation density of 200 sensors/km^3 the effective volume in ice is larger by a factor of $1.5 - 7$, depending on the energy. Accounting for the larger Grüneisen parameter in ice, the slightly denser sensor spacing of 280 sensors/km^3 in this work, efficiency of the reconstruction algorithm applied in [Kar06] and differences in the simulation of the hadronic energy fraction, the results are compatible. It should be kept in mind, however, that for typical sea states ambient noise will be $\mathcal{O}(100 \text{ mPa})$ [VGL05], disfavouring water as a detection medium.

In contrast, if ambient and sensor self-noise are as low as assumed, pursuit of the development of the acoustic detection technique for application in South Polar ice seems highly rewarding. The steps taken to develop corresponding sensors will be presented in the next chapter 5.

Chapter 5

Sensor and transmitter developement

Ultrasonic acoustic sensors for water (*hydrophones*) are widely used in civil and military maritime research. Specialised designs are available for a wide range of applications, and have been developed and improved over many decades. Ultrasonic sensors for solid media, in contrast, are mainly used for non-destructive testing (NDT) purposes, where the sensor is not embedded in the medium carrying the acoustic wave. For the special application of acoustic in-situ sensing in ice, neither commercial nor exploratory devices were found to exist. Corresponding sensors (*glaciophones*) and transmitters had thus to be developed first. A brief overview over the sensor and transmitter principles and designs as well as investigations for their calibration will be presented in this chapter.

5.1 Sensor principles

Same as hydrophones, acoustic sensors for ice can be conveniently built using piezo-electric ceramics. Alternative methods, such as measuring vibrations by changing resonance frequencies of a fiber-embedded Fabry-Perot-Interferometer [B⁺06a], are not fully developed yet. Therefore the generic sensor design used here consists of a piezo-electric ceramic, an amplifier and a housing to meet the environmental conditions outlined in section 3.5, such as high pressures and cold temperatures.

5.1.1 Piezoelectric ceramics

Due to the simplicity of application and large number of possibilities, most ultrasonic acoustic sensors are based on piezo-electric ceramics. One of the most commonly used types of ceramics is lead zirconate titanate (*PZT*). *PZT* crystals have the same face centred cubic structure that is found in perovskite (calcium titanium oxide, CaTiO_3) which therefore is also called *perovskite structure*. At temperatures above the Curie temperature $T_C \approx 300^\circ\text{C}$ the base cell depicted in figure 5.1 shows a cubic symmetry. Below the Curie temperature the base cell is orthorhombic, and no longer point symmetric around its center. This results in small dipole moments for the cells, which align within the Weiss region. Due to random orientation of the net dipole moments in different Weiss regions, untreated polycrystalline *PZT* will have a vanishingly small net dipole moment. In the *poling* process, a strong electric field ($\approx 2 \cdot 10^6 \frac{\text{V}}{\text{m}}$) is applied during the cooling that aligns the dipole moments in the Weiss

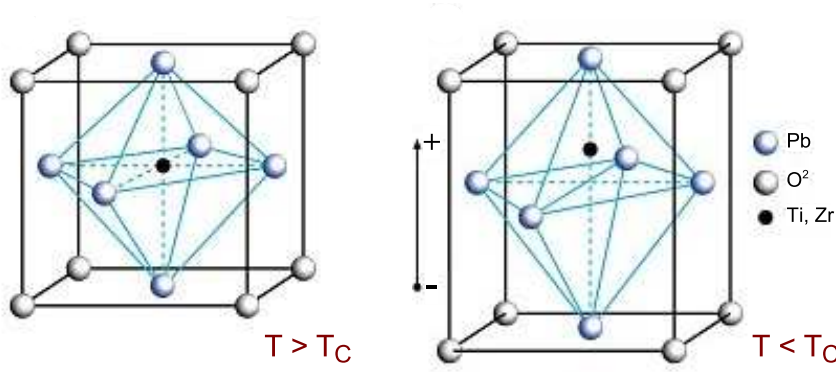


Figure 5.1: Perovskite crystal structure of lead zirconate titanate (*PZT*) above and below the Curie temperature T_C .

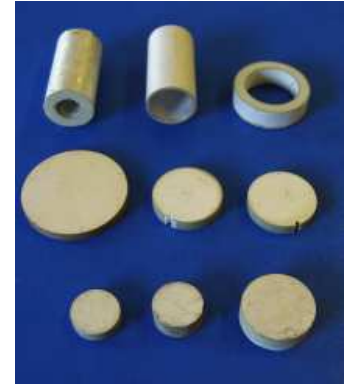


Figure 5.2: Picture of commercially available *PZT* ceramics in various shapes.

domains. Then the *PZT* ceramic has a strong net dipole moment, and a deformation of the ceramic along the dipole axis will result in a surface charge. At the same time, applying a voltage to the ceramic will result in a deformation.

This system can be described by two coupled linear equations [RD00]:

$$\begin{aligned} S_\alpha &= s_{\alpha\beta}^E T_\beta + d_{i\alpha} E_i \\ D_i &= \varepsilon_{ij}^T E_j + d_{i\alpha} T_\alpha \end{aligned} \quad i, j \in \{1, 2, 3\} \quad \text{and} \quad \alpha, \beta \in \{1, 2, 3, 4, 5, 6\} . \quad (5.1)$$

In the above equations, i and j denote the three orthogonal directions, where $i, j = 3$ is usually taken as the axis of polarisation. For $\alpha, \beta \leq 3$, they denote the same directions, whereas $\alpha, \beta \geq 4$ indicate rotations (or shear) around these three primary axis, respectively. $\vec{E} = (E_i)$ and $\vec{D} = (D_i)$ give the vectors of electrical field strength and displacement. $T_\alpha = \epsilon_{\alpha ij} T_{ij}$ and $S_\alpha = (2 - \delta_{ij}) \epsilon_{\alpha ij} S_{ij}$ with $\epsilon_{\alpha ij} = \delta_{\alpha i} \delta_{ij} + \delta_{\alpha(9-(i+j))}$ are contractions of the stress tensor $\vec{T} = (T_{ij})$ and strain tensor $\vec{S} = (S_{ij})$ that implement the symmetry of the crystal in $ij \leftrightarrow ji$. For example $T_6 = T_{12}$ is the shear component of the stress tensor around the 3-axis, while $S_6 = 2S_{12}$ is the corresponding strain. Finally, $s_{\alpha\beta}^E$ gives the compliance modulus for constant electric field, ε_{ij}^T is the electric permittivity at constant stress and $d_{i\alpha}$ are called the *piezoelectric constants*, that relate electrical and mechanical effects.

The main piezo-electric effect is usually along the axis of polarisation, i.e. $d_{22} = d_{11} = d_{12} = d_{13} = d_{21} = d_{23} \approx 0$. Due to symmetry in the crystal and orientation, *PZT* ceramics usually also show symmetric response in the plane perpendicular to the 3-axis, i.e. $d_{31} = d_{32}$. So in absence of shear effects (for which $d_{i\alpha}$ components are also usually small), only two values d_{31} and d_{33} are needed to describe the piezoelectric response.

Using *PZT* the technical properties of the material can be varied by doping with other elements such as nickel and bismuth. The material *PIC151* of the ceramics used for the investigations presented here was specially selected for a large piezo-electric constant and high permittivity of $\varepsilon_{33} d_{33} \approx 500 \frac{\text{pC}}{\text{m}}$. A large variety of different shapes can also be realised, as shown in figure 5.2. Unless specified otherwise, a cylindrical geometry of height $h = 5 \text{ mm}$

and diameter $d = 10$ mm has been selected. To collect the charge, the surfaces are silver-coated. Piezo-ceramics can be directly soldered on, if care is taken that the temperatures will stay well below the Curie temperatures. To retain a flat surface for good mechanical contact it is more useful in most cases to attach a thin conducting foil, e.g. with a conducting glue.

In order to verify the piezo-electric properties, a simple measurement has been devised: The piezo-ceramic is short-cut with a resistor and loaded with a static heavy weight of a mass $m = \mathcal{O}(\text{kg})$ on its polarisation axis. From 5.1, the resulting surface charge Q is

$$Q = \varepsilon_{33} D_3 A = \varepsilon_{33} d_{33} m \cdot g, \quad (5.2)$$

where $\vec{E} = \vec{0}$ has been set. The force on the ceramic along the 3-axis has been taken as $F_3 = T_3 A = m \cdot g$. The charge on the order of a few nC is usually quickly drained through the input resistance of any applied voltmeter, so that no static voltage can be measured. Yet by removing the load, the previously drained charge will flow back through the measurement device, resulting in a current spike. This spike can be measured and the charge is obtained by integrating over the pulse. Figure 5.3 shows the result of such a calibration measurement. Using different shunt resistor values R_{shunt} gives consistent results and the systematic and statistic error is small. The deviation of the obtained piezo-electric charge constant of $\varepsilon_{33} d_{33} = 613 \pm 26_{stat} \pm 17_{syst} \frac{\text{pC}}{\text{N}}$ from the nominal value is a result of the natural fluctuations in the manufacturing process.

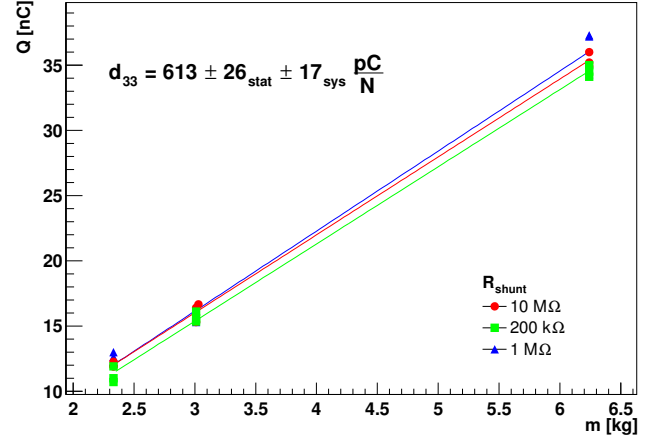


Figure 5.3: Induced surface charge Q for a *PZT* ceramic loaded with a mass m and measured with different shunt resistor values R_{shunt} .

5.1.2 Impedance and materials

In the linear regime of elasticity, acoustic waves and their propagation in a medium or system can always be described with an electromagnetic equivalent. Each acoustic property has a corresponding electromagnetic property, so that e.g. the voltage U can be associated with the stress \bar{T} , while the charge Q is related to the divergence of the particle displacement $\nabla \vec{u}$ (including some proportionality factors).

Similar to the ohmic conductivity σ , each isotropic medium has an acoustic impedance for longitudinal modes Z_l and transversal modes Z_t . For a planar wave they are given by

$$Z_l = \rho v_l \quad \text{and} \quad Z_t = \rho v_t, \quad (5.3)$$

where ρ is the density of the medium and v_l and v_t are the speed of compressional and transversal waves, respectively. For the design of acoustic sensors, this parameter is important since it describes how well elastic waves will couple from one medium to the other. In the most simple cases of two isotropic semi-infinite joint media without shear forces (such

as fluids), the reflectivity $r = A_r/A_i$ denoting the ratio of incoming wave amplitude A_i and reflected wave amplitude A_r is given by

$$r = \frac{A_r}{A_i} = \frac{Z_l^1 \cos \theta_1 - Z_l^2 \cos \theta_2}{Z_l^1 \cos \theta_1 + Z_l^2 \cos \theta_2} . \quad (5.4)$$

The angle of incoming wave θ_1 and transmitted wave θ_2 are given with respect to the axis perpendicular to the plane and are determined by $\sin \theta_1 / \sin \theta_2 = v_l^1 / v_l^2$ where superscripts 1 and 2 denote properties of the traversed media. For good transmission from one medium to another with a similar sound velocity and independent of the incident angle the reflectivity r should be small. This can be best obtained by choosing materials such that $Z_l^1 \approx Z_l^2$, which is called *impedance matching*. Using Z_t instead of Z_l , equation 5.4 is also valid for transversal waves in isotropic solids with linear polarisation vertical to the plane of deflection. In the more general case of oblique incidence on a solid-solid interface of a non-polarized transversal or a longitudinal wave, conversion from longitudinal to shear waves and vice versa occurs, with an amplitude also depending on the ratio v_l/v_t . However, the qualitative statement still remains and a matched impedance gives a smaller distortion of the waves.

Table 5.1 shows a summary of the impedance values of some materials. The values may vary with temperature and composition and production conditions of the material. Polyurethane, with an impedance close to that of water is a commonly used material for hydrophones, but is not as well suited for application in ice. Allowing to cast very different shapes, polyepoxide (also *epoxy* or *PE*) has been investigated for in-ice application. However, its impedance is lower than that of ice, causing defocussation from the sensor center at the ice-polyepoxide boundary. Common and easy machinable materials such as brass or steel also do not match to ice well, but fit rather well to the piezo-ceramic's impedance. Glass has an intermediate impedance, so it is in principle well suited, but lacks good machinability. Having different advantages and disadvantages, all four materials have been tested in sensor prototypes, as will be described below.

5.1.3 Resonances

So far, only propagation in infinite and semi-infinite media has been considered. In a finite medium, reflections at the walls occur. Especially if the impedance of the adjoining medium is very small – as in the case of air (see table 5.1) – the reflection will be close to total, i.e. $r \approx 1$. In this case, steady waves occur at wavelengths of multiples of the dimensions of the body. The frequency for which the amplitude of these oscillation modes – or resonances – is largest is the resonance frequency, analogue to a resonance frequency in an electric circuit. In consequence, the impedance of the system will no longer be frequency independent, and may

material	ice	water	air	PE	steel	glass	brass	PZT
$\rho \left[\frac{\text{kg}}{\text{m}^3} \right]$	920	1000	1.2	900	7800	2600	8600	7700
$v_l \left[\frac{\text{m}}{\text{s}} \right]$	3980	1425	343	1950	5940	5930	4700	5000
$Z \left[\frac{\text{kg}}{\text{m}^2\text{s}} \right]$	$3.6 \cdot 10^6$	$1.48 \cdot 10^6$	412	$1.8 \cdot 10^6$	$46.2 \cdot 10^6$	$15.4 \cdot 10^6$	$40.4 \cdot 10^6$	$38.5 \cdot 10^6$

Table 5.1: Acoustic properties of various materials (from [Mil87]). The values are temperature dependent.

also incorporate a phase to describe the retardation of change in particle displacement versus pressure. As in the electric equivalent, the impedance $Z \rightarrow \mathbf{Z}(\omega)$ is then given as a complex vector. Moreover, a one-dimensional linear acoustic system with inertia, a damping factor and an elastic constant will follow the same wave equation as a closed electric circuit with an inductance L (corresponding to inertia), a resistance R (corresponding to the damping factor) and a capacity C , which can be associated with the stiffness. For a multi-dimensional system, where coupled oscillation modes exist, the electric analogue will have more than one LRC branch.

This way, the acoustic properties of the system can be described by their electrical equivalents. For the special case of a piezo-ceramic, the electrical and elastic states are linked, as shown in equation 5.1. This can be exploited to derive the mechanical response of a system by measuring the electrical impedance. The total electrical impedance \mathbf{Z}_{el} can be taken as an inverse sum of the purely electrical part \mathbf{Z}_C and a mechanical equivalent part $\mathbf{Z}_{LRC}(\omega) \propto \mathbf{Z}(\omega)$

$$\frac{1}{\mathbf{Z}_{el}(\omega)} = \frac{1}{\mathbf{Z}_C(\omega)} + \frac{1}{\mathbf{Z}_{LRC}(\omega)}, \quad \text{where} \quad \mathbf{Z}_{LRC} = \sum_j \left(i\omega L_j + \frac{1}{i\omega C_j} + R_j \right). \quad (5.5)$$

Neglecting its small inductance, $\mathbf{Z}_C = (i\omega C_p)^{-1}$ can be well approximated by the static capacitance of the piezo-ceramic. Measurement of the electrical impedance thus reveals the mechanical resonances of the piezo-ceramics, as shown in figure 5.4 for a cylindrical piezo-ceramic of 10 mm diameter and 5 mm diameter. At low frequencies, the capacitive character of the ceramic element is dominant. The impedance falls as $Z_C \propto 1/\omega$, resulting in a signal amplitude $U = \omega Q \cdot Z_C \propto Q$ directly proportional to the surface charge and a sensitivity that is frequency independent. Above 100 kHz, mechanical oscillations result in strong resonance and anti-resonance peaks in the impedance and in the sensitivity. The measurement is also compared to a *finite element* simulation [S⁺04a], which is in very good agreement.

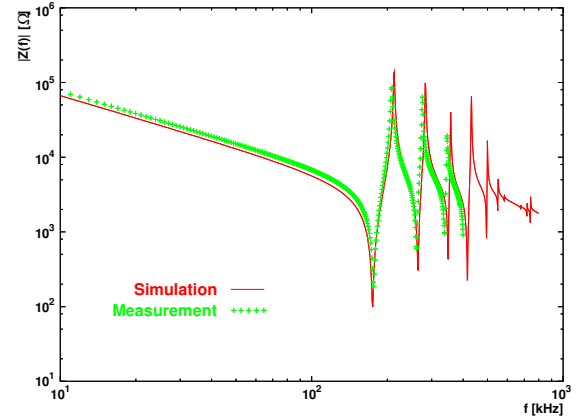


Figure 5.4: Measured and simulated impedance of a free piezo-ceramic. (from [Ste04])

From figure 5.4 it is obvious that the piezo-ceramics can be chosen small enough that the resonance frequencies are above the frequency range of interest for acoustic neutrino detection. However, it should not be chosen too small since the surface charge depends on the total surface of the ceramics. To build a sensitive transducer, the ceramic cannot be used as a single element. In the quasi-static regime below the resonance frequencies we can use equation 5.1 to see that in a closed loop circuit ($E_j = 0$) the displaced charges on the ceramic directly relate to the stress on it.

Now let us consider two extreme cases:

1. a massless piezo-ceramic mounted on a vibrating surface: In this case the inertia of the ceramic is zero, and it will freely move along with the vibrating surface. Hence its stress and deformation will be zero.
2. a massive piezo-ceramic mounted in between a vibrating surface and an infinitely rigid wall: Now the inertia of the system is infinite, and the force exerted by the vibrating surface will apply stress to the ceramics.

In practice, small piezo-ceramics are not massless, but light. They should thus not be mounted on the surface of the detection medium, but either be held in place by a rigid mounting or be embedded in a stiff material. In principle, the embedding material could be the acoustic medium itself – e.g. water or ice. The surface of the piezo-ceramics needs to be equipped with electrodes to collect the charge. Conductivity in water would short-cut the ceramics. In ice, such a design is possible, but impractical since the following amplifier stage needs a pressure housing. A ceramic embedded in the medium will need a feedthrough into the housing, which is expensive and known to be critical for freeze-in in high-pressure environments. Following these design principles, two different types of sensors have been developed as depicted in figure 5.5.

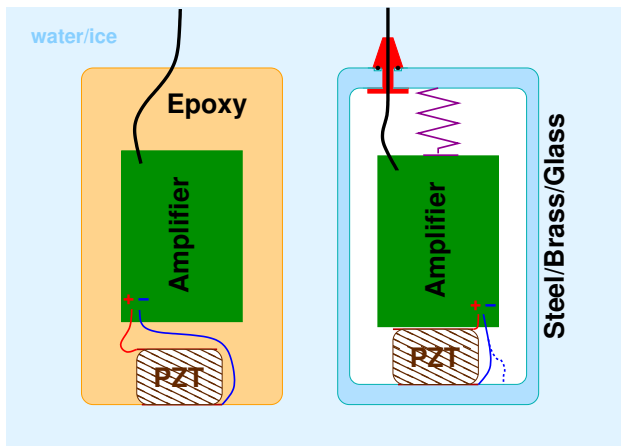


Figure 5.5: Schematic drawing of an embedded sensor (left) and a sensor in a pressure housing (right).

In both cases, the piezo-active element is mounted close to the amplifier board to reduce electromagnetic interference on the amplifier input. For the embedded sensor, the embedding material – epoxy in this case – acts as a stiffness element to restrain the piezo-ceramics, while at the same time protecting the amplifier from damage. In the second case, an air filled pressure housing is used, in which the ceramics is tightly clamped against a wall surface by a stiffness element (depicted as a spring in figure 5.5). The stiffness of the element should be in the same order of magnitude as the stiffness of the

piezo-ceramic itself. As the amplifier board is preferably mounted close to the ceramics, in some cases the tension from the stiffness element is exerted on the ceramics via the board instead of directly on the ceramics.

The disadvantage of the above scheme is of course, that in both cases the housing of the sensor will dramatically influence the acoustic behaviour. From the velocity of sound given in table 5.1 a frequency of 80 kHz gives wavelengths of 7.4 cm in glass and steel, 5.9 cm in brass and 2.5 cm in epoxy. Since neither piezo-electric elements nor amplifiers and housings can be built arbitrarily small, for any practical purposes, any housing designed to hold a piezo-ceramics will have resonance frequencies in the frequency range of interest. Even for a rather simple geometry like a cylinder, the resulting mode pattern can be rather complex, as seen in the impedance curve 5.4. For more complex designs, possible resonance

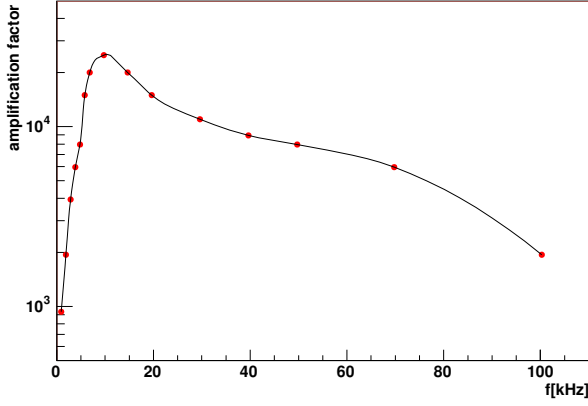


Figure 5.6: Measured overall amplification factor of the 3-stage amplifier.

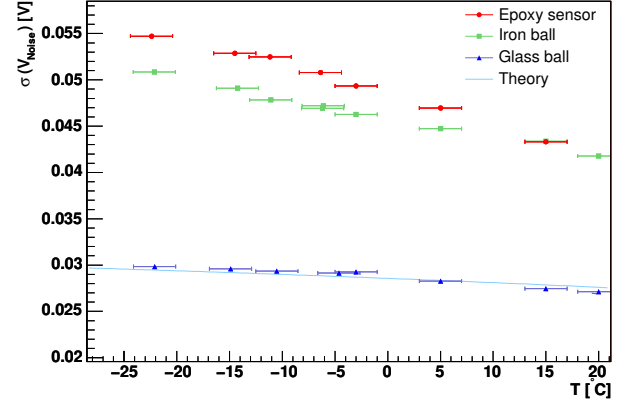


Figure 5.7: Noise development with temperature for different sensor types. The solid line is the theoretical prediction.

modes will get very numerous, inhibiting a description by an electric equivalent due to the sheer amount of LRC parameters. Finite element simulations will still yield good results, but are time consuming both in implementation and calculation time. For the frame of this work, therefore an empirical approach was chosen to optimise the sensor design. Four complementary approaches have been tested and will be presented in detail in section 5.2 – one of them embedding the amplifier and piezo-sensor in epoxy resin (the *epoxy sensor*), and three of them using steel (*iron ball*) or glass (*glass ball* and *glass bowl*) as pressure housing materials. The latter three also house more than one piezo-ceramic and amplifier channel.

5.1.4 Amplifier

Finally, the signal from the piezo-ceramic needs to be amplified. For typical stresses of $\mathcal{O}(\text{mPa})$, the surface charge on the piezo-ceramics described above will be of $\mathcal{O}(10^{-16} \text{ C}) = \mathcal{O}(10^3 \text{ e})$. So even for a digitisation close to the piezo-ceramics, a preamplifier is needed to raise signal levels to scales that can be used with common data acquisition methods such as oscilloscopes and analogue-to-digital converter circuits (*ADCs*). If analogue signals are also to be transmitted over long distances, as e.g in case of the SPATS setup described in chapter 7, even higher amplification is needed to overcome cable losses and ensure a good signal to noise level. For the latter, it is also especially advisable to use *differential* signal transmission, where the signal itself and the inverted signal are transmitted on the two wires of a wire-pair (instead of the *single-ended* mode with one signal wire and one ground). The original signal is obtained by taking half of the difference of the signal levels on the two wires. This way, *common mode* noise which affects both signals in the same way is automatically rejected.

For these reasons, all sensors presented in this work were equipped with a differential three-stage amplifier system with a particularly high input impedance matching that of the piezo-ceramics. The first stage is based on the low-noise operational amplifier AD745JR (wide temperature version) with a bandwidth of 20 MHz and a self noise of only $n_\sigma = 2.9 \text{ nV}/\sqrt{\text{Hz}}$ despite the very high input impedance. The nominal amplification factor is set to

100, with an additional RC element providing a 5 kHz high pass to suppress low frequency signals. The second stage is an AC coupled inverting amplifier with again a nominal gain of 100, which is bypassed by an RC element to reduce the gain to unity for frequencies above ≈ 500 kHz. The third stage finally is a differential line driver with a gain set to 1, resulting in a total nominal gain factor of 10^4 . More details on the amplifier chain can be found in [Ste04].

The actual frequency dependent gain has been measured for the complete chain and is shown in figure 5.6. The sharp drop below 10 kHz is a result of the implemented low-pass filters. At high frequencies, the limited gain-bandwidth product of the preamplifier limits the amplification factor. In the most interesting range from 20 – 80 kHz, the gain is sufficiently stable, especially if compared to variations of the acoustic impedance of the sensor housing. Using an input bandwidth of $\Delta f \approx 200$ kHz at the preamplifier, with an average gain of 10^4 the sensor self noise can be estimated to

$$\sigma(V_n^{\text{self}}) = n_\sigma \cdot \sqrt{\Delta f} \cdot \text{gain} \approx 2.9^{\text{nV}}/\sqrt{\text{Hz}} \cdot \sqrt{2 \cdot 10^5 \text{ Hz}} \cdot 10^4 = 12 \text{ mV} . \quad (5.6)$$

An additional contribution stems from the thermal noise of the comparatively large capacitance of the piezo-ceramics of $C_{\text{piezo}} \approx 260$ pF that is increased by another capacitance of $C_1 \approx 330$ pF at the ground side of the input to obtain a symmetric behaviour. Both have to be taken in parallel, resulting in a thermal noise level at room temperature of

$$\sigma(V_n^{\text{piezo}}) = \sqrt{\frac{k_B T}{C_{\text{piezo}} + C_1}} \cdot \text{gain} \approx \sqrt{\frac{8.61 \cdot 10^{-5} \text{ eV/K} \cdot 1.60^{-19} \text{ C/e} \cdot 300 \text{ K}}{260 \text{ pF} + 330 \text{ pF}}} \cdot 10^4 = 26 \text{ mV} . \quad (5.7)$$

The total RMS noise voltage at room temperature is thus expected to be

$$\sigma(V_n) = \sqrt{\sigma(V_n^{\text{piezo}})^2 + \sigma(V_n^{\text{self}})^2} = 28 \text{ mV} . \quad (5.8)$$

This is in very good agreement with the values obtained for the *glass ball* sensor shown in figure 5.7, which gives noise levels depending on temperature for three of the four sensor types that will be introduced in the following section 5.2. From equation 5.7, an increase of noise with temperature would be expected. However, this effect is compensated by the gain-bandwidth product, that decreases by $\approx 6.7 \cdot 10^{-2} \text{ K}^{-1}$ in absolute terms. The resulting theoretical noise level depending on temperature is shown as a continuous line in figure 5.7 and describes the observation with the *glass ball* very well. Yet for the *iron ball* and *epoxy sensors*, much higher noise values occur. While unclear for the *epoxy sensor*, for the *iron ball* two possible sources can be suggested, which may cause high noise levels by interference in between the channels:

1. In contrast to the *glass ball* sensors, the two amplifiers in the *iron ball* sensors are not individually shielded.
2. Both amplifiers in the *iron ball* are grounded with respect to the steel housing through one electrode of the piezo-ceramic.

Nonetheless, the noise levels in all three sensors can be considered low with respect to the amplification factor and obtained sensitivity. Especially the sensitivity will increase with decreasing temperature much faster than the self noise, ensuring even better signal-to-noise conditions at lower temperatures.

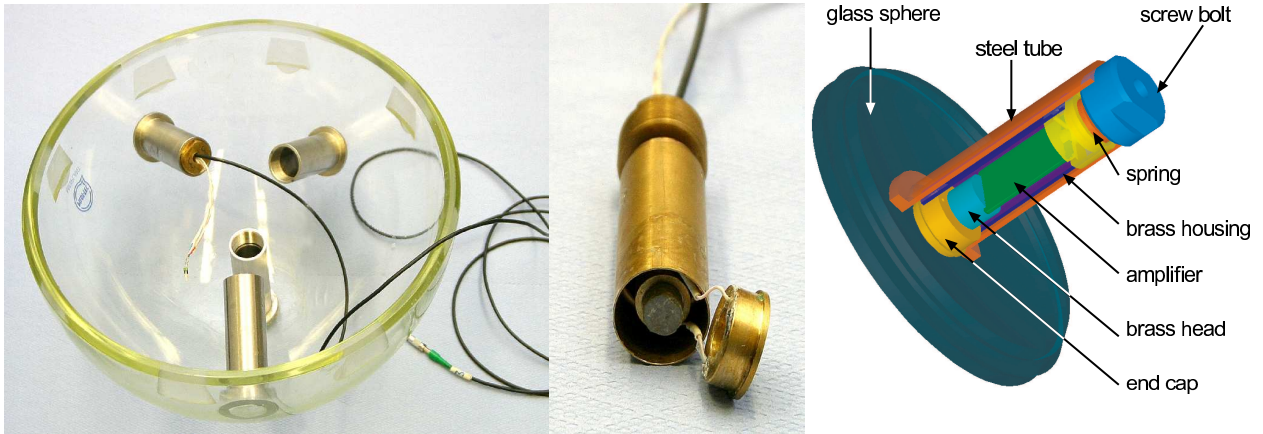


Figure 5.8: Pictures of the *glass bowl* sensor (left) an acoustic channel (middle) and a schematic drawing (right).

5.2 Sensor prototypes

The four different sensor prototypes that have been developed will be shortly presented here. For an extensive discussion, please see [Ste04]. A fifth prototype design – the *brass sensor* – did not yield satisfactory results when used in ice and will be omitted here.

With future application within the ICECUBE detector in mind, a first attempt to build an acoustic sensor module was made by adding acoustic channels to an ICECUBE optical module. First the amplifier board is soldered to a small circular brass head with a recess in which the piezo-electric ceramic is placed. The amplifier board is mounted in a cylindrical brass housing for shielding. It is equipped with a rounded end cap to fit the curvature of the glass sphere on one side as shown in the middle of figure 5.8. The pressure housings of the ICECUBE *DOMs* are made of two 33 cm diameter glass spheres of 12 mm wall thickness. For the acoustic sensor module stainless steel tubes were glued into one of the half sphere at different positions. The piezo-ceramic and amplifier system is inserted in these tubes. A screw bolt and an inside thread in the steel tubes can be used for prestressing the system.

Showing good results in the first attempts, the design proved to be problematic for several reasons. Apart from an undesired damping of high frequency signals as will be shown below, especially the large size of the system caused problems in testing. A full sphere would not fit in any of the available water basins with sufficient spacing at the sides, so that the *glass bowl* sensor module could only be used as a half-sphere floating on the water or partially embedded in the ice. Especially in the proton beam tests described in chapter 6 low signal amplitudes were observed in this configuration. Integration of acoustic sensors in the *DOMs* was also found to be premature and the design was abandoned for smaller, independent configurations.

The most simple sensor design is implemented in the *epoxy sensor* shown in figure 5.9. The piezo-element is glued to a small brass head, on which the amplifier board has been soldered. The other electrode of the surface is covered with the same copper foil and signals are brought to the amplifier board by two thin wires. The system is then moulded in epoxy

resin. Applying negative pressure during the curing process ensures that no bubbles will occur within the resin. On the outside, the system is also covered with copper foil for electromagnetic shielding. For testing purposes in the laboratory no connector was needed but a sufficiently long cable is directly connected to the output of the amplifier board.

Apart from the small dimensions of 40 mm diameter and 40 mm height, the main advantage of the *epoxy sensor* are ease of production and low cost. However, the design causes a high non-uniformity of the sensor. For the azimuthal response this may be circumvented by the use of a cylindrical ceramics (as frequently used in hydrophones), which raises the cost of the sensor by about a factor of five. Non-accessability of the components, e.g. the amplifier board, did not turn out to be critical due to the high reliability of the design.

In an effort to partially regain omnidirectional sensitivity by having multiple channels in one sensor module the *glass ball* and *iron ball* sensors were designed. In the *glass ball* sensor a glass sphere similar to the ICECUBE spheres but with a smaller diameter of 12 cm is used. A metal pad to fit the curvature is glued into each of the half spheres. The piezo-ceramic – again equipped with a small brass head to which the amplifier board is soldered – is pressed against the pad by two metal clips as shown on the right in figure 5.10. A copper casing is placed around each of the amplifier boards, completing the shield with the glued-in pad. Eventually, both half spheres are put on top of each other and the system is evacuated and sealed.

As shown in figure 5.7 the *glass ball* design has the lowest noise level of the developed sensors, probably due to the good shielding of the amplifier boards. Supposedly due to the smaller glass sphere diameter, it also does not show a suppression of the high-frequency part as the *glass bowl* sensor did. Yet, in water applications not as high sensitivities were reached in the intermediate frequency range from 10 – 50 kHz as for the *iron ball*. This effect can presumably be attributed to the less rigid fixation of the *PZT* element, which is kept small to be included in the shielding. Also the glass spheres with custom drilled holes for the connectors are comparatively expensive.

No optical transparency is needed, so that the glass can as well be replaced by another material, e.g. steel as done for the *iron ball* sensor shown in figure 5.11. While the *iron ball* sensor has the same diameter of 12 cm, it is not closed by underpressure, but a sleeve nut and a seal ring are used. Another main difference in the design to the *glass ball* sensor is the realisation of the contact pressure of the ceramics-amplifier system. In the *iron ball* sensor it is granted by a central disc in each half sphere, acting both as a back-plane for providing the pressure and as an electronic shielding of the two amplifiers in the half-spheres. While the higher noise level (see figure 5.7) indicates that these still interfere, the *iron ball* sensor shows good overall sensitivity.

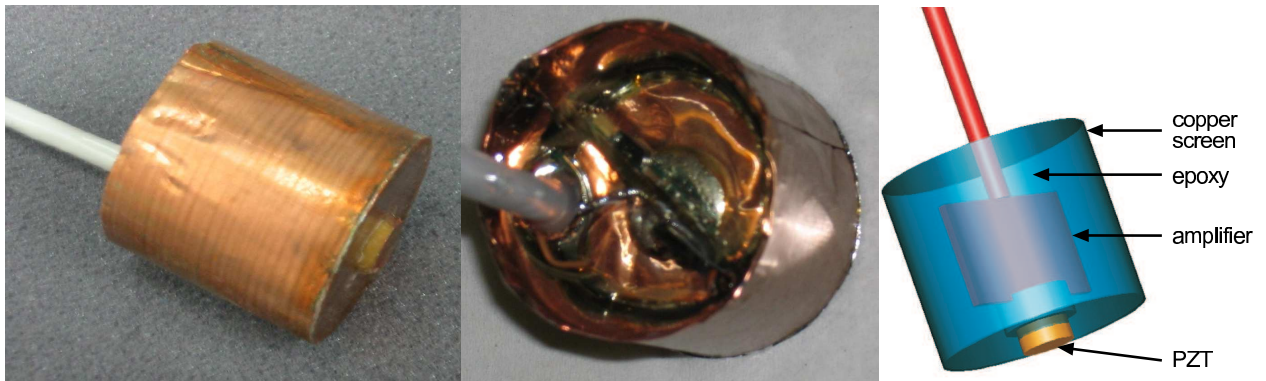


Figure 5.9: Pictures (left) and schematic drawing (right) of an *epoxy sensor*.

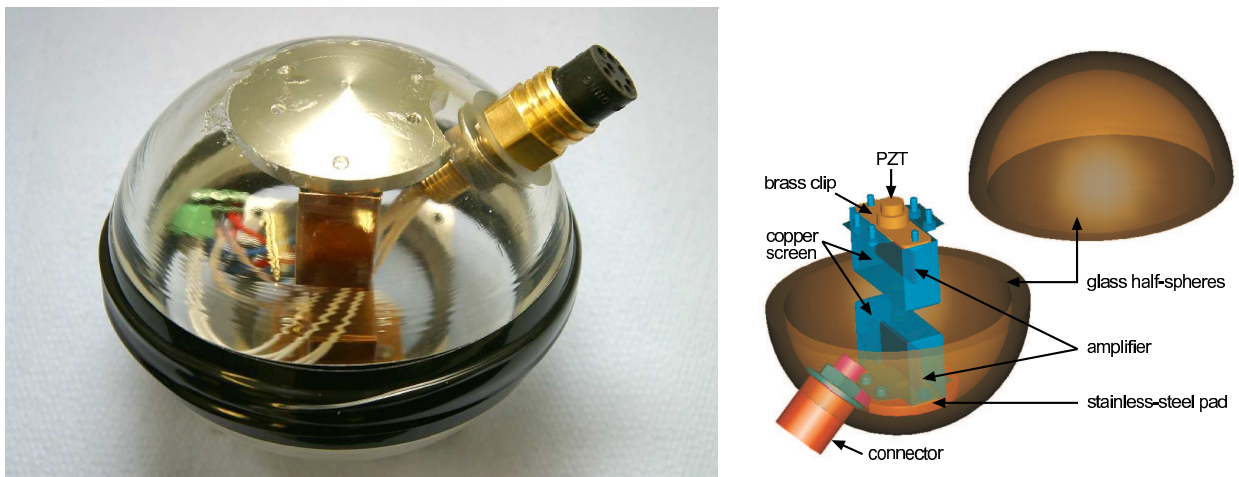


Figure 5.10: Picture (left) and schematic drawing (right) of the *glass ball sensor*.

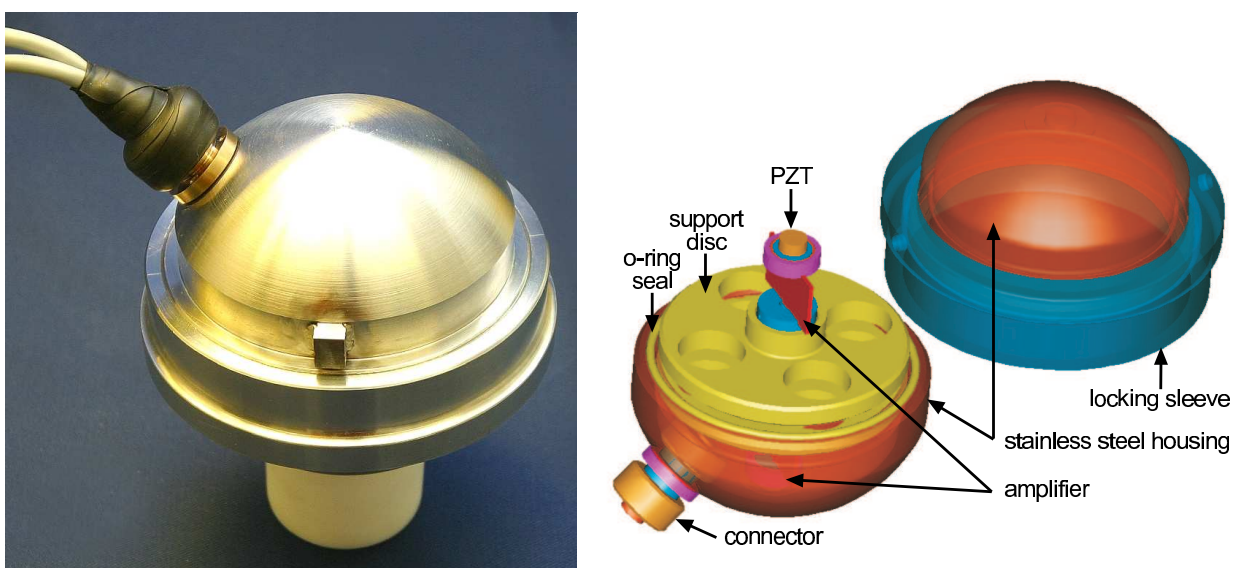


Figure 5.11: Pictures of the *iron ball sensor* (left) and a schematic drawing (right).

5.3 Sensor evaluation

For the evaluation of the sensor prototypes, measurements in both water and ice have been performed. In order to fully characterise an acoustic sensor, three quantities need to be known:

- the **sensitivity**, which is the ratio between the output voltage and the (acoustic) signal amplitude at a certain frequency.
- the **phase response**, that gives the phase angle between the electric and acoustic signals at this frequency. Together with the sensitivity, from these two the *transfer function* can be determined, which describes the sensors response to an arbitrary input signal.
- the **self noise level** as a function of frequency, that needs to be known in order to determine the detection threshold for a certain signal shape.

5.3.1 Calibration methods

The self noise of the sensor (i.e the electronic noise of the ceramics and amplifier system) is usually measured by simply recording the electronic noise of the sensor in a quiet environment. This can be achieved by putting the sensor in vacuum, where no sound can be transmitted. Comparison with measurements in a well insulated box showed the latter be sufficient. To measure the transfer function, several methods are possible and used in ultrasonic and hydrophone calibrations. First of all a distinction between absolute and relative calibration has to be made.

A **relative** calibration is obtained by comparing the electric signal of a previously calibrated hydrophone A to the signal obtained by the sensor to be calibrated (B) if subjected to the same acoustic wave(s). In water, the time dependent acoustic signal is described by a pressure $p(t)$ and the time derivative of the displacement $\dot{u}(t)$ along the geometric sensor-transmitter axis, while the electric signal is given by a voltage $U(t)$ and a current $I(t)$. These can be related by the frequency dependent complex transfer matrix $\mathbf{M}(\mathbf{f})$ that relates acoustic and electric signals at the transducer:

$$\begin{pmatrix} U_i \\ I_i \end{pmatrix} = \mathbf{M}_i \begin{pmatrix} p \\ \dot{u} \end{pmatrix}, \quad i \in \{A, B\} . \quad (5.9)$$

Since p and \dot{u} are connected by the acoustic impedance $|\mathbf{Z}_a| = p/\dot{u}$ of the medium and U and I by the electrical impedance $|\mathbf{Z}_{el}| = U/I$, only one of the quantities (U or I) needs to be measured. Knowing \mathbf{M} for the calibrated reference, the acoustic signal can be determined. Applying the same acoustic signal to the sensor under test, one can use equation 5.9 to determine its transfer matrix and calculate the sensitivity and phase shift. If shear waves and pressure waves are treated independently, the same will also directly apply to solids. Both are typically generated together, but can be separated by their very different propagation speeds. While this method is most easy to apply, it is of course limited by the accuracy of the calibration of the reference device.

For an independent determination of the **absolute** sensitivity, typically the *reciprocity calibration* method [ICE95] is used in hydrophone applications. This method relies on the reciprocity theorem, which – following equations 5.1 – states the reversibility of the application of stress and voltage to a piezo-electric ceramic. In mathematical terms, this means the matrix \mathbf{M} can be inverted. This reciprocity is exploited in a setup using one transmitter (A) and two hydrophones (B, C), one of which can be also used as a transmitter (e.g. C). For the signal of the hydrophone i , we obtain

$$\begin{pmatrix} U_i \\ I_i \end{pmatrix} = \mathbf{M}_i P(d) \mathbf{M}_A^{-1} \cdot \begin{pmatrix} U_A \\ I_A \end{pmatrix}, \quad i \in \{B, C\}, \quad (5.10)$$

where \mathbf{M}_A^{-1} is the inverted transfer matrix of the transmitter, \mathbf{M}_i the transfer matrix of the sensor i and $P(d)$ is a propagation term incorporating distance dependent effects such as absorption. Since none of the \mathbf{M}_i , $i \in \{A, B, C\}$ is known a priori, the two equations cannot be resolved. Therefore a third equation is obtained by using the reversible hydrophone C as a transmitter together with hydrophone B , which yields

$$\begin{pmatrix} U_B \\ I_B \end{pmatrix} = \mathbf{M}_B P(d) \mathbf{M}_C^{-1} \cdot \begin{pmatrix} U_C \\ I_C \end{pmatrix}. \quad (5.11)$$

Together with equation 5.10 this can be used to resolve the system. In this case, however, the phase relation might be different for transducer C and the transmitter A , so that at least at one point also the current needs to be measured.

While the advantage of the reciprocity method yielding an independent absolute calibration is obvious, it is of course a non-trivial technical effort. For a relative calibration the characteristics of the amplifier at the sensor are typically considered part of the transfer matrix. In a reciprocity calibration, one transducer has to be used as a sensor and a transmitter. For this, it either has to be used without amplifier requiring very large signal amplitudes and low noise conditions, or the amplifier characteristics need to be known very well.

5.3.2 Calibration in water

Independent of the above, usually **free-field conditions** are required, i.e. sender and receiver need to be placed far enough from each other that interference of the two, e.g. by waves bouncing from the sensor and back on the transmitter are small enough to be negligible. In addition, the test volume boundaries must also be such that any reflection from the walls can be neglected. If the transmitter is isotropic, this is not easily obtained in steady operation since the total acoustic energy is conserved. Anechoic chambers can be used where specially prepared walls dilute the signal intensity by scattering. In most cases it is easier to use a time selective method, as typically sensors are designed to operate in a limited frequency range.

Instead of a continuous wave, in the widely used *gated burst* method an electrical sine pulse train of several wave cycles is applied to the transducer for each frequency. For a limited time, both transmitter and sensor are driven in a "forced oscillation" mode at the applied frequency. If both the sensitivity and phase relations would not depend on frequency, the onset of the oscillation at the input frequency would be immediate. As this is usually

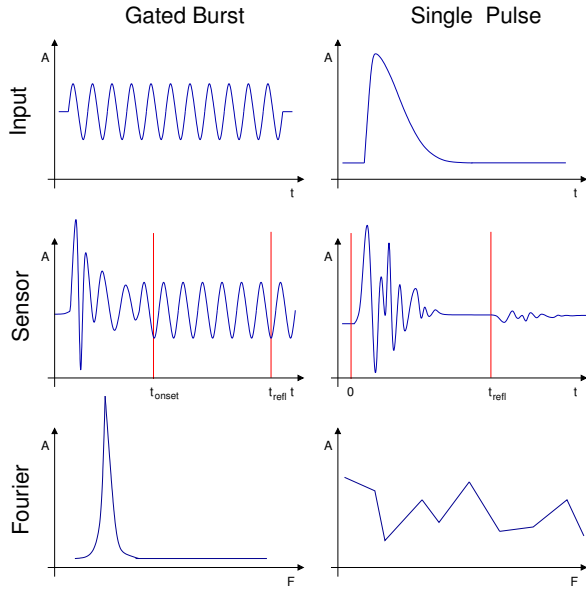


Figure 5.12: Scheme of the different input pulses (top), the corresponding sensor response (middle) and its Fourier spectrum (bottom) for the *gated burst* (left) and *single pulse* (right) method.

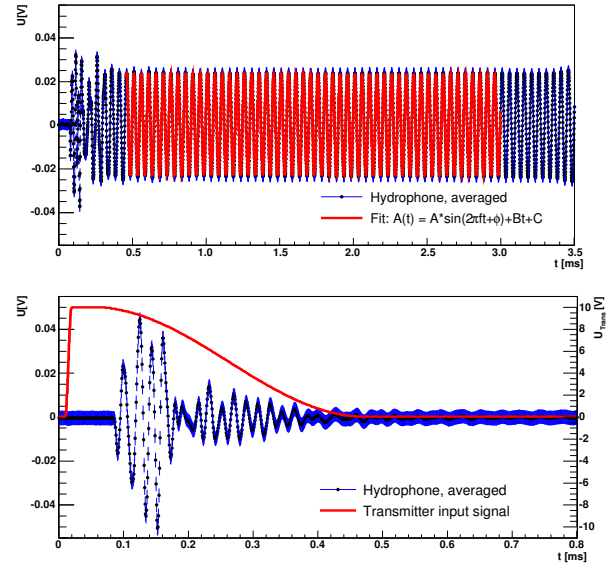


Figure 5.13: Example of the sensor response of the reference hydrophone to a *gated burst* signal (top) and a *single pulse* (bottom). The fit to determine the amplitude for the *gates burst* signal (top) and the electrical input signal to the transmitter (bottom) are also shown.

not the case, higher frequency components from the abrupt onset of the electrical signal will distort the shape in the beginning, but will be damped after some time t_{onset} . This time t_{onset} is not known a priori, but as the same transient excitation occurs when the sine wave signal is switched off, it can be determined by measuring the time it takes for the signal to fall below the noise level. The signal time window that can be used for analysis is then restricted to the time after t_{onset} until the time t_{refl} where the first reflected signal arrives from the nearest surface. This limits the number of sine wave cycles contained in the measurement interval, leading to some uncertainty in the determination of the frequency as schematically in figure 5.12, which especially limits the applicability at lower frequencies. With this method, only one frequency point can be measured at a time, with a repetition rate limited by the damping time of the acoustic signal in the test volume, so that a sufficiently large volume is needed for this approach.

In order to circumvent these restrictions, another calibration method was introduced which is called the *single pulse* method. Instead of a sinusoidal signal of a certain frequency, a short pulse containing a broad frequency spectrum is send from the transmitter. As illustrated in figure 5.12, this will result in a transient signal at the amplifier that again contains a broad spectrum. Where for the *gated burst* method the amplitude at a single frequency is used for comparison (e.g. to a reference hydrophone), in the *single pulse* method after Fourier transformation a broad range of frequencies is available at the same time. The signal time window the Fourier spectrum is taken of can extend from the beginning of the pulse up to t_{refl} . Since the sensor response is short, the test volume might be chosen smaller than in the previous method. Restrictions come from the noise conditions: While for the

gated burst method very good signal-to-noise ratios can be achieved for each frequency, in the *single pulse* method the total power is spread over a large frequency range, so care must be taken that it does not fall below the noise power density in certain frequency intervalls.

For a comparison both methods have been tested in a large water tank at the HAMBURGISCHE SCHIFFSBAU VERSUCHSANSTALT (HSVA). The relative calibration method was applied for both the *glass ball* and the *iron ball* sensor with a SENSORTECH SQ03 hydrophone as a reference. A cylindrical piezo-ceramic with a diameter of 10 mm and a thickness of 5 mm cast in epoxy on one side for electrical insulation was used as a transmitter. The 12 m \times 10 m \times 5 m deep section of a the otherwise 70 m long and 3 m deep water basin was used to mount the transmitter and one sensor pairwise in the centre of the volume at a distance of 10 cm. The positioning was verified measuring the time delay of the reflections from the surrounding surfaces. In the same effort, the speed of sound was measured to be $1410 \pm 3 \frac{\text{m}}{\text{s}}$ in good agreement with the predicted value of $1413 \frac{\text{m}}{\text{s}}$ [Wil60] for a salinity of 7 ppm and a temperature of -0.1°C . Two different input waveforms for the different methods were used with the transmitter, and 100 events were recorded at a sampling frequency of 1.25 MHz in each configuration for each of the three sensors. To compensate for sensitivity variations by more than two orders of magnitude the input pulse amplitude was varied in the range of $0.1 V_{\text{pp}}$ to $20.0 V_{\text{pp}}$ to obtain good signal-to-noise ratios while not exceeding the dynamic range of the individual sensors. This has been corrected for by linear scaling of the obtained amplitudes.

For the *gated burst* method, sinusoidal waves at six different frequencies were applied to the ceramics. The resulting signal recorded with the reference hydrophone is shown in figure 5.13 (top). The transient excitation at the beginning of the pulse is obvious. From the closest distance of 2.5 m to the water surface a free-field time of $t_{\text{refl}} = 3.5 \text{ ms}$ can be calculated, in good agreement with the observations. To determine the respective amplitudes, a sine function with free frequency f , amplitude A and phase ϕ plus a linear offset term to compensate for low-frequency ambient background was fitted to the measured signal in the respective time window as also shown in figure 5.13. By comparison of the derived amplitudes measured by the hydrophone and the respective sensor, a relative sensitivity has been obtained for each frequency point.

In the *single pulse* method, a short step-function with a rise time of $\approx 10 \mu\text{s}$ and a much slower return to the baseline was used instead, so that peak frequencies up to 100 kHz are expected. The input signal voltage U_{Trans} is shown in the lower part of figure 5.13, together with the signal recorded from the hydrophone. As mentioned above, for this method good signal-to-noise ratios for all frequencies are vital. To obtain the noise spectrum, two methods have been used: First each of the 100 events was Fourier transformed separately. For each frequency, the variation from event to event can be attributed to the noise. So the noise spectrum can be taken from the RMS spread of measured Fourier amplitudes at each frequency. This has been compared with a noise spectrum measured in an off-signal region. The signal spectrum is given by the average of the spectra of the single events and was compared to a signal spectrum obtained by Fourier transformation of the average of the 100 events. Good agreement was found for both signal and noise spectra. To obtain relative sensitivities the signal spectrum for each sensor is divided by the signal spectrum of the reference hydrophone. Frequency bands where either of the spectra falls below the amplitude of the noise spectrum were excluded.

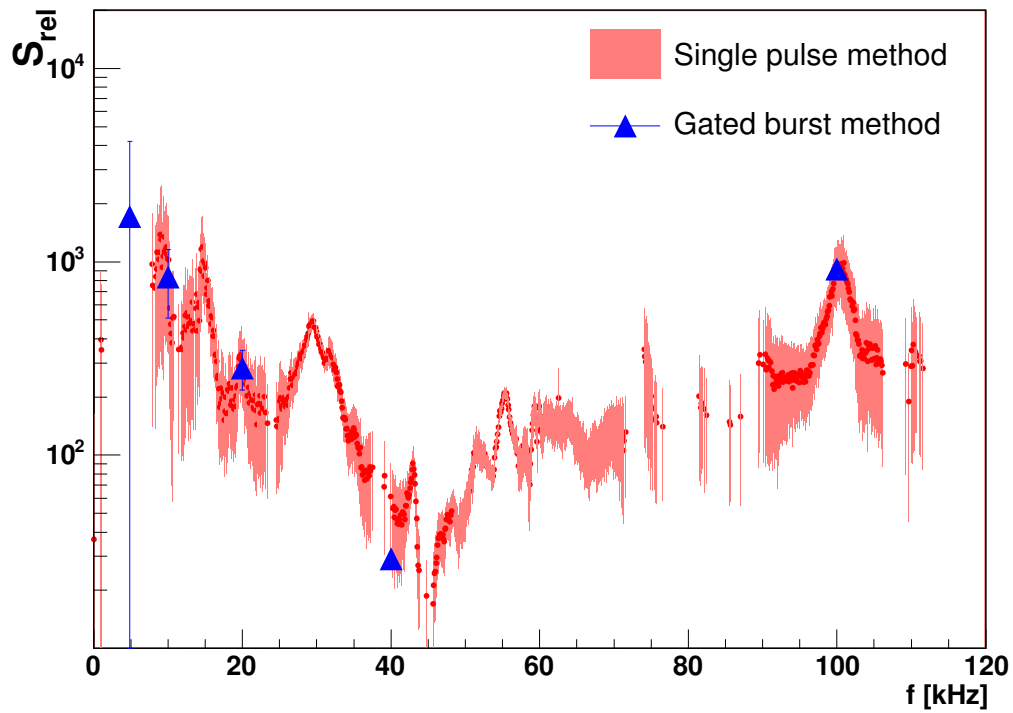


Figure 5.14: Sensitivity of the *glass ball* sensor relative to the reference hydrophone determined with the *gated burst* and *single pulse* method.

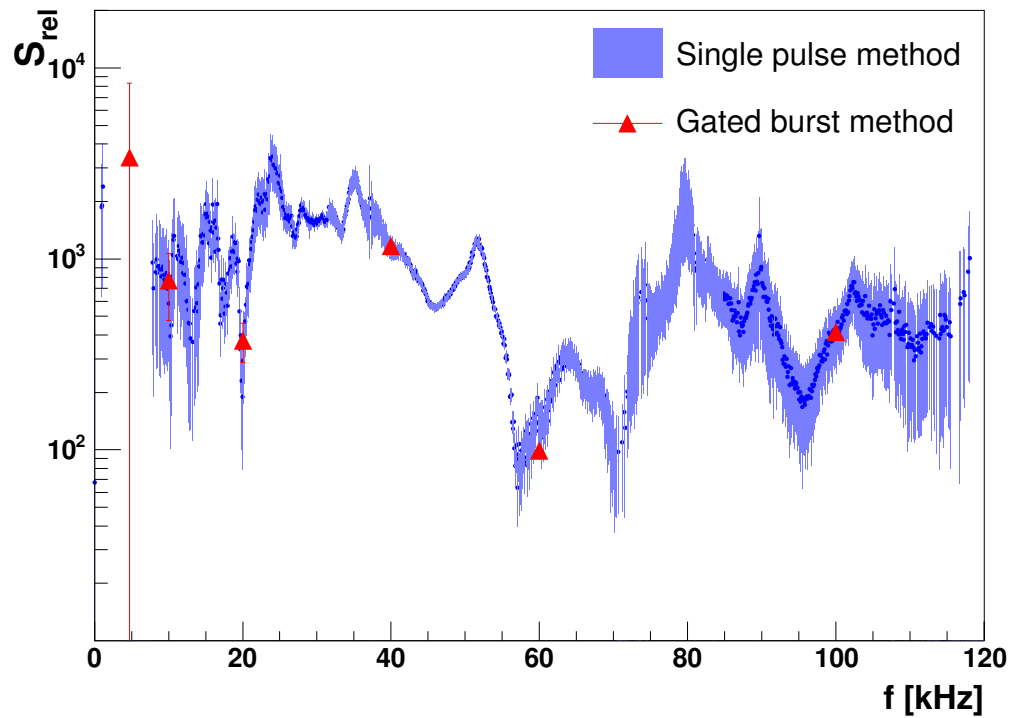


Figure 5.15: Sensitivity of the *iron ball* sensor relative to the reference hydrophone determined with the *gated burst* and *single pulse* method.

f [kHz]	100	60	40	20	10	glass ball 5
<i>gated burst</i>	919 ± 84	—	29.2 ± 2.4	283 ± 65	830 ± 320	1700 ± 2500
<i>single pulse</i>	957 ± 337	160 ± 34	61 ± 60	284 ± 108	1020 ± 690	—

f [kHz]	100	60	40	20	10	iron ball 5
<i>gated burst</i>	415 ± 38	99.4 ± 7.4	1170 ± 97	374 ± 86	770 ± 300	3300 ± 4900
<i>single pulse</i>	395 ± 114	141 ± 35	1107 ± 136	293 ± 119	580 ± 40	—

Table 5.2: Relative sensitivities at different frequencies obtained with the *gated burst* and the *single pulse* method.

Figures 5.14 and 5.15 finally show the obtained relative sensitivities from both methods for both the *glass ball* and the *iron ball* sensor. For a better comparison, the values for the frequencies used in the *gated burst* method are also shown in table 5.2. (The 60 kHz data point for the *glass ball* measurement with the *gated burst* method is missing due to corrupted data files.) Both methods show excellent agreement within their respective errors. It can also be seen that for the *gated burst* method, for high frequencies the uncertainties are well below those of the *single pulse* method. At low frequencies, however, they increase drastically due to ambient acoustic background in the water basin. While the uncertainty in the *single pulse* method is rather large in comparison, apart from some gaps it yields a full sensitivity spectrum with the same amount of measurement time. By proper choice of the input signal and a more elaborate analysis technique including an independent noise spectrum estimate these can be avoided as shown in section 7.2 and [Fis06]. In principle, both methods also allow to derive the phase relation between the acoustic and the electric signal. This has not been attempted since no information on the phase response is available for the reference device.

In addition the *equivalent self noise* spectrum was calculated – which is the self noise spectrum of the sensor divided by the sensitivity spectrum. It gives a measure of the acoustic signal amplitude needed at a certain frequency to overcome the self noise of the sensor. Electronic self noise spectra were recorded for all sensor in an acoustically well isolated environment. To obtain absolute values, a frequency independent sensitivity of -163.3 dB rel. $1 \frac{\text{V}}{\mu\text{Pa}}$ for the frequency range from 5 kHz to 65 kHz was assumed for the reference hydrophone as specified by the manufacturer. In order to obtain comparable numbers, also the *equivalent self noise* level was obtained by an inverse Fourier transform of the *equivalent self noise* spectra in the range given above. The *equivalent self noise* level is then given by the RMS signal amplitude in the time domain and listed in table 5.3. These absolute values should be taken with care. In a later recalibration of the reference hydrophone [Fis06] for the cali-

	Hydrophone	Glass Ball	Iron Ball
σ_{noise} [mPa]	40.3 ± 8.3	15.9 ± 1.7	4.7 ± 0.7

Table 5.3: Equivalent self noise level in the frequency range from 5 – 65 kHz.

bration measurements in chapter 7 a significantly lower sensitivity of -168 ± 1 dB rel. $1 \frac{\text{V}}{\mu\text{Pa}}$ was obtained. Nevertheless, in water, the *iron ball* and *glass ball* sensor not only show a $\mathcal{O}(10^2 - 10^3)$ times higher sensitivity than the reference hydrophone, which can be mainly attributed to a higher amplifier gain, but also a better signal-to-noise ratio, and hence a lower detection threshold. On the other hand, they show a very non-uniform sensitivity spectrum (and also phase shift spectrum) with large fluctuations even in small frequency ranges.

Yet, most important, the *single pulse* method was shown to give a reliable and fast calibration method, which could be further exploited for calibration of all 75 channels of the SPATS setup that is described in chapter 7.

5.3.3 Evaluation in ice

While even a calibration in water was not possible in standard laboratory conditions due to the required large water tank, an evaluation of the sensor properties in ice is even more difficult. Three major problems arise, that could not be easily circumvented :

- Compared to water, the velocity of sound in ice is larger by around a factor of three, increasing the wavelength at a fixed frequency by the same amount. To retain free-field conditions in the same time window as in the water measurement, three times the dimensions of the test volume are required, i.e. an ice volume of at least $5 \text{ m} \times 5 \text{ m} \times 5 \text{ m}$. Natural occurrences of these dimensions, e.g. in glaciers, are typically remote and not well suited for continuous testing and development purposes. For production of ice in the laboratory, two freezers capable of cooling down to -28°C and -85°C , respectively, have been available. It is the dimensions of these freezers that constrain the dimensions of the possible test containers to $140 \text{ cm} \times 35 \text{ cm} \times 45 \text{ cm}$ and $120 \text{ cm} \times 40 \text{ cm} \times 50 \text{ cm}$ respectively. Commercially available ice blocks were also not found in significantly larger dimensions. With containers being made either of wood or aluminium and thin walls compared to the wavelength, in both containers close to total reflection occurs at the container boundaries. Even if sensor and transmitter are placed right next to each other, the reflected signal will not be delayed by more than 0.1 ms , corresponding to one wavelength at 10 kHz . Reducing the reflectivity as in anechoic chambers by uneven surfaces will also not work since for effective scattering the structures need to be the same dimensions as the wavelength, leaving no space for installation of devices. Hence all signals recorded in small ice volumes are heavily affected by signals reflected from the boundaries.
- Secondly, if a water-filled container is cooled below zero, under normal conditions freezing will start from above, trapping the dissolved gases and salts in the water below the surface. Normally these are not embedded in the ice crystals and their concentration increases with continued freezing. Finally, the concentration will exceed the solubility, leading to oxygen bubbles and salt grains. Being usually small compared to the wavelength, it is not the single bubbles or grain, but their sheer density that may significantly inhibit sound propagation. Furthermore, with a melting enthalpy of water of $333 \frac{\text{kJ}}{\text{kg}}$, complete freezing of the water volumes introduced above will take \approx

80 MJ. Together with the rather small heat conductivity of $2.33 \frac{\text{W}}{\text{mK}}$ the corresponding freezing time is on the order of one week. So even in these small volumes, clear ice is not easily obtained. In contrast to water, sensors and transmitter cannot be moved in a frozen ice block, so this severely limits the possibilities to realise different configurations. Furthermore, the low heat conductivity also limits the possibility of temperature dependent measurements. For a 5°C change in temperature, roughly 12 hrs are needed to achieve a good new thermal equilibrium of the whole ice block.

- So far no calibrated acoustic transducers, neither sources nor receivers were found to exist. Using the *reciprocity calibration* method introduced above, this could be circumvented. However, realisation of the three different configurations is a considerably larger effort than in water due to the long freezing times. No absolute calibration has therefore been possible so far.

Despite these problems, a number of results revealing some basic characteristics of the sensors have been achieved in laboratory tests and will be outlined in this section.

Ice preparation

Various attempts have been made to achieve bubble-free ice [Ste04, Kri06]. Finally, a method was used similar to what is described in [GP81]. In order to avoid trapping of the gas in the water volume, the container is insulated at the top, while good heat conductivity is arranged from the bottom. This way, despite the anomalous density gradient of cold water, the growing of the ice will start at the bottom. As the solubility of oxygen in water increases with decreasing temperature, this alone will not resolve the problem – bubbles will still build at inhomogeneities in the ice crystal surfaces. Trapping of these bubbles in the growing ice can be avoided by agitating the water, e.g. with a pump. The gas bubbles will be mechanically removed by the water current and brought to the surface.

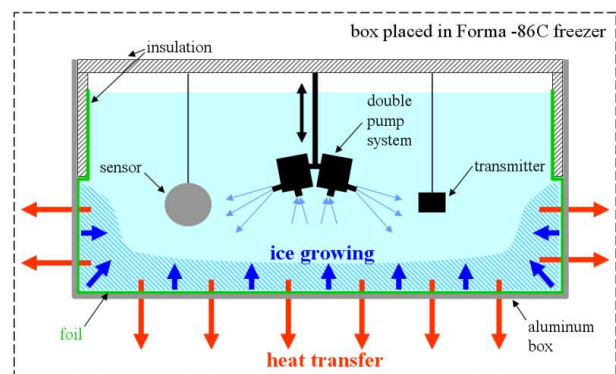


Figure 5.16: Setup for growing large blocks of clear ice (from [Kri06]).

As shown in figure 5.17, small samples of clear ice can be quickly obtained with this method. For larger ice blocks, a dedicated setup was developed that is shown in figure 5.16. Two pumps with a combined flow of $\approx 5000 \frac{\text{dm}^3}{\text{hrs}}$ were needed to get the necessary water circulation. To prevent the freezing of water in or unwanted heat input from supply pipes, both pumps are directly operated in the water, requiring adjustments of the pump positions with growing ice thickness. Due to the space required for the pumps, the water volume cannot be completely frozen – after a sufficient amount of ice has grown, the remaining water is removed and the surface can be made even by melting surmounting parts. Using



Figure 5.17: Clear ice from a small test volume (from [Kri06]).



Figure 5.18: Epoxy sensor in a ≈ 40 cm thick block of clear ice (from [Kri06]).

this technique, about 40 cm high blocks of very good ice clarity could be obtained. Figure 5.18 shows an *epoxy sensor* in such an ice block with a weight at the bottom for stable positioning.

Signal generation

In absence of a calibrated reference, characteristics of the sensors may be obtained if details about the emission of the transducer are known. A prediction of the absolute magnitude of stress and shear waves generated in ice would involve detailed modelling of the piezo-ceramics, the ice and the container. Some basic properties can be derived from a simplified model. As long as frequencies are below the resonant regime, one is in the quasi-static case where the *PZT* element reacts on an applied voltage quicker than the timescale on which the voltage changes. Taking the upper part of equation 5.1 and in the absence of stress,

$$u = l \cdot S_\alpha = d_{i\alpha} E_i \cdot l = d_{i\alpha} U_i \quad (5.12)$$

for a height l of the *PZT* ceramic. The total deformation length u , i.e. the displacement of the surface elements of the ceramics, is proportional to the applied voltage. Using NEWTON'S law the normal force F^n exerted on a small volume element of mass m in front of the moving surface depends on the mechanical displacement as

$$F^n = m \cdot \ddot{u} \propto \ddot{U} . \quad (5.13)$$

If the *PZT* element is in a medium, deformation is of course not free, but some stress will occur. The reduction in deformation it causes is small relative to the deformation of the piezo-electric ceramic. This can be seen from the significantly lower impedance of water and ice than for *PZT* (see table 5.1). So the approximation of no stress as in equation 5.12 is still valid¹. For frequencies below the resonant regime, the amplitude of the stress wave

¹Consider in contrast a ceramic rigidly clamped in polarisation direction, for which the strain $S_3 = 0$ and from equation 5.1 the stress $T_3 \propto E_3 = Ul$.

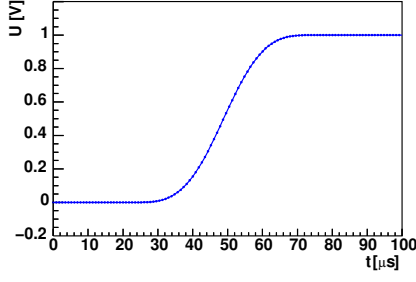


Figure 5.19: Electric signal applied at a *PZT* element.

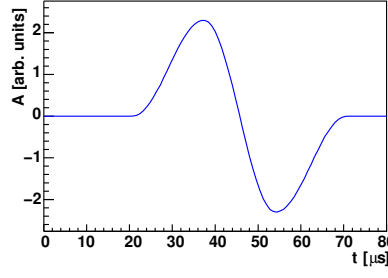


Figure 5.20: Emittted acoustic signal.

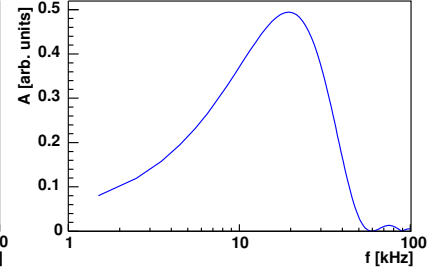


Figure 5.21: Spectrum of acoustic signal.

travelling through the medium will thus be proportional to the second time derivative of the applied voltage signal at the *PZT* element.

For a continuous single-frequency signal, reflections at the container boundaries will lead to steady phase relations at each point of the volume, i.e. standing waves with a varying amplitude throughout the volume. In principle, different sensors could be compared by mounting them at the exact same positions, but the mounting accuracy is limited and the sensor itself will partially reflect the waves, influencing the interference pattern. Again, short pulses are needed instead. Following equation 5.13, a short bipolar pulse will arise from a smoothed step function, which can be generated by an *arbitrary function generator*. For an applied signal

$$U(t) = \begin{cases} 0 & \text{for } t - t_0 < 0 \\ U_{in}(1 - \cos(\frac{2\pi}{\tau}(t - t_0))) & \text{for } 0 < t - t_0 < \frac{1}{2}\tau \\ U_{in} & \text{for } \frac{1}{2}\tau < t - t_0 \end{cases} \quad (5.14)$$

shown in figure 5.19 and equation 5.13, the acoustic signal shown in figure 5.20 is obtained. The characteristic length of the pulse is given by the rise-time of the step function τ , which also determines the peak frequency $f_{peak} = \tau^{-1}$ of the spectrum of the emitted acoustic signal shown in figure 5.21. Being short in the time-domain, these signals need to span a certain range in the frequency domain, yet it is dominated by a comparatively small range around f_{peak} . This can be used to probe the frequency dependent behaviour of different sensors. In practice, also other effects such as varying electrical output impedance of the function generator will influence the actual emitted signal and spectrum, so that in absence of a detailed model results should be interpreted qualitatively instead of quantitatively.

To avoid effects of interference from the reflected pulse and the direct signal, the amplitude of the first peak of the acoustic signal is taken as a measure of the sensor response. Figure 5.22 shows the result of a measurement in the small water tank used for ice preparation. For three different sensor types mounted in the same position relative to a piezo-ceramic transducer the amplitude of the first peak of the signal is given in dependence of the peak frequency. $\ddot{U} \propto 1/\tau^2 = f_{peak}^2$ is obtained from equation 5.14, so that the acoustic signal strength increases with frequency if $U_{in} = \text{const.}$ While for low f_{peak} , the response of all three sensors is similar, at higher frequencies the *glass bowl* sensor shows significantly lower response. This may well be an effect of a very low resonance frequency because of geometric

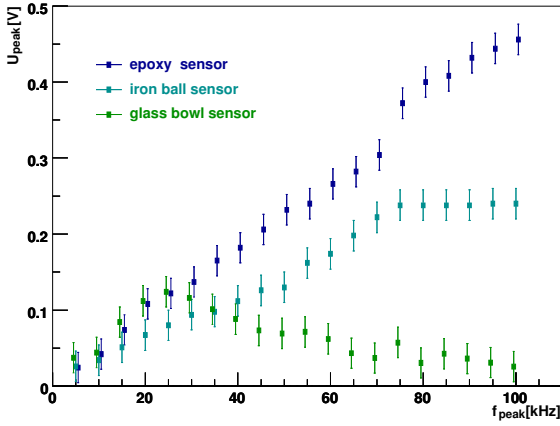


Figure 5.22: Signal amplitude of 1st peak vs. peak frequency for the *iron ball*, *glass bowl* and *epoxy sensor* for $U_{in} = 0.2$ V in water (from [Ste04]).

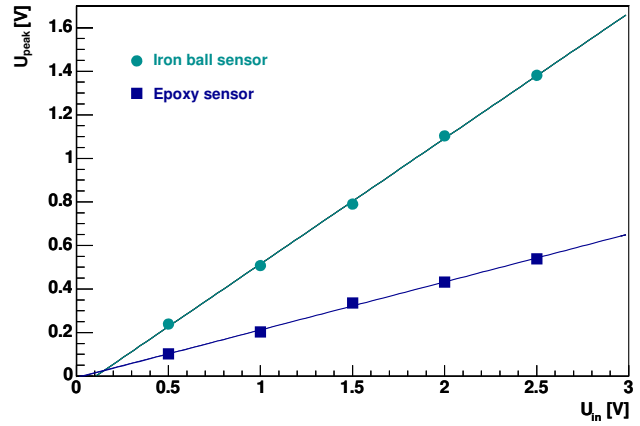


Figure 5.23: Signal amplitude of 1st peak vs. input peak amplitude for the *iron ball* and *epoxy sensor* for $f_{peak} = 25$ kHz in ice (from [Ste04]).

dimensions much larger than those of the other two. In any case, for the purposes considered here, this behaviour is undesired. In figure 5.23 the scaling of the amplitude of the first peak of the signal with the input signal amplitude U_{in} is shown for a configuration in a small ice volume. As can be seen from equations 5.13 and 5.14, the dependence is linear, showing that all components such as amplifiers, elastic deformation of the ice and piezo-ceramics, etc. are well within their linear regime. So for a constant acoustic signal shape a linear dependence of the electric signal amplitude is always expected. The effect of impedance matching is also nicely demonstrated in figures 5.22 and 5.23. From equation 5.4 and table 5.1 for a perpendicular incident wave the transmittivity $t = 1 - r$ at the steel-medium interface decreases by $\approx 60\%$ if changing from ice to water. For epoxy it increases by $\approx 40\%$. As a consequence, in water the *epoxy sensor* gives larger signals, while in ice the sensitivity of the *iron ball* sensor is higher.

Ideas for calibration in ice

As mentioned before, no absolute sensitivity for any of the developed acoustic sensors could be derived so far in ice. Some ideas to circumvent the problems listed on page 80 shall be outlined here. One of the major problems resides in obtaining (approximate) **free-field conditions**. The obvious solution of accessing a large enough volume of ice, such as a glacier or the south polar ice sheet itself is typically prohibitive not only for remoteness reasons. Also installation of the device in a depth of several metres requires substantial technical efforts, and even more the subsequent retrieval. To alleviate the reflection problem also in smaller test volumes, two methods have been thought of:

- Instead of the rather omnidirectional emission of a standard *PZT* element, a source with a higher directivity can be used. If the acoustic signal is emitted only in a small beam in one direction, significant extensions of the test volume are only required in that direction. Therefore, a strongly focused emitter has been developed as is described in [Kri06]. A parabolic mirror from stainless steel shown in figure 5.24 is used to

focus the acoustic emission of a small piezo-ceramic disc in a narrow region along the symmetry axis. An emission pattern in the plane through the symmetry axis has been obtained in a water setup by turning the source with respect to a fixed *epoxy sensor*. For a test in ice, three *epoxy sensors* were mounted at different angles with respect to the source instead. The results of the measurements given in figures 5.25 and 5.26 show a high degree of focusing in both cases. In an ice block of 40 cm width at a sensor-transmitter distance of 30 cm only acoustic emission from a polar angle of larger than 60° will reach the receiver after only one reflection. From figure 5.26 a reduction of the transmitted amplitude to less than 20 % of the directly transmitted signal can be expected.

- Instead of trying to avoid interference by signals reflected at the volume boundaries, one can also try to subtract them from the measured signal. To disentangle them from the direct signal, mathematical modelling could be used, which requires good knowledge of the boundary conditions and will be difficult, e.g in case of uneven surfaces. The reflected part in a signal may also be accessed experimentally by changing the boundary conditions of the volume. At an ice-air boundary, for example, the reflectivity will be close to 1.00, while at an ice-water boundary it can be as low as 0.42. For a single configuration, only signals reflected at fixed angles from the source will reach the sensor directly after reflection. So by changing the boundary conditions, the reflected part of the acoustic amplitude at the sensor – which is the superposition of the direct and reflected signals – will be reduced by a fixed factor, but will not be altered in phase relation. From two measurements with an ice block hoisted in air and submerged in a water basin (which itself needs to be large enough), by subtraction of the signals the reflected part scaled by the change in transmittivity will be obtained. Scaling to unity and subtraction from the signal measured while in air should then reveal the direct signal without first order reflected signals. An effective increase of the free-field volume by a factor of three in all dimensions should be obtained this way.

While both of the above might resolve the limitations imposed by small ice volumes, they will not solve the problem of a missing **reference** for an absolute calibration. As outlined in section 5.3.1, the standard approach to this problem is the reciprocity calibration method. To use the *PZT* element of a sensor also as a source it cannot be stimulated through an amplifier stage. Either the amplifier stage needs to be bypassed for the transmit mode or very large signal amplitudes have to be used. In both cases, the amplifier will not, or only in receive mode, be part of the calibration process, so that its properties need to be well known in advance. Another issue arises from the realisation of the different source-receiver configurations, which may be very time-consuming for freeze-in times if deployed in a large natural ice volume or ice block production times in lab-sized setups. Furthermore for



Figure 5.24: Directional acoustic emitter with parabolic reflector (from [Kri06]).

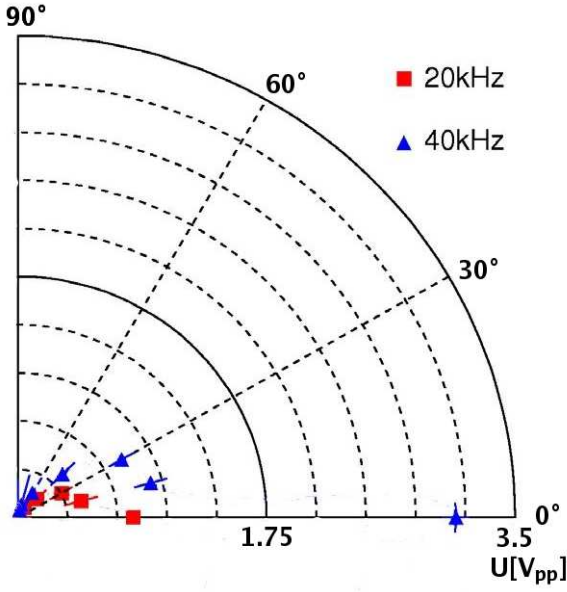


Figure 5.25: Amplitude of acoustic signal vs. polar angle in a water setup for $f_{peak} = 20$ kHz and $f_{peak} = 40$ kHz (from [Kri06]).

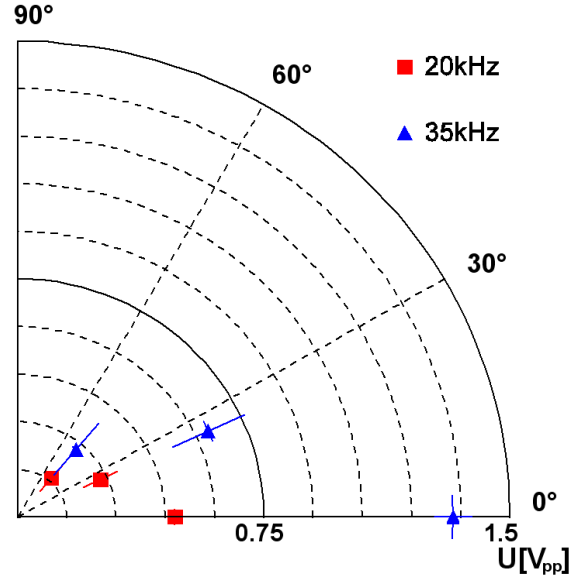


Figure 5.26: Amplitude of acoustic signal vs. polar angle in an ice setup for $f_{peak} = 20$ kHz and $f_{peak} = 35$ kHz (from [Kri06]).

deployment in a large volume, the transducers may not be retrievable. For a cylindrical symmetric sensor, e.g. as build from a hollow piezo-ceramic cylinder, one solution may reside in a triangular configuration of the three acoustic transducers. If the sensitivity is independent of azimuthal angle, in an equilateral triangle the propagation term in equation 5.10 should be alike for all three sides. If all three acoustic transducers can be operated as sensors and transmitters, the system of six equations will even be overconstrained, so that systematic effects due to orientation might be revealed.

Such a configuration still needs a $\mathcal{O}(\text{m}^3)$ sized ice block to avoid large impacts of close transducer spacing. For small ice blocks absolute amplitudes may be obtained by an independent measurement of the deformation on the surface of the ice block. Surface mounted sensors as in non-destructive testing applications may yield good results here, but will probably need theoretical modelling to obtain sensitivities valid in ice applications. A contactless method to measure surface deformation is provided by a *laser vibrometer*: A laser beam is split in two parts, one of which is reflected on the testing surface. By the changing phase relation of the two beams, from the interference signal the deformation of the surface can be deduced. Laser vibrometers are commercially available either as single point devices or as scanning laser vibrometers where deformation of a whole area is scanned consecutively. Yet with a sensitivity to deformation of a fraction of the laser wavelength of $\mathcal{O}(100 \text{ nm})$, only large acoustic signal amplitudes may be measured this way.

So while an absolute sensitivity calibration of acoustic in-ice transducers is not impossible, substantial efforts are required that could not be taken within the frame of this work.



Figure 5.27: Transmitter with a cylindrical *PZT* element cast in epoxy.



Figure 5.28: Transmitter with a ring-shaped *PZT* element sealed with o-rings.

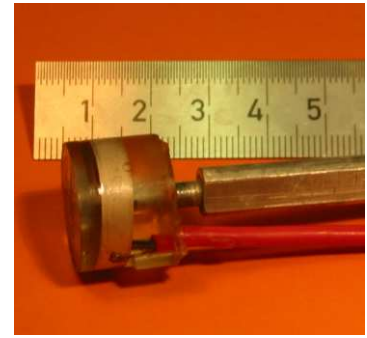


Figure 5.29: Transmitter with a ring-shaped *PZT* element cast in epoxy.

5.4 Transmitter

Apart from suitable sensors, also acoustic transmitters are needed – not only for the evaluation of the sensor properties as described above, but also for probing the ultrasonic ice properties as will be discussed in chapter 7. Depending on the purpose, different attributes may be required from a transmitter, such as directed or isotropic emission, a single frequency or a broad spectrum.

In contrast to a sensor, where small acoustic signals require an amplifier close to the *PZT* element, applying voltages of $\mathcal{O}(1\text{ V})$ directly to the piezo-electric ceramic will give acoustic amplitudes sufficient for laboratory applications. *PZT* based sources are thus most easily produced by attaching electric contacts to a *PZT* element. For testing in water, also an electrical insulation is useful. Figures 5.27 to 5.29 show three transmitter models. In figure 5.27 a cylindrical piezo-ceramic of 16 mm diameter and 3 mm thickness is contacted with copper foil on both sides and cast in epoxy for insulation and equipped with a polyurethane handle for better mounting and handling. This will introduce resonances at the frequencies corresponding to the dimensions of the epoxy and handle. Electrical insulation by means of o-ring seals has been tried for the 20 mm diameter and 5 mm high thick radially polarised ring-shaped ceramic shown in figure 5.28. Two end-caps with the o-rings in the same size as the *PZT* ring are pulled together by a screw with the ring in between. While very loud acoustic signals could be generated with this device, for large signal amplitudes the system did not prove to be water-tight, probably due to leakage between the o-rings and the vibrating piezo-ceramics. Ring-shaped ceramics have some advantages, so that in order to use them again they have been cast in epoxy as shown in figure 5.29. Dimensions and polarisation directions are summarised in table 5.4.

For an isotropic emitter, the signal amplitude will fall inversely proportional to the distance from the source. For a long range transmitter therefore very large acoustic signals are needed. Again *PZT* ceramics are well suited as they can be driven linearly with signals up to $\mathcal{O}(\text{kV})$. This is shown in figure 5.30 for a ring-shaped ceramic in water. The electric input pulse is generated by a large inductance ($L = \mathcal{O}(\text{mH})$) of a low resistance R , through which for a short time $\tau_{\text{charge}} > R/L = \mathcal{O}(\text{ms})$ a large current is driven. The current is switched by a power transistor in series with the coil, to which the *PZT* ceramic is connected in parallel.

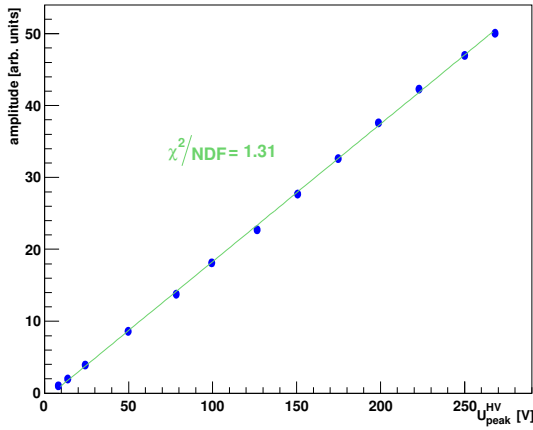


Figure 5.30: Acoustic signal amplitude vs. peak electric input amplitude for a ring-shaped piezo-ceramic in water.

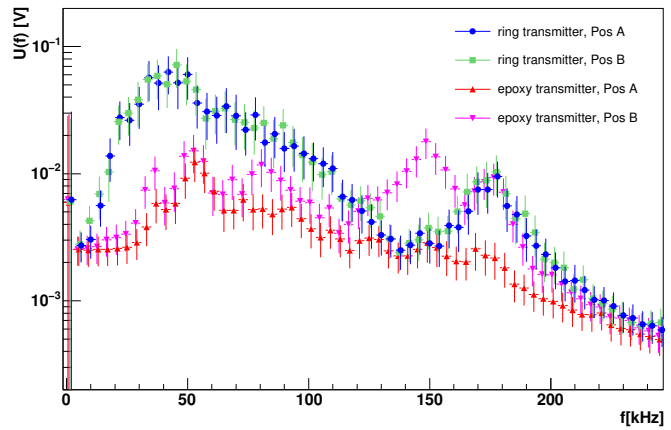


Figure 5.31: Acoustic signal spectrum of ring-shaped and cylindrical *PZT* emitters activated by a white noise electrical signal at different geometric configurations.

When switched off, the magnetic flux in the coil will self-induce a short voltage spike of time $\tau_{\text{discharge}} = Z_{\text{piezo}} \cdot C_{\text{piezo}} = \mathcal{O}(10 \mu\text{s})$ at the piezo-electric element, similar to the pulse shown in figure 7.13. The amplitude of the high-voltage signal $U_{\text{peak}}^{\text{HV}}$ will scale linearly with the magnetic flux and thus linear with the charging voltage of the coil, as has been verified with a high resistance voltage divider in parallel to the piezo-ceramic. This way very large acoustic signals can be generated.

Determining the emissivity, e.g. from the inverse of transfer matrix introduced above, is of course as difficult as measuring the sensitivity itself. Yet one advantage that can be exploited is the large voltages that can be applied to a transmitter. This can be used to circumvent the free-field problem in small volumes. In a continuous white noise signal, the phases of the single frequency components are randomly distributed. Thus no steady waves can build and each position in the system is alike. The frequency spectrum of the signal emitted by the ceramic to which the white noise signal is applied will be altered by the impedance characteristics of the ceramics.

Figure 5.31 shows the result of a measurement with the reference hydrophone at two positions, for both the ring-shaped and cylindrical transmitters introduced above. At both positions, the obtained spectra agree well. The source of the deviation at around 150 kHz for the cylindrical transmitter are unknown, but due to the limited white noise amplitude that could be generated by the *arbitrary function generator*, the signal-to-background noise amplitude of the measurement was comparatively poor. The result also incorporates the frequency response of the reference hydrophone, that is flat only up to 65 kHz. Still, a significantly higher emission of the larger ring-shaped ceramic in the 20 – 100 kHz band is observed.

Not only the frequency spectrum, but also the emission pattern of a piezo-ceramic transducer depends on its geometry. Figure 5.32 shows the amplitude of the first peak of the signal for a pulsed excitation with $f_{\text{peak}} = 25 \text{ kHz}$ versus the polar angle, i.e. the angle relative to the symmetry axis of the cylinder. Three different cylindrical ceramics with the dimensions

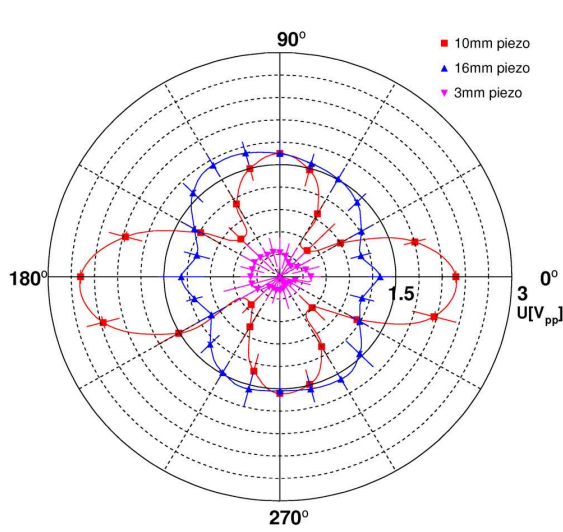


Figure 5.32: Pulse amplitude vs. polar angle of cylindrical ceramics for different ceramic diameters (from [Kri06]).

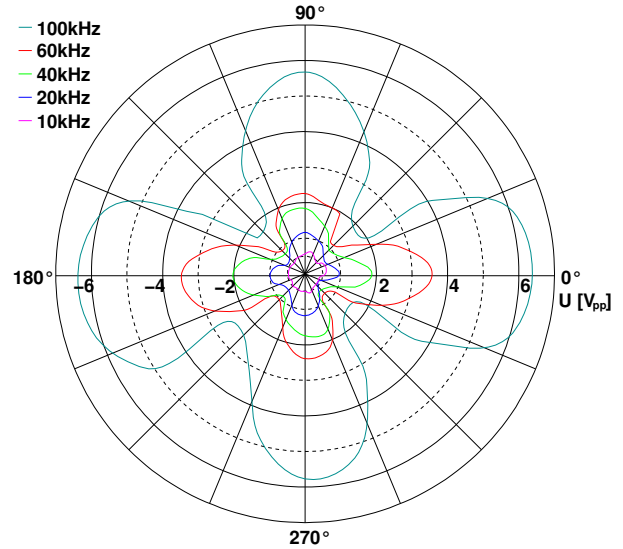


Figure 5.33: Pulse amplitude vs. polar angle of cylindrical ceramics for different values of f_{peak} (from [Kri06]).

given in table 5.4 have been used. For the smallest ceramic with geometric dimensions well below the wavelength of the acoustic signal the emission is more or less isotropic. For larger *PZT* ceramics the emission is mainly focused in the directions along and perpendicular to the symmetry axis. This can be thought of as an interference of the signals of acoustic waves emitted at different points of the surface of the ceramics. The effect also strongly depends on the frequency of the emitted signal. Figure 5.33 shows the amplitude of the first peak versus the polar angle for a 10 mm diameter ceramic for different values of f_{peak} . For small values of f_{peak} , i.e. for wavelengths significantly larger than the ceramics dimensions, again nearly isotropic emission is obtained, while with increasing f_{peak} the emission pattern becomes more and more distinct. For the transmitter with the ring-shaped ceramics polar and azimuthal emission pattern are shown in figures 7.15 and 7.16. Especially in the polar planes the emission is much more isotropic.

This is also reflected in the change of the signal amplitude with distance. For an isotropic source, due to energy conservation the intensity will fall as $1/d^2$ with increasing distance d , so that the amplitude will only fall as $1/d$. Figure 5.34 shows the peak-to-peak signal amplitude versus inverse distance for the ring-shaped transmitter measured with the reference hydrophone in a large water tank. As shown by the fit, the $1/d$ dependence is well described

	ring	cylinders			
outer diameter	20 mm	16 mm	10 mm	3 mm	
inner diameter	18 mm	—	—	—	
height	5 mm	3 mm	5 mm	5 mm	
polarisation direction	⊥	∥	∥	∥	

Table 5.4: Geometry and polarisation direction with respect to the symmetry axis for the different *PZT* elements.

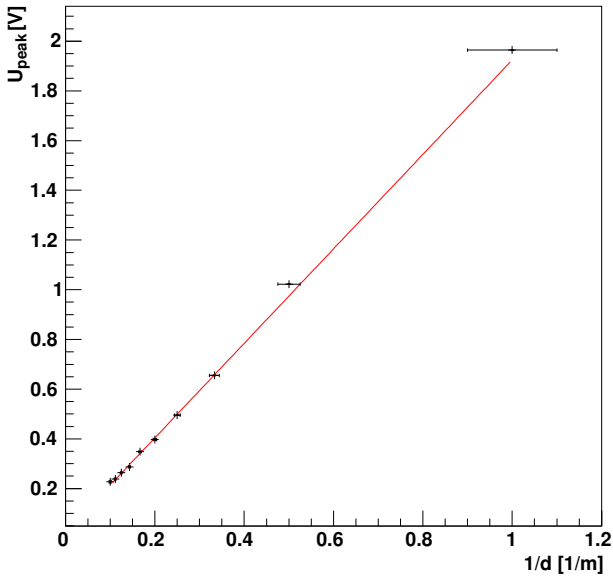


Figure 5.34: Signal amplitude vs. inverse distance for a ring-shaped ceramic in a large water tank (from [Fis06]).

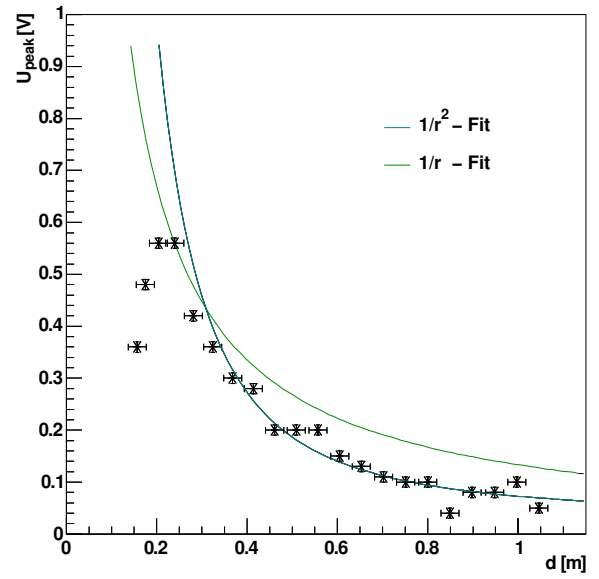


Figure 5.35: Signal amplitude vs. distance for a surface mounted transmitter on a small ice block (from [Ste04]).

by the data. In ice, again, as the source-receiver distance cannot be changed, such a measurement is not as easily obtained. Different distances in such a configuration can most easily be obtained by using a *PZT* element as a surface mounted transmitter. Good coupling to the ice even on uneven surfaces is achieved by melting a thin layer of ice before putting the piezo-ceramic in place. It will then freeze to the ice block, and provide sufficiently large acoustic signals if weighed down with an additional weight. The result of such a measurement is shown in figure 5.35, where signals were recorded with an *epoxy sensor* centrally mounted in the ice block and pointing horizontally. In contrast to the water measurement, here the amplitudes cannot be well described by a $1/d$ dependence, since the anisotropic sending and receiving efficiencies of both the *epoxy sensor* and the *PZT* element have to be taken into account. At close distances, the acoustic wave is travelling perpendicular to the symmetry axis of the *epoxy sensor*, where it needs to traverse ≈ 1 cm of epoxy resin before reaching the sensitive element. At larger distances, the direct acoustic signal will be emitted under a larger angle from the *PZT* element, where emission efficiency is smaller as shown in figure 5.33.

In summary, evaluation of *PZT* based transmitters in ice reaches similar limitations as evaluation of the ultrasonic sensor. Nevertheless, high sensitivity receivers and powerful transmitters could be achieved. An independent verification of their properties might be obtained by using an independent, well understood excitation mechanism. Apart from piezo-ceramics, ultrasonic signals can e.g. also be generated thermo-acoustically, as will be shown in the next chapter 6. For water, the mechanism is believed to be understood well enough that first calibration efforts based on thermo-acoustically generated sounds have been attempted [dBC06]. In ice instead, the primary goal first had to be the verification of the thermo-acoustic model.

Chapter 6

Thermo-acoustic sound generation

For the verification of the Cherenkov light yield of charged leptons induced by high-energy neutrinos the neutrino interactions themselves are much too rare. Instead atmospheric muons at the same energies are used as a calibration source. The atmospheric muon flux has a steeply falling spectrum. Thus in the case of acoustic detection, no such alternative *test beam* of ultra-high energy deeply penetrating particles exists that could be used for in-situ signal verification.

In order to verify the thermo-acoustic model of sound generation introduced in section 3.4, some way of instantaneously depositing an energy of $\mathcal{O}(1\text{ J})$ inside a medium is needed. Instead of a single particle carrying all the energy, this can be achieved by a high-intensity beam of lower energy particles, such as photons, protons or electrons. In water, the principle features of the thermo-acoustic model have been tested before both with a proton beam [L⁺78, S⁺79, HJM⁺81b] and with a laser [HJM81a]. In solids, thermo-acoustic sound generation has been studied shooting an electron-beam on piezo-electric ceramics [Whi63, BBH⁺70, BH69] and protons [B⁺75] or laser pulses [WX02] on metal plates.

Again no measurements with ice targets were found to exist. Using both a proton beam and a *Nd:YAG* laser, extensive investigations in water and ice have been undertaken in collaboration with the ANTARES group of the University Erlangen-Nürnberg and a group from Uppsala University. After a brief introduction of expected signals from both methods, the results obtained in these tests will be summarised here.

6.1 Signal predictions

As shown in section 3.4, the thermo-acoustically generated signal – apart from material parameters such as speed of sound, specific heat capacity and expansion coefficient – solely depends on the spatial and temporal evolution of the energy deposit $\epsilon(\vec{r}, t)$. Relativistic particles will propagate close to speed of light in the medium, i.e. they cross the heated volume quasi-instantaneously, so that the energy deposit function $\epsilon(\vec{r}, t)$ can be split in a time and space dependent part:

$$\epsilon(\vec{r}, t) = \epsilon_r(\vec{r}) \cdot \epsilon_t(t) . \quad (6.1)$$

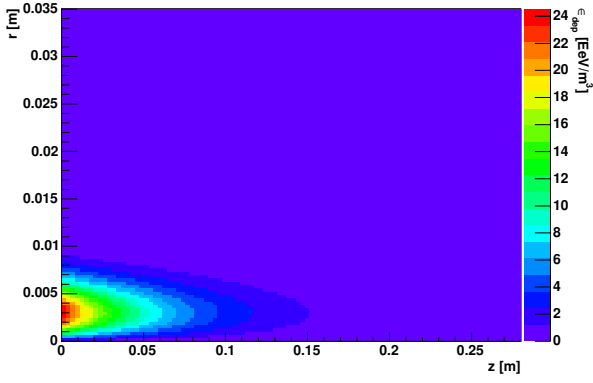


Figure 6.1: Calculated energy deposit as a function of radius r and distance z along the beam axis for a $Nd:YAG$ laser of 62.4 PeV per pulse in ice.

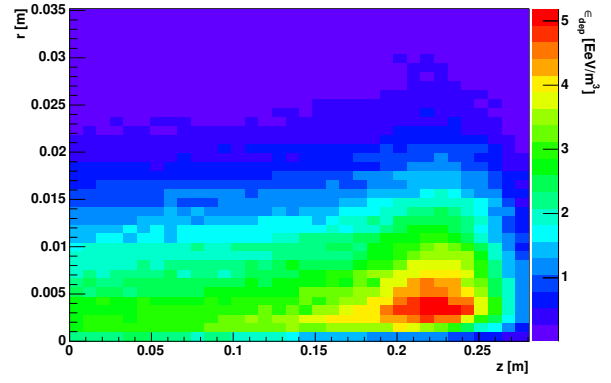


Figure 6.2: Simulated energy deposit as a function of radius r and distance z along the beam axis for a 38.7 PeV bunch of protons at 177 MeV in ice.

In many cases, the pulse durations $\tau_{\text{pulse}} \ll c_s \cdot d$ will be fast compared to the acoustic energy diffusion time over the size of the heated volume d , so that $\epsilon_t(t) \approx \delta(t - t_0)$ can be approximated as the delta function.

For the $Nd:YAG$ laser as a source, no secondaries are generated in the interactions of the photons, so that the spatial dependence $\epsilon(\vec{r})$ may be obtained analytically. Considering only the effective absorption length λ_{abs} and for a radial symmetric Gaussian beam profile of width σ_{beam} , the light intensity $I(\vec{r})$ is given by

$$I(\vec{r}) = I_0 \sqrt{\frac{2}{\pi}} \frac{\lambda}{\sigma_{\text{beam}}} \cdot \exp\left(-\frac{2(x^2 + y^2)}{\sigma_{\text{beam}}^2}\right) \cdot \exp\left(-\frac{z}{\lambda_{\text{abs}}}\right) \quad \text{with} \quad \vec{r} = \begin{pmatrix} x \\ y \\ z \end{pmatrix}, \quad (6.2)$$

where z is the direction along the beam. The absorption length at a wavelength $\lambda = 1064$ nm in water of $\lambda_{\text{abs}}(\text{water}) = 6.0 \pm 0.1$ cm [GAH⁺06] is very similar compared to $\lambda_{\text{abs}}(\text{ice}) = 5$ cm that has been measured in ice [GP81]. Figure 6.1 shows the corresponding energy deposit for a laser beam with $\sigma_{\text{beam}} = 6$ mm and a pulse energy of $E_{\text{pulse}} = 10$ mJ shot in an ice block. Qualitatively, the same distribution is expected in water with appropriate scaling of the z -axis.

For modelling the energy deposit from a proton beam, a simulation was done using the *GEANT4* simulation package. Ionisation energy losses and bremsstrahlung events were calculated for each of 10^4 protons individually. The result from a simulation of a $\sigma_{\text{beam}} = 3$ mm proton beam at a single proton energy of $E_{p^+} = 177$ MeV is shown in figure 6.2. While for the laser beam most of the energy is deposited right at the beam entrance, protons have the highest energy loss in the prominent Bragg peak at $z = 24$ cm for ice. The main difference in water is a higher density, that shifts the Bragg peak to $z = 22$ cm. So for both proton beam and laser excitation, the generated sonic field is supposed to be rather similar in shape for water and ice.

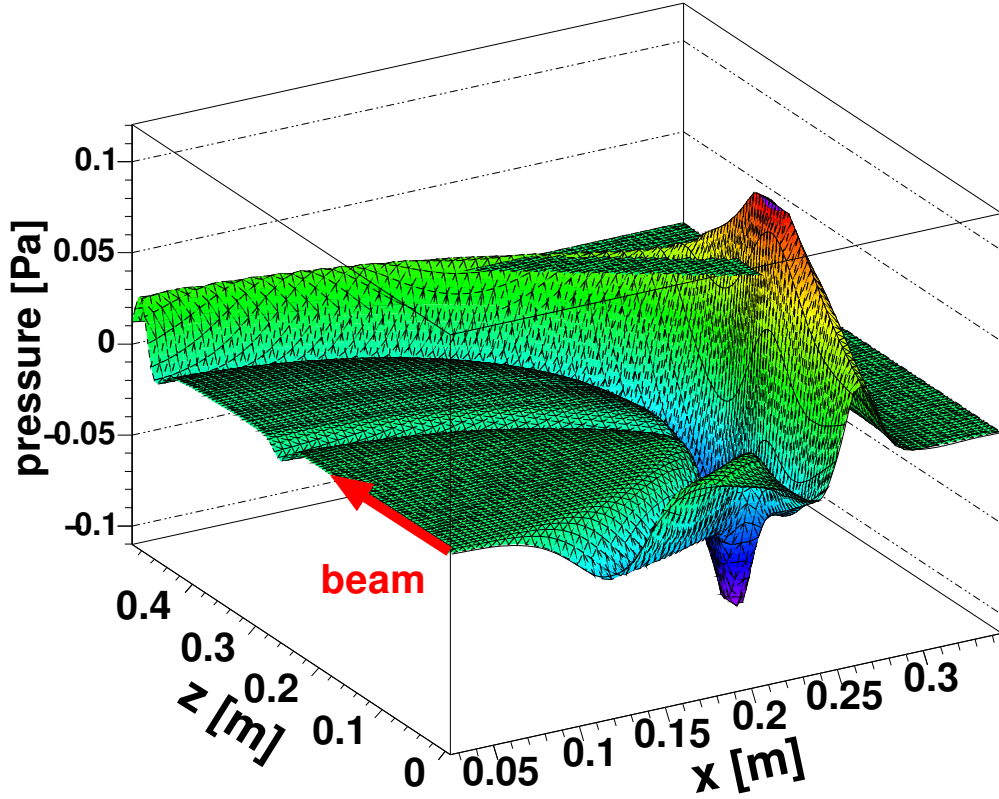


Figure 6.3: Acoustic amplitude as generated by a 177 MeV proton beam in water for a bunch energy of 18 PeV at the time $t = 0.2$ ms (from [Gra04])

By numeric integration of the thermo-acoustic equations 3.12 or 3.35, the energy deposit can be used to calculate the acoustic pulse amplitude as a function of time and position. For many accelerators, the *beam extraction time* or *spill time* τ_{spill} is of $\mathcal{O}(\mu\text{s})$ and must be taken into account. Figure 6.3 shows the sonic field that is generated in a water tank by the same proton beam assuming a Gaussian extraction profile with a width of $\tau_{\text{spill}} = 24 \mu\text{s}$. The sonic field is displayed as acoustic amplitude at the time $t = 0.2$ ms after the beam first enters the water volume. Two distinct contributions can be identified – from the point-like energy deposit in the Bragg peak, a spherical wave arises, that is overlaid by a second contribution confined in the plane perpendicular to the beam axis from the cylindrical source region before the Bragg peak. The maximum amplitude appears at a depth $z = 12$ cm along the beam axis.

6.2 Experimental results

As mentioned above, previous results have been obtained shooting proton beams and lasers in water. In [S⁺79], three sets of experiments at different accelerators with the characteristic properties given in table 6.1 are described. The resulting complementary set of data allowed to determine the basic dependencies of the generated acoustic signal on a wide number of variables. A linear relation of the acoustic signal with the beam energy could be established,

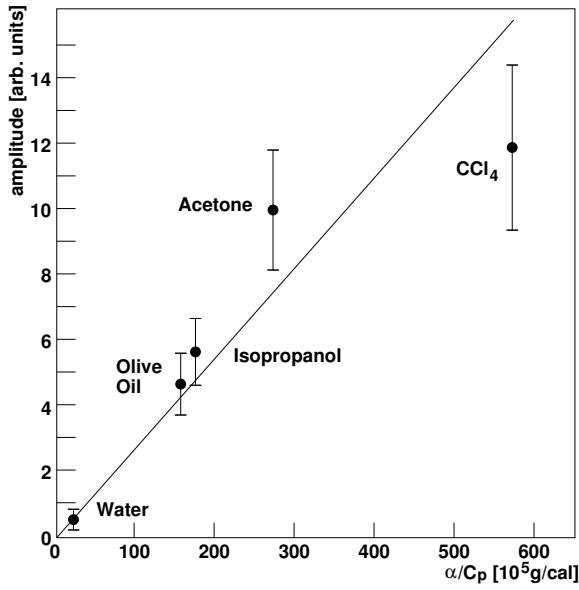


Figure 6.4: Acoustic signal amplitude from a proton beam for various materials, corrected for penetration depth (from [S⁺79]).

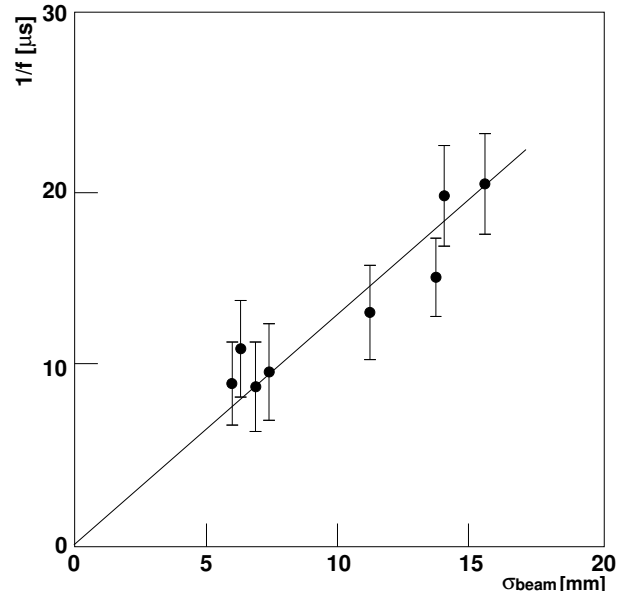


Figure 6.5: Characteristic frequency f as a function of beam width σ_{beam} (from [S⁺79]).

as well as a dependence on the beam spill time in accordance with the prediction. For the very short pulses from a linear accelerator (the *FEB* beam), where the spill can be considered instantaneous, also the expected linear scaling of the characteristic pulse period with the beam diameter could be demonstrated as shown in figure 6.5. Both linearity and dependence on beam diameter have also been independently confirmed by [A⁺01]. In [S⁺79], most notably, also the dependence on specific heat capacity C_p and the expansion coefficient α could be established by using different target materials. Figure 6.4 shows a linear dependence of the signal amplitude (corrected for the different penetration depth of the protons in the medium) with the ratio α/C_p , as expected. While this by itself is good evidence for the thermo-acoustic origin of the generated signals, in water also the temperature dependence of α can be exploited. Due to the anomaly of water, which has its highest density at $T = 4.0^\circ\text{C}$, the sign of α will be negative below that temperature. As a result, the acoustic signal will not only scale with $\alpha(T)$, but also vanish at 4.0°C and reverse its polarity below.

This effect has been confirmed in the same measurements by [S⁺79], but also by [HJM⁺81b]. However, in both cases the zero-crossing of the acoustic signal amplitude versus temperature was not observed at the expected value, but around 6°C . The authors of [HJM⁺81b] claim the existence of a tripolar acoustic signal of higher frequency, as e.g. proposed from collapsing micro-bubbles generated in the energy deposit [VP77]. A similar deviation has been found by the same authors in investigations with a laser beam [HJM81a], but with a reduced zero-crossing point at $2.5 - 3.0^\circ\text{C}$. In [HJM81a] also micro-bubble formation is given as a possible source of this deviation. By variation of the ambient pressure and thus of the boiling point of the water the authors of [S⁺79] exclude this as a source of acoustic signals.

So while the existence of acoustic signals due to the thermo-elastic effects in water has been well established, other sources of acoustic signals could not be unambiguously excluded.

Accelerator	E_{p^+}	E_{tot}	τ_{spill}	σ_{width}	Reference
BNL linac	200 MeV	$10^{19} - 10^{21}$ eV	$3 - 200 \mu s$	4.5 cm	[S ⁺ 79]
Havard cycl.	158 MeV	$> 10^{15}$ eV	$50 \mu s$	1 – 10 cm	[S ⁺ 79]
FEB linac	28 GeV	$> 10^{19}$ eV	$2 \mu s$	0.5 – 2.0 cm	[S ⁺ 79]
ITEP synch.	125/200 MeV	$10^{16} - 10^{18}$ eV	$0.07 \mu s$	1.0 – 4.5 cm	[A ⁺ 01, DL ⁺ 06]
AGS BNL	30 GeV	10^{23} eV	$1.5 - 3 \mu s$	0.9 cm	[HJM ⁺ 81b]
TSL synch.	177 MeV	$10^{16} - 10^{18}$ eV	$23 \mu s$	0.6 – 2.0 cm	[Gra04, GAH ⁺ 06], this work

Table 6.1: Properties of the proton beams used in the different experiments to verify the thermo-acoustic effect.

In a collaborative effort with the Universities of Erlangen-Nürnberg and Uppsala, therefore another set of experiments was conducted using more modern data acquisition techniques. The efforts of the group of Erlangen-Nürnberg University were thereby concentrated on precision measurements in the temperature range around 4 °C [Gra04], while the authors of [Ste04] and of this work investigated ice as a target medium. The 177 MeV-cyclotron at the THE SVEDBERG LABORATORY (TSL) was used for the investigations with a proton beam, providing intermediate values for spill time and beam diameter, as well as total bunch energies comparable to the other accelerators listed in table 6.1. Access to this beam facility was granted by the TSL experimental program committee, who approved a cumulative beam time of ≈ 60 hrs. Technical support in conducting the experiments was provided by the TSL operator team as well as the scientific staff at the Department of Radiation Physics at Uppsala University. Independent investigations with laser beams were also conducted by both groups for water [Sch05] and ice [Kri06], respectively. Results of both the efforts in water and ice will be presented here.

6.2.1 Water as a target

The setup used with a water target is shown in figures 6.6 and 6.9. A tank with the dimensions of 60 cm \times 60 cm \times 60 cm is filled with tap water. Several calibrated hydrophones are mounted on short poles and can be installed at variable positions by sledges gliding on a rail. The beam enters the water volume through a plastic tube inserted in the wall of the tank that are closed by a thin polyimide (*Kapton*) foil. This way, the point where the beam enters the water is moved from the container walls inside the volume, and reflections of the signal at the walls will be delayed accordingly.

To realise different temperatures, first two cooling elements of 240 aluminium tubes with 28.5 kg of ice at -30°C are inserted in the tank, bringing the temperature down to $\approx 1^\circ\text{C}$.

Laser	λ	E_{tot}	τ_{spill}	σ_{width}	Reference
<i>Nd:YAG</i>	1064 nm	$10^{17} - 10^{19}$ eV	8 ns	1 cm	[Sch05, GAH ⁺ 06]
<i>Nd:YAG</i>	1064 nm	$6.24 \cdot 10^{15}$ eV	6 ns	0.3 cm	[Kri06], this work

Table 6.2: Properties of the laser beams used to verify the thermo-acoustic effect.

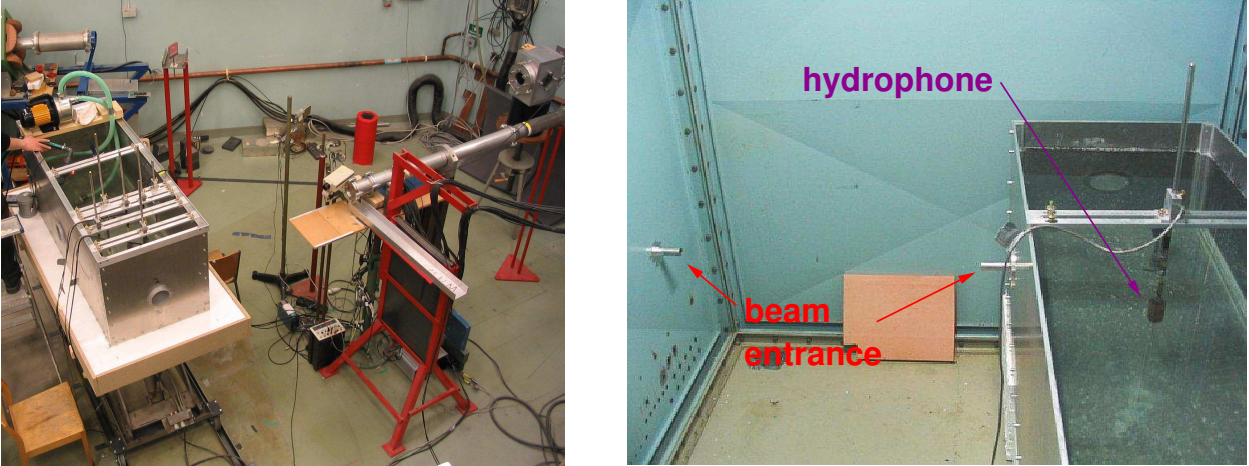


Figure 6.6: Picture of the water setup at the proton beam (from [Gra04], left) and laser beam (from [GAH⁺06], right).

After removal of the elements, the temperature of the water can be adjusted by controlled heating with an accuracy of 0.1 °C. Homogeneity is ensured by a pump quickly circulating the water.

The same setup has been installed, both at the cyclotron beam and a powerful laser, whose properties are given in table 6.2. Due to the high intensity of the laser, an optical absorber was introduced at the end of the beam line to avoid signals generated by the beam hitting the backwall of the water tank. The dependence of the signal on the water temperature for two hydrophone positions at the depth at and before the Bragg peak in 10 cm distance from the beam line is shown in figure 6.7 for laser excitation and in figure 6.8 for proton beam excitation. Both cases reveal a temperature dependence closely following

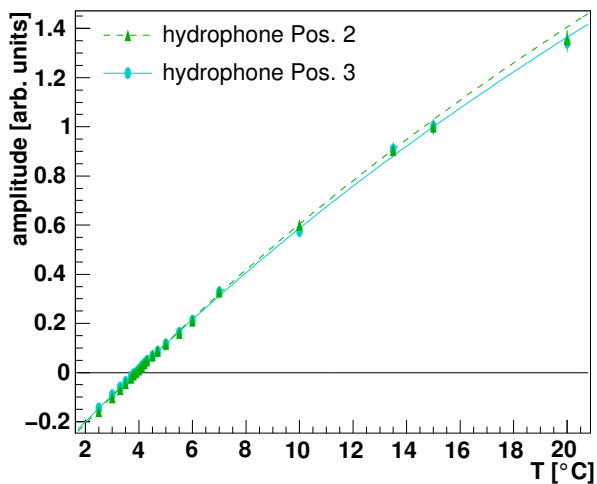


Figure 6.7: Temperature dependence of thermo-acoustic signal amplitude in water from a laser [GAH⁺06].

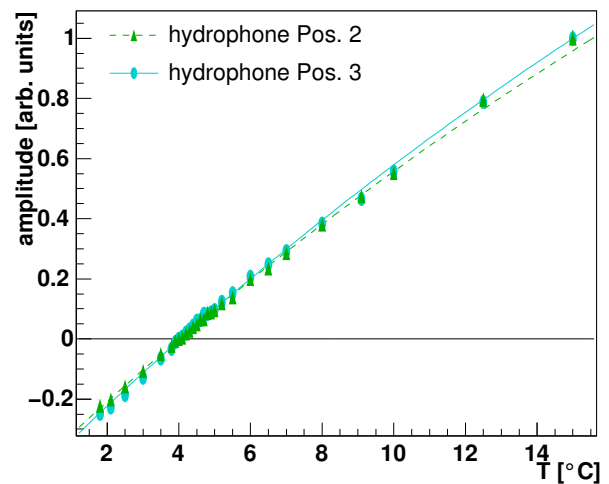


Figure 6.8: Temperature dependence of thermo-acoustic signal amplitude in water from a proton-beam [GAH⁺06].

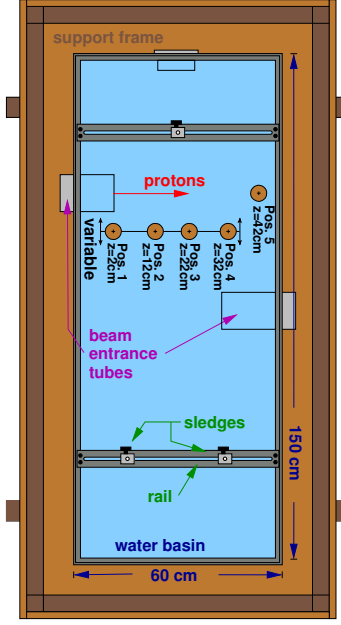


Figure 6.9: Schematic drawing of the setup in the water tank (from [Gra04]).

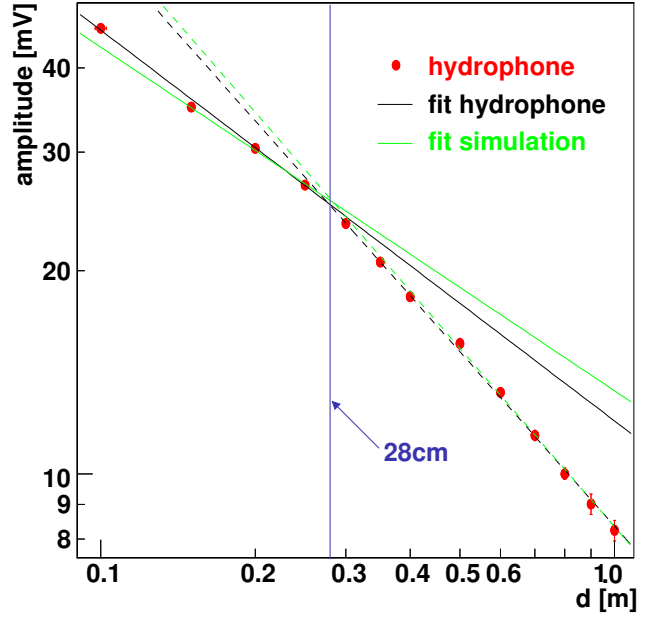


Figure 6.10: Signal amplitude vs. distance for the proton beam setup in water [GAH⁺06].

the expectations from a variation of the thermal expansion coefficient $\alpha(T)$. While for the laser beam, a zero-crossing at 4 °C was immediately observed, in the proton beam data a zero-crossing point at 4.5 °C is obtained [GAH⁺06] at first. In figure 6.8 the residual signal at 4 °C has been subtracted from the signals at all other temperatures. No signal at 4 °C is observed with the laser stimulation, indicating that the residual signal might be caused by the electrical charge deposited in the proton beam experiments [GAH⁺06].

Apart from the temperature dependence, the proton beam data fits the expectations from a purely thermo-acoustically generated signal very well. As an example, the signal amplitude as a function of the lateral distance to the beam direction is shown in figure 6.10 for the data taken at the proton beam and for a simulation. Close to the proton beam, in the near field of the emitting region, the peak signal amplitude from the cylindrical emission region is roughly proportional to $1/\sqrt{d}$. At larger distances, the emission region can be considered point-like in the far field approximation, causing a steeper dependence of $1/d$. This is only true for an ideally cylindrical emission region. Accurate exponents have been obtained from the simulation, with excellent agreement both in the near-field and in the far field. Figure 6.10 shows the results from a fit of the distance behaviour of the simulation and the experimental data.

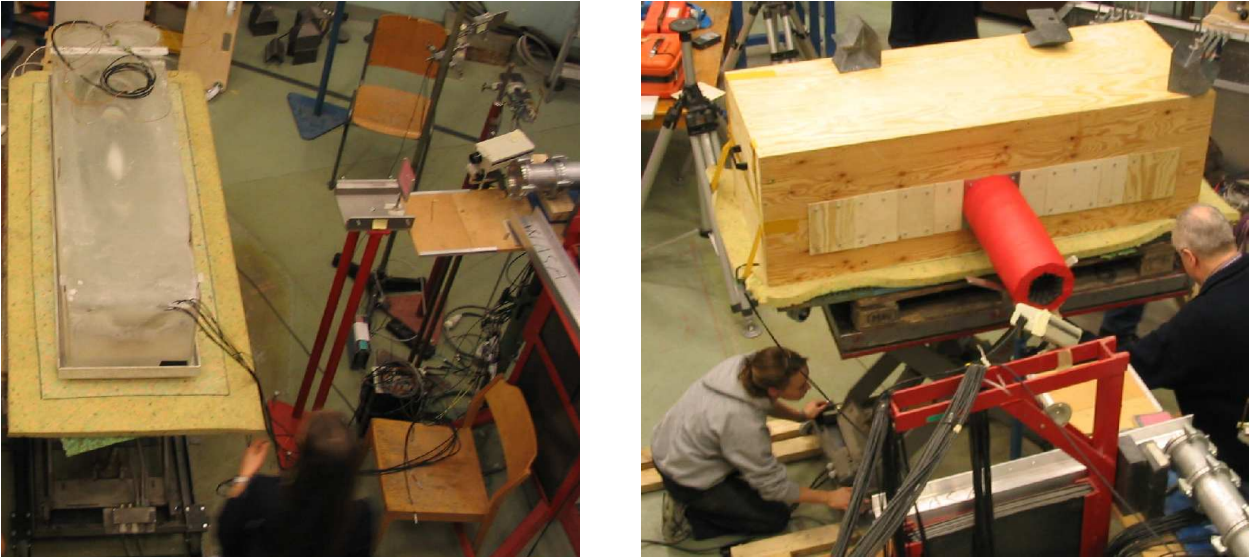


Figure 6.11: Picture of the ice setup at the proton beam without (left) and with (right) insulation.

6.2.2 Ice as a target

The setup used for the ice targets is shown in figures 6.12 and 6.11. Despite the long production time two different configurations could be realised for the proton beam test. In one setup, the *glass ball* sensor was installed close to one side of the ice, while an array of five *epoxy* sensors was installed close to the opposite wall. In a second configuration, only the *iron ball* sensor and two *epoxy* sensors were mounted at the same of the ice volume. All ice blocks showed good optical clarity and were manufactured in wooden boxes that could be removed after the block was frozen. Thus, any effects of the beam interacting with the ice container could be excluded.

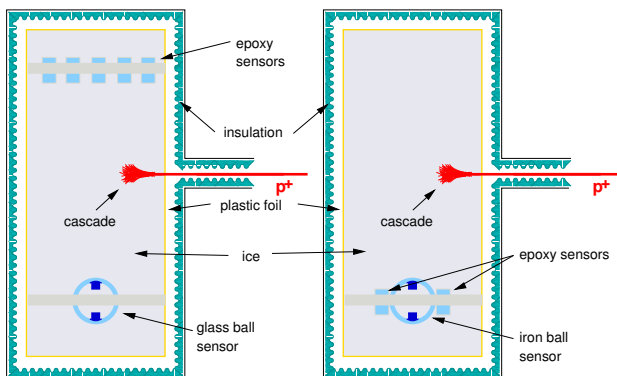


Figure 6.12: Schematic drawing of the setup in the two ice blocks.

In order to prevent the ice from melting over the course of the measurement and reduce the ambient noise, an acoustic and thermal insulation box was put over the block. The beam entered through a $50\text{ cm} \times 20\text{ cm}$ circular baffle shown in red on the right of figure 6.11. This baffle was moved along the side of the ice block to allow for different entry points of the beam in the ice. Limited by the low thermal conductivity of ice and the long time needed to achieve homogeneous conditions even over the small blocks of $140\text{ cm} \times 40\text{ cm} \times 30\text{ cm}$, three

different temperatures could be realised during the time the proton beam was available.

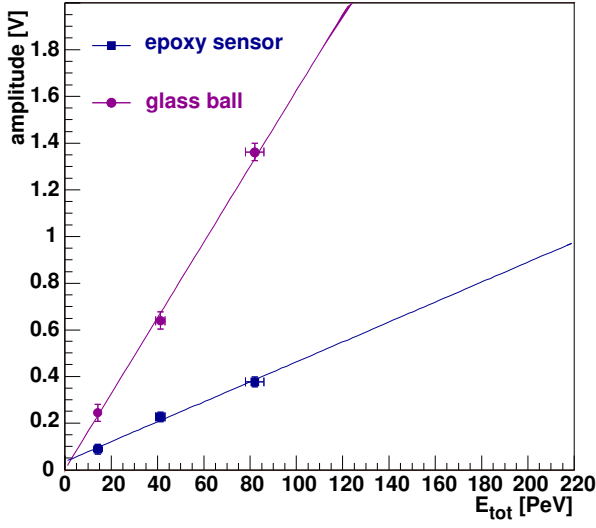


Figure 6.13: Acoustic signal amplitude vs. proton bunch energy for the setup with the *glass ball* sensor at $T = -25^\circ\text{C}$ and $d = 65\text{ cm}$ (from [Ste04]).

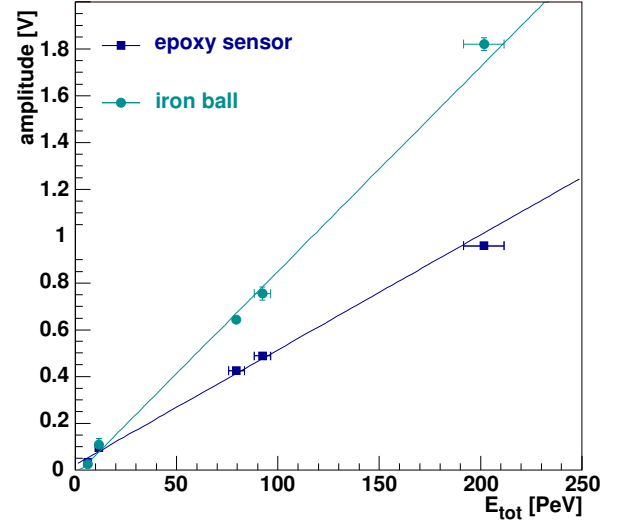


Figure 6.14: Acoustic signal amplitude vs. proton bunch energy for the setup with the *iron ball* sensor at $T = -15^\circ\text{C}$ and $d = 20\text{ cm}$ (from [Ste04]).

In contrast to the measurements with water as a target medium, no calibrated glacio-phones have been available for ice. Still some basic properties have been established previously as explained in section 5.3 and could be confirmed in ice. As an example, for piezo-electric excitation, good linearity of the recorded signal amplitude with the amplitude of the electric input signal was found. Although not expected from the theory of piezo-electricity and elastic waves, this could still be achieved by non-linear effects that act inversely on the receiver and emitter side. Figures 6.13 and 6.14 show the signal amplitudes of the first signal peak as a function of the total bunch energy E_{tot} of the proton beam for the setups holding the *glass ball* and *iron ball* sensors, respectively. With the latter setup, more than one order of magnitude in beam current has been covered. For all sensors, excellent linear relation of the signal amplitude to the beam energy is observed, as expected from thermo-acoustic theory. This independently confirms the linearity of the acoustic sensor response in ice. A significantly higher sensitivity of the *iron ball* and *glass ball* sensors with respect to the *epoxy sensors* can also be observed. It should be also noted that the signals of the *epoxy sensors* have been obtained at different temperatures T and distances d of the sensor from the interaction region. Yet the sensitivity for the *epoxy sensors* in both ice blocks seems comparable. Given an approximate $1/d$ behaviour of the signal amplitude with distance as will be shown below, this indicates a strong temperature dependence.

The thermo-acoustic interpretation of the signals is also strongly supported by the signal arrival times. Figure 6.15 shows the signal shape in the time domain. A delay Δt_{prop} of the signal from the entrance time of the beam in the ice block due to propagation of the acoustic signals is apparent. The vertical bars give the theoretical expectations for the arrival time of the signal and the arrival time $\Delta t_{\text{prop}} + \Delta t_{\text{ref}}$ of the signal reflected on the nearest boundary of the ice block. A clear distortion of the signal shape is observed at the arrival time of the reflected signal. Yet even where superimposed by reflections the shape of the signal does not

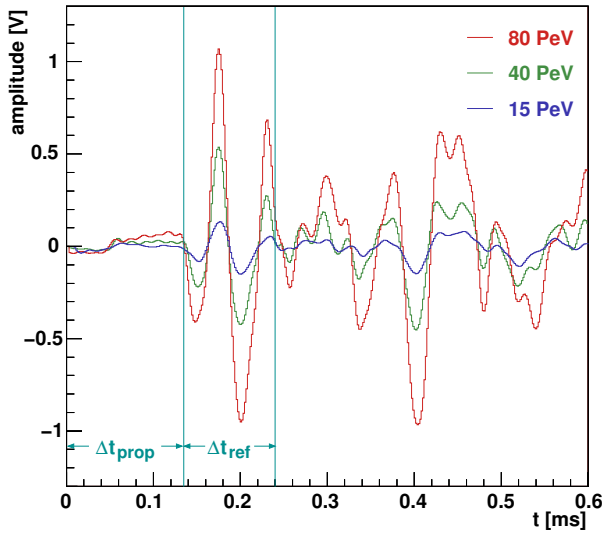


Figure 6.15: Signal shape of the *epoxy sensor* at different beam energies at $T = -25^\circ\text{C}$ and $d = 65\text{ cm}$ (from [Ste04]).

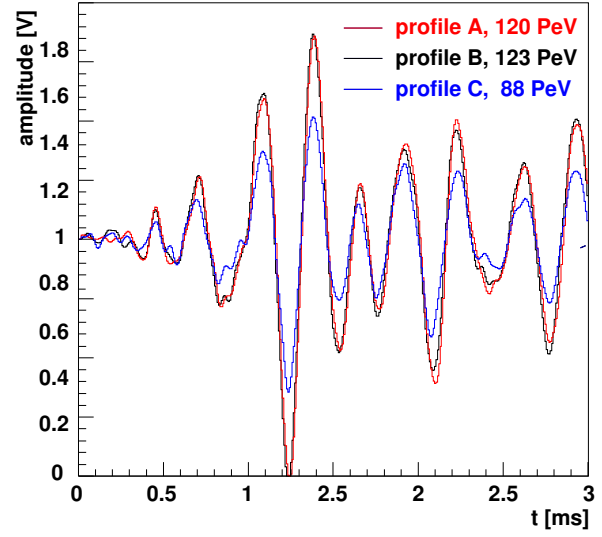


Figure 6.16: Signal shape of the *glass ball* sensor for different beam profiles at similar energies at $T = -15^\circ\text{C}$ and $d = 20\text{ cm}$ (from [Ste04]).

vary for different bunch energies. The amplitude of the reflected signal will have a certain fraction of the direct signal. So also their superposition is assumed to scale linearly with beam energy as shown in figure 6.15.

Different beam geometries as listed in table 6.3 have been realised to see the effect of a varying beam width on the signal shape. Compared to the spreading of the beam by multiple scattering of the cascade particles shown in figure 6.2, the variation in the beam profile that could be established is small. Keeping the temporal bunch profile constant, as expected, no significant variation in the signal shape is observed. The slightly lower amplitude of the signal obtained with profile C in figure 6.16 is in good agreement with the lower beam energy for this configuration.

Finally, also the sonic field generated by the acoustic signal has been scanned by shooting the proton beam in the ice block at different distances. Figure 6.17 shows the amplitude of the first peak with respect to the orthogonal distance d from the beam line. As for the water setup, the data can be well described by a $d^{-\gamma}$ relation with a smaller degradation factor γ in the near field region than in the far field.

profile	σ_x	σ_y
A	0.58 cm	0.70 cm
B	0.56 cm	0.60 cm
C	1.6 cm	0.94 cm

Table 6.3: Beam width in horizontal (σ_x) and vertical (σ_y) direction for the three different beam configurations

In the absence of a simulation yielding acoustic signal amplitudes, the distance behaviour has been modelled with a generic $\gamma = 0.5$ in the near field and $\gamma = 1$ in the far field as obtained from a cylindrical source. Figure 6.17 also shows two fits, one to the *glass ball* sensor data for the far field and a combined far-field near-field fit to the *epoxy sensor* data, where the transition point was left as a free parameter. From the generic cylindrical source model the near-field to far-field transition is supposed to occur at a distance $d_t = L_{src}^2/\lambda$, where L_{src} is the length of the cylinder, while λ is the wavelength that is determined by the width of the cylinder. For water, a transition value of $d_t = 28$ cm is observed in the simulation, in good agreement with data. Inversely scaling the length of the energy deposit by the density of the medium, in ice a slightly higher value is expected. A transition distance of $d_t = 20$ cm is obtained from the fit. Due to the crudeness of the argument, which e.g. neglects the different geometrical configurations, and the small number of data points in the near-field, this is not in obvious contradiction.

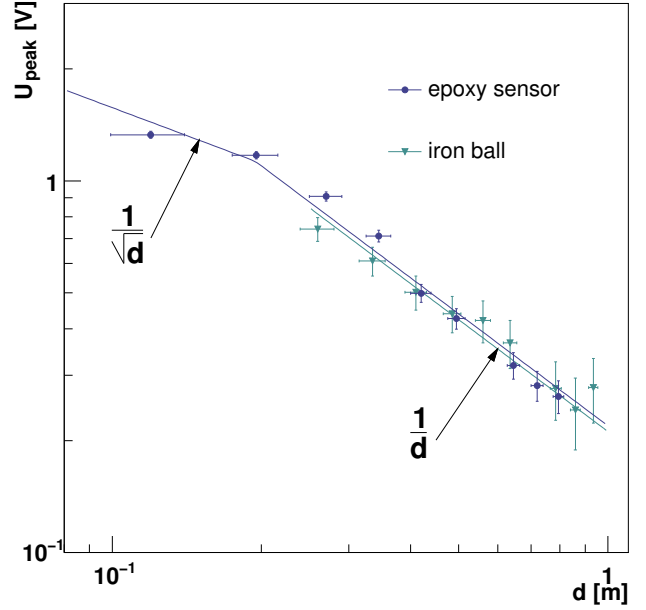


Figure 6.17: Signal amplitude vs. distance for the *iron ball* and *epoxy sensor*. The lines show a (combined) near-field and far-field fit.

At last, despite the long thermal adaptation time of about one day, temperature dependent measurements were performed both with the proton and laser beams described in tables 6.1 and 6.2. A range of about -5°C down to -25°C could be covered, although with limited statistics. Figure 6.18 shows the effective sensitivity $S_{eff} = U_{sig}/E_{tot}$ obtained as the ratio of signal amplitude U_{sig} to beam energy E_{tot} from linear fits as in figure 6.13. For the laser, more values could be obtained at intermediate energies, but due to the high intensity and the small region of energy deposit the direct acoustic signal of the laser resulted in a saturation of the amplifier stage. Thus, the signal amplitude shown in figure 6.19 had to be acquired from a signal region overlaid by reflections from the container walls. In both cases, a strong increase of signal amplitude is observed with decreasing temperature, which is more prominent in the proton beam data.

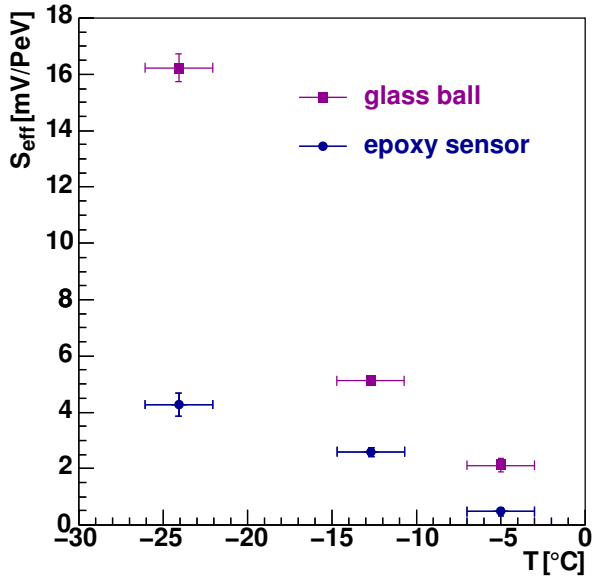


Figure 6.18: Temperature dependent signal amplitude of the *glass ball* and *epoxy sensor* excited with a proton beam (from [Ste04]).

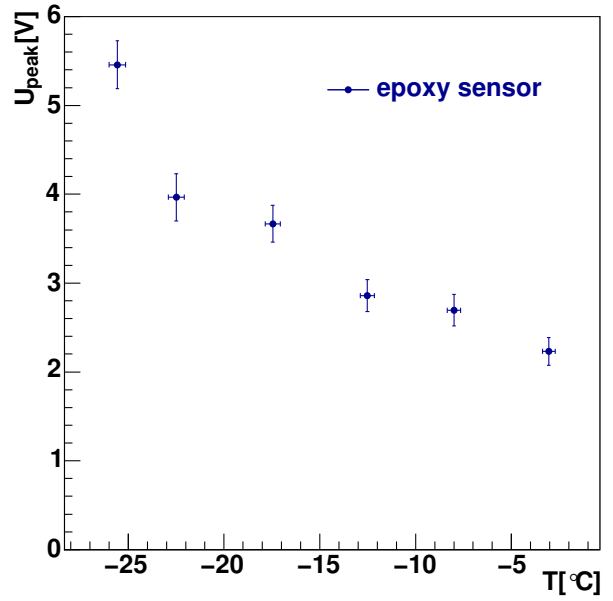


Figure 6.19: Temperature dependent signal amplitude of the *epoxy sensor* excited with a laser beam (from [Kri06]).

Several causes can contribute to this effect, that are difficult to disentangle, but may be grouped in source, propagation and receiver side effects.

1. On the **receiver** side, thermal effects of the piezo-electric element, its housing and the amplifier have to be taken into account:
 - For the housing, different thermal expansion coefficients may lead to a variation of the static stress on the housing and especially the piezo-electric element. However, as long as in the linear regime of elasticity, the elastic properties, i.e. the strain due to a certain stress should be independent of any static stress applied in addition.
 - For the piezo-electric element itself, also variation of the electric and piezo-electric coefficients need to be accounted for. From the manufacturer, a variation of $(d_{33|T=0^\circ\text{C}})^{-1} \cdot \frac{d}{dT} d_{33} = 2.23 \cdot 10^{-3} \text{ K}^{-1}$ for the piezoelectric constant and $(\varepsilon_{33|T=0^\circ\text{C}})^{-1} \cdot \frac{d}{dT} \varepsilon_{33} \approx 1.5 \cdot 10^{-3} \text{ K}^{-1}$ for the dielectric constant are quoted. Also the mechanical parameters of the *PZT* ceramic are subject to only little variation with temperature. A coefficient of $(f_R|T=0^\circ\text{C})^{-1} \cdot \frac{d}{dT} f_R = 0.57 \cdot 10^{-3} \text{ K}^{-1}$ is given for the resonance frequency f_R .
 - Finally, for the amplifier, a relative increase of the gain-bandwidth product with decreasing temperature of about $-2.77 \cdot 10^{-3} \text{ K}^{-1}$ has to be considered, that has been confirmed by the self noise measurements described in section 5.1.4.

So while the piezo-electric factors should lead to a small decrease in sensitivity, this should be roughly compensated by the increasing amplifier gain. The sensitivity of the sensors is therefore not expected to exhibit a strong temperature dependence. This could also be confirmed by measurements with an *epoxy sensor* inside an ice block

receiving signals from a surface mounted piezo-electric transducer [Kri06]. Only an approximate 10 % increase was observed from -5°C to -30°C from six data points with a 15 % statistical error on a single measurement.

2. For the **propagation**, different effects have to be considered:

- As shown in section 3.5, the absorption that is theoretically predicted for south polar ice shows a strong temperature dependence, but absorption coefficients that make the effect negligible for the dimensions considered here. Yet, while for south polar ice absorption by molecular reorientation is assumed to be dominant, this must not be true for lab-grown ice samples [Pri06]. All absorption effects due to relaxation processes should provide a temperature dependence proportional to $e^{\left(\pm \frac{U}{k_B T}\right)}$, with $U = \mathcal{O}(10^{-1}\text{eV})$ and the sign depending on the frequency regime [Pri93]. At high frequencies, the exponent will carry a negative sign and a decrease of absorption with decreasing temperature is observed. Moreover, some of the field ice data presented in [Pri93] showed absorption coefficients $\alpha_{abs} = \mathcal{O}(1\text{m}^{-1})$. Such a strong contribution is not supported by the observed amplitude to distance relations shown with piezo-ceramic excitation in figure 5.35. But e.g. crystal sizes and density of impurities may vary significantly from ice block to ice block, so that a significant contribution from absorption to the observed increase in signal amplitude cannot be excluded.
- Furthermore, the speed of sound changes with temperature. For high-density polar ice the coefficient is rather small [Alb04]. In less dense laboratory ice samples changes with temperature of up to $-30 \frac{\text{m}}{\text{s}}\text{K}^{-1}$ have been observed [B⁺58]. Similar values were obtained from the signal arrival times in the proton beam setup [Ste04]. Apart from the arrival time, the direct signal is not further affected. Yet the relation of distances to wavelength and therefore the superposition of direct and reflected waves will change. Especially for the laser beam measurements, where no separation of the direct and reflected signal has been possible, a variation in the interference of reflected and direct signal is expected to contribute to the temperature dependence of the observed amplitude.

3. Finally the effects concerning the signal **generation** have to be regarded.

- In contrast to water, where the temperature dependence of the thermal expansion coefficient is strong and it even changes the sign, in ice the corresponding effects are much smaller. From the variation of the crystal lattice constants the expansion coefficient for ice is calculated in [EK69]. Also the heat capacitance C_p is given as a function of temperature. As α decreases with decreasing temperature, so does the heat capacitance C_p . The effect is non-linear for the expansion coefficient close to 0°C , causing a non-monotonic effect. Yet the absolute value of α/C_p is changed by less than 1.5 % in the probed temperature range.
- A change in the speed of sound v_l will not change the amplitude in the propagation, but it will change the amplitude of the emitted signal. Higher sound velocity means larger wavelength relative to the size of the emission region. A better coherence of the emitted signal is achieved, increasing its amplitude. For

an ideal cylindrical source, the effect of coherence is given by equation 3.15. The peak amplitude A_{peak} depends on the characteristic frequency f_{peak} of the signal as $A_{peak} \propto f_{peak}^2$, where $f_{peak} = \frac{v_l}{2d}$ and d is the diameter of the assumed cylinder. With a signal increase of more than 50 % going from 0 °C to −30 °C by this naive argument, this may be a significant contribution. Yet, as shown in [Ste04] by taking the values of v_l obtained from the proton beam measurements themselves, the effect is not sufficient to describe the observed strong rise in amplitude.

- Another probable cause rises again from the change in v_l . As discussed above, along with the amplitude the peak frequency f_{peak} of the emitted signal is increased. An increasing sensitivity of the sensor at higher frequencies may such cause larger amplitudes at lower temperatures. A strong increase of the signal amplitude of the *epoxy sensor* with frequency is observed in water as shown in section 5.3.3. Pulsed excitation was used in the water test, generating acoustic signals similar to what is obtained from the proton beam. Albeit the observed effect in water is likely to stem from an increase in the emitted acoustic amplitude, an increase of the sensitivity with frequency of the *epoxy sensor* can not be fully excluded, neither in water nor in ice. Accounting the full magnitude of the observed increase in water to an increase in sensitivity, and assuming the same behaviour for ice, a several ten percent effect could arise from this.

None of the effects mentioned above is likely to cause the full magnitude of the temperature dependence, but from the sum of all the observed increase in signal amplitude does not seem implausible. To disentangle the different contributions, more extensive investigations, and especially a calibrated glaciophone will be required.

Considering these uncertainties, in summary, it can be stated that the observations in ice - as in water - fit the expectations from the thermo-acoustic model. In water, apart from an additional contribution observed at 4 °C, also the full amplitude and shape in time and space of the observed signals agrees well with the prediction from a simulation of the thermo-acoustic mechanism in water. In ice, some of the basic relations of the model, such as linearity with energy could be established, while detailed comparisons lack once more a calibrated sensor. Yet given the good agreement in water and since first experiments in ice did not show any apparent deviation from the expectations, the thermo-acoustic generation of the signals should not be considered the main uncertainty in the quest for acoustic detection of neutrinos. Polar ice properties, in contrast, are mainly based on theoretical expectations. A dedicated setup to explore these will therefore be described in the next chapter 7.

Chapter 7

South Pole acoustic test setup (SPATS)

Three properties are most relevant for acoustic neutrino detection in the South Polar ice – the absorption length, the depth dependence of the speed of sound and the ambient noise level. In an effort dedicated to measure these, the *South Pole Acoustic Test Setup* (SPATS) has been created. It will also be the first installation of acoustic transducers for this frequency range in a natural ice volume of this depth, and can thus give valuable experience for future transducer designs. In addition, it serves as a test bed for technical solutions such as outdoor computer installation in the South Pole climate for the implementation of a future array with much larger dimensions.

7.1 Overview

The basic element of SPATS is a *stage*, that consists of a sensor and a transmitter module. Seven of these stages are arranged in one hole in the ice at different depths, each module connected to a cable leading to the surface. The cables are bundled and together with the stages form a *string*. Each string is independently controlled by its *String-PC* – an industrial computer rated for low temperatures. Together with other electronics components it is mounted in an *acoustic box* that will be buried 2 m deep in the snow close to the top of the hole. Three complete strings and their corresponding *acoustic boxes* will be installed. Communication and power supply to the *acoustic box* are provided through previously unused wires in the ICECUBE surface cables, through which the *String-PCs* can be accessed from a *Master-PC*.

The geometry of the setup is shown in figure 7.1. The acoustic stages are located at depth levels of 400 m, 320 m, 250 m, 190 m, 140 m, 100 m and 80 m. An uneven spacing was chosen in order to have a higher module density in the upper ice layers, where the density and hence also acoustic properties are expected to change more rapidly. Both density and the velocity of sound reach stable values at a depth of around 250 m with comparatively little change at greater depth (see figures 3.19 and 3.20).

However, even for this relatively shallow installation as e.g compared to the ICECUBE experiment, drilling costs and logistic as well as technical efforts are already substantial. In order to limit them, the SPATS strings will be deployed in the same hot-water boreholes as

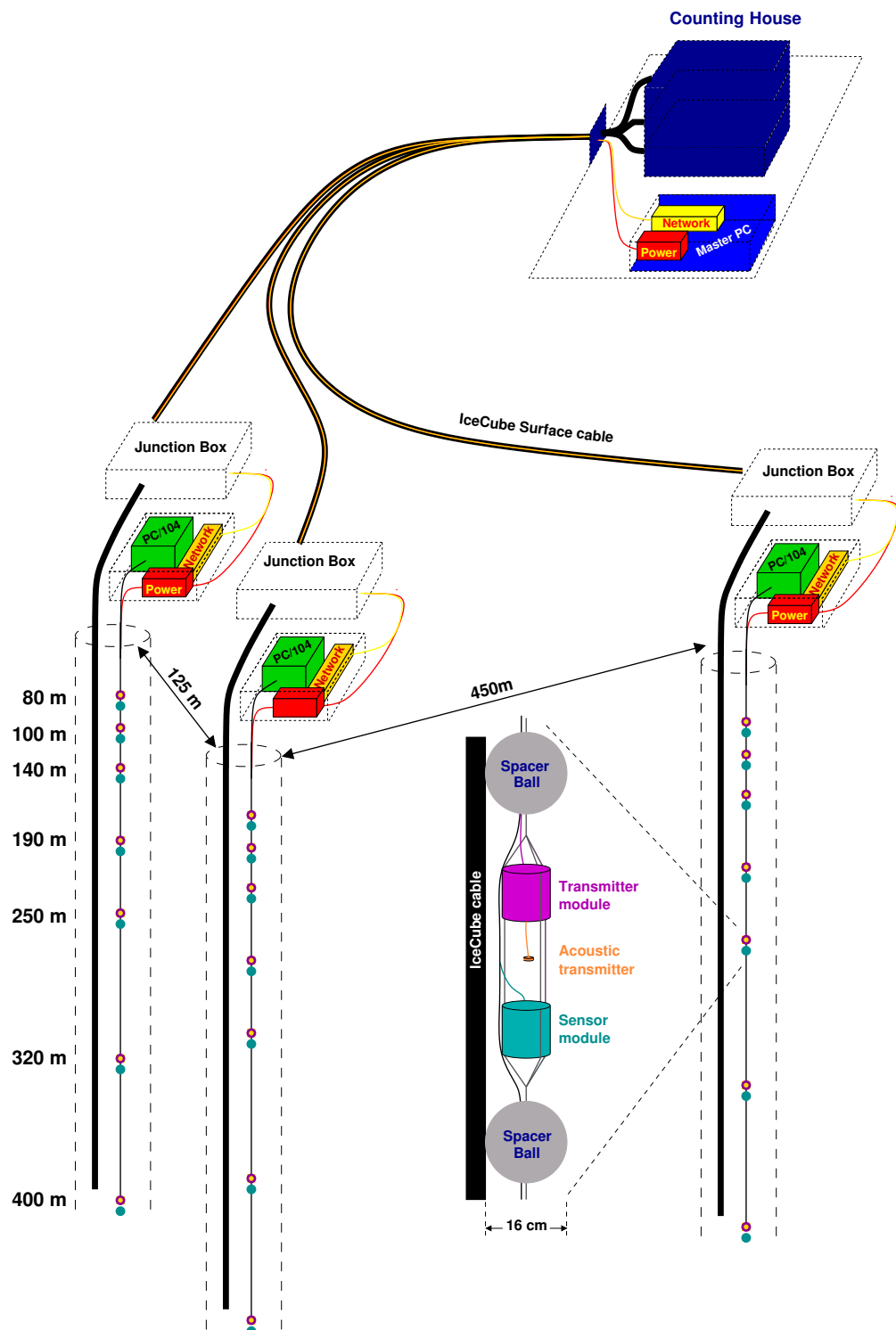


Figure 7.1: Schematic drawing of the SOUTH POLE ACOUSTIC TEST SETUP.

the ICECUBE strings, which do not have any installations in the indicated depth range apart from the several centimetre thick ICECUBE cable itself. The disadvantage of this approach is a non-optimal spacing of the strings, that are now bound to the locations of ICECUBE holes. As will be further discussed in section 7.5, a string spacing on the order of the absorption length would be desirable in order to see a significant impact on the transmitted signals. The maximum distance of two strings in the ICECUBE array will be around 1 km. However, due to limited accessibility of the South Pole, the array is installed in several sequences over more than six years. Taking advantage of this maximal distance would result in an undue delay of the measurement of the acoustic properties. For this reason, the choice of possible locations is limited to the much shorter distances provided by the holes that will be drilled for ICECUBE in the polar season 2006/2007. The holes are chosen to provide two strings at the maximal obtainable distance of 450 m and the third string at the smallest possible distance of 125 m as indicated in figure 7.1. To which extent this limits the capabilities of the setup will also be discussed in section 7.5.

7.2 Sensors and transmitters

A picture of an acoustic stage is shown in figure 7.2. To ensure a good control on systematic effects and allow for redundancy, each stage in SPATS is equipped with a sensor as well as a transmitter module. Both sensors and transmitters are built in 10.2 cm diameter steel housings with a welded bottom and a cap nut secured lid to withstand the ambient pressure. This pressure can be up to tens of bars above the static pressure expected in the depth of the installation due to the effect that the borehole re-freezes first from the top and from the bottom. The hole is then closed off at the top and the density decrease of $\approx 8.5\%$ from water to ice gives rise to an additional pressure. Due to the low plasticity of the ice this overpressure reduces very slowly. To allow for sufficient safety margin, the sensor and transmitter housings have been tested at pressures up to 120 bar. A finite element calculation showed that the maximum deformation occurs at the central perimeter of the cylinder and is smaller than a few nanometers [Hel04].

The transmitter module is mounted above the sensor module. Both are fastened to three ropes that are joined at the top and at the bottom onto a threaded ring. Iron bolts running through two thin plastic spheres above and below extend the device to the uppermost and lowermost threaded ring. The spheres have large holes to allow fast water inflow. The diameter of the spheres of 16 cm was chosen to ensure a minimum distance of the devices to the ICECUBE cable when deployed in the hole.



Figure 7.2: Picture of an acoustic stage.

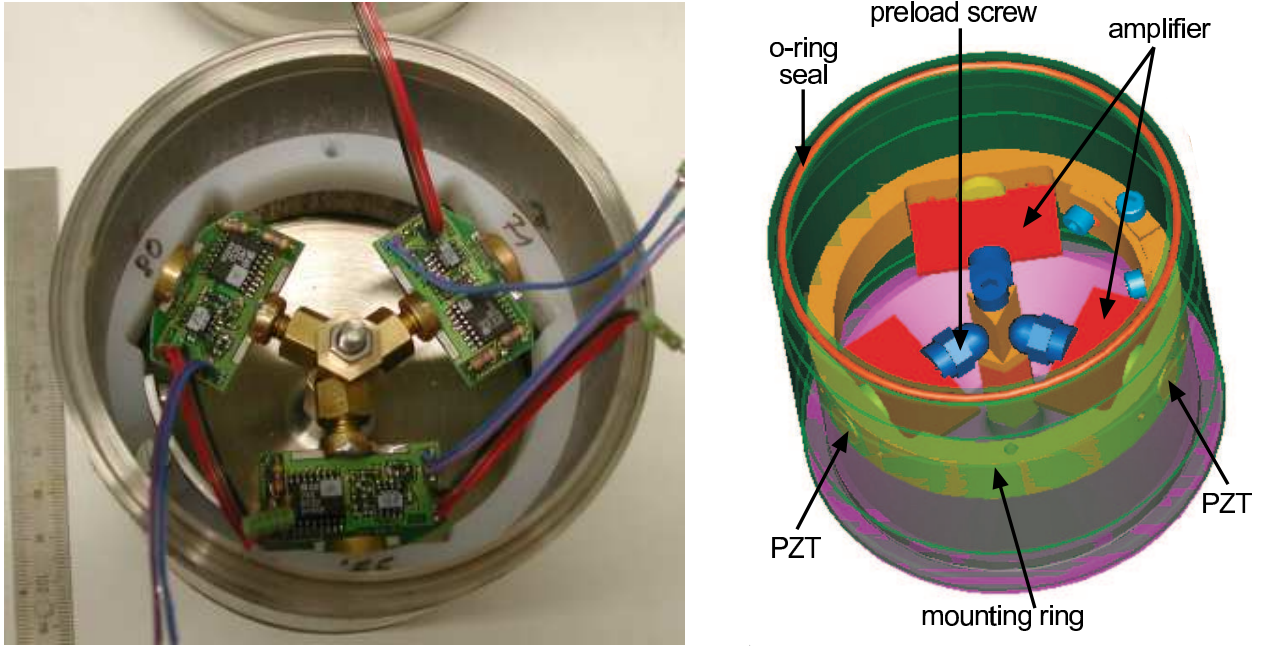


Figure 7.3: Picture and schematic drawing of an open SPATS sensor module seen from above.

Although only 21 stages are needed for the setup described above, 25 complete stages have been produced and tested. This will allow for easy exchange of stages that fail in a final acceptance test before deployment. In addition, the remaining spares can be retrieved after installation of the setup at South Pole to perform further tests and studies.

7.2.1 Sensor design

The SPATS sensors are designed following the same basic principles as the other sensors introduced in chapter 5. A schematic drawing of a sensor is shown in figure 7.3. Since the azimuthal orientation cannot be controlled during the deployment, three channels are installed in one housing to obtain good angular coverage. Again, cylindrical piezo-ceramics of 10 mm diameter and 5 mm height are used as sensitive elements. The same three stage differential amplifier board described in section 5.1.4 with an amplification of $\mathcal{O}(10^4)$ is closely attached to the *PZT* element. The steel housing is flattened at three positions to ensure good mechanical contact to the piezo-ceramics. For ease of mounting a plastic ring is inserted to hold the piezo-ceramics and amplifier boards in place. Mechanical force is exerted on the ceramics through the amplifier board by a *preload* screw pressing against a central bolt to ensure mechanical stiffness of the system.

7.2.2 Sensor calibration

The effective sensitivity of the SPATS sensor design described above first depends on the properties of the sensitive parts, i.e. the piezo-ceramics. Therefore, the d_{33} coefficient has been determined individually for all ceramics of the total batch of 100 ceramics. The setup is depicted in figure 7.4. A weight is exerting a static force on the piezo-ceramics. If lifted in a sudden movement, in this case by a counter-weight, the before compressed ceramic

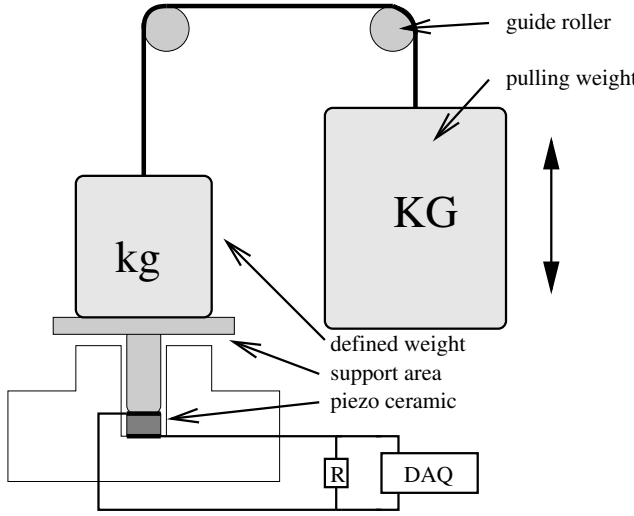


Figure 7.4: Schematic of the setup to measure the d_{33} coefficient of a piezo-ceramic.

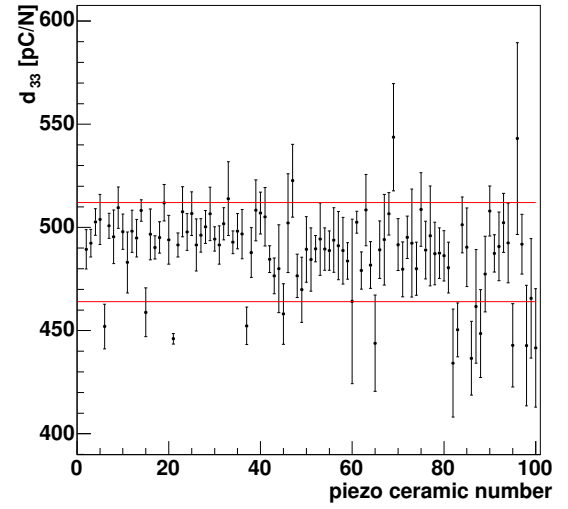


Figure 7.5: Measured d_{33} coefficient versus piezo-ceramic numbers. The red lines indicate the range of ceramics used for the SPATS sensors.

will expand. This results in a surface charge Q that is proportional to the gravitational force $m \cdot g$ that was before exerted by the mass m as shown in equation 5.2. The charge can be measured by use of a shunt resistor and integration over the discharging pulse. To reduce systematic errors, the d_{33} coefficient was not determined from a single measurement, but from a series of measurements with different weights (for a more detailed description see [Fis06]). The resulting values for the full batch are shown in figure 7.5. The average piezo-electric constant was found to be $\langle d_{33} \rangle = 488 \frac{\text{pC}}{\text{N}}$ with an RMS spread of $20 \frac{\text{pC}}{\text{N}}$, which is in reasonable agreement with the nominal value of $500 \frac{\text{pC}}{\text{N}}$ provided by the manufacturer. To reduce the impact of d_{33} variation on the sensitivity, only ceramics with a piezo-electric constant within $24 \frac{\text{pC}}{\text{N}}$ of the mean value have been used for building the SPATS sensors.

These ceramics are glued to small brass heads, on which the amplifier board is directly soldered. As described in 5.1.4, the actual amplification has been measured as a function of frequency, showing a peak gain of $\approx 250 \cdot 10^3$ at around 10 kHz with a steady drop above. The measurement was done for only one amplifier, but the differences in the electronics components are on the level of a few percent and variations from board to board are expected to be small.

Especially for a measurement of the absorption length an absolute calibration of the sensors, would have been desirable. However, due to the problems discussed in section 5.3.3, this is not easily achievable. For the measurements that are to be performed with SPATS, in particular for measuring the absorption length, therefore a relative comparison of the different channels is necessary. To obtain a handle on the variation of the response of the different sensors, a sensitivity measurement in water using the single-pulse relative calibration method introduced in chapter 5.3.2 has been performed for each channel in each sensor module.

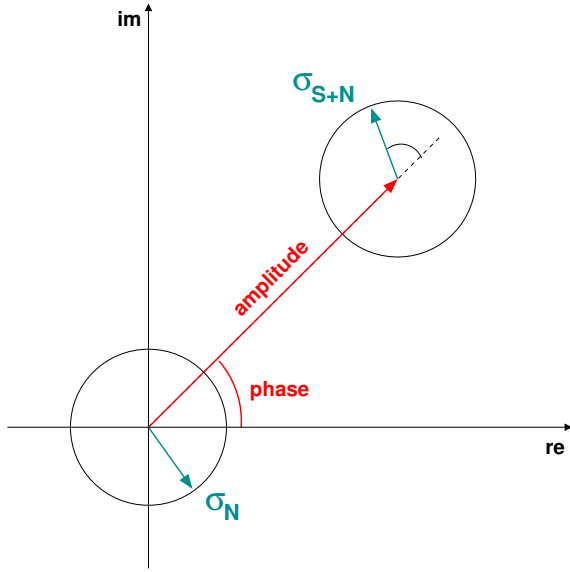


Figure 7.6: Schematic illustration of the noise contribution to a steady sensor response for a single frequency in the complex plane.

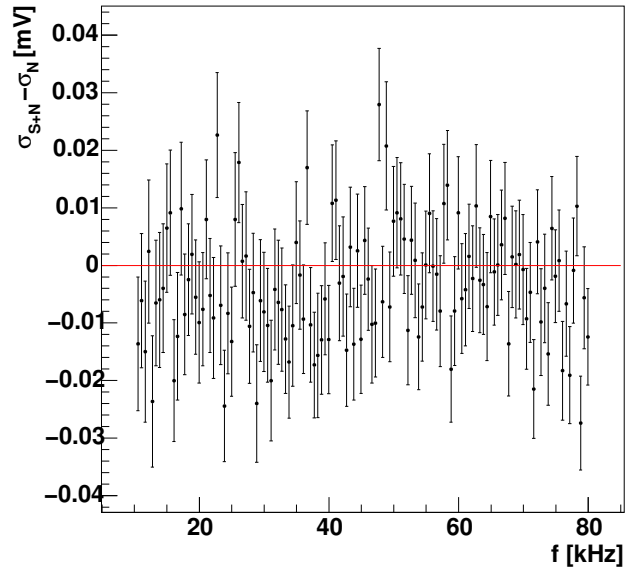


Figure 7.7: Difference of *white noise* amplitude spread σ_N to amplitude spread in presence of a signal σ_{S+N} for different frequencies.

A well calibrated reference hydrophone and a powerful transmitter have been mounted on long poles in the centre of a large water tank¹ at a distance of around 1 m. A short pulse with a broad frequency spectrum is emitted by the source and recorded by the reference hydrophone. The Fourier spectrum of the signal in the free-field time interval is compared to the Fourier spectrum of signals recorded by the SPATS sensors that are mounted in the same position. Three measurements were taken for each sensor module with consecutively one channel facing towards the projector. From this a relative frequency dependent sensitivity for the individual channels could be derived. With the calibration information of the reference this can be transformed into an absolute sensitivity spectrum.

Three main problems were encountered in this approach:

1. The same transmission amplitude was used for both measurements with the reference hydrophone and the SPATS sensors. Although sufficient for SPATS sensors with a signal to noise ratio $S/N > 10$, only a rather poor $S/N \approx 3$ was reached for the reference hydrophone. Consequently, ten times more statistics had to be accumulated with the reference hydrophone as compared to the SPATS sensors, for which 100 events per channel were recorded.
2. Limited availability of the water tank required a fast exchange of sensors for the individual measurement. As a result of this and the long poles used for mounting a swinging motion of some of the SPATS sensors with an amplitude of up to ≈ 2 cm was revealed in the data. Due to the good signal to noise ratio, this could be well corrected for by aligning the single events in the time domain on the position of the first peak.

¹The same $70 \text{ m} \times 10 \text{ m} \times 3 \text{ m}$ water tank with a $12 \text{ m} \times 10 \text{ m} \times 5 \text{ m}$ deep section as in section 5.3.2.

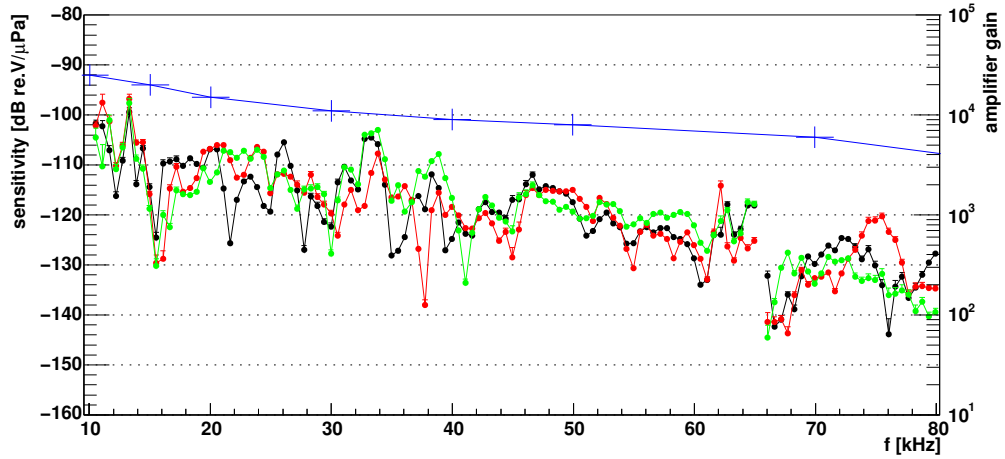


Figure 7.8: Sensitivity spectrum of SPATS sensor module #3 for all three channels: A (black), B(red), C(green) and amplifier gain (blue).

3. Finally, in order to obtain a handle on the noise contribution and the errors, not just the average of the recorded signals has been used to generate the spectra. Instead, all recorded events have been transformed individually. In absence of variations from other than ambient noise sources the signal part of the Fourier transform will for all events result in a steady amplitude and phase, that can be visualised by a steady vector in the complex plane for each frequency as shown in figure 7.6. In contrast, any white noise has a random phase and amplitudes following a Rayleigh function, leading to a two-dimensional Gaussian spreading of the Fourier coefficients in the same complex plane. From the off-signal region of the waveforms in the time-domaine, e.g. before the pulse, the ambient noise contribution to this spreading per frequency can be estimated. Figure 7.7 shows the difference in RMS spread of the signal amplitudes obtained for each frequency in the presence (σ_{S+N}) and absence (σ_N) of the calibration signal. No significant contribution to the noise for any frequency above the ambient noise has been observed for any frequency. This way, a comparatively small limit on the statistical error in the measurement could be derived, which is well below the ambient noise contribution.

An extensive description of the measurements and analysis can be found in [Fis06]. Figure 7.8 shows the sensitivity spectra of the three different channels in one SPATS module. The general trend to lower sensitivity at higher frequencies is mainly due the decreasing gain of the amplifier board that is also shown in figure 7.8. The much finer structure of the sensitivity is not due to statistical fluctuation in the measurement – errors are also shown, but not well visible due to their small size – but rather due to the complex mechanical design of the sensor. This results in a multitude of resonance modes over the full frequency range. Some of these are common for all three channels in a module, e.g. the eigenmodes of the housing, whereas others depend on the individual channel configuration, such as exact mounting angles. However, given the complexity of the system, reasonable agreement is observed. Especially, as a result of the triangular geometry in which the channels are arranged, the pre-load force is roughly equal for all channels within one module, resulting in good agreement in the absolute normalisation. As this pretension is adjusted manually,

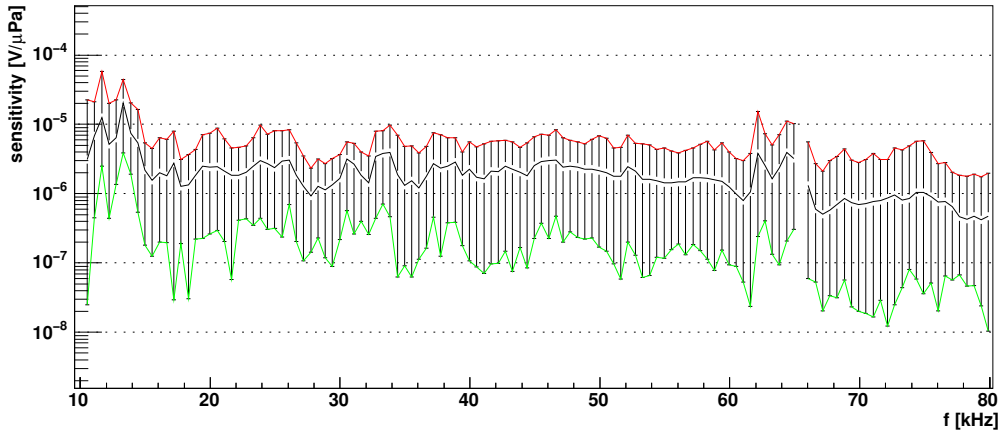


Figure 7.9: Sensitivity range per frequency and mean sensitivity of all SPATS sensors.

the absolute sensitivity level varies considerably from module to module. Figure 7.9 shows the sensitivity range per frequency that is covered by all SPATS channels in all sensor modules as well as the average sensitivity. On average, the variation is more than one order of magnitude. Keeping in mind that only relative measurements are to be performed with the SPATS setup, this is of minor importance as will be explained in section 7.5.

It has to be noted that a strict application of the obtained values for sensitivity is only valid for water. Yet, due to the better impedance matching, an in general higher sensitivity than in water is expected in ice.

Finally, to obtain a performance estimate of the sensors the equivalent self noise spectrum was determined. Self noise recordings have been performed in an acoustically and electromagnetically well isolated environment. By comparison with the sensitivity spectrum $S(f)$, the equivalent self noise spectrum $E(f)$ is calculated from the self noise spectrum $N(f)$ as $E(f) = N(f)/S(f)$. For each frequency, this gives the pressure amplitude needed to overcome the sensor self noise. The detection capabilities for a certain signal can then easily be determined by comparing the spectrum of the waveform with the equivalent self noise spectrum. The equivalent self noise therefore is a better figure of merit to describe a sensor than the sensitivity, which can be easily altered by e.g. changing the amplifier gain. Figure 7.10 shows the equivalent noise spectra for the three different channels in one SPATS sensor module in comparison to the reference hydrophone. The decrease of sensitivity at higher frequencies together with nearly flat self noise spectra in the range of interest consequently result in an increase of equivalent self noise. Although showing a much smoother behaviour due to its much less frequency dependent sensitivity, the equivalent self noise levels of the reference hydrophone are substantially larger over nearly the whole frequency range. In terms of detection capability, the SPATS sensors clearly outperform the commercial device. The range of the equivalent self noise level over the full frequency range as well as its mean is shown for each channel in each module in figure 7.11, showing that in terms of detection capability, the SPATS modules are more alike than in terms of sensitivity.

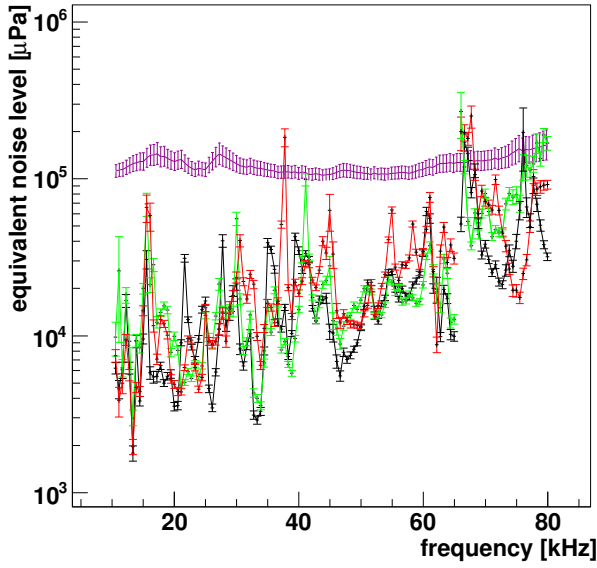


Figure 7.10: Equivalent self noise spectrum for the three channels: A (black), B (red) and C (green) in the SPATS sensor module #3 and for the reference hydrophone (purple).

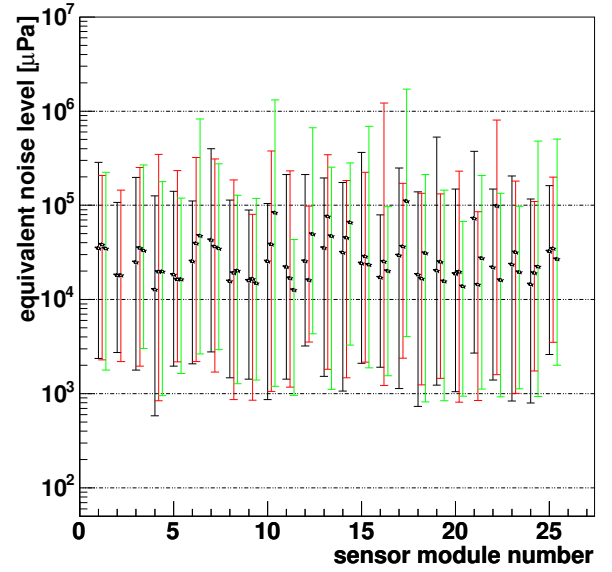


Figure 7.11: Range of the equivalent self noise spectrum for all SPATS sensors: channels are A (black), B (red) and C (green) respectively.

7.2.3 Transmitter design

Following the reciprocity theorem, acoustic emitters are conveniently built from piezoceramics as discussed in section 5.4. Very high voltages can be applied that are needed to overcome the $1/R$ scaling of the amplitude with distance R for an isotropically emitting source. For the distances of several hundred metres in the SPATS setup, kV-pulses are required to obtain good signal-to-noise-ratios.

In order to test frequency-dependent effects of the sound propagation, sinusoidal waveforms would be preferable. Yet the generation of these signals at kV-amplitudes requests non-trivial technical solutions. In order to drive a $f = 100$ kHz continuous sine wave with an amplitude $U_0 = 1$ kV on the specific ceramics used in this setup with a capacitance of $C_{ring} \approx 16$ nF, the peak current in the system will be $I_0 = 2\pi f C_{ring} U_0 \approx 16$ A. Even if no further losses are introduced, following manufacturer specifications the fraction of the power that will be converted to acousto-mechanical energy is $k_{33} = 0.34$ and the radiated acoustic power $P_{rad} = k_{33} \langle U(t)I(t) \rangle \approx 2.7$ kW will be difficult to sustain.



Figure 7.12: Ring-shaped ceramics cast in epoxy as used for the SPATS transmitters.

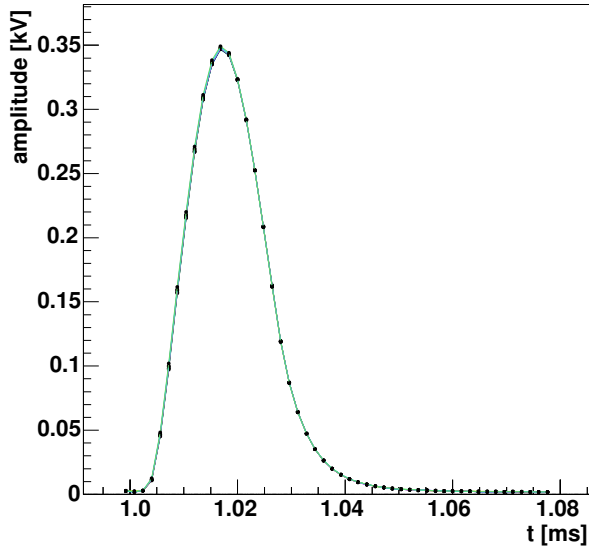


Figure 7.13: Superimposed electrical high-voltage pulses generated with SPATS transmitter #1.

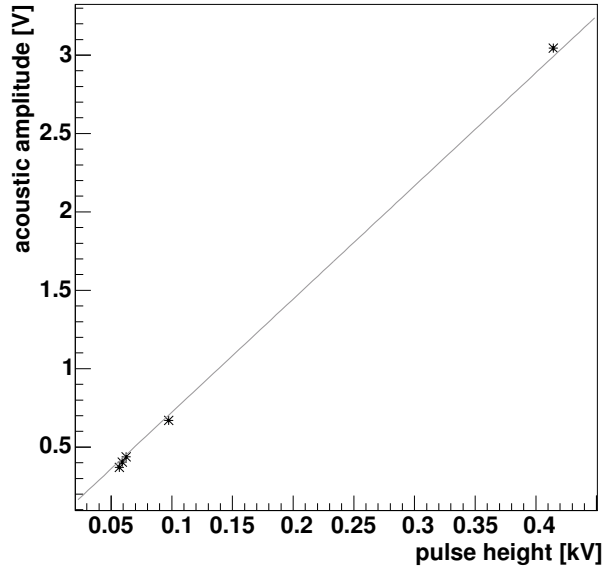


Figure 7.14: Amplitude of acoustic pulse versus peak amplitude of the high-voltage pulse applied to the ceramics.

Given the power constraints for all installations at South Pole, no longer than $\mathcal{O}(\sim 1 \text{ ms})$ pulses can be generated for the use within this setup. Similar to what is described in section 5.4, high-voltage pulse generation in the SPATS transmitter is therefore done using a 5.6 mH coil that is *charged* by an adjustable steady current. Controlled by a *TTL* pulse, the charging is disrupted by a high-voltage power transistor. With the piezo-ceramics as a mostly capacitive element connected in series to the inductivity, the system starts to oscillate, but is short-connected to ground after one half cycle by a damping diode. The resulting unipolar pulse of the width $\tau_{FWHM} \approx 17 \mu\text{s}$ is shown in figure 7.13. Seven pulse shapes averaged over ten pulses each are displayed with statistical error bars, showing a very high repetition stability. As shown in figure 7.14, the amplitude of the generated acoustic pulse also depends linear on the peak electric amplitude shown in figure 7.13. The effective acoustic output amplitude can thus be monitored by recording the high voltage pulse. In the SPATS setup, this will not be done using a 1 : 100 voltage divider on the output as for the measurements presented here, but with a dedicated amplifier circuit of the same gain, which drives the signals over the long in-ice cables.

For ease of production, the transmitter electronics sits in the same type of housing as used for the SPATS sensor modules. For the sensors the preamplifier needs to sit close to the active ceramic element to limit electromagnetic interference on the input. In contrast, the high voltages that are used for driving the transmitting ceramics allow to place the ceramics outside of the housing where a more efficient coupling to the ice is possible. Since ice is non-conducting, in principle not even electrical insulation would be needed. In order to avoid short contacts when testing the devices in water and to avoid mechanical destruction by shear forces that may occur in the freeze-in process, the ring-shaped ceramics has been cast in an epoxy cylinder of the same diameter. Figure 7.12 shows a picture of the cast-in ring with dimensions of $5 \text{ mm} \times 20 \text{ mm}$ and 2 mm wall thickness.

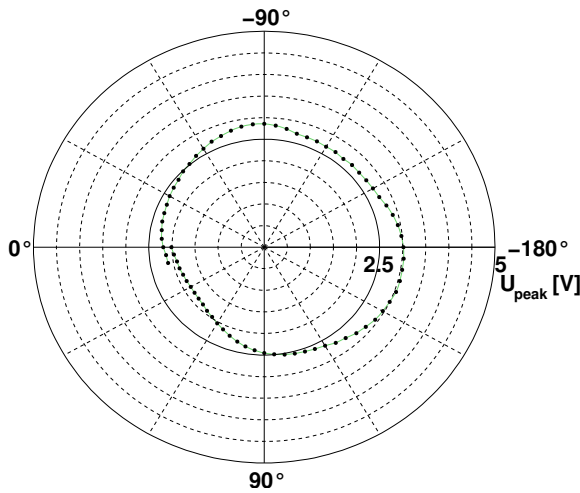


Figure 7.15: Peak pulse amplitude of ring transmitter in the azimuthal plane.

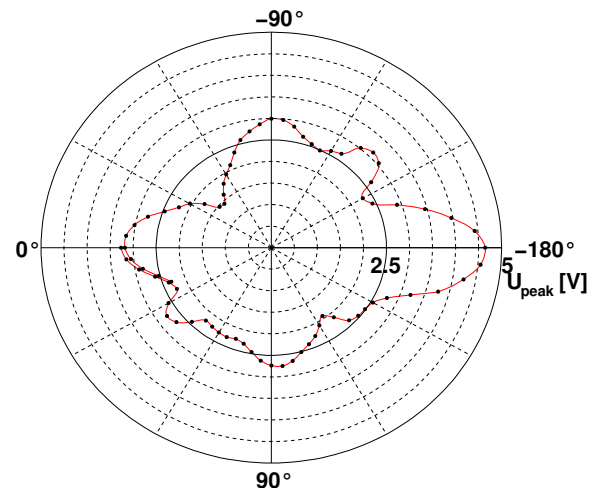


Figure 7.16: Peak pulse amplitude of ring transmitter in the polar plane.

The choice of the ring-shaped ceramics was not only stimulated by the emission spectrum but also by the emission pattern. Signals will be transmitted in between strings at the same but also at different depth levels, so that isotropic emission is desired. For a ring-shaped ceramic driven with the high-voltage pulse described above, the peak amplitude versus azimuthal angle is shown in figure 7.15 and versus polar angle in figure 7.16. Both emission patterns are much more isotropic than in case of a disc shaped piezo-ceramics that is shown in figure 5.32. The asymmetry observed in both cases is probably mainly an effect of a slightly skew mounting of the ceramics inside the epoxy for this particular transmitter.

7.2.4 Transmitter calibration

A waveform of an acoustic pulse as generated by a SPATS transmitter is shown in figure 7.17. A short high-frequency pulse is followed by some lower frequency mechanical resonance signals of lower amplitude (probably within the epoxy resin) that quickly fade out in a few cycles. In order to determine the output efficiency of the different SPATS transmitters, the gradient of a linear fit of the high voltage peak height versus the output peak-to-peak amplitude has been determined in a large water tank for all SPATS transmitters. The distribution of the gradient is shown in figure 7.18. The rather large RMS spread of 33% is probably a result of several effects:

- Transmitter ceramics have not been preselected, so that the spread in the piezo-ceramic coefficients is expected to be on the same order as for the cylindrical ceramics used for the sensors.
- Only one azimuthal direction has been sampled, so that variations in the azimuthal emission, e.g. due to skew mounting within the epoxy may affect the signal.

However, again as for the sensors the above output calibration is only valid for water. For application in ice, signals received by different sensors from the same transmitter have to be compared as will be demonstrated in section 7.5.

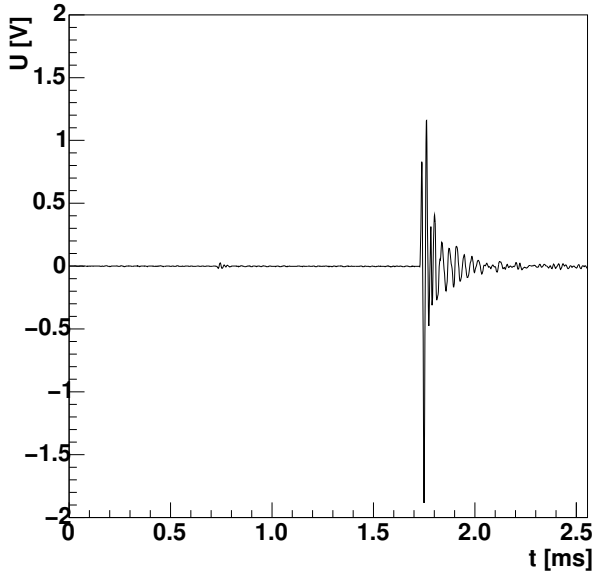


Figure 7.17: Acoustic pulse generated by a SPATS transmitter and recorded with the reference hydrophone.

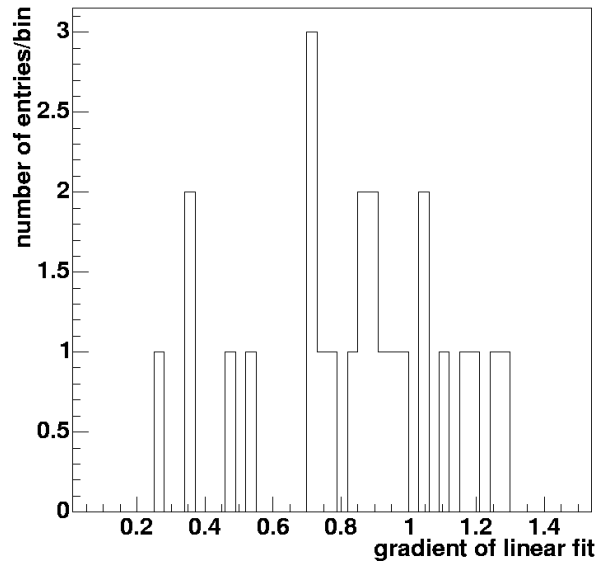


Figure 7.18: Distribution of the gradient of a linear fit of acoustic pulse amplitude versus high-voltage pulse for all SPATS transmitters.

7.3 System control, data acquisition, communication and time synchronisation

As power supply of the sensor and transmitter modules, 24 V_{DC} are provided through a cable in the ice. The ohmic resistance of the cable is $\approx 0.08\ \Omega/\text{m}$, which together with a nominal current of 110 mA through the sensor leads to a voltage drop of around 4.7 V at the lowest stage. To avoid depth-dependent amplifier gain, an additional voltage regulation built from two transistors in an emitter follower configuration provides $\pm 5\text{ V}_{\text{DC}}$ in the sensor module. For the transmitters, cable losses are compensated by the charging current adjustment: a low-current control voltage is used to regulate the charging voltage of the transistor stage within a range of $0 - 11.3\text{ V}_{\text{DC}}$. In addition, each transmitter module holds a Pt1000-based temperature sensor with a compensated linear output circuit providing a current through the circuit of $4 - 20\text{ mA}$ for a temperature range of $-70\text{ }^{\circ}\text{C}$ to $+10\text{ }^{\circ}\text{C}$. At the lowest stage in each string, this sensor is replaced by a commercial absolute pressure sensor with the same linear output current range of $4 - 20\text{ mA}$ for the pressure range of $0 - 60\text{ bar}$.

In-ice connections are done with 10-pin wet-mateable connectors, that have been tested for temperature and pressure. Each of the sensor and transmitter modules is connected to the surface with a cable of eight twisted-pairs that is globally shielded. To reduce electromagnetic interference, this shield is also connected to the housing of the modules and the *acoustic box* on the surface. At each stage the two cables join the bundle of cables from the other stages, that are kept together with a thin yarn. This cable assembly is helically wound around a rope in the centre which supports the weight of the stages. To keep signal damping and cable costs small, all signals are immediately digitised at the surface. Nonetheless, the costs for in-ice cables and connectors amount to more than $1/3$ of the total.

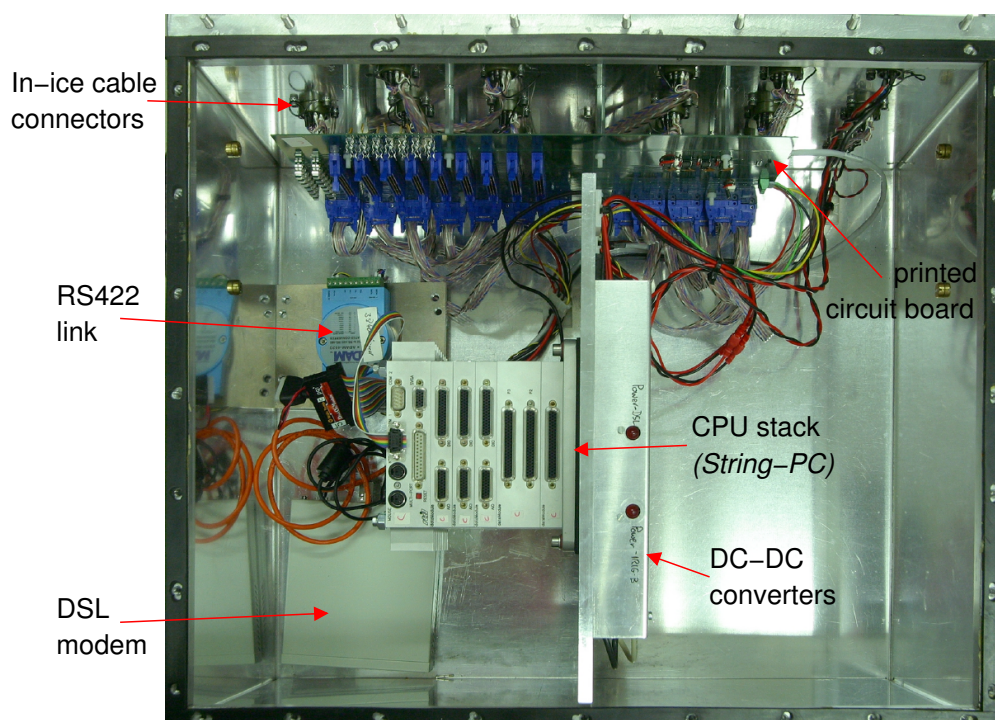


Figure 7.19: Top-view into an *acoustic box*.

All electronic components at the surface are located in the *acoustic box* that is made of a rigid aluminium box of $30\text{ cm} \times 50\text{ cm} \times 80\text{ cm}$. The box, shown in figure 7.19, is split in two compartments. The front compartment (not shown in the figure) holds the sockets for connection of the in-ice cables. Rigid military style but not waterproof connectors are used at this end. In the sealed back compartment that is shown in figure 7.19, all signals are first routed to a printed circuit board, from which they are distributed to the *String-PC*. This board also holds small electronics components such as fuses, line drivers for the transmitter trigger pulses and precision resistors to convert the temperature and pressure signals from $4 - 20\text{ mA}$ to a suitable voltage range.

Expected ambient temperatures at the *acoustic box* can be as low as -60°C , posing strong limitations to the electronics components here. Low-noise DC-DC converters rated for -55°C to $+105^\circ\text{C}$ with an efficiency up to 90% provide the necessary *DC* voltages. The *String-PC* is built from stackable components following the industrial *PC/104* standard, all temperature rated from -40°C to $+80^\circ\text{C}$. The stack consists of

- One **CPU module** with a 600 MHz processors and 512 Mb RAM that cannot only be used for system control and data acquisition but will also allow complex filter algorithms,
- Three **fast ADC boards** with eight differential analogue input channels each and a maximum sampling rate of 1.25 MHz that can be distributed among the channels. The three channels in one sensor module are read out by one of the three different boards each, allowing for synchronous sampling. In addition, analogue and digital output lines allow to control the amplitude and send trigger pulses to the transmitter.

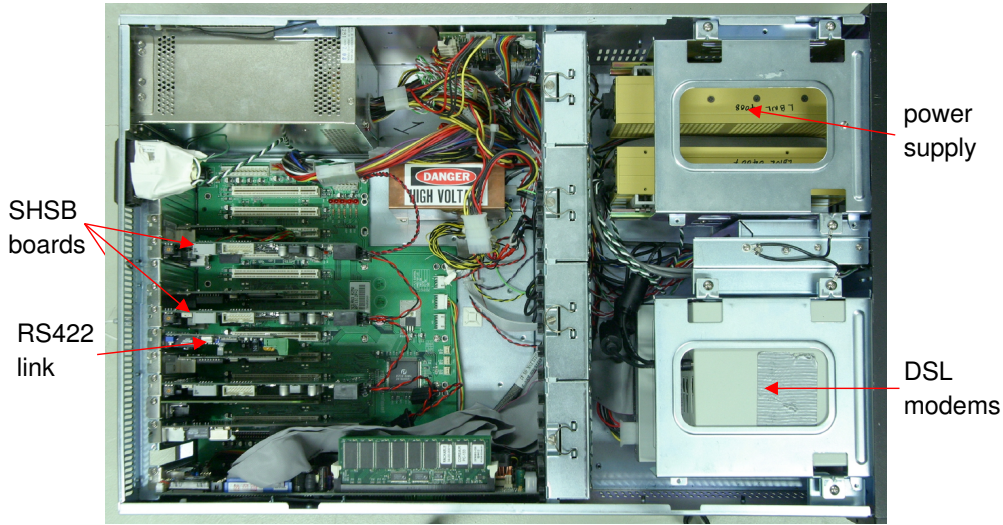


Figure 7.20: Top-view into the *Master-PC*.

- One **relay board** provides 16 relays to switch the power for each sensor and transmitter module on and off separately. The power to the temperature sensors and pressure sensors is controlled by the remaining two relays.
- One **slow ADC board** with a sampling rate of only 500 kHz is used to read back the high voltage pulses.

All acquired data will first be stored on a local flash memory. For transfer of the data to the *Master-PC* and power supply to the *String-PC* restrictions in cost and manpower do not allow deployment of dedicated cables. Instead, two four-wire cables (*quads*) in the ICECUBE cable that is routed from the central computing facility (ICECUBE *laboratory*) to each of the holes is split off at the hole and used to connect the *acoustic box*.

In the ICECUBE *laboratory* the quads from all three strings are joined at the *Master-PC*. A top-view into the *Master-PC* is shown in figure 7.20. Two power supplies within the *Master-PC* provide $+96\text{ V}_{\text{DC}}$ to the *acoustic box*. This comparatively high voltage was chosen to limit cable losses and follow the standard used in other ICECUBE applications. With $\approx 35\text{ W}$ in normal operation and a maximum of $\approx 55\text{ W}$, the power consumption of one *acoustic box* is comparatively low. Nevertheless, one pair in each of the quads is required to keep the voltage drop in the up to 1 km long surface cables below the working limits of the DC-DC converters in the *acoustic box*.

On the remaining two pairs, communication to the *String-PC* is possible in two different ways: A *LAN* connection is provided via a 2.3 Mbps connection using DSL signal encoding. DSL modems are placed at both ends. However, commercially available *DSL modems* were not found with a temperature rating of lower than -20°C . An additional half-duplex serial connection using the RS422 standard provides a backup solution, but with a much more limited bandwidth of only 38.4 kbps.

In addition, an *IRIG-B* standard time synchronisation signal is generated from a *GPS* signal recorded with an antenna outside the *Master-PC* and distributed one pair to all three *acoustic boxes*. This digital signal uses a 10 ms pulse width binary encoding and is sampled at the *String-PC* together with the analogue signals. The edge time and thus the actual timing resolution is much shorter than the pulse width and sub-millisecond timing information can be generated using the timing signal to control a set of hardwired cascaded counters in the *String-PC* stack.

Both DSL and RS422 communication signals and the timing signal as well as the supply voltage are routed through a custom made *PCI* control board, the *SPATS Hub Service Board (SHSB)*. The *SHSB*, not only provides current and voltage control and monitoring to one *acoustic box*. It also offers the possibility to set individual current and voltage limitations. If exceeded, e.g. in case of a short circuit, fast security shutdown of the system is provided by an *FPGA* based control logic. Of the two wire-pairs available for communication and timing signals, one is permanently used for the DSL signal. Controlled by the *SHSB*, the other pair can be alternatively used for the timing or serial (RS422) communication signal.

Finally, the *Master-PC* is connected to the local South Pole network, that can be accessed via a satellite link. Being only part-time available and shared by all experiments at South Pole, this link will provide the main bottle neck for data transfer to the north. The estimated bandwidth that can be allocated for the SPATS experiment is on the order of 50 kbps. Therefore all computers in the setup are running on *Linux* based operating systems, which allows low data rate command line login to the *Master-PC* as well as to the *String-PCs*. Note that the satellite link will mainly be needed for system control and retrieval of test data, while the main chunk of data can be stored on locally available tape drives. However, due to limited access to the South Pole station, transfer of these tapes to the northern hemisphere is only possible during the station opening times in austral summer.

7.4 System verification

Being not only the first dedicated acoustic installation, but also the first experiment extensively using outdoor computing power at South Pole, the SPATS setup is breaking new ground in several respects. The lack of experience with this type of installations makes a most intensive testing of the equipment necessary. These tests have been performed regarding several different aspects of the setup.

7.4.1 Performance at low temperatures

With around -50.9°C , the temperature in the ice is lowest just a few metres below the surface, from where it slowly increases to a value of -49.7°C at 400 m. As a consequence, all in-ice devices have been tested down to temperatures of -55°C in a freezer.

For the acoustic stages repeated functionality tests were performed: the sensors and transmitters were cooled to -55°C , then taken out of the freezer and connected to a small test setup to show basic performance. All 25 sensor and transmitter modules passed this test without problems.

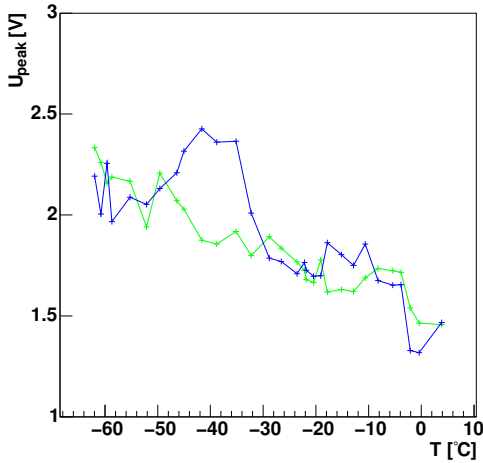


Figure 7.21: Peak-to-peak amplitude versus temperature of two channels of a SPATS module for acoustic transmission through air.

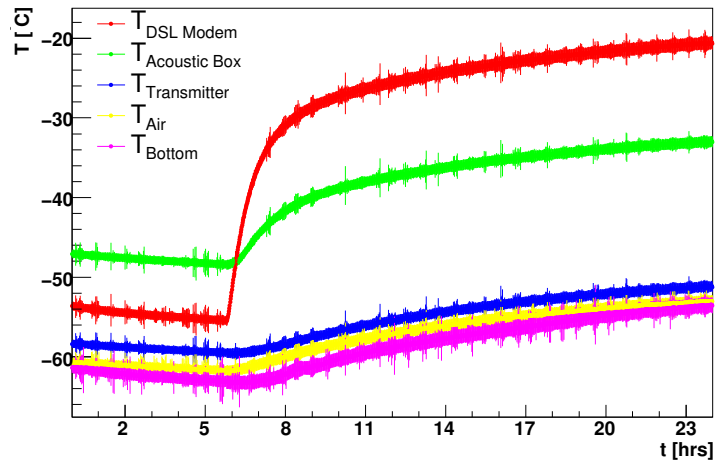


Figure 7.22: Temperature development over 24 hours at different positions in the freezer: at the bottom (pink), in the air next to (yellow) and inside (green) the *acoustic box* and on the outside of the DSL modem (red). The *String-PC* was powered up at 5 : 30 hrs.

A test in ice at different temperatures would have been desirable, but could not be performed due to the low heat conductivity of ice and the very long time needed to cool an ice block to these temperatures with the available equipment. Instead, the temperature dependence has been measured in air [Fis06]. Figure 7.21 shows the increase of the signal amplitude with decreasing temperatures. Although due to the different medium this measurement is not representative in absolute scale, an increase of signal strength with a decrease of temperature may also be expected in an in-ice configuration.

Since the change of ohmic resistance of copper with temperature is well known, the in-ice cables have been mainly tested mechanically at these low temperatures. In a first test using a cheaper cable the outer mantle of the cable became very brittle, making any handling impossible. A more expensive cable using the same type of cladding material as the ICECUBE cables remained elastic in the cold and will be used in the setup.

The *acoustic box* and components therein had to undergo the most extensive temperature testing. The *String-PC* has been tested both within the *acoustic box* and by itself. No problems have been encountered within the specified range of operation. However, in a stand-alone test the *String-PC* would not operate at temperatures below -45°C . A variety of DSL modems have also been tested at different temperatures. While none of them is rated for temperatures below -20°C , with a comparatively large power consumption of $\mathcal{O}(10\text{ W})$ some models showed to heat themselves quickly enough that no external heating is required. This self heating effect has been taken advantage of. Not only is the DSL modem closely mounted to the *String-PC* with good thermal conduction, but in addition both are thermally well isolated from the aluminium housing. Figure 7.22 shows the temperature development in different points of the system when turned on after reaching -55°C at the CPU stack. Self heating is quick enough that both the *String-PC* and the DSL modem turn on almost immediately.

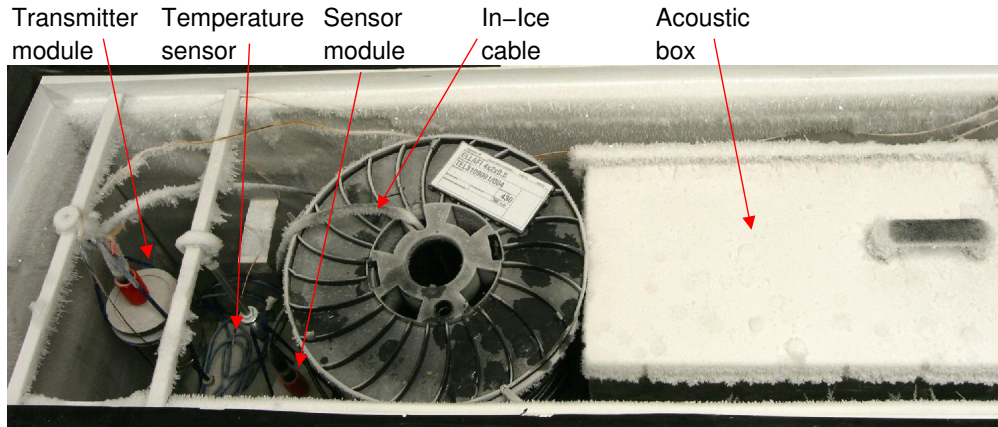


Figure 7.23: Setup of an acoustic stage connected by 430 m test cables to an *acoustic box* in the freezer.

Figure 7.23 shows the setup in which these measurements have been performed. A sensor and a transmitter module is suspended in a freezer in air, connected by two 430 m test cables to an *acoustic box*. Snow is accumulated around the freezer to simulate conditions in the firn. Temperatures are read out every minute at various points in the setup. Together with the *acoustic boxes* in the fridge, two other *acoustic boxes* are connected to the *Master-PC* to study inter-string effects. This installation remained for a period of several months to explore the long-term behaviour of the equipment. Temperatures down to -60°C inside the *acoustic box* in the freezer were reached in the test, throughout which the performance remained perfectly stable for the whole time.

7.4.2 Interference with ICECUBE

Extensive studies have also been performed to ensure that no interference of the SPATS equipment with the ICECUBE installation occurs. The in-ice part is well separated from the shielded ICECUBE cable, so that electromagnetical interference can be practically excluded in this part. Only for communication from the *acoustic box* to the *Master-PC* a common cable is shared with the ICECUBE experiment. Different quads (i.e. different four-wire sub-cables) in that main cable are used by the different experiments. Lacking such a multi-quad cable, the following tests have been made on a single quad, with one pair in the quad used for power supply, time code signals or DSL communication for the SPATS setup and the other pair used for ICECUBE communication or time synchronisation. No effect at all has been observed on the ICECUBE communication. For ICECUBE time calibration, short bipolar pulses are sent from the surface to the in-ice modules (*DOMs*) and after a fixed delay back to the surface. The time delay is estimated from the zero-crossing of the bipolar pulse and the timing resolution given by the spread of these time delays. With a *DOM* connected to one pair of the quad and the other pair not connected a timing resolution of $0.67 \pm 0.3 \text{ ns}$ was obtained. No effect on the timing resolution has been observed with the other pair in the quad used for power transmission under varying load conditions. Also the *IRIG-B* time coding signal did not affect the ICECUBE timing. Only for DSL communication on the

other pair, an increase of the timing resolution to 3.31 ± 0.1 ns has been observed for the maximum communication speed of 2.3 Mbps. This is however not a critical effects since

1. the inter-quad crosstalk is expected to be smaller than the cross-talk within one quad.
2. the communication speed of the DSL modems can be adapted to lower values. For 1 Mbps the measured timing resolution is 1.14 ± 0.4 ns and 0.67 ± 0.5 ns for 200 kbps.
3. the observed timing resolution for *DOMs* already installed at South Pole has shown larger values than under the laboratory conditions found here, so that the relative effect is smaller. The ICECUBE specification limit is 3 ns.

7.4.3 Performance over long distances

Only the holes that will be drilled in the season where the SPATS setup will be installed can be accessed to deploy acoustic stages. For measuring absorption, to obtain a maximal effect the largest possible distance is sought for. For the planned installation season, this maximal distance will be in the range of ≈ 450 m. To test the performance of SPATS on these distances, a long-range test has been performed at a large lake in north Sweden, yielding a first glimpse of the performance of the setup as will be described here.

Location and setup

In any water volume, signals are quasi totally reflected at the surface due to the abrupt change in impedance. In order to obtain a long base line at good free-field conditions, the water volume has not only to be large but also deep enough. First tests were done at the only 3 – 5 m deep *Zeuthen* lake, which is conveniently located close to the institute where the setup has been developed. They showed a strongly distorted long distance behaviour, probably due to interference of the direct and reflected signal [Ste04]. Only a rather limited distance range could be tested in this first attempt. An effort to enlarge the range using a boat instead of a pier did not give satisfactory results due to instability of the positioning of the acoustic devices.

To obtain larger distances in an easy fashion, test have also been done in the water when the lake was frozen. Drilling small holes through the ice surface allowed quick installation at various distances covering a range up to 100 m. Yet in addition to a high ambient noise level, these measurements were again affected by marginal free-field conditions due to the low depth of the lake.

To circumvent these problems but maintain the ease of installation on a frozen lake, finally lake *Torneträsk* ($68^{\circ}21'N, 18^{\circ}49'E$) was chosen as a site. The lake has an average depth of 52 m and was covered by an ice sheet of ≈ 90 cm in March 2006, when the measurements took place. The necessary infrastructure, such as ice-drilling equipment and a shelter for data acquisition, was kindly provided from the ABISKO SCIENTIFIC RESEARCH STATION in THE ROYAL SWEDISH ACADEMY OF SCIENCES.

Figure 7.24 shows a picture of the measurement setup. A stage and a transmitter were connected to an *acoustic box* by 420 m in-ice cables as used in the SPATS setup. Via a short

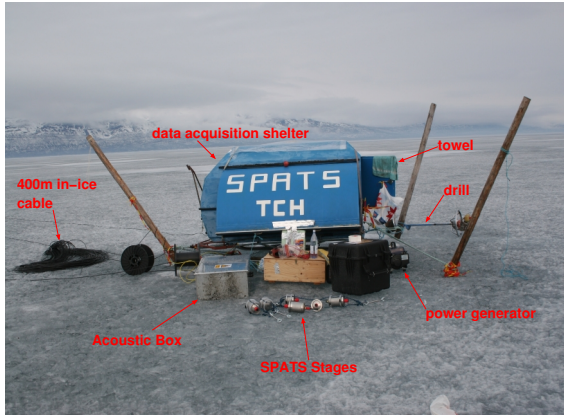


Figure 7.24: Picture of the equipment used in the long range SPATS module test at the frozen lake *Torneträsk* in northern Sweden.

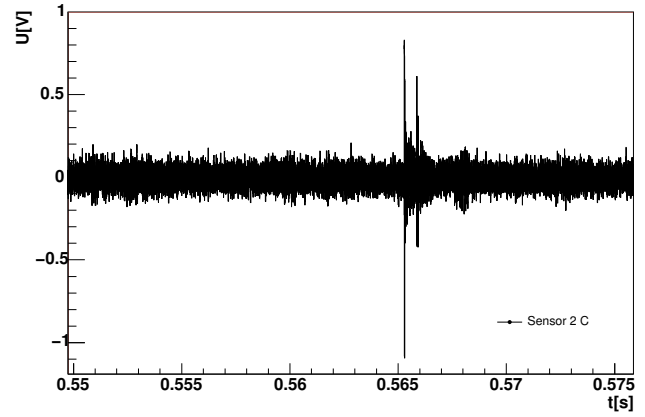


Figure 7.25: Signal from a SPATS transmitter recorded with a SPATS sensor at a distance of ≈ 800 m in water.

LAN cable, the *acoustic box* was connected to a laptop computer, which was operated inside a temporary data acquisition shelter (*Temporary Counting House, TCH*). From this laptop computer all data acquisition was controlled. Weather conditions were favourable, with air temperatures ranging from -5°C to $+5^{\circ}\text{C}$. Only on one day measurements were rendered useless by a hail storm inducing very high acoustic noise levels in the water. Yet flawless operation in these harsh conditions gave trust in the robustness of the SPATS system.

All measurements were carried out using one receiver and one source at a time. SPATS sensors and a calibrated reference hydrophone were used as receivers, whereas only SPATS transmitters were available as a source. Holes were drilled through the ice at the *TCH*, in distances of 100 m, 180 m and 400 m to one direction (for convenience labelled *north*) and at 180 m and 400 m in the opposite directions (labelled *south*). Figure 7.26 shows the scale of the setup. From geographic maps a flat floor of the lakes in a depth ≈ 70 m was found over the range of the installation. During all measurements, either the sender or the receiver was kept stable at one position, while the other was lowered by hand in the hole in steps. Data was recorded every 2 m for a depth from 6 m to 42 m. Figure 7.25 shows the recorded signal from a measurement with both a SPATS sensor and transmitter at a depth of ≈ 30 m at about 800 m distance from each other. The signal is delayed by more than 0.5 s due to



Figure 7.26: Picture of the large scale setup at Abisko: the position of the data acquisition shelter, the 400 m *north* hole and the 400 m *south* hole (outside the picture on the left) are indicated.

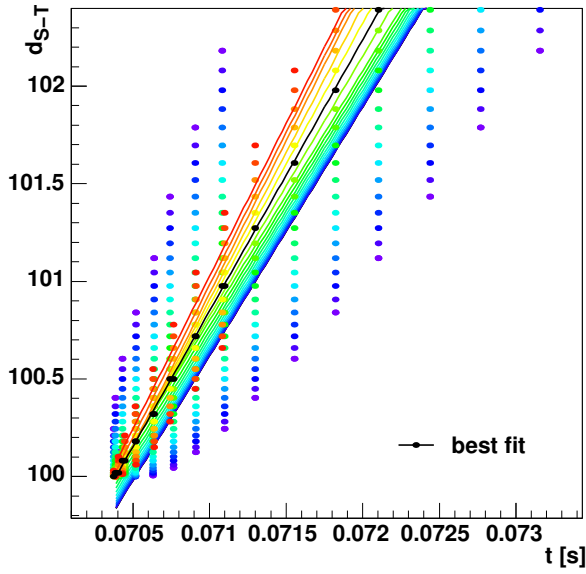


Figure 7.27: Calculated sensor transmitter distance d_{S-T} vs. signal arrival time for different assumptions of the transmitter depth (colours) and best fit values.

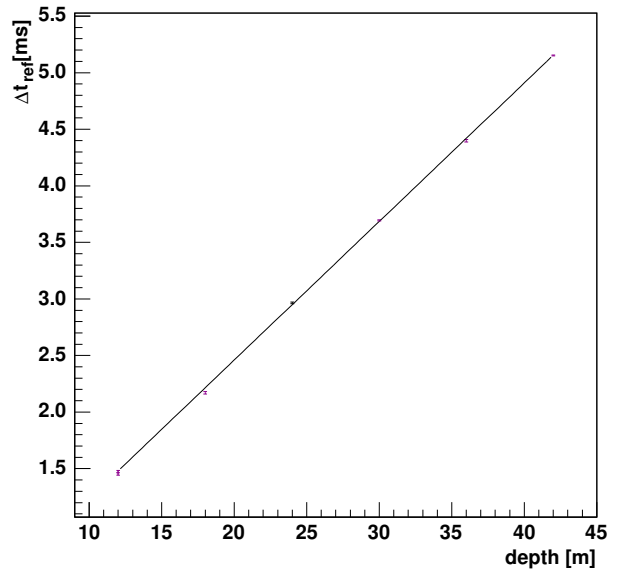


Figure 7.28: Delay Δt_{ref} of reflected signal relative to the direct signal vs. depth of the sensor. The solid lines is a theoretical prediction (from [Des06]).

propagation in the water. Despite the large distance a good signal-to-noise ratio of $S/N > 10$ is obtained. A clearly separated second pulse from the reflection at the surface is observed shortly after the direct signal.

Speed of sound and reflections

The arrival times of the signals can also be used to precisely measure the positions of the fixedly installed module, which may be systematically affected by stretching of the cable it is hanging from. The temperature profile of the lake – measured independently by the temperature sensors installed in the SPATS module and a $100\,\Omega$ platinum resistor in a 4-wire configuration – showed values close to zero with less than 0.6°C variation over the full depth range. No strong effects from refraction are therefore expected. The signal arrival times should then linearly correspond to the geometric distance from sensor to transmitter d_{S-T} . For a 100 m distance setup using the hydrophone, figure 7.27 shows the signal arrival times in dependence of the geometric distance d_{S-T} . This distance is calculated for a small range of transmitter depth around the nominal value. Values for each assumed transmitter depth are displayed in a different colour in figure 7.27. A linear fit can be used to test the transmitter depth hypothesis. By minimising χ^2 the best fit is found for a transmitter depth of 32.1 ± 0.1 m. Compared to a nominal value of 30 m this is in good agreement if accounting for some stretching of the rope on which the transmitter module is mounted. The velocity of sound is obtained from the slope of the fit as $v_l = 1402.1 \pm 2.4 \frac{\text{m}}{\text{s}}$ in accordance with the predicted value of $1404.4 \frac{\text{m}}{\text{s}}$ [Cop81]. The offset of the fit for $t = 0$ s finally reveals also the systematic offset in the distance measurement of 1.3 m.

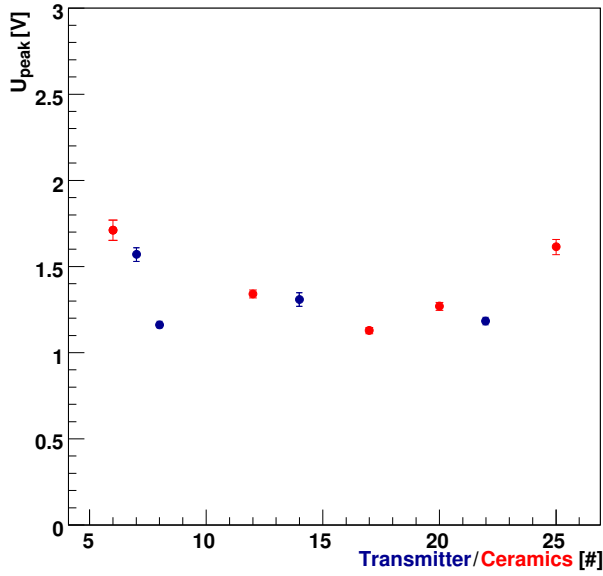


Figure 7.29: Variation of signal amplitude for different transmitter modules and different piezo-ceramics at the same transmitter module at a distance of 100 m averaged over the depth (from [Des06]).

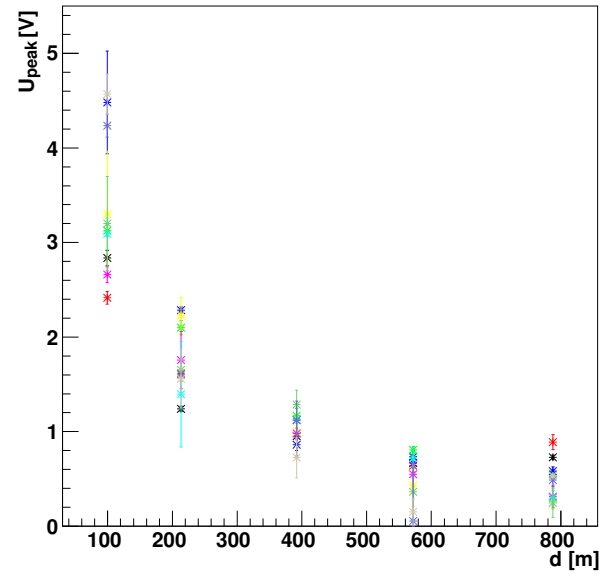


Figure 7.30: Signal amplitude averaged over 10 events for various distances and depth (colours) using different transmitters (from [Des06]).

More information on positioning can also be obtained from the reflected signal. For a horizontal distance d from sensor to transmitter the travel time of the direct signal is given by

$$t_{\text{direct}} = v_l^{-1} \sqrt{d^2 + (z_S - z_T)^2}, \quad (7.1)$$

whereas for the reflected signal we obtain

$$t_{\text{ref}} = v_l^{-1} \sqrt{d^2 + (z_S + z_T)^2}. \quad (7.2)$$

For transmitter and sensor depth $z_{S|T} \ll d$, the travel time difference $\Delta t_{\text{ref}} = t_{\text{ref}} - t_{\text{direct}}$ can be very well approximated by a linear relation, as also observed in the data shown in figure 7.28. The arrival times of the reflected signal can thus be used to further constrain the geometric situation. At the same time the good agreement with the predictions shows once more that refraction is negligible in this configuration.

After verification of the geometry, the amplitudes can be used to gain more information on the SPATS sensor and transmitter modules. Due to time limitations, only measurements for one polar and azimuthal angle could be performed in the water calibration efforts described in section 7.2 for each sensor module channel. Also for the transmitter modules, only data in the plane of the transmitter ceramics has been taken. Knowledge about the polar variation of the emission is based on a measurement of on a single piezo-ceramic element. In the installation process of the setup at south Pole, the modules will be free to assume any azimuthal orientation. While the polar angles of the modules themselves should be rather well constrained by the weight of the acoustic string itself, the short cable supporting the

transmitter ceramic may be bend before or in the installation process, allowing for significant deviation from a vertical orientation.

To assess the variability introduced by these effects, investigations with a SPATS sensor fixedly installed in the 400 m *south* hole at a depth of -30 m throughout the measurement have been performed. At the *TCH*, different transmitter modules and a single transmitter module with different piezo-electric transducer elements installed were consecutively lowered in the water over a range from -6 m to -46 m. At this large distance, only a small polar angle is covered and no significant variation in sensitivity of the sensor module is expected. The obtained variation can rather be attributed to azimuthal dependence of the transmitter emission, that may turn when lowered into the hole. Consistent with previous measurements on a single ceramic, an RMS spread of $\approx 40\%$ is found for the different transmitter modules as well as for the different piezo-ceramics on the same module. Signal amplitudes averaged over the full depth range for the single modules and single ceramics with statistical errors from the measurement are shown in figure 7.29.

Keeping this result in mind, now also the signal amplitudes at other distances can be investigated. Figure 7.30 show measurements where this time the transmitter remained untouched, while the sensor was taken to different depths and distances. Each colour represents the measurement at one depth. The error bars give the statistical error over the 10 events that were recorded. Close to the transmitter, a larger polar angle is covered by the depth range covered by the sensor. So in addition to azimuthal variations, also polar variations have to be taken into account. For large distances azimuthal variations should be dominant. From this data, the variability of the sensor module sensitivity with azimuthal and polar variation can be determined, with a combined value of $\approx 60\%$ [Des06].

Regardless of the large uncertainties, also an estimate of the absorption length has been tried. Given the large errors, only upper limits could be derived using the data obtained at the different depth levels independently. While each of the single estimates will not yield a significant limit on the absorption length, from a combination of the results a lower limit in the range of $\mathcal{O}(1 \text{ km})$ has been obtained [Des06]. Using the polar and azimuthal uncertainty values calculated above, the limitation power of the full SPATS setup can now be estimated using a more advanced method as will be shown in the next section 7.5, by which despite the much shorter baseline, similar limit values can be obtained.

7.5 Principle of measurements and performance estimates

As mentioned above, three main targets shall be addressed with SPATS– measurement of the absorption length, the sound velocity profile and the ambient background noise. The expected capabilities of the setup with respect to these measurements will be outlined in the following.

7.5.1 Ambient background noise

Because of the problems described in section 5.3.3 no absolute calibration of the sensors in ice is currently available. So the absolute amplitude of the ambient background noise cannot be measured. However, it is expected that the ambient noise is very small and probably

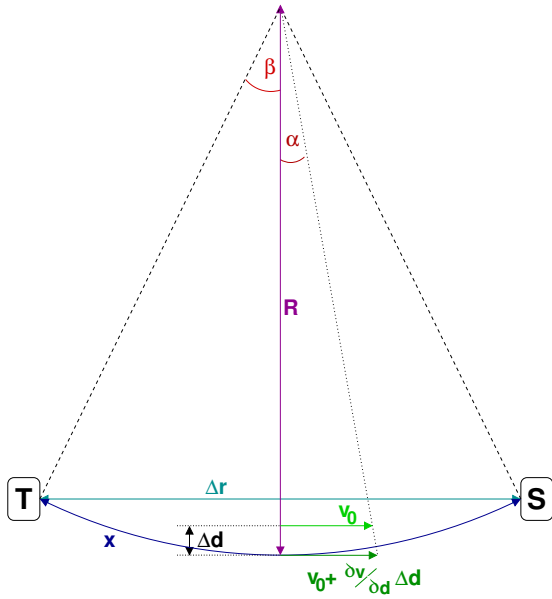


Figure 7.31: Scheme of a refracted acoustic wave emitted from transmitter T and received by sensor S. In the presence of a velocity gradient $\frac{\partial v}{\partial d}$ the wave will travel along the curved path x .

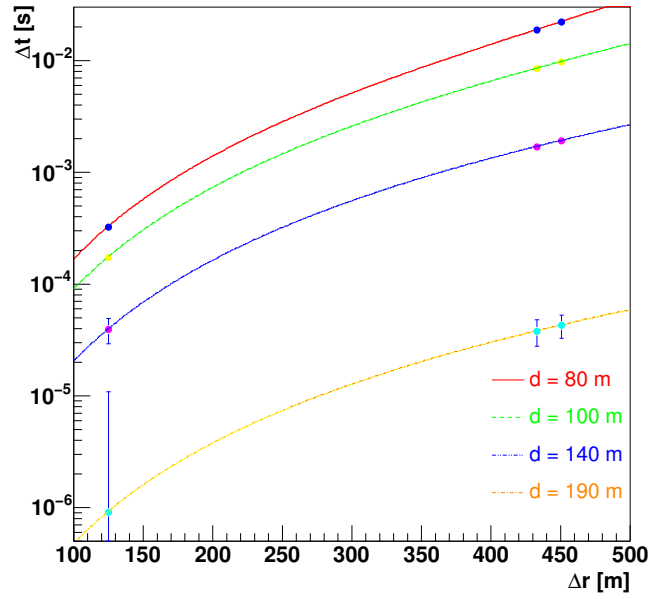


Figure 7.32: Arrival time delay Δt at different sender-receiver distances Δr as expected at different depth levels d . The points and error bars show the expected configuration in the SPATS setup.

below the self noise level of the SPATS sensors. In this case, the noise level of the sensors installed in the ice can be compared to the purely electronic self noise levels of the sensor as measured in the lab. In addition, even in the absence of a calibration it is a reasonable assumption that the sensitivity of the SPATS sensors in ice is not smaller than in water as discussed in section 5.3.3. Thus, if no excess is found in any channel a limit on the self noise can be deduced which is at the level of the equivalent self noise level of the SPATS sensors in water.

Different to the characterisation of the constant ambient noise, for short transient noise events not so much the amplitude but more the frequency of occurrence is important. These events might be generated e.g. due to anthropogenic activities at the surface of the ice or cracks in the bulk ice or at the very bottom from the tension generated in the glacial movement. For the first case, due to the strong refraction only a very small amount of the signal is expected to reach the array. For the latter case, these events might be identified either by their vertex or their supposedly isotropic emission. With no specific source being known and hence no features of these events, any statement on the possibility to reject these events remains speculative.

What can be learned from SPATS about ambient noise in the south polar ice can only be said after the data from the installation will be available.

7.5.2 Refraction and velocity of sound

If signal amplitudes are large enough to be clearly separated from the noise, for measuring the velocity of sound and the refraction, only signal travel times and the geometry are important. In case of SPATS, both parameters can be obtained at each depth level using only the three sensors and transmitters at this level.

In order to calculate the effect of refraction, imagine a planar vertical wave front at a depth d . In the presence of a velocity gradient $\partial v/\partial d$, the central part of the wave front will travel with the speed $v_0(d)$, whereas at a slightly larger depth $d + \Delta d$ the wave front will travel at speed $v_0(d) + \partial v/\partial d \Delta d$, as illustrated in figure 7.31. As a consequence the acoustic wave will not propagate straight, but on a curved path. After a short travelling time dt , the angle α of the wave front with respect to the vertical is given by $\tan(\alpha) = \partial v/\partial d dt$. The local curvature radius $R(d)$ is then given by

$$R(d) = \frac{v_0(d) \cdot dt}{\tan(\alpha)} = \frac{v_0(d)}{\partial v/\partial d} . \quad (7.3)$$

If now the distance from sensor to transmitter $\Delta r \ll R$ as for most depths of the SPATS setup, $\partial v/\partial d$ does not change along the propagation path, which can be approximated by a segment of a circle. The length of the segment $x = 2\beta R$, with $\sin(\beta) = \Delta r/2R$. To calculate the travel time delay with respect to a straight propagation, in principle not only the path elongation due to curvature but also varying propagation speed along the path have to be taken into account, but will be neglected here for simplicity. Instead the wave is assumed to travel with speed v_0 along the whole path.

The deviation in arrival time Δt as compared to a straight propagation is then given by

$$\Delta t = \frac{2}{\partial v/\partial d} \arcsin\left(\frac{\partial v/\partial d \Delta r}{2v_0(d)}\right) - \frac{\Delta r}{v_0(d)} . \quad (7.4)$$

Figure 7.32 shows this time delay in dependence of Δr for the first four depth levels d of the SPATS setup with $v_0(d)$ and $\partial v/\partial d$ estimated from figure 3.20. The points indicate the distances that will be realised in the SPATS setup, together with an estimate of the error on arrival time and distance measurements.

While the position of the holes themselves will be very accurately measured, the main uncertainty in the horizontal positioning of the stages will be due to non-straightness of the hole. Inclination data taken during the drilling of previous holes showed a horizontal deviation from vertical of up to ≈ 2 m over the full drilling depth of 2450 m. Given that only the first 400 m of these holes will be used for SPATS, where the drilling is supposed to be much more stable, and accounting for another 0.5 m uncertainty due to free placement of the acoustic string within the ICECUBE hole a total distance uncertainty of 2 m is assumed. The contribution from the uncertainty in vertical positioning – which is of the same order of magnitude – is negligible. The timing precision of the *IRIG-B* time signal sampled at the *acoustic boxes* has been measured using a very stable function generator. From the function generator, a square wave signal with the same number of edges in a certain time interval was sent to the *ADCs* of the *String-PC* over a short cable.

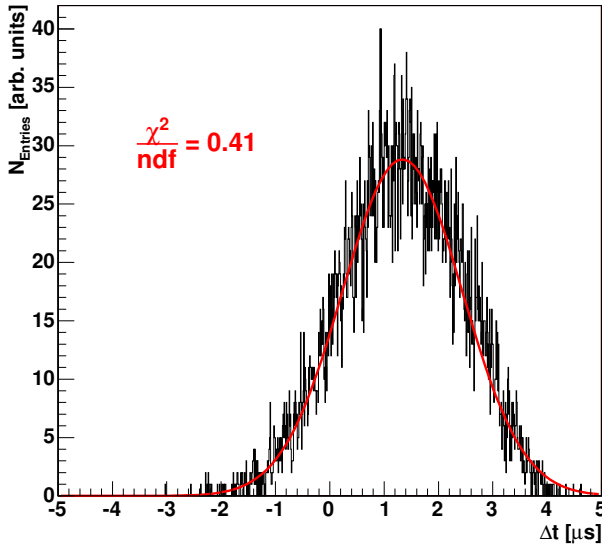


Figure 7.33: Offset corrected time difference of rising edges from external square wave and *IRIG-B* time code.

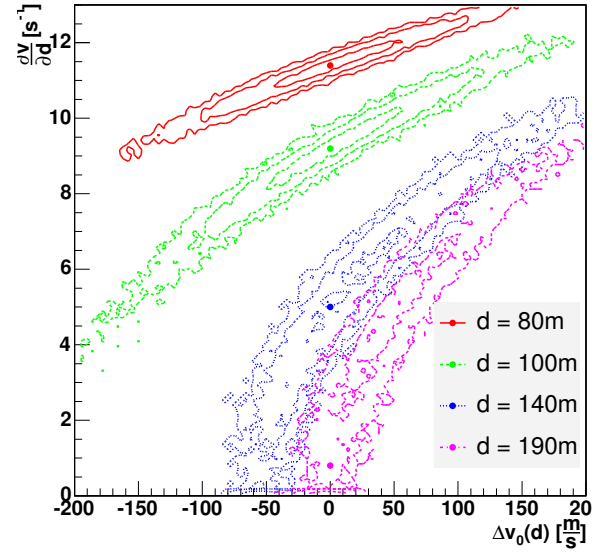


Figure 7.34: Distribution of resulting velocity gradients $\frac{\partial v}{\partial d}$ and difference to nominal speed of sound Δv for fits to the simulated time and distance measurements for various depth levels d . The contour lines show 50 %,10 % and 1 % of the peak values, the dots give the nominal values.

Figure 7.33 shows the distribution in difference of arrival time for the edges from the sampled square wave to the edge of the *IRIG-B* time signals. A linear offset accounting for the slightly different frequencies of the timing signal and the square wave has been subtracted. The distribution is gaussian, with an RMS spread of $1.09 \mu\text{s}$, close to the sampling resolution of $0.8 \mu\text{s}$. The main contribution to timing uncertainty is therefore assumed to come from the phase response that varies from sensor to sensor. An inverted phase at all frequencies will simply invert the signal shape, but other cases might lead to a slower rise of the signal above the chosen threshold. As a conservative estimate, one half of the initial cycle of the signals that were measured in a large lake (see section 7.4.3) was taken. The corresponding $50 \mu\text{s}$ were used as an estimate for the signal arrival time uncertainty at all sensors. To determine the effect on the measurement, the nominal values for the three sensor transmitter distances shown in figure 7.32 were varied within the given uncertainty. The resulting values were fitted with the function in equation 7.4. Figure 7.34 finally shows the distribution of the obtained difference $\Delta v_0(d)$ to the nominal value $v_0(d)$ versus the $\frac{\partial v}{\partial d}$ obtained from the fit. Contour levels at different height of the peak values and nominal values are given for the first four depth levels in SPATS.

Since additional time delay is obtained from increased curvature or slower sound propagation, at low depth levels, where the refraction is strong, the uncertainties in $\frac{\partial v}{\partial d}$ and $v_0(d)$ are highly correlated. For deeper levels, the curvature is smaller making the $\frac{\partial v}{\partial d}$ measurement less precise. At the same time, propagation is more like in the non-refracted case, which decreases the error on the determination of $v_0(d)$.

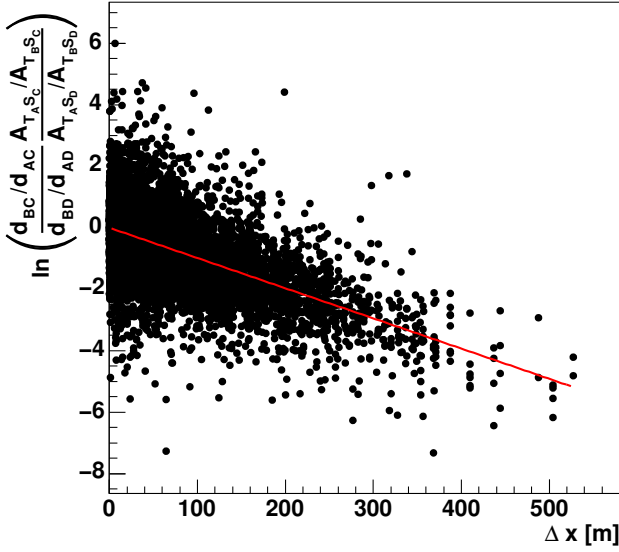


Figure 7.35: Sensitivity and transmittivity independent amplitude ratio vs. distance for one possible detector configuration. The red line indicates the fit result.

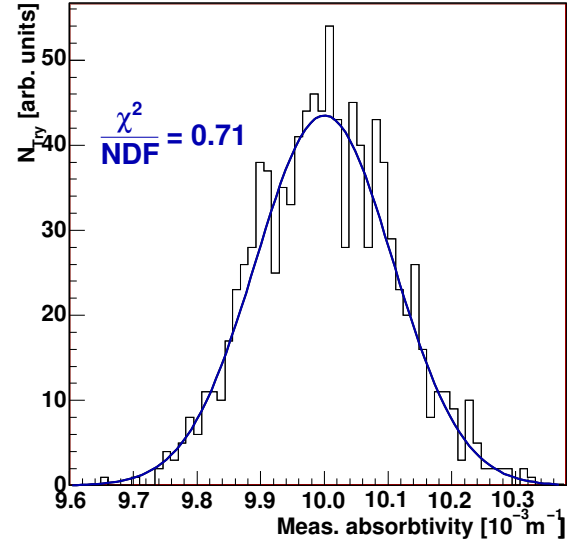


Figure 7.36: Distribution of absorptivity derived from the fit. The blue line shows a Gaussian fit to the distribution.

It must be noted that for the 80 m depth level, $R/d \approx 1$ and the approximations above are actually not valid. In addition, for a proper evaluation, the additional time delay due to varying speed of sound along the propagation path cannot be neglected. On the other side, great improvement is expected from obtaining more constraints by using signals travelling from one depth layer of the setup to another. Considering also the crude estimates on the uncertainties, the above results should only be regarded as qualitative but not quantitative.

7.5.3 Absorption length

For the measurement of the absorption length, again the main limitation is the missing absolute calibration of sensors and transmitters. While for this reason, no conclusion on absorption can be done with a single sensor and transmitter pair, the multitude of sensors and transmitters in the SPATS setup still allows conclusions on absorption length by comparison of different sensor-transmitter pair combinations.

A numerical study has been performed in order to derive the potential of the setup in this respect. The amplitude $A_{T_AS_B}(d_{AB})$ measured at a specific sensor B of a signal generated by a certain transmitter A at a distance d_{AB} is supposed to be given by

$$A_{T_AS_B}(d_{AB}) = \frac{1}{d_{AB}} S_B \cdot T_A \cdot e^{-\alpha d_{AB}}, \quad (7.5)$$

where S_B and T_A are the sensitivity and transmitter amplitude of the sensor and transmitter module respectively. The absorptivity α in principle is depth dependent, but as shown in figure 3.23 the variation is supposed to be no more than 10 % over the range of depth covered by the SPATS setup. For simplicity, a constant absorption value is adopted. Also refraction

in the ice is neglected, which will enhance the path length of the signal and slightly increase absorption effects. Refraction will also cause defocusing of horizontally emitted waves, which will lead to systematically lower amplitudes at larger distances. Neglecting these effect in first approximation straight geometrical distances and a $1/d$ dependence of the signal amplitude on the distance will be assumed here.

In absence of any knowledge on sensitivities and transmitter efficiencies, using a pair of sensors S_C and S_D and a pair of transmitters T_A and T_B one can then build following amplitude ratios:

$$\frac{d_{BC}/d_{AC}}{d_{BD}/d_{AD}} \cdot \frac{A_{T_A S_C}/A_{T_B S_C}}{A_{T_A S_D}/A_{T_B S_D}} = e^{-\alpha((d_{AC}-d_{BC})-(d_{AD}-d_{BD}))} =: e^{-\alpha \Delta x} . \quad (7.6)$$

Theoretically, this eliminates any dependence on the sensors and transmitter performance, so that one of the measurements would yield the absorption length. In reality, however, both sensors and transmitters do not have a uniform emission or sensitivity in all directions. For the transmitters, the non-uniformity has been measured for one transmitter as shown in figures 7.15 and 7.16. Assuming a random azimuthal orientation and a polar angle range according to the setup geometry described in section 7.1, a variation of $\Delta T \approx 40\%$ has to be taken into account. Using the data taken in the lake setup described in section 7.4.3 where either sensor or transmitter were fixed while changing the other without control over azimuthal orientation and comparing different depth levels to account for polar variations, the same value could be established for the angular variance of $\Delta S \approx 40\%$ in the sensor response.

This uncertainty will enter equation 7.6 for each sensor and transmitter module, i.e. twice for all four amplitudes, resulting in a total uncertainty of $\sqrt{4 \cdot (\Delta S^2 + \Delta T^2)} = 113\%$, rendering a single measurement practically useless.

Yet, as many as 8820 of these amplitude ratios can be built, if cases with sensor and transmitter on the same stage or in the same hole are excluded. Figure 7.35 shows the outcome of a potential measurement, using the detector configuration introduced in section 7.1 and including one possible realisation of the configuration uncertainties stated above for every possible combination. The absorption length was assumed to be 100 m. A clear dependence of the logarithm of the amplitude ratio on the distance is obtained from the multitude of possibilities. The red line in figure 7.35 shows the result of a linear fit to the points, the slope of which gives the estimate of the absorptivity that would have been obtained in the measurement. Confidence intervals for these *measured absorptivity* can now be constructed by repeating the procedure for another realisation of the configuration uncertainties. Figure 7.36 shows the resulting absorptivity value distribution for 1000 different realisations of the configuration uncertainties. The distribution is gaussian, with a central value very well fitting the input absorptivity. The uncertainty for a real measurement following the same procedure can then be estimated from the RMS width of the distribution.

To establish the validity of the approach, the procedure has been repeated for different values of the input absorptivity ranging from $(30 \text{ m})^{-1}$ to $(21870 \text{ m})^{-1}$. Figure 7.37 shows the resulting mean values of the obtained absorptivity distribution, which are in very good agreement with the assumed input absorptivities. In addition, the RMS spread of the obtained distributions is shown, which is on average $\langle \sigma(\alpha_{meas}) \rangle = 0.1074 \pm 0.0052 \text{ km}^{-1}$, independent of input absorptivity.

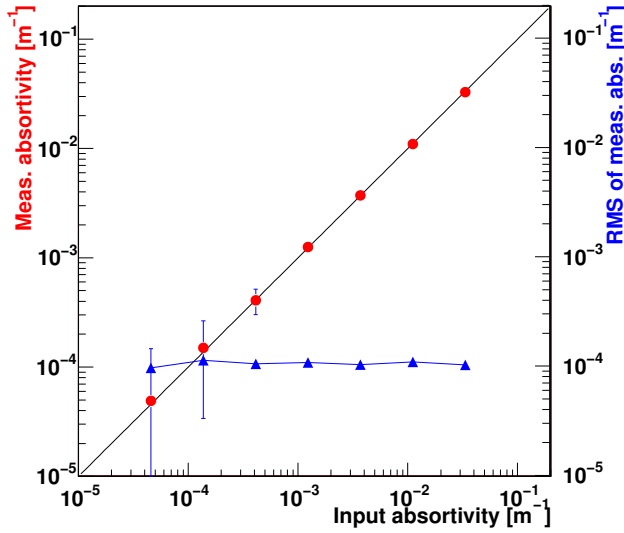


Figure 7.37: Derived mean absorptivity (red points) and Gaussian error (blue points and lines) vs. input absorptivity.

e.g. that for 68 % of the hypothetical configurations (or with a 68 % probability for the one configuration that will be present), the constraints that can be set on the absorption length will range from $\lambda_{abs} > 1.80 \text{ km}$ to $\lambda_{abs} > 2.94 \text{ km}$, assuming the same confidence of 3σ . Note that these results might still be improved, if e.g. the values of T_A and T_B are not assumed to be random. Relative transmission powers have been measured as shown in figure 7.18, that should be the same for water as for ice.

In summary, it can be stated that while SPATS will be able to address all relevant issues for acoustic neutrino detection, it might not yield definite measurements on noise levels and absorption length. Provided favourable conditions in the polar ice, an extension of the array to larger distances or a more sensitive instrument might be needed to obtain accurate values — the realisation of which should be beyond question in this case. In any case, SPATS will provide the largest test setup for acoustic neutrino detection, and thus also serve as a test-bed not only for data handling such as background reduction, etc., but also for technical issues such as acoustic sensor and transmitter operation in the antarctic ice, CPU operation in extreme environments and many more. As every first attempt, it will yield a rich number of results, the span of which is hard to foresee.

The precision of the measurement will therefore not depend on the actual value of the absorptivity. Yet interpretation of the result has to be taken with care. Only for an absorptivity larger than $3 \langle \sigma(\alpha_{meas}) \rangle = 0.323 \text{ km}^{-1}$ (i.e. absorption length **smaller** than $\lambda_{abs} = 1/\alpha_{abs} = 3.10 \text{ km}$) positive evidence of absorptivity at a 3σ confidence levels will be possible. Assuming an absorption length $\lambda_{abs}^{theo} \approx 8 \text{ km}$ as predicted by theoretical calculation, only limits will be possible to set on the absorption, the power of which will depend on the actual outcome of the measurement. The probability of obtaining a certain limit can also be obtained from the probability distribution of measuring a certain value α_{meas} for a given input absorptivity. It can thus be stated

Chapter 8

Summary and outlook

A careful analysis of the existing prerequisites presented in chapter 3 showed, that the detection of neutrinos by acoustic waves is a promising method to extend and complement the radio and optical detection methods at South Pole. Neutrino interactions will yield dense hadronic and electromagnetic cascades. At energies in the EeV range as discussed here, the latter will be significantly extended by the LPM effect. This will reduce the energy deposit per unit volume, the resulting thermal expansion and hence also the acoustic signal amplitude. The main contribution to acoustic waves comes from the hadronic showers initiated in the recoil of the nucleus. Hadronic showers are significantly more compact even at EeV energies and also show less fluctuation in the shower development. Their longitudinal and radial profiles can be well described by Monte Carlo simulations of only a few events.

Knowing the spatial distribution of the energy density deposited in the cascade, the acoustic signal amplitude can be calculated in liquids by integration over the Kirchhoff equation 3.13. Using different parametrisations for the profile of the cascade, a number of independent results have been obtained for sea water. All of them predict a bipolar pressure pulse in a ring around the shower axis that radially expands with time. The signal is highly collimated in the plane perpendicular to the shower axis. The peak amplitude of the bipolar pulse was found to be especially sensitive on the core density of the shower.

In solids, the possibility of shear waves requires a more detailed treatment of the thermo-acoustic mechanism of sound generation. By derivation of the respective wave equations in section 3.4.2, it could be shown that no transversal waves will be generated in an isotropic solid. For ice, which has an hexagonal crystal structure, quantitative arguments are given to demonstrate that the excitation of the quasi-longitudinal mode in hexagonal ice is nearly as effective as in the isotropic case. Signal predictions for neutrino interactions in ice can therefore be obtained the same way as in sea water. Due to a higher Grüneisen parameter, the amplitudes will yet be significantly larger. By qualitative reasoning, excitation of shear waves from the quasi-longitudinal waves at crystal boundaries was also shown to be negligible for the small sizes and random orientations expected for the ice crystal at South Pole in the depth range that is of interest.

From a theoretical calculation of the expected absorption length, the upper few hundred metres were identified as most promising for acoustic detection as discussed in section 3.5. For larger depth, the increasing temperature will increase the absorptivity, which in contrast to sea water is independent of the wavelength in the frequency range 10 – 100 kHz of the thermo-acoustic signal in ice. Scattering was found to be negligible for practically the whole

frequency range of interest. A sound velocity profile was derived over the full depth range, showing that refraction is strong in the upper 200 m, but small at greater depth. This provides a natural protection against anthropogenic noise from the surface. Other well-known sources of background noise that hinder acoustic detection in the oceans, such as waves and animal sounds, can be excluded as well.

The detection threshold of an acoustic array will critical depend on the equivalent self noise level of the ultra-sonic sensors. In the absence of commercially available solutions, an own development of acoustic sensors for in-ice application was started. Different glaciophones with varying levels of complexity were realised and are described in chapter 5. In the simplest approach, a single channel sensor was built from a piezo-ceramic element and a three-stage low-noise amplifier that are cast into epoxy resin. Several ceramic-amplifier channels were also combined in pressure housings made from either steel or glass. Using the reciprocity of the piezo-electric effect, suitable high-power transmitters could be developed along with the sensors. The calibration in water presented in section 5.3.2 showed that despite a strongly non-uniform frequency response, very high sensitivities at a very low self noise level could be reached. Significant improvement in the effective detection threshold with respect to a commercial hydrophone was found. In the same effort, a new calibration method based on short single broadband pulses could be established and gave results in very good agreement with the existing gated burst method. This method proved advantageous especially in small calibration volumes with limited free-field conditions.

Yet, no such calibration in ice could be achieved. Due to the small heat conductivity, the production of large ice blocks is extraordinarily time consuming. If freezing from top to bottom, trapped oxygen will form bubbles that will significantly affect the propagation of sonic waves. Still blocks of clear ice with a volume exceeding 200 dm³ could be achieved by circulating the water during the freezing process as described in section 5.3.3. Only one possible configuration can be realised in an ice block at a time, further limiting the possible number of tests. Despite these restrictions, a qualitative evaluation of the developed sensors could be obtained favouring the steel-housed sensors. Several proposals were made for a quantitative measurement of glaciophone sensitivities using either large natural occurrences of ice, beamed emitters or changing boundary conditions to allow for offline subtraction of the reflected signals.

The suitability of the developed acoustic sensors was further demonstrated in the recording of ultra-sonic pulses generated by a high intensity proton or laser beam hitting an ice or water target. This way, the mechanism of thermo-acoustic sound generation could be probed as discussed in chapter 6. In water, several such efforts had been previously performed, in general confirming the thermo-elastic origin of the acoustic waves. On the other hand, observations close to the point of highest density at 4 °C in water, where the acoustic signal is expected to vanish, had not shown consistent results. In a combined effort with the universities of Uppsala and Erlangen-Nürnberg another series of tests has therefore been performed. Water as well as ice were used as target media. Comparison of the simulation in section 6.1 of the energy deposit for both the laser and the proton beam shows very similar profiles in ice as well as in water.

For the water measurements, a numerical calculation of the acoustic pulse including also

the temporal evolution of the energy deposit was compared to the data obtained with calibrated reference hydrophones at several positions relative to the beam entrance. Very good agreement of the recorded signals with the simulation was found for all positions. A comparison of the laser and proton beam measurements showed that the residual signals recorded with the proton beam at 4 °C may possibly be caused by the excess charge deposited with the proton bunch. While the absence of a calibrated sensor prohibited such elaborate studies in ice, several basic relations predicted by the thermo-acoustic model could be confirmed. The increasing delay of the acoustic signal for increasing distances of the beam entrance point with respect to the sensor was found to match the corresponding increase in sound propagation time. As in the case of the water measurements, a near-field to far-field transition was observed. For all three different sensors used in the setup, the signal amplitude scaled linearly with the proton bunch energy, while the signal shape in the time domain remained stable. Investigations at different temperatures ranging from -2°C to -30°C showed a very strong increase of the signal amplitude for lower temperatures. Although being likely a combination of several effects, an increase in the velocity of sound and higher sensitivity at the correspondingly higher frequencies are suggested as dominant sources, but also an increased absorption at higher temperatures cannot be excluded.

In contrast, for the much colder but also more pure ice at South Pole with a temperature of -51°C close to the surface, an absorption length in the order of 8 km is expected. To establish this prediction, as well as the calculated sound velocity profiles and predicted low ambient noise levels, the dedicated experiment presented in chapter 7 has been devised and implemented. The South Pole Acoustic Test Setup (SPATS) consists of three strings, each equipped with seven stages at various depth from 80 m to 400 m. Each stage holds a three-channel sensor module along with a piezo-ceramic high-power transmitter following the designs described in chapter 5. Apart from the lowest level, which holds a pressure sensor to determine the installation depth, each level also holds a temperature sensor. Both sensor and transmitter modules are connected by electrical cables bearing analogue and digital signals to a control and data-acquisition computer (*String-PC*) embedded in the snow at the surface. From a *Master-PC* in the counting house, communication and data transfer to the *String-PCs* of all three strings is provided by electrical service wires in the ICECUBE surface cables. Time synchronisation of the *String-PCs* is achieved by a GPS based time synchronisation signal. The system is designed to be operated independent from the ICECUBE system through a satellite link from the northern hemisphere.

As shown in section 7.4, the full setup was extensively tested regarding three aspects. In a freezer, all in-ice equipment was tested for full functionality down to -55°C . For the *String-PCs*, that will be buried in a depth of only ≈ 2 m and may be subject to annual temperature variations, a test with changing temperatures down to -60°C lasting around two months was performed. Extensive tests were also conducted to avoid possible interference with any ICECUBE installation.

The system also showed excellent performance under the harsh conditions met in an outdoor test on a frozen lake. Deploying one sensor and one transmitter at a time in the water below the ice, the capability of the setup in sending and recording pulses over distances of more than 800 m were proven. At the same time, an estimate of the variation of sensitivity of transmittivity of the sensor and transmitter modules respectively could be obtained. A

non-uniformity of around 40% was found for both modules. Lacking a calibration possibility in ice, all SPATS sensors and transmitters were also calibrated in water using the single pulse method that has previously been established. Precise sensitivity and equivalent self noise spectra could be measured for all sensor modules. Again, a very high sensitivity dropping with higher frequencies due to a dropping amplifier gain combined with a low self noise level was found, but with considerable variation from sensor to sensor. Variation in the transmitters power was on the level expected from variation in the piezo-electric constant of the ceramics.

As could be shown in a simulation study in section 7.5, when comparing the signal amplitudes obtained from the same transmitter by different sensors these module to module variations will not harm the performance of the setup. From a semi-analytic approximation the qualitative performance measuring the sound velocity profile was shown. The quantitative capabilities in measuring absorption were determined in a Monte Carlo simulation. Due to the short distances of the strings, the setup will not be able to provide positive evidence of absorption on a 3σ confidence level, if the predictions on absorptivity are correct. Yet at the same time, the limits that can then be obtained on the absorption length for the same confidence level, may well exceed the measured attenuation length for Cherenkov light by two orders of magnitude.

Albeit being mainly designed for that purpose, the SPATS setup should not only be regarded as an experiment to measure the ultrasonic properties of antarctic ice. After its installation in the austral summer 2006/2007, it will be the largest installation that has been built in the framework of detection of neutrinos by ultrasonic waves. It will therefore also act as a precursor to future acoustic neutrino detection experiments. A proposal for such a detector by expanding the currently under construction ICECUBE array with an array of radio and acoustic receivers is presented in chapter 4. In a simulation, 91 additional strings with 10 radio and 300 acoustic receivers each are assumed in a hexagonal grid of 1 km spacing. In addition, 13 more optical strings are assumed to complement the ICECUBE array to enhance its effective volume at very high energies. The response of each of the detector components – optical, radio and acoustic – was simulated for a common set of neutrino events in the energy range of 10^{16} eV to 10^{20} eV. Effective neutrino volumes are calculated for each of the methods alone, as well as for all possible combinations of fulfilled trigger conditions. Above energies of 1 EeV, the radio and acoustic method clearly outperform the optical detector. For a conservative estimate of the flux of GZK neutrinos more than 10 events per year are expected in both subdetectors, with a significant fraction of overlay that will allow for cross calibration of the methods.

As has been shown in the discussion of the prerequisites in chapter 3, the lower estimates predicted for the flux of cosmogenic neutrinos agree rather well, so that such an array would indeed yield an independent probe for the absorption of cosmic rays in the GZK cutoff. As shown in chapter 2 the neutrino flux is closely linked to the cosmic ray absorption effect. Even with a few ten neutrino events, constraints especially on the composition of cosmic ray at the highest energies should be possible. Other neutrino generation models predict fluxes that are considerably higher, and will therefore be tested as well. At the same time, the rapidly increasing absorption of horizontal neutrinos in the earth mantle close to the horizon provides a good handle on the total neutrino-nucleon cross section. Exotic models

predicting cross sections well above those of the Standard Model should be possible to test with a handful of neutrino events.

While the sheer size of the proposed array of about 50 km^3 makes this a seemingly daunting idea, it needs to be compared to the simulation of corresponding arrays in water, where detector volumes exceeding 1000 km^3 are necessary to obtain comparable results. The size will provide a challenge for the technical implementation.

If based on piezo-electric ceramics, acoustic sensors are considerably simpler to build and quite more robust concerning mechanical stress than e.g. the photomultipliers used in the optical detection of neutrinos. Due to the comparably low frequency of the signal, the requirements on digitisation electronics are weak compared to those for radio detection, where GHz sampling rates are needed. The same holds true for the requirements on time synchronisation, that may in rough approximation be weakened by a factor $v_l/c = 10^{-5}$ corresponding to the different propagation speeds of the signals.

Considering the high fraction of the costs of electric cable already for the much smaller SPATS installation, the proposed very close vertical spacing of 300 channels per string may seem another challenge. Digitisation of the signals in ice as successfully shown by the ICECUBE experiment and multiplexing of signals of many sensors on the same electrical cables can provide a solution here. Also piezo-electric ceramics and $k\text{Hz}$ data acquisition technology are cheap, so that the costs for a single sensor channel should be significantly lower than in the case of a radio or optical detector. At the same time, acoustic sensors are much smaller than the currently used optical detectors, which need a certain size of the photo-cathode to efficiently collect the light. Combined with the fact that for acoustic detection, the upper ice layers seem favourable, not only due to better suited ice properties but also due to a lower absorption of the neutrinos in the ice above the detector, the holes for an acoustic neutrino detector can be not only smaller in diameter but also more shallow. This will significantly decrease the cost of these holes, if compared to the holes currently drilled for ICECUBE. A preliminary estimate of the overall cost of an acoustic neutrino detection array as proposed in chapter 4 resulted in a total that will be a fraction of the cost of the ICECUBE detector. Granted that the predictions of the ultra-sonic ice properties are experimentally confirmed in the near future, the realisation of an acoustic neutrino detector for the highest energies may be in reach even within the next decade.

Bibliography

- [A⁺01] Albul, V. I.; et al.: Measurements of the parameters of the acoustic radiation accompanying the moderation of an intense proton beam in water. In: *Instrum. Exp. Tech.*, volume 44:pp. 327–334, 2001.
- [A⁺04a] Ackermann, M.; et al.: Search for neutrino-induced cascades with AMANDA. In: *Astropart. Phys.*, volume 22:pp. 127–138, 2004.
- [A⁺04b] Ahrens, J.; et al. (ICECUBE): Sensitivity of the ICECUBE detector to astrophysical sources of high energy muon neutrinos. In: *Astropart. Phys.*, volume 20:pp. 507–532, 2004. [astro-ph/0305196](#).
- [A⁺05a] Abbasi, R. U.; et al. (The High Resolution Fly’s Eye): Observation of the ankle and evidence for a high-energy break in the cosmic ray spectrum. In: *Phys. Lett.*, volume B619:pp. 271–280, 2005. [astro-ph/0501317](#).
- [A⁺05b] Ackermann, M.; et al.: Flux limits on ultra high energy neutrinos with AMANDA-B10. In: *Astropart. Phys.*, volume 22:pp. 339–353, 2005.
- [A⁺05c] Ahlers, M.; et al.: Neutrinos as a diagnostic of cosmic ray galactic / extra-galactic transition. In: *Phys. Rev.*, volume D72:p. 023001, 2005. [astro-ph/0503229](#).
- [A⁺05d] Antoni, T.; et al. (KASCADE): KASCADE measurements of energy spectra for elemental groups of cosmic rays: Results and open problems. In: *Astropart. Phys.*, volume 24:pp. 1–25, 2005. [astro-ph/0505413](#).
- [A⁺05e] Aramo, C.; et al.: Earth-skimming UHE tau neutrinos at the fluorescence detector of Pierre Auger Observatory. In: *Astropart. Phys.*, volume 23:pp. 65–77, 2005. [astro-ph/0407638](#).
- [A⁺06a] Ardouin, D.; et al.: CODALEMA: a cosmic ray air showers radiodetection experiment. In: Nahnauer and Böser [NB06], pp. 192–196. Also published in *Int. J. Mod. Phys. A*, Vol. 21, Supp. 01, URL <http://www.ifh.de/arena>.
- [A⁺06b] Aynutdinov, V.; et al.: Status and new results from the BAIKAL detector. In: *J. Phys. Conf. Ser.*, volume 39:pp. 441–443, 2006.
- [A⁺06c] Aynutdinov, V. M.; et al.: A device for detection of acoustic signals from super high energy neutrinos. In: Nahnauer and Böser [NB06], pp. 202–206. Also published in *Int. J. Mod. Phys. A*, Vol. 21, Supp. 01, URL <http://www.ifh.de/arena>.

- [ABO⁺05] Ave, M.; Busca, N.; Olinto, A. V.; Watson, A. A.; Yamamoto, T.: Cosmogenic neutrinos from ultra-high energy nuclei. In: *Astropart. Phys.*, volume 23:pp. 19–29, 2005. [astro-ph/0409316](#).
- [ABS⁺04] Arndt, R. A.; Briscoe, W. J.; Strakovsky, I. I.; Workman, R. L.; Pavan, M. M.: Dispersion relation constrained partial wave analysis of πn elastic and $\pi n \rightarrow \eta n$ scattering data: The baryon spectrum. In: *Phys. Rev.*, volume C69:p. 035213, 2004. [nucl-th/0311089](#).
- [AD77] Askar'yan, G. A.; Dolgoshein, B. A.: Acoustic recording of high-energy neutrinos. In: *Pisma Zh. Eksp. Teor. Fiz.*, volume 25:pp. 232–233, 1977.
- [ADKM79] Askar'yan, G. A.; Dolgoshein, B. A.; Kalinovsky, A. N.; Mokhov, N. V.: Acoustic detection of high-energy particle showers in water. In: *Nucl. Instrum. Meth.*, volume 164:pp. 267–278, 1979.
- [AFG02] Anchordoqui, L. A.; Feng, J. L.; Goldberg, H.: p-branes and the GZK paradox. In: *Phys. Lett.*, volume B535:pp. 302–308, 2002. [hep-ph/0202124](#).
- [AGJ⁺05] Acharya, B. S.; Gupta, S.; Jagadeesan, P.; Jain, A.; Karthikeyan, S.; Morris, S.; Suresh, T., editors: *Proceedings of the 29th International Cosmic Ray Conference (ICRC 2005), Pune, India*. Tata Institute of Fundamental Research, Mumbai, 03.-10. August 2005.
- [AJY00] Athar, H.; Jezabek, M.; Yasuda, O.: Effects of neutrino mixing on high-energy cosmic neutrino flux. In: *Phys. Rev. D*, volume 62(103007), 2000. [hep-ph/0005104](#).
- [Alb98] Albert, D.G.: Theoretical modeling of seismic noise propagation in firn at the South Pole, Antarctica. In: *Geophys. Res. Lett.*, volume 25(23):pp. 4257–4260, 1998.
- [Alb04] Albert, Donald G.: private communication, 2004.
- [AMZ97] Alvarez-Muniz, J.; Zas, E.: Cherenkov radio pulses from EeV neutrino interactions: The LPM effect. In: *Phys. Lett.*, volume B411:pp. 218–224, 1997. [astro-ph/9706064](#).
- [AMZ98] Alvarez-Muniz, J.; Zas, E.: The LPM effect for EeV hadronic showers in ice: Implications for radio detection of neutrinos. In: *Phys. Lett.*, volume B434:pp. 396–406, 1998. [astro-ph/9806098](#).
- [AMZ99] Alvarez-Muniz, J.; Zas, E.: EeV hadronic showers in ice: The LPM effect, 1999. [astro-ph/9906347](#).
- [ART06] Ahlers, M.; Ringwald, A.; Tu, Hu.: Strongly interacting neutrinos as the highest energy cosmic rays: A quantitative analysis. In: *PoS*, volume JHW2005:p. 014, 2006. [astro-ph/0512439](#).

- [ASJ75] Allan, H. R.; Sun, M. P.; Jones, J. K.: Experimental work on radio emission from EAS at HAVERAH PARK. In: Pinkau [Pin75], pp. 3082–3085.
- [Ask57] Askar'yan, G. A.: Hydrodynamic radiation from the tracks of ionizing particles in stable liquids. In: *Sov. J. Atom. Energ.*, volume 3(8):pp. 921–923, 1957.
- [Ask62] Askar'yan, G. A.: Excess negative charge of an electron-photon shower and its coherent radio emission. In: *Sov. Phys. JETP*, volume 14:pp. 441–443, 1962.
- [B⁺58] Bogorodskii, V. V.; et al.: The elastic characteristics of ice. In: *Sov. Phys. Acoust.*, volume 4:pp. 19–23, 1958.
- [B⁺75] Borshkoysky, I. A.; et al.: On proton acoustic effect in condensed media. In: *Lett. Nuovo Cim.*, volume 12:pp. 638–640, 1975.
- [B⁺85] Baltrusaitis, R. M.; et al.: Limits on deeply penetrating particles in the $> 10^{17}$ – eV cosmic ray flux. In: *Phys. Rev.*, volume D31:p. 2192, 1985.
- [B⁺93] Bird, D. J.; et al. (HiRES): Evidence for correlated changes in the spectrum and composition of cosmic rays at extremely high-energies. In: *Phys. Rev. Lett.*, volume 71:pp. 3401–3404, 1993.
- [B⁺98] Butkevich, A. V.; et al.: Prospects for radio-wave and acoustic detection of ultra- and superhigh-energy cosmic neutrinos (cross sections, signals, thresholds). In: *Phys. Part. Nucl.*, volume 29:pp. 266–272, 1998.
- [B⁺06a] Bagnolo, P. E.; et al.: Fiber laser hydrophones as pressure sensors. In: Nahnhauser and Böser [NB06], pp. 102–106. Also published in *Int. J. Mod. Phys. A*, Vol. 21, Supp. 01, URL <http://www.ifh.de/arena>.
- [B⁺06b] Barwick, S. W.; et al. (ANITA): Constraints on cosmic neutrino fluxes from the ANITA experiment. In: *Phys. Rev. Lett.*, volume 96:p. 171101, 2006. [astro-ph/0512265](http://arxiv.org/abs/astro-ph/0512265).
- [BBGS05] Barwick, S.; Besson, D. Z.; Gorham, P.; Saltzberg, D.: South Polar in situ radio-frequency ice attenuation. In: *J. of Glaciology*, volume 51:pp. 231–238, 2005.
- [BBH⁺70] Beron, B. L.; Boughn, S. P.; Hamilton, W. O.; Hofstadter, R.; Martin, T. W.: Mechanical oscillations induced by penetrating particles. In: *IEEE Trans. Nucl. Sci.*, volume 17:pp. 65–66, 1970.
- [BBN⁺05a] Besson, D.; Böser, S.; Nahnhauser, R.; Price, P. B.; Vandenbroucke, J. A.: Simulation of a hybrid optical / radio / acoustic extension to ICECUBE for EHE neutrino detection. In: Nahnhauser and Böser [NB06], pp. 259–264. [astro-ph/0512604](http://arxiv.org/abs/astro-ph/0512604), URL <http://www.ifh.de/arena>.
- [BBN⁺05b] Besson, D.; Böser, S.; Nahnhauser, R.; Price, P. B.; Vandenbroucke, J. A.: Simulation of a hybrid optical / radio / acoustic extension to icecube for EeV neutrino detection. In: Acharya et al. [AGJ⁺05]. [astro-ph/0512604](http://arxiv.org/abs/astro-ph/0512604).

- [Bec06] Becherini, Y. (ANTARES): Status report of the ANTARES experiment. In: *J. Phys. Conf. Ser.*, volume 39:pp. 444–446, 2006. [astro-ph/0603570](#).
- [Ber05a] Berezhinsky, V.: SuperGZK neutrinos. To appear in the proceedings of 11th International Workshop on Neutrino Telescopes, Venice, Italy, 22-25 Feb 2005, 2005. [astro-ph/0509675](#).
- [Ber05b] Bergman, D. R. (HiRES): Fitting the HiRES spectra and monocular composition. In: *Int. J. Mod. Phys.*, volume A20:pp. 3143–3146, 2005.
- [BGK06] Bichsel, H.; Groom, D. E.; Klein, S. R.: *Review of Particle Physics*, chapter 27. Passage of particles through matter. Volume 33 of [Y⁺06], 2006. URL <http://pdg.lbl.gov>.
- [BH69] Beron, B. L.; Hofstadter, R.: Generation of mechanical vibrations by penetrating particles. In: *Phys. Rev. Lett.*, volume 23:pp. 184–186, 1969.
- [BHS92] Bhattacharjee, P.; Hill, Ch. T.; Schramm, D. N.: Grand unified theories, topological defects and ultrahigh- energy cosmic rays. In: *Phys. Rev. Lett.*, volume 69:pp. 567–570, 1992.
- [BK05] Baier, V. N.; Katkov, V. M.: Concept of formation length in radiation theory. In: *Phys. Rept.*, volume 409:pp. 261–359, 2005. [hep-ph/0309211](#).
- [Bos96] Bosetti, P. C. (DUMAND): DUMAND status report. In: *Nucl. Phys. Proc. Suppl.*, volume 48:pp. 4660–468, 1996.
- [Bös02] Böser, Sebastian: *Separation of atmospheric neutrinos with the AMANDA-II detector*. Diploma thesis, Technische Universität München, April 2002.
- [Bot05] Bottai, S. (EUSO): EUSO and neutrino detection. In: *Nucl. Phys. Proc. Suppl.*, volume 143:pp. 381–386, 2005.
- [Bow78] Bowen, T.: Sonic particle detection. In: Christov et al. [C⁺78], pp. 277–282.
- [BS00] Bhattacharjee, P.; Sigl, G.: Origin and propagation of extremely high energy cosmic rays. In: *Phys. Rept.*, volume 327:pp. 109–247, 2000. [astro-ph/9811011](#).
- [BW01] Bahcall, J. N.; Waxman, E.: High energy astrophysical neutrinos: The upper bound is robust. In: *Phys. Rev.*, volume D64:p. 023002, 2001. [hep-ph/9902383](#).
- [C⁺78] Christov, C. Ya.; et al., editors: *Proceedings of the 23rd International Cosmic Ray Conference (ICRC 1977), Plovdiv, Bulgaria*. B’lgarska Akademiia na Naukite, Sofia, 13.-26. August 1978.
- [C⁺01] Capone, A.; et al.: Hydro-acoustic detection of ultra-high and extremely high energy neutrinos. In: Kampert et al. [KHS⁺01], pp. 1264–1266.
- [C⁺06] Chechin, V. A.; et al.: Concept of the LORD instrument. In: Nahnauer and Böser [NB06], pp. 237–241. Also published in *Int. J. Mod. Phys. A*, Vol. 21, Supp. 01, URL <http://www.ifh.de/arena>.

- [Car01] Carroll, S. M.: The cosmological constant. In: *Living Rev. Rel.*, volume 4:p. 1, 2001. [astro-ph/0004075](#).
- [Col03] Colless, M.: Cosmological results from the 2dF galaxy redshift survey, 2003. [astro-ph/0305051](#).
- [Con06] Conolly, A.: Measuring the neutrino-nucleon cross section with SALSA. In: Nahnauer and Böser [NB06], pp. 163–167. Also published in *Int. J. Mod. Phys. A*, Vol. 21, Supp. 01, URL <http://www.ifh.de/arena>.
- [Cop81] Coppens, A. B.: Simple equations for the speed of sound in Neptunian waters. In: *J. Acoust. Soc. Am.*, volume 69(3):pp. 862–863, 1981.
- [CR04] Chirkin, D.; Rhode, W.: Muon Monte Carlo: A high-precision tool for muon propagation through matter, 2004. [hep-ph/0407075](#).
- [D⁺94] Dedenko, L. G.; et al.: Acoustic signal from neutrinos of ultrahigh-energy and background conditions for an acoustic neutrino telescope in the Ionian Sea. In: *Bull. Russ. Acad. Sci. Phys.*, volume 58:pp. 2075–2077, 1994.
- [D⁺97a] Dedenko, L. G.; et al.: SADCO: Hydroacoustic detection of super-high energy cosmic neutrinos, 1997. [astro-ph/9705189](#).
- [D⁺97b] Dedenko, L. G.; et al.: Prospects for deep-sea acoustic detection of neutrinos. In: *Bull. Russ. Acad. Sci. Phys.*, volume 61:pp. 469–471, 1997.
- [DA81] Dziewonski, A.; Anderson, D.: Preliminary reference earth model. In: *Phys. Earth and Planetary Interiors*, volume 25:p. 297, 1981.
- [dBC06] de Bonis, G.; Capone, A.: Preliminary results on hydrophone calibration with proton beam. In: Nahnauer and Böser [NB06], pp. 112–116. Also published in *Int. J. Mod. Phys. A*, Vol. 21, Supp. 01, URL <http://www.ifh.de/arena>.
- [Des06] Descamps, Freija: private communication, 2006.
- [DeY05] DeYoung, T. (ICECUBE): Status of the ICECUBE neutrino telescope. In: *Int. J. Mod. Phys.*, volume A20:pp. 3160–3162, 2005.
- [DL⁺06] Demidov, V. S.; Lyashuk, V. I.; et al.: ITEP investigation of acoustic phenomena from high energy particles. In: Nahnauer and Böser [NB06], pp. 122–126. Also published in *Int. J. Mod. Phys. A*, Vol. 21, Supp. 01, URL <http://www.ifh.de/arena>.
- [DM05] De Marco, D.: Propagation of UHECRs, 2005. [astro-ph/0506412](#).
- [DMSS06] De Marco, D.; Stanev, T.; Stecker, F. W.: Cosmogenic neutrinos from cosmic ray interactions with extragalactic infrared photons. In: *Phys. Rev.*, volume D73:p. 043003, 2006. [astro-ph/0512479](#).
- [DPR03] Donea, A. C.; Protheroe, R. J.; Reimer, A.: Cosmic rays from the nucleus of M87. In: Kajita et al. [KAK⁺03], pp. 695–698.

- [dVS03] de Vega, H. J.; Sanchez, N. G.: Extreme energy cosmic rays: Bottom-up vs. top-down scenarii. Lectures given at 4th International Workshop on New Worlds in Astroparticle Physics, Faro, Portugal, 5-7 Sep 2002., 2003. [astro-ph/0301039](#).
- [EHO⁺05] Eidelman, S.; Hayes, K.G.; Olive, K.A.; et al.: Review of Particle Physics. In: *Phys. Lett. B*, volume 592, 2004 and 2005. Partial update for edition 2006, URL <http://pdg.lbl.gov>.
- [EK69] Eisenberg, David; Kauzmann, Walter: *The structure and properties of water*. Clarendon Press, Oxford, 1969. ISBN 0-19-857026-0.
- [ER98] Epele, L. N.; Roulet, E.: On the propagation of the highest energy cosmic ray nuclei. In: *JHEP*, volume 10:p. 009, 1998. [astro-ph/9808104](#).
- [ERSW04] Eberle, B.; Ringwald, A.; Song, L.; Weiler, Th. J.: Relic neutrino absorption spectroscopy. In: *Phys. Rev.*, volume D70:p. 023007, 2004. [hep-ph/0401203](#).
- [ESS01] Engel, R.; Seckel, D.; Stanev, T.: Neutrinos from propagation of ultra-high energy protons. In: *Phys. Rev.*, volume D64:p. 093010, 2001. [astro-ph/0101216](#).
- [FG82a] Francois, R. E.; Garrison, G. R.: Sound absorption based on ocean measurements: Part I: Pure water and magnesium sulfate contributions. In: *J. Acoust. Soc. Am.*, volume 72(3):pp. 896–907, 1982.
- [FG82b] Francois, R. E.; Garrison, G. R.: Sound absorption based on ocean measurements. part ii: Boric acid contribution and equation for total absorption. In: *J. Acoust. Soc. Am.*, volume 72(6):pp. 1879–1890, 1982.
- [Fis06] Fischer, Jan H.: *Acoustic transducer for the South Pole Acoustic Test Setup*. Diploma thesis, Humboldt-Universität, Berlin, June 2006.
- [FKR02] Fodor, Z.; Katz, S. D.; Ringwald, A.: Relic neutrino masses and the highest energy cosmic rays. In: *JHEP*, volume 06:p. 046, 2002. [hep-ph/0203198](#).
- [FKRT03a] Fodor, Z.; Katz, S. D.; Ringwald, A.; Tu, H.: Bounds on the cosmogenic neutrino flux. In: *JCAP*, volume 0311:p. 015, 2003. [hep-ph/0309171](#).
- [FKRT03b] Fodor, Z.; Katz, S. D.; Ringwald, A.; Tu, H.: Electroweak instantons as a solution to the ultrahigh energy cosmic ray puzzle. In: *Phys. Lett.*, volume B561:pp. 191–201, 2003. [hep-ph/0303080](#).
- [FKRT04] Fodor, Z.; Katz, S. D.; Ringwald, A.; Tu, H.: Strong neutrino nucleon interactions at ultrahigh energies as a solution to the GZK puzzle, 2004. [hep-ph/0402102](#).
- [Fuk03] Fukuda, Y.: Status of solar neutrino observation at SUPER-KAMIOKANDE. In: *Nucl. Instrum. Meth.*, volume A503:pp. 114–117, 2003.
- [G⁺04] Gorham, P. W.; et al.: Experimental limit on the cosmic diffuse ultrahigh-energy neutrino flux. In: *Phys. Rev. Lett.*, volume 93:p. 041101, 2004. [astro-ph/0310232](#).

- [G⁺05] Gorham, P. W.; et al.: Accelerator measurements of the Askaryan effect in rock salt: A roadmap toward teraton underground neutrino detectors. In: *Phys. Rev.*, volume D72:p. 023002, 2005. [astro-ph/0412128](#).
- [G⁺06] Gemmeke, H.; et al.: Advanced detection methods of radio signals from cosmic rays for KASCADE Grande and AUGER. In: Nahnauer and Böser [NB06], pp. 242–246. Also published in *Int. J. Mod. Phys. A*, Vol. 21, Supp. 01, URL <http://www.ifh.de/arena>.
- [GAH⁺06] Graf, K.; Anton, G.; Hössl, J.; Karg, T.; et al.: Testing thermo-acoustic sound generation in water with proton and laser beams. In: Nahnauer and Böser [NB06], pp. 127–131. Also published in *Int. J. Mod. Phys. A*, Vol. 21, Supp. 01, URL <http://www.ifh.de/arena>.
- [Gan03] Gangui, A.: Cosmology from topological defects. In: *AIP Conf. Proc.*, volume 668:pp. 226–262, 2003. [astro-ph/0303504](#).
- [Giu06] Giuliani, A.: Review of neutrino mass measurements. In: *AIP Conf. Proc.*, volume 815:pp. 9–18, 2006.
- [GKCW88] Gagnon, R. E.; Kieft, H.; Clouter, M. J.; Whalley, E.: Pressure dependence of the elastic constants of ice *Ih* to 2.8 kbar by Brillouin spectroscopy. In: *J. Chem. Phys.*, volume 89:pp. 4522–4528, 1988.
- [Gor06] Gorodetzky, Ph. (The EUSO): EUSO in september 2004. In: *Nucl. Phys. Proc. Suppl.*, volume 151:pp. 401–406, 2006. [astro-ph/0502187](#).
- [Gow62] Gow, A. J.: Results of measurements in the 309 meter bore hole at Byrd Station, Antarctica. In: *J. of Glaciology*, volume 4(31):pp. 771–784, 1962.
- [GP81] Grenfell, T. C.; Perovich, D. K.: Radiation absorption coefficients of polycrystalline ice from 400–1400 nm. In: *J. Geophys. Research*, volume 86(C8):pp. 7447–7450, 1981.
- [GQRS96] Gandhi, R.; Quigg, Ch.; Reno, M. H.; Sarcevic, I.: Ultrahigh-energy neutrino interactions. In: *Astropart. Phys.*, volume 5:pp. 81–110, 1996. [hep-ph/9512364](#).
- [GR62] Gow, A. J.; Ramseier, R. O.: Age hardening of snow at the South Pole. In: *J. of Glaciology*, volume 4(31):pp. 521–536, 1962.
- [Gra04] Graf, Kay: *Teststrahlmessung zur akustischen Neutrinodetektion: Thermoakustische Schallerzeugung in Wasser*. Diploma thesis, Friedrich-Alexander Universität, Erlangen-Nürnberg, July 2004.
- [Gre66] Greisen, K.: End to the cosmic ray spectrum? In: *Phys. Rev. Lett.*, volume 16:pp. 748–750, 1966.
- [GSS05] Gaisser, T.K.; Stanev, T.; Sokolsky, P.V.: *Review of Particle Physics*, chapter 24. Cosmic Rays. Volume 592 of [EHO⁺05], 2004 and 2005. Partial update for edition 2006, URL <http://pdg.lbl.gov>.

- [H⁺00] Hayashida, N.; et al.: Updated AGASA event list above $4 \cdot 10^{19}$ eV, 2000. [astro-ph/0008102](#).
- [H⁺05] Horneffer, A.; et al. (LOPES): Measuring radio pulses from air showers with LOPES. In: *Int. J. Mod. Phys.*, volume A20:pp. 6828–6830, 2005.
- [H⁺06] Horneffer, A.; et al.: Radio detection of cosmic ray with LOPES. In: Nahnauer and Böser [NB06], pp. 168–181. Also published in *Int. J. Mod. Phys. A*, Vol. 21, Supp. 01, URL <http://www.ifh.de/arena>.
- [Hel04] Heller, Rainer: private communication, 2004.
- [HF06] Huege, T.; Falke, H.: Monte carlo simulations of radio emission from cosmic ray air showers. In: Nahnauer and Böser [NB06], pp. 60–64. Also published in *Int. J. Mod. Phys. A*, Vol. 21, Supp. 01, URL <http://www.ifh.de/arena>.
- [HH04a] Halzen, F.; Hooper, D.: ICECUBE-Plus: An ultra-high energy neutrino telescope. In: *JCAP*, volume 0401:p. 002, 2004. [astro-ph/0310152](#).
- [HH04b] Han, T.; Hooper, D.: The particle physics reach of high energy neutrino astronomy. In: *New J. of Phys*, volume 6:p. 150, 2004. URL <http://www.njp.org/>.
- [HJM81a] Hunter, S. D.; Jones, W. V.; Malbrough, D. J.: Nonthermal acoustic signals from absorption of a cylindrical laser beam in water. In: *J. Acoust. Soc. Am.*, volume 69(6):pp. 1563–1567, June 1981.
- [HJM⁺81b] Hunter, S. D.; Jones, W. V.; Malbrough, D. J.; Buren, A. L. Van; Liboff, A.; Bowen, T.; Jones, J. J.; Learned, J. G.; Bradner, H.; Pfeffer, L.; March, R.; Camerini, U.: Acoustic signals of nonthermal origin from high energy protons in water. In: *J. Acoust. Soc. Am.*, volume 69(6):pp. 1557–1562, June 1981.
- [HTS05] Hooper, D.; Taylor, A.; Sarkar, S.: The impact of heavy nuclei on the cosmogenic neutrino flux. In: *Astropart. Phys.*, volume 23:pp. 11–17, 2005. [astro-ph/0407618](#).
- [Hun99] Hundertmark, S.: *AMASIM* neutrino detector simulation program. In: Spiering [Spi99]. DESY-Proc-1999-01.
- [HZS91] Halzen, F.; Zas, E.; Stanev, T.: Radiodetection of cosmic neutrinos: A numerical, real time analysis. In: *Phys. Lett.*, volume B257:pp. 432–436, 1991.
- [ICE95] Measurement microphone, part 3: Primary method for free-field calibration of laboratory standard microphones by the reciprocity technique. International standard, International Electrotechnical Committee, November 1995. CEI/IEC 1094-3:1995, URL <http://www.iec.ch/>.
- [K⁺06] Kravchenko, I.; et al.: RICE limits on the diffuse ultra-high energy neutrino flux. In: *Phys. Rev.*, volume D73:p. 082002, 2006. [astro-ph/0601148](#).

- [KAK⁺03] Kajita, T.; Asaoka, Yo.; Kawachi, A.; Sasaki, M.; Matsubara, Y., editors: *Proceedings of the 28th International Cosmic Ray Conference (ICRC 2003)*, Tsukuba, Japan. Universal Academy Press, Tokio, 31. July - 7. August 2003.
- [Kar06] Karg, Timo: *Detection of ultra high energy neutrinos with an underwater very large volume array of acoustic sensors: A simulation study*. Ph.D. thesis, Friedrich-Alexander Universität, Erlangen-Nürnberg, Februar 2006.
- [Kat06] Katz, U. F.: KM3NET: Towards a km³ Mediterranean neutrino telescope. Presented at 2nd VLVNT Workshop on Very Large Neutrino Telescope (VLVNT2), Catania, Italy, 8-11 Nov 2005, 2006. astro-ph/0606068.
- [Kay06] Kayser, B.: *Review of Particle Physics*, chapter 13. Neutrino mass, mixing, and flavor change. Volume 33 of [Y⁺06], 2006. URL <http://pdg.lbl.gov>.
- [KHS⁺01] Kampert, K.-H.; Hainzelmann, G.; Spiering, C.; Simon, M.; Lorenz, E.; Pohl, M.; Droege, W.; Kunow, H.; Scholer, M., editors: *Proceedings of the 27th International Cosmic Ray Conference (ICRC 2001)*, Hamburg, Germany. Copernicus Gesellschaft e.V., Lindau, 07.-15. August 2001.
- [KKSS02a] Kalashev, O. E.; Kuzmin, V. A.; Semikoz, D. V.; Sigl, G.: Ultra-high energy cosmic rays from neutrino emitting acceleration sources? In: *Phys. Rev.*, volume D65:p. 103003, 2002. hep-ph/0112351.
- [KKSS02b] Kalashev, O. E.; Kuzmin, V. A.; Semikoz, D. V.; Sigl, G.: Ultra-high energy neutrino fluxes and their constraints. In: *Phys. Rev.*, volume D66:p. 063004, 2002. hep-ph/0205050.
- [Kri06] Krieger, Kevin: *Optimisation of a Laboratory Setup for Testing of Acoustic Neutrino Detectors in Ice*. Diploma thesis, Westsächsische Hochschule Zwickau (FH), July 2006.
- [KS06] Karlik, Y.; Svet, V.: Converted hydroacoustic antenna MG-10M as basic module for a deep water neutrino-telescope. In: Nahnauer and Böser [NB06], pp. 197–201. Also published in *Int. J. Mod. Phys. A*, Vol. 21, Supp. 01, URL <http://www.ifh.de/arena>.
- [Kur06] Kurahashi, N.: Study of acoustic ultra-high energy neutrino detection phase II. In: Nahnauer and Böser [NB06], pp. 217–220. Also published in *Int. J. Mod. Phys. A*, Vol. 21, Supp. 01, URL <http://www.ifh.de/arena>.
- [KW05] Kashti, T.; Waxman, E.: Flavoring astrophysical neutrinos: Flavor ratios depend on energy. In: *Phys. Rev. Lett.*, volume 95:p. 181101, 2005. astro-ph/0507599.
- [L⁺78] Levi, M.; et al.: Experimental studies of the acoustic signature of proton beams traversing fluid media. In: *IEEE Trans. Nucl. Sci.*, volume 25:pp. 325–332, 1978.

- [L⁺06] Lahmann, R.; et al.: Integration of acoustic detection equipment into ANTARES. In: Nahnauer and Böser [NB06], pp. 227–232. Also published in Int. J. Mod. Phys. A, Vol. 21, Supp. 01, URL <http://www.ifh.de/arena>.
- [LAG⁺02] Lehtinen, N. G.; Adam, Sh.; Gratta, G.; Berger, Th. K.; Buckingham, M. J.: Sensitivity of an underwater acoustic array to ultra-high energy neutrinos. In: *Astropart. Phys.*, volume 17:pp. 279–292, 2002. [astro-ph/0104033](#).
- [Lea79] Learned, J. G.: Acoustic radiation by charged atomic particles in liquids: An analysis. In: *Phys. Rev.*, volume D19:pp. 3293–3307, 1979.
- [Lea93] Leahy, D. A., editor: *Proceedings of the 23rd International Cosmic Ray Conference (ICRC 1993), Calgary, Canada*. The University of Calgary, Calgary, 19.-30. July 1993.
- [LGJRD04] Lehtinen, N. G.; Gorham, P. W.; Jacobson, A. R.; Roussel-Dupre, R. A.: FORTE satellite constraints on ultra-high energy cosmic particle fluxes. In: *Phys. Rev.*, volume D69:p. 013008, 2004. [astro-ph/0309656](#).
- [LM00] Learned, J. G.; Mannheim, K.: High-energy neutrino astrophysics. In: *Ann. Rev. Nucl. Part. Sci.*, volume 50:pp. 679–749, 2000.
- [LP53a] Landau, L. D.; Pomeranchuk, I.: Electron cascade process at very high-energies. In: *Dokl. Akad. Nauk Ser. Fiz.*, volume 92:pp. 735–738, 1953.
- [LP53b] Landau, L. D.; Pomeranchuk, I.: Limits of applicability of the theory of bremsstrahlung electrons and pair production at high-energies. In: *Dokl. Akad. Nauk Ser. Fiz.*, volume 92:pp. 535–536, 1953.
- [LW93] Learned, J. G.; Wilkes, R. J.: Acoustical detection of cascades in DUMAND. In: Leahy [Lea93].
- [Man95] Mannheim, K.: High-energy neutrinos from extragalactic jets. In: *Astropart. Phys.*, volume 3:pp. 295–302, 1995.
- [Man05] Mantsch, P. M. (AUGER): The Pierre Auger Observatory: Progress and first results. In: Acharya et al. [AGJ⁺05]. [astro-ph/0604114](#).
- [Mil87] Millner, Rudolf: *Ultraschalltechnik - Grundlagen und Anwendung*. VEB Fachbuchverlag, Leipzig, 1987. ISBN 3-87664-106-3.
- [MPP06] Miele, G.; Pastor, S.; Pisanti, O.: The aperture for UHE tau neutrinos of the AUGER fluorescence detector using a digital elevation map. In: *Phys. Lett.*, volume B634:pp. 137–142, 2006. [astro-ph/0508038](#).
- [MPR01] Mannheim, K.; Protheroe, R. J.; Rachen, J. P.: On the cosmic ray bound for models of extragalactic neutrino production. In: *Phys. Rev.*, volume D63:p. 023003, 2001. [astro-ph/9812398](#).

- [MSTV03] Maltoni, M.; Schwetz, T.; Tortola, M. A.; Valle, J. W. F.: Status of three-neutrino oscillations after the SNO-salt data. In: *Phys. Rev.*, volume D68:p. 113010, 2003. [hep-ph/0309130](#).
- [NB05] Niess, V.; Bertin, V.: Underwater acoustic detection of ultra high energy neutrinos. to be published in *Astropart. Phys.*, 2005. [astro-ph/0511617](#).
- [NB06] Nahnhauser, R.; Böser, S., editors: *Acoustic and Radio EeV Neutrino Detection Activities – Proceedings of the International Workshop (ARENA 2005), DESY Zeuthen, Germany, May 17-19, 2005*. World Scientific Publishing Co. Pte. Ltd, May 2006. ISBN 981-256-755-0. Also published in *Int. J. Mod. Phys. A*, Vol. 21, Supp. 01, URL <http://www.ifh.de/arena>.
- [Nie05] Niess, Valentin: *Detection acoustique sous-marine de neutrinos de ultra haute energie dans le cadre de l'experience ANTARES*. Ph.D. thesis, Université de la Méditerranée, Aix-Marseille, September 2005.
- [Per06] Perkin, J.: ACORNE simulation work. In: Nahnhauser and Böser [NB06], pp. 207–211. Also published in *Int. J. Mod. Phys. A*, Vol. 21, Supp. 01, URL <http://www.ifh.de/arena>.
- [Pin75] Pinkau, K., editor: *Proceedings of the 14th International Cosmic Ray Conference (ICRC 1975), Munich, Germany*. Max Planck Institute, Munich, 15.-29. August 1975.
- [PJ96] Protheroe, R. J.; Johnson, P. A.: Propagation of ultrahigh-energy protons over cosmological distances and implications for topological defect models. In: *Astropart. Phys.*, volume 4:p. 253, 1996. [astro-ph/9506119](#).
- [PL68] Pounder, E.R.; Langleben, M.P.: Acoustic attenuation in sea ice. In: *General Assembly of Bern: 25 September – 7 October 1967*, volume 79, pp. 161–169. International Association of Scientific Hydrology, 1968.
- [PNB⁺02] Price, P. B.; Nagornov, O. V.; Bay, R.; Chirkin, D.; He, Yu.; Miocinovic, P.; Richards, A.; Woschnagg, K.; Koci, B.; Zagorodnov, V.: Temperature profile for glacial ice at the South Pole: Implications for life in a nearby subglacial lake. In: *Proc. Nat. Acad. Sciences*, volume 99(12):pp. 7844–7847, 2002.
- [Pri93] Price, P. B.: Mechanisms of attenuation of acoustic waves in Antarctic ice. In: *Nucl. Instrum. Meth.*, volume A325:pp. 346–356, 1993.
- [Pri96] Price, P. B.: Comparison of optical, radio, and acoustical detectors for ultrahigh-energy neutrinos. In: *Astropart. Phys.*, volume 5:pp. 43–52, 1996. [astro-ph/9510119](#).
- [Pri06] Price, P. B.: Attenuation of acoustic waves in glacial ice and salt domes. In: *J. Geophys. Research*, volume 111(B02201), 2006. [astro-ph/0506648](#).
- [Pro66] Proctor, Th. M., Jr.: Low-temperature speed of sound in single-crystal ice. In: *J. Acoust. Soc. Am*, volume 39(5A):pp. 972–977, May 1966.

- [R⁺06] Rubtsov, G. I.; et al.: Upper limit on the ultra-high-energy photon flux from AGASA and YAKUTSK data. In: *Phys. Rev.*, volume D73:p. 063009, 2006. [astro-ph/0601449](#).
- [RD00] Royer, Daniel; Dieulesaint, Eugène: *Elastic Waves in Solids I*. Springer-Verlag, Berlin, Heidelberg, New York, 2000. ISBN 3-540-65932-3.
- [Rei05] Reil, K. (SALSA): SALSA: A teraton UHE neutrino detector. In: , 2005. Contributed to Particles and Nuclei International Conference (PANIC 05), Santa Fe, New Mexico,.
- [Ric06] Riccobene, G.: The NEMO acoustic test facility. In: Nahnauer and Böser [NB06], pp. 132–136. Also published in *Int. J. Mod. Phys. A*, Vol. 21, Supp. 01, URL <http://www.ifh.de/arena>.
- [Rin06] Ringwald, A.: Extremely energetic cosmic neutrinos: Opportunities for astrophysics, particle physics and cosmology. In: Nahnauer and Böser [NB06], pp. 12–19. Also published in *Int. J. Mod. Phys. A*, Vol. 21, Supp. 01, URL <http://www.ifh.de/arena>.
- [Rot03] Rottgering, H.: LOFAR, a new low frequency radio telescope. In: *New Astron. Rev.*, volume 47:pp. 405–409, 2003. [astro-ph/0309537](#).
- [RS01] Reil, K. A.; Springer, R. W. (HiRES): Preliminary stereo results from the High Resolution Fly’s Eye cosmic ray observatory. In: Kampert et al. [KHS⁺01], pp. 367–369.
- [RSBM01] Razzaque, S.; Seunarine, Su.; Besson, D. Z.; McKay, D. W.: Signal characteristics from electromagnetic cascades in ice. In: *AIP Conf. Proc.*, volume 579:pp. 139–146, 2001. [astro-ph/0101315](#).
- [S⁺79] Sulak, L.; et al.: Experimental studies of the acoustic signature of proton beams traversing fluid media. In: *Nucl. Instr. Meth.*, volume 161:p. 203, 1979.
- [S⁺04a] Salomon, K.; et al.: Studies of piezoelectric sensors by FE methods. In: *Verhandlungen der DPG Frühjahrstagung, Mainz*, p. T 202.1. Deutsche Physikalische Gesellschaft, 2004.
- [S⁺04b] Stecker, F. W.; et al.: Observing the ultrahigh energy universe with OWL eyes. In: *Nucl. Phys. Proc. Suppl.*, volume 136C:pp. 433–438, 2004. [astro-ph/0408162](#).
- [S⁺06] Spergel, D. N.; et al.: Wilkinson Microwave Anisotropy Probe (WMAP) three year results: Implications for cosmology, 2006. [astro-ph/0603449](#).
- [Sch05] Schwemmer, Stefanie: *Testmessungen zur akustischen Neutrinodetektion mit einem Nd:YAG-Laser*. Diploma thesis, Friedrich-Alexander Universität, Erlangen-Nürnberg, April 2005.

- [Sec98] Seckel, D.: Neutrino photon reactions in astrophysics and cosmology. In: *Phys. Rev. Lett.*, volume 80:pp. 900–903, 1998. [hep-ph/9709290](#).
- [Shi06] Shinozaki, K. (AGASA): AGASA results. In: *Nucl. Phys. Proc. Suppl.*, volume 151:pp. 3–10, 2006.
- [Slo06] Sloan, T.: Shower generation from ν interactions in water. In: Thompson et al. [T⁺06]. URL <http://www.shef.ac.uk/physics/arena/>.
- [Som05] Sommers, P. (Pierre Auger): First estimate of the primary cosmic ray energy spectrum above 3-EeV from the Pierre Auger Observatory. In: Acharya et al. [AGJ⁺05], pp. 101–106. [astro-ph/0507150](#).
- [Spi99] Spiering, C., editor: *Proceedings of the Workshop on Simulation and Analysis Methods for Large Neutrino Telescopes*. DESY, Zeuthen, Zeuthen, Germany, 1999. DESY-Proc-1999-01.
- [SS05] Seckel, D.; Stanev, T.: Neutrinos: The key to UHE cosmic rays. In: *Phys. Rev. Lett.*, volume 95:p. 141101, 2005. [astro-ph/0502244](#).
- [Sta81] Stauffer, B.: Analysis of air bubble composition, crystal size and pore shape in firn from south pole, 1980-1981. In: *Antarctic J.*, volume 16(5):pp. 76–78, 1981.
- [Ste04] Stegmaier, Jutta: *Optimierung akustischer Detektoren zum Nachweis hochenergetischer kosmischer Teilchen*. Diploma thesis, Johannes-Gutenberg Universität, Mainz, August 2004.
- [T⁺06] Thompson, L.; et al., editors: *International Conference on Acoustic and Radio EeV Neutrino detection Activities (ARENA 2006)*. 2006. URL <http://www.shef.ac.uk/physics/arena/>.
- [Uri96] Urlick, Robert J.: *Principles of underwater sound for engineers*. Peninsula Pub., 3rd edition, 1996. ISBN 0-932-14662-7.
- [Urr03] Urry, C. M.: AGN unification: An update, 2003. [astro-ph/0312545](#).
- [Van04] Vandenbroucke, Justin A.: private communication, 2004.
- [VGL05] Vandenbroucke, J.; Gratta, G.; Lehtinen, N.: Experimental study of acoustic ultra-high-energy neutrino detection. In: *Astrophys. J.*, volume 621:pp. 301–312, 2005. [astro-ph/0406105](#).
- [VP77] Volovik, V. D.; Popov, G. F.: Acoustic peak of protons in liquids. In: *Russ. Phys. J.*, volume 20(8):pp. 1056–1059, 1977.
- [WB99] Waxman, E.; Bahcall, J. N.: High energy neutrinos from astrophysical sources: An upper bound. In: *Phys. Rev.*, volume D59:p. 023002, 1999. [hep-ph/9807282](#).
- [Wei63] Weihaupt, J. G.: Seismic and gravity studies at the South Pole. In: *Geophysics*, volume 28(4):pp. 582–592, 1963.

- [Whi63] White, R. M.: Generation of elastic waves by transient surface heating. In: *J. of Appl. Phys.*, volume 34(12):pp. 3559–3567, December 1963.
- [Wil60] Wilson, W. D.: Equation for the speed of sound in sea water. In: *J. Acoust. Soc. Am.*, volume 32(10):p. 1357, October 1960.
- [WX02] Wang, Xi.; Xu, Xi.: Thermoelastic wave in metal induced by ultrafast laser pulses. In: *J. Therm. Stresses*, volume 25(5):pp. 457–473, May 2002.
- [Y⁺06] Yao, W.-M.; et al.: Review of Particle Physics. In: *J. Phys. G*, volume 33:pp. 1+, 2006. URL <http://pdg.lbl.gov>.
- [YT93] Yoshida, S.; Teshima, M.: Energy spectrum of ultrahigh-energy cosmic rays with extragalactic origin. In: *Prog. Theor. Phys.*, volume 89:pp. 833–845, 1993.
- [ZHS92] Zas, E.; Halzen, F.; Stanev, T.: Electromagnetic pulses from high-energy showers: Implications for neutrino detection. In: *Phys. Rev.*, volume D45:pp. 362–376, 1992.
- [ZK66] Zatsepin, G. T.; Kuzmin, V. A.: Upper limit of the spectrum of cosmic rays. In: *JETP Lett.*, volume 4:pp. 78–80, 1966.

Acknowledgement

First of all, I have to thank my supervisor, Dr. Rolf Nahnauer, for the endurance with which he supported my PhD work, as well as for the vigorous engagement he showed for the SPATS project. Without his diplomacy and foresight, acoustic neutrino detection in ice would not be where it is today. I also want to thank Prof. Dr. Hermann Kolanoski for taking the responsibility for this work, as well as for some very fruitful discussions.

My special thanks goes to all the members of the SPATS team. Among them, Allan Hallgren provided excellent hospitality in the three extended stays I enjoyed at Uppsala University during my PhD time. Not only in one of these stays, but also at many other occasions working with Justin Vandenbroucke provided excellent fun and good results in a unique combination. Spending the longest car ride in my life with Freija Descamps proved to be a pleasure, as much as working together with her at many other times. I also want to thank Stephan Hundertmark for learning about life and Linux, as well as for a formidable stay at his home.

During my PhD time, I had the pleasure to supervise three diploma students: Jutta Stegmaier, Jan Fischer and Kevin Krieger. Most of the results presented here would not have been possible without their engagement. The same must be said for the electronic engineers Kalle Sulanke and Mario Pohl, to whom I am in deep debt for the professional and virtuous electronic solutions they provided. I am equally grateful to our mechanical engineer in the project, Rainer Heller, for the design of numerous components, each of which worked perfectly fine, as well as to the DESY mechanical workshop, who provided all of them in due time.

The simulation of the hybrid detector would not have been possible without the experience of Dave Besson, whom I want to thank for a particularly friendly collaboration. An equally nice experience was the preparation of the proton beam test together with Kay Graf, whom I owe thanks along with the rest of the acoustic group at the University Erlangen-Nürnberg.

I am thankful to the Experimental Program Committee for approving the proton beam studies at the Thé Svedberg Laboratory, as well as to the TSL beam operator team for their support in conducting the experiments. Their commitment allowed for maximal scientific profit from a limited shift time. For the infrastructure to do the long range measurements at lake Torneträsk, as well as for most picturesque housing, I am in debt to the team of the Abisko National research station, who also offered me the great experience of driving

a snow-scooter. Special thanks goes to Karl-Ulrich Evers of the Hamburgische Schiffsbau-Versuchsanstalt. The frosty temperatures in the *Ice Tank* at their site, which was used in several calibration efforts, were in strong contrast to the warm welcome provided by the HSVA staff. The temperatures I enjoyed during the stay at the Institute of Acoustics "O.M. Corbino" were most pleasurable, as well as the hospitality provided by Silvano Buogo. For providing hydrophone calibration and access to their water tank as well as big support in the measurements I am in debt to him.

Finally, my thanks goes to the whole astro-particle group in Zeuthen. I spent a most pleasurable time with them. Especially I want to mention my fellow PhD students Henrike Wissing, Markus Ackermann, Oxana Tarasova, Bernhard Voigt and Stefan Klepser. Very good pizza and true espresso are only a few of the things I have to thank Elisa Bernardini for.

Most of the people named before, as well as Delia Tosi, Martin Tluzykont and Mike Walter I also want to thank for intensive proof-reading of my thesis.

Among the members of the ICECUBE collaboration, special thanks goes to Elisa Resconi, who taught me how to stay fresh in every situation.

Last, but for sure not least, I want to thank my family and all my friends for the unbelievable amount of support they gave me during all the hard times in the last four years. The patience to overcome the small and not so small problems I had to face is built on my trust in them.

Selbständigkeitserklärung

Hiermit erkläre ich, diese Arbeit selbstständig und nur unter Verwendung der angegebenen Hilfsmittel erstellt zu haben.

Berlin, 3. August 2007